Long-term Chemical Characterization and Source Apportionment of $PM_{2.5}$ in the San Joaquin Valley

Final Report
Contract 22RD038

Prepared for:
California Air Resources Board

Principal Investigator:
Qi Zhang

Department of Environmental Toxicology
University of California, Davis
One Shields Avenue, Davis, CA, 95616

January 30, 2026

DISCLAIMER

The statements and conclusions in this report are those of the University and not necessarily those of the California Air Resources Board. The mention of commercial products, their source, or their use in connection with material reported herein is not to be construed as actual or implied endorsement of such products.

ACKNOWLEDGEMENTS

The information provided in this report was supported by postdoctoral and student researchers with guidance from their faculty mentors. The core team consisted of the following individuals:

- Wenqing Jiang – postdoctoral scholar, Environmental Toxicology Dept, UC Davis
- Ashutosh Shukla – postdoctoral scholar, Environmental Toxicology Dept, UC Davis
- Christopher Niedek – postdoctoral scholar, Environmental Toxicology Dept, UC Davis
- Justin Trousdell – Ph.D. student, Atmospheric Sciences Graduate Group, UC Davis
- Ryan Farley – Ph.D. student, Agricultural and Environmental Chemistry Graduate Group, UC Davis

The authors would like to thank Drs. Chinmoy Sarkar and Morteza Amini (CARB) for providing grant management support. The authors also acknowledge additional grant management support provided by Drs. Yue Huang, and Toshihiro Kuwayama (CARB).

This Report was submitted in fulfillment of 22RD038, Long-term Chemical Characterization and Source Apportionment of $PM_{2.5}$ in the San Joaquin Valley by the University of California, Davis under the sponsorship of the California Air Resources Board. Work was completed as of 31 December 2025.

TABLE OF CONTENTS

LIST OF FIGURES AND TABLES

ABSTRACT

The San Joaquin Valley (SJV) continues to experience persistent air quality challenges associated with fine particulate matter ($PM_{2.5}$), including frequent exceedances of the 24-hour $PM_{2.5}$ National Ambient Air Quality Standards (NAAQS). In support of State Implementation Plan (SIP) attainment efforts and black carbon (BC) reduction requirements under Senate Bill 1383 (SB 1383), this project characterized long-term non-refractory $PM_{2.5}$ (NR-$PM_{2.5}$) composition, sources, and formation processes using real-time, high-time-resolution measurements combined with advanced source apportionment analyses.

Sub-hourly, continuous measurements of key particulate species (i.e., organic aerosol, nitrate, sulfate, ammonium, and chloride) have been conducted at Fresno and Bakersfield, California using Aerosol Chemical Speciation Monitors (ACSMs) since summer 2023 and are ongoing. These measurements provide a seasonally resolved characterization of NR-$PM_{2.5}$ mass and chemical composition across a broad range of pollution regimes. Positive Matrix Factorization (PMF) and constrained multilinear modeling were applied to the ACSM datasets to resolve major primary and secondary $PM_{2.5}$ sources and to quantify their seasonal and diurnal variability. Source apportionment results indicate that organic aerosol pollution in the SJV reflects contributions from multiple sources, including biomass burning associated with human activities and wildfires, as well as mobile and cooking-related emissions. However, secondary organic aerosol formed through atmospheric processing of emissions from these sources generally accounts for a major fraction of organic $PM_{2.5}$ mass, including during winter periods characterized by enhanced primary emissions. Comparisons with prior CARB-funded ACSM measurements (Contract #17RD008) indicate changes in $PM_{2.5}$ composition consistent with emission control efforts, while also highlighting secondary formation pathways that continue to impede attainment of the $PM_{2.5}$ NAAQS.

At both Fresno and Bakersfield, late fall and winter consistently represent the most polluted periods of the year. Although organic aerosol persistently dominates $PM_{2.5}$, accounting for approximately 75% of the annual average NR-$PM_{2.5}$ mass at both sites, wintertime $PM_{2.5}$ is also characterized by substantial contributions from ammonium nitrate. A complementary intensive field campaign conducted in Fresno during winter 2023-2024 employed a high-resolution Soot Particle Aerosol Mass Spectrometer (SP-AMS) and a long time-of-flight Chemical Ionization Mass Spectrometer with a Filter Inlet for Gases and Aerosols (FIGAERO-CIMS), providing unprecedented insight into source attribution and secondary organic aerosol formation during severe winter pollution episodes. A novel combined-PMF (c-PMF) framework developed in this study further demonstrates that elevated $PM_{2.5}$ concentrations are sustained by complex interplays among secondary inorganic and organic aerosol formation processes, including aqueous-phase processing, nocturnal chemistry, and residual-layer dynamics.

1. EXECUTIVE SUMMARY

1.1 Background

The San Joaquin Valley (SJV) continues to face persistent air quality challenges and remains one of the most polluted regions in the United States, despite decades of regulatory efforts. Exceedances of the 24-hour $PM_{2.5}$ National Ambient Air Quality Standard (NAAQS) of 35 μg m^{-3} occur most frequently during late fall and winter, when stagnant meteorological conditions, shallow boundary layers, and enhanced emissions promote severe pollution episodes.

$PM_{2.5}$ in the SJV is dominated by organic aerosol and ammonium nitrate, with contributions from mobile emissions, residential wood burning, cooking, agricultural activities, and, increasingly, wildfires. Black carbon, produced by incomplete combustion of biomass and fossil fuels, is an important component of $PM_{2.5}$ in urban areas such as Fresno and Bakersfield and has implications for both air quality and climate. $PM_{2.5}$ concentrations and composition exhibit strong diurnal and seasonal variability driven by changes in emissions, boundary layer dynamics, and secondary aerosol formation, underscoring the complexity of $PM_{2.5}$ sources and atmospheric processing in the region.

The State Implementation Plan (SIP) establishes $PM_{2.5}$ reduction milestones through 2025, while Senate Bill 1383 mandates a 50% reduction in anthropogenic black carbon emissions below 2013 levels by 2030. Evaluating progress toward these goals requires continuous, long-term, chemically resolved $PM_{2.5}$ measurements. Recent CARB-funded work has demonstrated that sub-hourly Aerosol Chemical Speciation Monitor (ACSM) measurements provide critical insight into non-refractory $PM_{2.5}$ components and their temporal variability. Extending these measurements and applying advanced source apportionment techniques provides a robust framework for assessing emission control strategies and informing future air quality management decisions in the SJV.

1.2 Objectives and Methods

The overall goal of this project is to improve understanding of emission sources, chemical pathways, and meteorological drivers of ambient $PM_{2.5}$ pollution in the San Joaquin Valley. Building on prior CARB-funded work, this project conducted sub-hourly ACSM measurements of NR-$PM_{2.5}$ concentration and composition in Fresno, California, alongside parallel long-term measurements in Bakersfield over a three-year period. These measurements were integrated with co-located observations of air pollutants and meteorological conditions to support advanced source apportionment analyses.

In addition, a focused intensive field campaign was conducted in Fresno during winter 2023-2024 using state-of-the-art online mass spectrometers (SP-AMS and FIGAERO-CIMS), providing

enhance quantitative constraints on the contributions of primary emissions and secondary aerosol formation processes to ambient $PM_{2.5.}$ Together, the long-term measurements from both sites and the intensive campaign dataset from Fresno were used to quantify contributions from major $PM_{2.5}$ sources and to assess the roles of secondary formation pathways and nocturnal residual-layer chemistry in shaping $PM_{2.5}$ pollution in the San Joaquin Valley.

To achieve these objectives, UCD carried out the following tasks:

Task 1: Conduct continuous, sub-hourly measurements of NR-$PM_{2.5}$ species using ACSMs at Fresno and Bakersfield over three years, with rigorous quality assurance and data processing.

Task 2: Perform a month-long intensive measurement campaign in Fresno during winter 2023-2024 using SP-AMS and FIGAERO-CIMS to enhance characterization of organic aerosol sources and formation processes.

Task 3: Apply advanced source apportionment analyses to ACSM, intensive-campaign, and co-located CARB data to quantify primary and secondary $PM_{2.5}$ sources, assess meteorological and nocturnal influences, examine temporal variability, and compare results between Fresno and Bakersfield to inform air quality modeling and emission reduction strategies.

Task 4: Communicate findings through stakeholder engagement and dissemination activities.

Detailed results are presented in the chapters that follow. Chapter 2 summarizes the long-term measurements and compares NR-$PM_{2.5}$ composition at Fresno and Bakersfield. Chapter 3 presents the development and application of advanced source apportionment methods, including rolling-window ME-2 analyses, to long-term ACSM datasets from Fresno and Bakersfield, providing insights into the temporal variability and contributions of major organic aerosol sources. Chapter 4 examines wintertime emission sources and secondary formation processes of $PM_{2.5}$ in Fresno based on the winter 2023-2024 intensive campaign, integrating SP-AMS and FIGAERO-CIMS measurements to resolve detailed source contributions and atmospheric processing pathways. Chapter 5 focuses on improving the characterization and quantification of cooking-related organic aerosol (COA) using chemically informed source apportionment of SP-AMS measurements, enabling the resolution of distinct cooking emissions sources under complex wintertime conditions.

1.3 Results

High–time-resolution ACSM measurements in Fresno and Bakersfield show strong agreement with co-located BAM $PM_{2.5}$ observations, demonstrating the reliability of ACSM data for long-term monitoring of $PM_{2.5}$ composition in the San Joaquin Valley. ACSM-measured non-refractory

$PM_{2.5}$ (NR-$PM_{2.5}$) accounts for the majority of $PM_{2.5}$ mass, with differences relative to BAM largely attributable to refractory components (e.g., black carbon, dust and metal salts) that are not detected by the ACSM. Comparisons with U.S. EPA CSN data show good agreement for ammonium and nitrate, moderate agreement for sulfate, and larger discrepancies for organic aerosol, consistent with volatilization losses in filter-based measurements.

NR-$PM_{2.5}$ composition exhibits strong seasonal patterns at both sites. Organic aerosol (OA) dominates year-round, contributing approximately 70 – 75% of NR-$PM_{2.5}$ mass, while wintertime $PM_{2.5}$ is characterized by substantial contributions from ammonium nitrate, which can account for up to ~ 50% of $PM_{2.5}$ during high-pollution episode. Fresno generally exhibits higher NR-$PM_{2.5}$ concentrations and stronger nighttime enhancements due to residential combustion and stagnant meteorology, while Bakersfield shows a greater influence of refractory material and more regionally uniform secondary aerosol contributions. Rolling-window ME-2 source apportionment of multi-year ACSM datasets resolved six OA factors at both sites and showed that secondary OA dominates OA mass throughout the year, including during winter periods with elevated primary emissions.

A winter 2023–2024 intensive field campaign in Fresno, integrating high-resolution aerosol mass spectrometry with chemical ionization mass spectrometry measurements, enabled application of combined PMF (cPMF) to resolve OA sources and formation pathways at enhanced chemical resolution. This analysis identified 19 distinct OA factors, linking bulk aerosol mass to molecular-level tracers. Results show that wintertime $PM_{2.5}$ episodes are driven by a combination of enhanced nighttime primary emissions—particularly biomass burning and cooking—and substantial secondary production. Secondary OA accounted for nearly half of total OA mass, with fog-driven aqueous processing (~20 – 25%) and nocturnal residual-layer chemistry (~10 – 15%) identified as key contributors.

1.4 Conclusions

This study demonstrates that integrating long-term ACSM measurements with advanced source apportionment methods and targeted intensive measurements campaigns provides a more comprehensive, process-level understanding of $PM_{2.5}$ sources and formation pathways in the SJV that cannot be achieved using traditional monitoring approaches alone. These enhanced insights support improved evaluation of emission control strategies and more effective air quality management.

The ACSM measurements have been thoroughly evaluated through intercomparisons with regulatory monitoring platforms, highlighting both the strengths and limitations of current approaches. ACSM measurements of NR-$PM_{2.5}$ show strong agreement with BAM $PM_{2.5}$ mass concentrations, confirming that non-refractory species account for the majority of fine particle

mass. Differences are primarily due to refractory components (e.g., black carbon and dust) not measured by the ACSM. Comparisons with CSN data show strong agreement for ammonium and nitrate, but larger discrepancies for organic aerosol and sulfate, consistent with volatilization losses of semi-volatile species – particularly semi-volatile organics and ammonium nitrate – in filter-based measurements. These findings underscore that real-time ACSM measurements more accurately represent semi-volatile $PM_{2.5}$ under ambient conditions. Inclusion of black carbon measurements would further improve mass closure and alignment with regulatory $PM_{2.5}$ observations, particularly at sites such as Bakersfield where refractory contributions are high.

While ACSM measurements combined with source apportionment effectively quantify bulk $PM_{2.5}$ composition and major sources, the addition of state-of-the-science high-resolution mass spectrometry (SP-AMS and FIGAERO-CIMS) significantly enhances source attribution and mechanistic understanding. Without these advanced measurements, secondary organic aerosol (SOA) would largely be represented as bulk oxygenated OA, limiting the ability to distinguish key formation pathways. Combined PMF (cPMF) analysis of SP-AMS and FIGAERO-CIMS data reveals that wintertime SOA arises from multiple distinct processes, including aqueous-phase reactions and nocturnal residual-layer chemistry, which cannot be resolved using ACSM data alone. These findings highlight the importance of integrating high-resolution measurements to inform interpretation of long-term datasets, at least via targeted intensive campaigns, to inform interpretation of long-term ACSM datasets and improve model representation of primary emission sources and secondary aerosol formation processes.

Across both Fresno and Bakersfield, organic aerosol dominates $PM_{2.5}$ mass (~70–75% on average), with SOA representing the largest fraction year-round. During winter, $PM_{2.5}$ is further enhanced by ammonium nitrate, contributing up to ~50% of $PM_{2.5}$ during high-pollution episodes. These episodes are driven by a combination of increased primary emissions, particularly biomass burning, cooking, and traffic, and efficient secondary formation under stagnant conditions. Secondary processes, including aqueous-phase chemistry and nocturnal residual-layer reactions, play a critical role in sustaining elevated $PM_{2.5}$ levels, even when daytime photochemistry is limited.

The findings have direct implications for air quality management in the SJV. Effective mitigation requires a dual focus on reducing both primary emissions and secondary aerosol precursors. Targeted controls on residential wood burning and other nighttime combustion activities are likely to be especially effective in reducing peak winter $PM_{2.5}$ levels. At the same time, sustained reductions in precursor gases (NO_x, VOCs, and NH_3) are necessary to limit persistent secondary aerosol formation. The observed differences between Fresno and Bakersfield further highlight the need for location-specific strategies that account for variations in emissions, meteorology, geophysical characteristics, and atmospheric processing.

Overall, this work provides a comprehensive and quantitative framework for understanding $PM_{2.5}$ sources and formation processes in the SJV, and offers strong critical guidance for improving air quality modeling and developing more effective, data-driven $PM_{2.5}$ mitigation strategies.

2. OVERVIEW OF ACSM MEASUREMENTS IN FRESNO AND BAKERSFIELD, CA

2.1 Introduction

The San Joaquin Valley (SJV) continues to experience persistent $PM_{2.5}$ air quality challenges, with exceedances of the 24-hour $PM_{2.5}$ National Ambient Air Quality Standard occurring most frequently during late fall and winter under stagnant conditions that promote pollutant accumulation (Chen et al., 2020). In addition, episodic but severe $PM_{2.5}$ pollution can occur during summer and fall due to increasing wildfire frequency and intensity across California (Altshuler et al., 2020; Jaffe et al., 2020), driven by emissions of primary organic aerosol (POA) and volatile organic compounds (VOCs) that contribute to secondary organic aerosol (SOA) formation (Zhang et al., 2018). Incomplete combustion of biomass and fossil fuels also produces black carbon (BC) – an important $PM_{2.5}$ component in urban centers such as Fresno and Bakersfield (Cappa et al., 2019; Chow et al., 2006; Collier et al., 2018; Farley et al., 2023; Zhang et al., 2016), with important implications for both air quality and climate forcing (Bond et al., 2006; Ding et al., 2016; Intergovernmental Panel on Climate Change, 2023; Koch and Del Genio, 2010; Ramanathan and Carmichael, 2008).

Ambient $PM_{2.5}$ concentrations and composition in the San Joaquin Valley (SJV) exhibit pronounced diurnal and seasonal variability driven by changes in emissions, meteorological conditions, boundary layer dynamics, and secondary aerosol formation processes (Betha et al., 2018; Chen et al., 2018, 2010; Collier et al., 2018; Ge et al., 2012b, a; Parworth et al., 2017; Pusede et al., 2016; Sun et al., 2022; Young et al., 2016). Previous studies have shown that $PM_{2.5}$ in the SJV is dominated by organic aerosol (OA) and ammonium nitrate, with predominant contributions from a range of anthropogenic sources including mobile emissions, residential wood burning, cooking, and agricultural activities (Chen et al., 2018; Chow et al., 2007; Ge et al., 2012a; Sun et al., 2022; Young et al., 2016).

Periods of elevated $PM_{2.5}$ in the region – particularly during late fall and winter and during multi-day pollution episodes – are typically associated with a combination of meteorological and chemical factors that limit pollutant dispersion and enhance particulate accumulation. These include stagnant conditions and weak ventilation that suppress horizontal and vertical mixing, strong nocturnal boundary layer inversions that trap emissions near the surface, increased primary emissions from residential, mobile, and other combustion sources, and efficient secondary aerosol production through both nighttime and daytime chemical processes (Brown et al., 2006; Chen et al., 2018; Ge et al., 2012a, b; Lurmann et al., 2006; Parworth et al., 2017; Prabhakar et al., 2017; Pusede et al., 2016; Sun et al., 2022; Young et al., 2016). Together, these factors promote the buildup and persistence of $PM_{2.5}$ over multiple days, result in severe pollution episodes and prolonged high-pollution seasons. The diversity of emission sources and the complexity of atmospheric processing in the SJV present significant challenges for effective air quality management and underscore the need for targeted control strategies focused on specific $PM_{2.5}$

components and source categories. Developing such strategies requires a comprehensive, process-level understanding of the emission sources, chemical pathways, and atmospheric processes that govern ambient $PM_{2.5}$ in the region.

The State Implementation Plan (SIP), including the 2018 Plan for the 1997, 2006, and 2012 $PM_{2.5}$ standards, establishes $PM_{2.5}$ reduction milestones through the 2024-2025 attainment years, while the Senate Bill 1383 mandates a 50% reduction in anthropogenic BC below 2013 levels by 2030. To meet these air pollution reduction goals, the SJV has implemented a range of regulatory and incentive-based control measures, including the phase-out of most open agricultural burning, stringent requirements for residential wood burning, reductions in $PM_{2.5}$ emissions from commercial cooking, industrial, and consumer-products sources, and financial incentives to replace high-emitting agricultural equipment, heavy-duty trucks, locomotives, and lawn and garden equipment (Carr and Kindred, 2024; SJVAPCD, 2024). In addition, statewide mobile-source and fuels programs have tightened tailpipe emission standards for new light- and heavy-duty vehicles and established cleaner fuel requirements, providing substantial $PM_{2.5}$ and precursor reductions in the region (CARB, 2024). Together, these programs are projected to reduce direct $PM_{2.5}$ emissions by about 16% between 2017 and 2030, supporting attainment of the federal 2012 annual $PM_{2.5}$ standard in the SJV (SJVAPCD, 2024). Evaluating the effectiveness of these mitigation efforts requires continuous, long-term monitoring of $PM_{2.5}$ concentrations and chemical compositions.

Several studies, including recent CARB-funded efforts (through contracts #17RD008 and #20AQP007), have demonstrated the value of highly time-resolved Aerosol Chemical Speciation Monitor (ACSM) measurements for quantifying non-refractory $PM_{2.5}$ (NR-$PM_{2.5}$) components and characterizing their temporal variability (Heikkinen et al., 2020; Parworth et al., 2015; Sun et al., 2022, 2015). Sun et al. (2022) reported the first long-term ACSM measurements in Fresno, providing detailed characterization of the major $PM_{2.5}$ constituents – organic aerosol (OA), nitrate (NO_3^-), sulfate (SO_4^{2-}), ammonium (NH_4^+), and chloride (Cl^-) – and their diurnal, weekly, seasonal, and interannual behavior (Sun et al., 2022). That work further demonstrated that advanced source apportionment of ACSM mass spectral data can identify the major emission sources driving seasonal $PM_{2.5}$ pollution episodes and support evaluation of the effectiveness of $PM_{2.5}$ control strategies currently being implemented in the SJV.

In this chapter, we present an overview of the ACSM measurement methods at Fresno and Bakersfield and summarize key results that illustrate the performance of the instruments and the diurnal and seasonal characteristics of NR-$PM_{2.5}$ composition at these two major cities in the SJV. Detailed discussion on the source apportionment of organic aerosol based on ACSM data is presented in Chapter 3. Subsequent chapters provide an in-depth analysis of measurements from the winter 2023-2024 intensive measurement campaign in Fresno, with emphasis on key emission sources and atmospheric processes driving wintertime $PM_{2.5}$ pollution in the SJV.

2.2 Experimental Methods

2.2.1 ACSM Measurements at Fresno and Bakersfield

In this project, UCD deployed two ACSMs, one at Fresno (3727 N. 1st Street, Suite 104, Fresno CA 93726; 36.78538ºN, 119.77321ºW; 97 m above sea level) and one at Bakersfield (5558 California Ave, Bakersfield CA 93309, 35.35662 ºN, 119.06261ºW; 119 m above sea level). Both instruments have been operated and maintained continuously since the summer of 2023 as part of this project.

The ACSM measures aerosol mass concentration and chemical composition by sampling particles through an aerodynamic lens into a high-vacuum chamber (Zhang et al., 2004; Zhang et al., 2002), where non-refractory particulate matter is flash vaporized on a heated surface. The resulting gaseous molecules are ionized using 70 eV electron impact ionization and analyzed by mass spectrometry (Ng et al., 2011a; Frohlich et al., 2013). In this project, both ACSMs were equipped with a $PM_{2.5}$ aerodynamic lens (Williams et al., 2013; Peck et al., 2016) and a capture vaporizer (CV) maintained at approximately 500 ºC. The CV minimizes particle bounce and achieves near-unity collection efficiency for NR-$PM_{2.5}$ (Hu et al., 2017; Xu et al., 2017). The configuration enables quantitative measurement of organic aerosol, nitrate, sulfate, ammonium, and chloride in $PM_{2.5}$ (Sun et al., 2022; Zhang et al., 2017; Zheng et al., 2020).

The ACSM deployed at Fresno was equipped with a time-of-flight mass spectrometer (ToF-ACSM), while the instrument deployed at Bakersfield uses a quadrupole mass spectrometer (Q-ACSM). Because the ToF-ACMS provides higher sensitivity than the Q-ACSM (Ng et al., 2011a; Frohlich et al., 2013), NR-$PM_{2.5}$ data at Fresno were collected at a higher time resolution than at Bakersfield (10 min vs. 20 min). Such time resolution is substantially higher than the typical hourly resolution used for long-term monitoring, improving the ability to capture short-term variability in $PM_{2.5}$ concentration and composition and enhancing subsequent source apportionment analyses.

Instrument performance was monitored daily using remote-access software (e.g., Teamviewer) and maintained through routine on-site calibrations that were conducted to determine the ionization efficiency (IE) and relative ionization efficiencies (RIEs) for ammonium and sulfate. Calibrations for IE and ammonium RIE were performed using size-selected ammonium nitrate particles (Canagaratna et al., 2007; Ng et al., 2011a), while pure ammonium sulfate particles were used to determine the sulfate RIE (Setyan et al., 2012). These procedures ensured stable instrument performance and improved accuracy of the reported concentrations of NR-$PM_{2.5}$ species. Data were automatically backed up to on-site external storage and copied periodically to a remote system at UC Davis to ensure data redundancy and security.

This report covers ACSM measurements collected in Fresno from June 2023 through December 2025 and in Bakersfield from August 2023 through December 2025. The beginning of the reporting period at Fresno corresponds to the start of the project, while the reporting period at Bakersfield corresponds to the initial deployment of the ACSM instrument at that site. Instrument uptimes,

calculated over the respective reporting periods, were approximately 87% at Fresno and 96% at Bakersfield. Data gaps were primarily attributable to occasional inlet clogging and intermittent periods of instrument calibration, maintenance, or repair. These uptime levels demonstrate the successful acquisition of high-quality, long-term datasets at both sites.

2.2.2 Sampling site and other instrumentation

Co-located meteorological and air quality measurements were obtained from the CARB air monitoring network (https://www.arb.ca.gov/aqmis2/aqdselect.php) and are available as hourly averages. These include $PM_{2.5}$ and PM_{10} mass concentrations measured by beta attenuation monitors (BAMs), ambient temperature, relative humidity (RH), wind speed and direction, and concentrations of key gas pollutants (CO, NO, NO_2, O_3 and SO_2). In addition, speciated $PM_{2.5}$ component concentrations (e.g., organic carbon, sulfate, nitrate, ammonium, chloride) were obtained from the US EPA Chemical Speciation Network (CSN). CSN measurements are based on 24-hour integrated $PM_{2.5}$ filter samples collected every 3 days and then analyzed using established offline methods (https://aqs.epa.gov/aqsweb/airdata/download_files.html).

2.2.3 ACSM data analysis

Mass concentrations of NR-$PM_{2.5}$ species, including organic aerosol, sulfate, nitrate, ammonium, and chloride, were derived from the ion signals detected by the ACSMs using the standard ACSM data analysis software. Data from the ToF-ACSM were processed using Tofware (v2.5.13), while data from the Q-ACSM were processed using ACSM Local (v1.6.2.1), both operated within the Igor Pro environment (Wave-Metrics, Inc., Oregon USA) and available through Aerodyne Research Inc. (https://support.aerodyne.com/hc/en-us/categories/12103106604823-ACSM).

The ACSM instruments were calibrated multiple times during the measurement period using pure ammonium nitrate and ammonium sulfate following established protocols described in Ng et al. (Ng et al., 2011a). These calibrations were used to determine relative ionization efficiency (RIE) values for ammonium and sulfate. Default RIE values were assumed for organics (1.4), nitrate (1.05), and chloride (1.3) (Ng et al., 2011b). ACSM data were batch-processed on a weekly basis and subjected to rigorous quality assurance and quality control (QA/QC) procedures. QA/QC evaluations included (1) determination of species-specific detection limits, (2) diagnostic examination of mass spectral signals, and (3) estimation of quantification uncertainties arising from electronic and ionic noise, particle sampling statistics, and background signals measured during particle-free sampling periods.

To assess the accuracy, precision, and overall performance of the ACSMs, NR-$PM_{2.5}$ mass concentrations were compared with co-located $PM_{2.5}$ measurements obtained from Federal Equivalent Method (FEM) and Federal Reference Method (FRM) instruments, as well as with PM measurements collected during the intensive field campaign in the winter of 2023-2024. Total

PM_{10} and $PM_{2.5}$ mass concentrations were measured using MetOne BAM-1020 instruments equipped with PM_{10} or $PM_{2.5}$ cyclones for size selection prior to collection on glass fiber filter tape. Hourly PM mass concentration data were obtained from the CARB Air Quality and Meteorological Information System (https://www.arb.ca.gov/aqmis2/aqmis2.php).

Speciated $PM_{2.5}$ component measurements were obtained from the U.S. EPA Chemical Speciation Network (CSN). Inorganic components (sulfate, nitrate, ammonium, and chloride) were collected using MetOne SASS or SuperSASS samplers on nylon filters. The filters were later extracted and analyzed using ion chromatography. Organic aerosol was sampled using URG3000N samplers with quartz filters, followed by thermal-optical analysis to determine total organic carbon (OC). CSN filter samples were collected as 24-hour integrated measurements every three days, and the corresponding data were obtained from the EPA Air Quality System website (https://aqs.epa.gov/aqsweb/airdata/download_files.html).

Because the ACSMs operated at higher time resolution (~10-20 minutes) than the BAM or CSN measurements, ACSM were post-averaged to match the temporal resolution of the comparison datasets (1-h or 24-h for BAM and 24-h for CSN). All available data were used for time series and temporal variability analyses. For quantitative inter-instrument comparisons, only periods with concurrent ACSM and corresponding BAM or CSN measurements were included. Where relevant, total NR-$PM_{2.5}$ is taken as the sum of the individual ACSM-measured components (Org, SO_4, NO_3, NH_4, and Chl). BAM and CSN measurements were used as-is without further processing.

2.3 Results and Discussion

2.3.1 Multi-year NR-$PM_{2.5}$ concentrations and chemical composition in Fresno and Bakersfield

Time-series of the organic aerosol, nitrate, sulfate, chloride, and ammonium concentrations measured by the ACSMs, along with their fractional contributions to the total NR-$PM_{2.5}$ mass, are shown in **Figure 2-1** for Fresno and **Figure 2-2** for Bakersfield. For comparison, co-located $PM_{2.5}$ mass concentrations measured by beta attenuation monitors (BAMs) are also presented. Together, these measurements provide a multi-year, high-time-resolution perspective on the temporal evolution and seasonal variability of $PM_{2.5}$ chemical composition in the SJV.

At both sites, total NR-$PM_{2.5}$ and $PM_{2.5}$ concentrations exhibit strong seasonal variability, with the highest levels occurring during the fall and winter and peak values generally observed in December. Among the study years (2023 – 2025), the 2024-2025 winter season stands out for exhibiting the highest and most sustained $PM_{2.5}$ concentrations, consistent with prolonged stagnation events and enhanced wintertime emissions.

As shown in the upper panels of **Figures 2-1** and **2-2**, elevated wintertime NR-$PM_{2.5}$ concentrations are mainly driven by a combination of increased primary organic aerosol (POA) emissions from combustion sources and enhanced secondary formation of particulate ammonium nitrate (NH_4NO_3) and secondary organic aerosol (SOA) under cold, stagnant conditions (Young et al., 2017). In contrast, lower concentrations during spring and summer reflect improved ventilation, reduced residential combustion, and less favorable thermodynamic conditions for NH_4NO_3 and semi-volatile SOA formation.

The chemical composition of NR-$PM_{2.5}$ exhibits pronounced seasonal variability, particularly in the relative contributions of OA and inorganic species. Over the full measurement period reported here, OA accounts for an average of 72 ± 13% (1σ) of NR-$PM_{2.5}$ mass in Fresno and 76 ± 12% in Bakersfield, highlighting the dominant role of OA at both sites. The fractional OA contribution peaks in late summer and early fall, coinciding with increased influence from wildfire smoke and, later in the year, the onset of residential wood burning. Elevated summertime OA contributions to $PM_{2.5}$ also reflect enhanced SOA production from photochemical oxidation of volatile organic compounds (VOCs) and increased biogenic VOC emissions. Detailed OA source apportion results are presented in Section 3.

In contrast, NH_4NO_3 is most abundant during late fall and winter, dominating the inorganic fraction and contributing up to ~50% of total NR-$PM_{2.5}$ mass during peak pollution periods. Ammonium sulfate ($(NH_4)_2SO_4$) becomes relatively more important in spring and summer, reflecting enhanced photochemical oxidation of SO_2 to sulfates and reduced thermodynamic stability of NH_4NO_3 at higher temperatures. Chloride constitutes a minor fraction of NR-$PM_{2.5}$ at both sites but generally covaries with OA throughout the year, suggesting common or closely related sources consistent with biomass burning. It is important to note that the ACSM measures only non-refractory chloride, primarily ammonium chloride, and has limited sensitivity to refractory metal chlorides (e.g., NaCl, KCl, or $CaCl_2$) present in sea salt or dust particles.

2.3.2 Comparison of ACSM-Measured NR-$PM_{2.5}$ to BAM-$PM_{2.5}$

The relationship between ACSM-measured NR-$PM_{2.5}$ and BAM-measured $PM_{2.5}$ mass concentrations is shown in **Figure 2-3** for 2023-2025 at each site, while **Figure 2-4** summarizes the corresponding annual-average concentrations along with BAM PM_{10}. Together, these comparisons indicate that non-refractory species contribute the majority of $PM_{2.5}$ mass at both Fresno and Bakersfield, particularly during wintertime pollution episodes. Fine particles in Fresno generally exhibit a larger absolute contribution from non-refractory species during high-pollution periods, whereas the greater differences between NR-$PM_{2.5}$ and BAM $PM_{2.5}$ in Bakersfield reflect a stronger influence of refractory components such as crustal material.

Hourly time series (**Figure 2-1** and **Figure 2-2**) show that NR-$PM_{2.5}$ closely tracks $PM_{2.5}$ at both sites, while scatter plot comparisons (**Figure 2-3**) demonstrated strong correlations throughout the

entire measurement period, with coefficient of determination (r^2) ranging from 0.72 (Bakersfield, 2025) to 0.86 (Bakersfield, 2023). However, the quantitative relationship between NR-$PM_{2.5}$ and BAM $PM_{2.5}$ varies by site and year. In Fresno, NR-$PM_{2.5}$ on average accounted for 0.94, 1.1, and 1.1 of BAM $PM_{2.5}$ in 2023, 2024, and 2025, respectively, whereas in Bakersfield the corresponding ratios were lower – 0.93, 0.82, and 0.80.

Slopes below unity are expected because $PM_{2.5}$ contains refractory components not detected by the ACSM, including elemental (black) carbon, crustal dust, and sea salt. The consistently lower NR-$PM_{2.5}$ vs. $PM_{2.5}$ regression slopes observed in Bakersfield indicate a higher refractory fraction at that location compared to Fresno. This interpretation is supported by **Figure 2-4**, which shows significantly higher PM_{10} concentrations at Bakersfield, and by the distribution of $PM_{2.5}/PM_{10}$ ratios (**Figure 2-5**), which indicates a larger contribution from coarse particles at that site. The $PM_{2.5}/PM_{10}$ ratio reflects the fraction of PM_{10} mass present in the fine mode, when refractory material contributes substantially to total PM, can serve as an indicator of the refractory fraction in $PM_{2.5}$. Lower $PM_{2.5}/PM_{10}$ ratios, indicating a greater influence of from coarse, refractory particles such as dust and sea salt, correspond to a reduced non-refractory fraction in fine particles, resulting in lower NR-$PM_{2.5}$ relative to total $PM_{2.5}$. In contrast, when fine particles dominate (i.e., $PM_{2.5\text{-}10}/PM_{10}$ approaching 0), NR-$PM_{2.5}$ more closely approximates total $PM_{2.5}$ mass (**Figure 2-3**), consistent with a $PM_{2.5}$ composition richer in non-refractory species.

At Fresno, regression slopes slightly greater than unity in 2024 and 2025 likely reflect underestimation of BAM $PM_{2.5}$ due to evaporation losses of semivolatile species, particularly ammonium nitrate and semi-volatile OA, during filter equilibration and measurement (Chiu and Carlton, 2024). In contrast, the ACSM, which samples in real time and near ambient temperature, is less susceptible to such volatilization artifacts. As a result, during periods dominated by semivolatile secondary aerosols, especially in winter, BAM measurements can underestimate $PM_{2.5}$ mass relative to the ACSM, resulting in regression slopes exceeding one (**Figure 2-3**). However, interpretation of year-to-year seasonal differences is complicated by uneven temporal coverage. For example, in 2024 there is full coverage of the winter season, whereas both 2023 and 2025 have only partial coverage of wintertime PM.

2.3.3 Intercomparison of ACSM Measurement of NR-$PM_{2.5}$ Chemical Composition with EPA CSN Data

The EPA Chemical Speciation Network (CSN) characterizes $PM_{2.5}$ chemical composition at the Fresno-Garland and Bakersfield monitoring sites using integrated 24-h filter samples collected every third day. **Figures 2-6** and **2-7** compare ACSM-measured NR-$PM_{2.5}$ components (organics, sulfate, nitrate, ammonium, and chloride) with corresponding CSN species for Fresno and Bakersfield, respectively, over the period August 2023 to June 2025.

Nitrate and ammonium exhibit the strongest correlations between the ACSM and CSN measurements at both sites. In Fresno, correlations are high (r^2 = 0.92 for nitrate and 0.90 for ammonium) with slopes near unity, indicating close agreement. Similar correlations are observed in Bakersfield (r^2 = 0.91 and 0.90), although the ACMS measured lower concentration – about 63% of CSN nitrate and 69% of CSN ammonium. This lower slope likely reflects the presence of nitrate and ammonium associated with refractory species (e.g., dust-bound nitrate or ammonium salts with crustal material) that are not efficiently detected by the ACSM. Sulfate shows a weaker correlation (r^2 = 0.6) and slopes of 0.66 in Fresno and 0.45 in Bakersfield, suggesting an even larger contribution from undetected forms such as metal sulfates.

While the ACSM and CSN measure comparable aspects of $PM_{2.5}$ composition, they differ in the range of species each detects. The ACSM quantifies only NR-PM components (e.g., ammonium salts of nitrate, sulfate, and chloride) that volatilize at approximately 500 ºC. In contrast, the CSN's filter-based method captures both non-refractory and refractory species, including metal salts and crustal components, but is susceptible to volatilization losses during sampling. These methodological differences can lead to systematic offsets in total mass and species composition between the two datasets.

The impact of these differences is most evident for chloride, which shows the weakest correspondence between the two datasets. In Bakersfield (r^2 = 0.47; slope = 0.25), ACSM chloride concentrations are substantially lower than CSN values, while the agreement is slightly better in Fresno. This discrepancy likely reflects the presence of refractory chloride (e.g., NaCl, $CaCl_2$) from sea salt and dust that the ACSM cannot detect. The higher PM_{10} levels in Bakersfield (**Figure 2-4**) support this interpretation and help explain the generally lower slopes observed for all NR-$PM_{2.5}$ components in Bakersfield relative to Fresno, consistent with a greater influence of refractory material at that site.

The comparison of ACSM-measured OA and OC reported by the CSN shows moderately strong correlations (r^2 = 0.72 in Fresno and 0.79 in Bakersfield) and slopes of ~ 2.5 at both sites. The CSN reports OC, which represents only the carbon mass and excludes associated heteroatoms (e.g., hydrogen, oxygen, and nitrogen), whereas the ACSM quantifies the total OA mass. Although the relationship between OA and OC varies with location and atmospheric processing, it is typically approximated using an organic-mass-to-organic-carbon (OM/OC) ratio. In urban environments, an OM/OC of ~ 1.6 is typical, while higher values (> 2) are associated with more oxidized, aged aerosols found in rural or remote regions (Turpin and Lim, 2001; Zhang et al., 2005). The observed OA-to-OC slope of 2.53 suggests systematically higher ACSM-measured OA, likely due in part to volatilization losses of semi-volatile organic compounds during CSN filter sampling. Such losses are minimized in the ACSM due to its real-time, near-ambient measurement approach.

2.3.4 Contrasting NR-$PM_{2.5}$ Concentrations and Chemical Composition in Fresno and Bakersfield

The composition of NR-$PM_{2.5}$ at both sites exhibited pronounced seasonal and interannual variability. On average, total NR-$PM_{2.5}$ concentrations were slightly higher in Fresno (10.89 μg m^{-3}) than in Bakersfield (10.33 μg m^{-3}), although the difference varied from year to year (**Figure 2-4**). The ACSM NR-$PM_{2.5}$ and BAM $PM_{2.5}$ measurements were generally well correlated at both sites (**Figure 2-3**).

There were significant seasonal variations in NR-$PM_{2.5}$ composition at both sites, although the monthly trends were largely similarly in Fresno and Bakersfield (**Figure 2-8** and **Figure 2-9**). Most components exhibit wintertime peaks, although organics could also spike in the summer months, likely due to biomass burning events. The chemical composition of NR-$PM_{2.5}$ also differed under varying $PM_{2.5}$ loadings. Using a $PM_{2.5}$ cutoff of 35 μg m^{-3} (the EPA 24-h $PM_{2.5}$ standard) to define "low" and "high" $PM_{2.5}$ periods, we found that low $PM_{2.5}$ conditions were characterized by a higher organic fraction (although lower absolute OA concentration) and a lower contribution from nitrate and ammonium (**Figure 2-9**). These trends suggest that high $PM_{2.5}$ episodes in Fresno are driven by a combination of primary emissions (e.g., residential wood burning and wildfire smoke) and secondary nitrate formation under cold, stagnant winter conditions.

The inter-site correlations of individual components of NR-$PM_{2.5}$ also varied seasonally and across years (**Figure 2-10**). As with the total NR-$PM_{2.5}$, correlations were strongest in late fall and winter, when NR-$PM_{2.5}$ concentrations peaked, and weakest in warmer months. Organics and nitrate, dominant NR-$PM_{2.5}$ components at both sites, generally showed the best agreement, while species with lower average mass concentrations were less correlated.

From 2023 to 2025, total NR-$PM_{2.5}$ declined at both sites, mostly due to large decreases in organics and sulfate in 2024 and decreases in nitrate in 2025. However, this decrease was faster and more consistent in Bakersfield than Fresno, where all NR-$PM_{2.5}$ components exhibited year-to-year reductions, resulting in smaller interannual slopes across components (**Figure 2-10**). Sulfate was the exception as the year-to-year correlation was consistent despite its overall decrease. In Fresno, modest increases in organics (2025) and nitrate and ammonium (2024) interrupted the downward trend, suggesting site-specific differences in source strength or meteorological influences.

2.3.5 Daily patterns in NR-$PM_{2.5}$ components

The high time resolution of the ACSM allows for investigation of the diel behavior of the various NR-$PM_{2.5}$ components (**Figure 2-11**). Select meteorological variables (wind speed/direction, precipitation) and O_3 are also included for context. Year-to-year, diel behavior of all measured species is remarkably consistent.

At both sites, the inorganic NR-$PM_{2.5}$ species – nitrate, sulfate, and ammonium – exhibit similar daily cycles, with exception of chloride, whose low over mass concentrations obscure hourly variability. Nitrate, sulfate, and ammonium typically increase rapidly beginning around 06:00 (PST), and peak around 10:00. The nitrate and ammonium then decline rapidly through the afternoon to a minimum around 16:00 while the sulfate exhibits a more gradual decline that extends into the evening. A small secondary nighttime peak in nitrate and ammonium occurred around 23:00. OA increases sharply in the last afternoon (16:00 – 19:00), followed by a slower decrease overnight. For all components, these diel trends are more evident in winter compared to summer where the diel trends become notably flatter.

The seasonal dependence of these cycles are distinct. The OA nighttime maximum is prominent from September to April but disappears from May to August. Instead, during these summer months the OA peaks during the late morning in Fresno (11:00) and early morning in Bakersfield (06:00-08:00) with a long tail towards the evening. For nitrate, while the wintertime diel behavior exhibits the same daytime decrease at both sites, generally only Fresno sees the large, initial morning spike. The difference is distinct enough to lead to an anti-correlation of nitrate between Fresno and Bakersfield in the morning. Throughout the summer months and most of the year in Bakersfield, the morning decrease in nitrate is well-correlated with a morning increase in O_3. However, in Fresno in winter, nitrate and O_3 both increase for a short period of time in the morning (07:00-09:00). This site-specific behavior lasts from September to April. In the warmer months, only small morning and evening increase in nitrate are observed. The same behavior can be found in ammonium and to a lesser extent chloride. Sulfate exhibits a peak around 10:00 for all months, albeit with a slight shift to later times from March-June. Altogether, these observations highlight the interplay between primary and secondary $PM_{2.5}$ sources and the influence of meteorological conditions on $PM_{2.5}$ composition and timing of formation.

2.4 Conclusions

Overall, the high time-resolution ACSM measurements of NR-$PM_{2.5}$ provide a valuable complement to existing $PM_{2.5}$ monitoring networks in the California's San Joaquin Valley. The ACSM-measured total NR-$PM_{2.5}$ concentrations compared favorably with co-located BAM $PM_{2.5}$ measurements across the entire study period in both Fresno and Bakersfield. The observed differences between the two instruments can be largely attributed to the presence of refractory $PM_{2.5}$ components, such as black carbon, crustal material, and sea-salt-derived compounds, which are included in BAM measurements but not detected by the ACSM.

The comparisons between ACSM and CSN measurements further underscore both the strengths and limitations of each technique. Nitrate and ammonium exhibited strong consistency across the two datasets, with slopes near unity in Fresno and slightly lower in Bakersfield, consistent with a greater contribution of refractory-associated material at that site. Sulfate correlations were moderate, while chloride showed weak agreement due to refractory contributions that the ACSM cannot measure. The largest discrepancies occurred for organic comparisons, where ACSM-

measured OA mass concentration significantly exceeded CSN-derived values, likely due to volatilization losses of semi-volatile organics during CSN filter sampling. Together, these findings indicate that while ACSM and CSN measurements are broadly comparable for major aerosol components, there are differences in what they represent: the ACSM measures non-refractory $PM_{2.5}$, whereas CSN captures total $PM_{2.5}$, including refractory material. In addition, the ACSM provides a more accurate representation of semi-volatile species due to its real-time, high-time-resolution measurements, while CSN data may be affected by volatilization losses inherent to filter-based sampling.

Similar seasonal patterns in NR-$PM_{2.5}$ composition were observed at both sites, with wintertime dominated by ammonium nitrate and organic aerosol, and lower concentrations during summer associated with improved dispersion and reduced emissions. However, notable year-to-year variations in both NR-$PM_{2.5}$ concentration and composition indicate that interannual changes in meteorology, emission sources, and atmospheric processing strongly influence aerosol behavior in the region.

Despite these similarities, the comparison between Fresno and Bakersfield revealed important spatial differences in NR-$PM_{2.5}$ dynamics. Fresno generally exhibited higher absolute concentrations and a greater fraction of non-refractory material, whereas Bakersfield showed a stronger influence from refractory material. Differences in diel patterns, especially in nitrate and OA, highlight the effects of local source activity, boundary layer evolution, and photochemical processing. Although both cities are located within the SJV and often experience similar surface meteorology, subtle differences in boundary layer structure, including residual layer formation, stability, and morning mixing, can lead to distinct temporal patterns. In Fresno, more effective nighttime accumulation and subsequent morning mixing likely drive the pronounced nitrate peaks in the morning, while in Bakersfield, differences in ventilation, terrain influences, or boundary layer growth may suppress this signal. These findings highlight the importance of site-specific atmospheric processes, beyond broad meteorological similarity, in determining local air quality.

Collectively, these results demonstrate the utility of high–time-resolution, speciated NR-$PM_{2.5}$ measurements for advancing understanding of aerosol sources and transformations. The ACSM provides detailed, process-level insights into temporal and compositional variability that cannot be resolved by traditional filter-based approaches. Such measurements can improve chemical transport model evaluation, enhance the design of emission control strategies, and support the development of data-driven air quality management approaches aimed at reducing $PM_{2.5}$ exposures and protecting public health across California.

2.5 References

Altshuler, S. L., Zhang, Q., Kleinman, M. T., Garcia-Menendez, F., Moore, C. T., Hough, M. L., Stevenson, E. D., Chow, J. C., Jaffe, D. A., and Watson, J. G.: Wildfire and prescribed burning impacts on air quality in the United States, Journal of the Air & Waste Management Association,

70, 961–970, https://doi.org/10.1080/10962247.2020.1813217, 2020.

Betha, R., Russell, L. M., Chen, C.-L., Liu, J., Price, D. J., Sanchez, K. J., Chen, S., Lee, A. K. Y., Collier, S. C., Zhang, Q., Zhang, X., and Cappa, C. D.: Larger Submicron Particles for Emissions With Residential Burning in Wintertime San Joaquin Valley (Fresno) than for Vehicle Combustion in Summertime South Coast Air Basin (Fontana), Journal of Geophysical Research: Atmospheres, 123, 10,510-526,545, https://doi.org/https://doi.org/10.1029/2017JD026730, 2018.

Bond, T. C., Habib, G., and Bergstrom, R. W.: Limitations in the enhancement of visible light absorption due to mixing state, Journal of Geophysical Research: Atmospheres, 111, https://doi.org/https://doi.org/10.1029/2006JD007315, 2006.

Brown, S. G., Hyslop, N. P., Roberts, P. T., McCarthy, M. C., and Lurmann, F. W.: Wintertime Vertical Variations in Particulate Matter (PM) and Precursor Concentrations in the San Joaquin Valley during the California Regional Coarse PM/Fine PM Air Quality Study, Journal of the Air & Waste Management Association, 56, 1267–1277, https://doi.org/10.1080/10473289.2006.10464583, 2006.

Canagaratna, M. R., Jayne, J. T., Jimenez, J. L., Allan, J. D., Alfarra, M. R., Zhang, Q., Onasch, T. B., Drewnick, F., Coe, H., and Middlebrook, A.: Chemical and microphysical characterization of ambient aerosols with the aerodyne aerosol mass spectrometer, Mass spectrometry reviews, 26, 185–222, 2007.

Cappa, C. D., Zhang, X., Russell, L. M., Collier, S., Lee, A. K. Y., Chen, C.-L., Betha, R., Chen, S., Liu, J., Price, D. J., Sanchez, K. J., McMeeking, G. R., Williams, L. R., Onasch, T. B., Worsnop, D. R., Abbatt, J., and Zhang, Q.: Light Absorption by Ambient Black and Brown Carbon and its Dependence on Black Carbon Coating State for Two California, USA, Cities in Winter and Summer, Journal of Geophysical Research: Atmospheres, 124, 1550–1577, https://doi.org/https://doi.org/10.1029/2018JD029501, 2019.

CARB: Discussion Draft: 2025 Mobile Source Strategy, California Air Resources Board, 2024.

Carr, L. and Kindred, A.: Review of the San Joaquin Valley 2024 Plan for the 2012 12 μg/m3 Annual PM2.5 Standard and Amendments to the Agricultural Equipment Incentive Measure and the 1997 15 μg/m3 State Implementation Plan Revision, California Air Resources Board, 1–68, 2024.

Chen, C. L., Chen, S., Russell, L. M., Liu, J., Price, D. J., Betha, R., Sanchez, K. J., Lee, A. K. Y., Williams, L., Collier, S. C., Zhang, Q., Kumar, A., Kleeman, M. J., Zhang, X., and Cappa, C. D.: Organic Aerosol Particle Chemical Properties Associated With Residential Burning and Fog in Wintertime San Joaquin Valley (Fresno) and With Vehicle and Firework Emissions in Summertime South Coast Air Basin (Fontana), Journal of Geophysical Research: Atmospheres, 123, 10,707-10,731, https://doi.org/10.1029/2018JD028374, 2018.

Chen, J., Ying, Q., and Kleeman, M. J.: Source apportionment of wintertime secondary organic aerosol during the California regional PM10/PM2.5 air quality study, Atmospheric Environment, 44, 1331–1340, https://doi.org/https://doi.org/10.1016/j.atmosenv.2009.07.010, 2010.

Chen, J., Yin, D., Zhao, Z., Kaduwela, A. P., Avise, J. C., DaMassa, J. A., Beyersdorf, A., Burton, S., Ferrare, R., Herman, J. R., Kim, H., Neuman, A., Nowak, J. B., Parworth, C., Scarino, A. J., Wisthaler, A., Young, D. E., and Zhang, Q.: Modeling air quality in the San Joaquin valley of California during the 2013 Discover-AQ field campaign, Atmospheric

Environment: X, 5, 100067, https://doi.org/https://doi.org/10.1016/j.aeaoa.2020.100067, 2020.

Chiu, Y. T. T. and Carlton, A. G.: Aerosol Thermodynamics: Nitrate Loss from Regulatory PM2.5 Filters in California, ACS ES&T Air, 1, 25–32, https://doi.org/10.1021/acsestair.3c00013, 2024.

Chow, J. C., Watson, J. G., Lowenthal, D. H., Solomon, P. A., Magliano, K. L., Ziman, S. D., and Richards, L. W.: PM10 and PM2.5 Compositions in California's San Joaquin Valley, Aerosol Science and Technology, 18, 105–128, https://doi.org/10.1080/02786829308959588, 1993.

Chow, J. C., Chen, L.-W. A., Watson, J. G., Lowenthal, D. H., Magliano, K. A., Turkiewicz, K., and Lehrman, D. E.: PM2.5 chemical composition and spatiotemporal variability during the California Regional PM10/PM2.5 Air Quality Study (CRPAQS), Journal of Geophysical Research: Atmospheres, 111, https://doi.org/https://doi.org/10.1029/2005JD006457, 2006.

Chow, J. C., Watson, J. G., Lowenthal, D. H., Chen, L. W. A., Zielinska, B., Mazzoleni, L. R., and Magliano, K. L.: Evaluation of organic markers for chemical mass balance source apportionment at the Fresno Supersite, Atmos. Chem. Phys., 7, 1741–1754, https://doi.org/10.5194/acp-7-1741-2007, 2007.

Collier, S., Williams, L. R., Onasch, T. B., Cappa, C. D., Zhang, X., Russell, L. M., Chen, C. L., Sanchez, K. J., Worsnop, D. R., and Zhang, Q.: Influence of Emissions and Aqueous Processing on Particles Containing Black Carbon in a Polluted Urban Environment: Insights From a Soot Particle-Aerosol Mass Spectrometer, Journal of Geophysical Research: Atmospheres, 123, 6648–6666, https://doi.org/10.1002/2017JD027851, 2018.

Ding, A. J., Huang, X., Nie, W., Sun, J. N., Kerminen, V.-M., Petäjä, T., Su, H., Cheng, Y. F., Yang, X.-Q., Wang, M. H., Chi, X. G., Wang, J. P., Virkkula, A., Guo, W. D., Yuan, J., Wang, S. Y., Zhang, R. J., Wu, Y. F., Song, Y., Zhu, T., Zilitinkevich, S., Kulmala, M., and Fu, C. B.: Enhanced haze pollution by black carbon in megacities in China, Geophysical Research Letters, 43, 2873–2879, https://doi.org/https://doi.org/10.1002/2016GL067745, 2016.

Farley, R. N., Collier, S., Cappa, C. D., Williams, L. R., Onasch, T. B., Russell, L. M., Kim, H., and Zhang, Q.: Source apportionment of soot particles and aqueous-phase processing of black carbon coatings in an urban environment, Atmospheric Chemistry and Physics, 23, 15039–15056, https://doi.org/10.5194/acp-23-15039-2023, 2023.

Fröhlich, R., Cubison, M. J., Slowik, J. G., Bukowiecki, N., Prévôt, A. S. H., Baltensperger, U., Schneider, J., Kimmel, J. R., Gonin, M., Rohner, U., Worsnop, D. R., and Jayne, J. T.: The ToF-ACSM: a portable aerosol chemical speciation monitor with TOFMS detection, Atmos. Meas. Tech., 6, 3225–3241, https://doi.org/10.5194/amt-6-3225-2013, 2013.

Ge, X., Zhang, Q., Sun, Y., Ruehl, C. R., and Setyan, A.: Effect of aqueous-phase processing on aerosol chemistry and size distributions in Fresno, California, during wintertime, Environmental Chemistry, 9, 221–235, https://doi.org/10.1071/EN11168, 2012a.

Ge, X., Setyan, A., Sun, Y., and Zhang, Q.: Primary and secondary organic aerosols in Fresno, California during wintertime: Results from high resolution aerosol mass spectrometry, Journal of Geophysical Research: Atmospheres, 117, https://doi.org/https://doi.org/10.1029/2012JD018026, 2012b.

Heikkinen, L., Äijälä, M., Riva, M., Luoma, K., Dällenbach, K., Aalto, J., Aalto, P., Aliaga, D.,

Aurela, M., Keskinen, H., Makkonen, U., Rantala, P., Kulmala, M., Petäjä, T., Worsnop, D., and Ehn, M.: Long-term sub-micrometer aerosol chemical composition in the boreal forest: inter- and intra-annual variability, Atmos. Chem. Phys., 20, 3151–3180, https://doi.org/10.5194/acp-20-3151-2020, 2020.

Hu, W., Campuzano-Jost, P., Day, D. A., Croteau, P., Canagaratna, M. R., Jayne, J. T., Worsnop, D. R., and Jimenez, J. L.: Evaluation of the new capture vaporizer for aerosol mass spectrometers (AMS) through field studies of inorganic species, Aerosol Science and Technology, 51, 735–754, https://doi.org/10.1080/02786826.2017.1296104, 2017.

Intergovernmental Panel on Climate Change: Climate Change 2021 – The Physical Science Basis, edited by: Masson-Delmotte, V., Zhai, P., Pirani, A., Connors, S. L., Péan, C., Berger, S., Caud, N., Chen, Y., Goldfarb, L., Gomis, M. I., Huang, M., Leitzell, K., Lonnoy, E., Matthews, J. B. R., Maycock, T. K., Waterfield, T., Yelekçi, O., Yu, R., and Zhou, B., Cambridge University Press, Cambridge, United Kingdom and New York, NY, USA, https://doi.org/10.1017/9781009157896, 2023.

Jaffe, D. A., O'Neill, S. M., Larkin, N. K., Holder, A. L., Peterson, D. L., Halofsky, J. E., and Rappold, A. G.: Wildfire and prescribed burning impacts on air quality in the United States, Journal of the Air and Waste Management Association, 70, 583–615, https://doi.org/10.1080/10962247.2020.1749731, 2020.

Koch, D. and Del Genio, A. D.: Black carbon semi-direct effects on cloud cover: review and synthesis, Atmos. Chem. Phys., 10, 7685–7696, https://doi.org/10.5194/acp-10-7685-2010, 2010.

Lurmann, F. W., Brown, S. G., McCarthy, M. C., and Roberts, P. T.: Processes Influencing Secondary Aerosol Formation in the San Joaquin Valley during Winter, Journal of the Air & Waste Management Association, 56, 1679–1693, https://doi.org/10.1080/10473289.2006.10464573, 2006.

Ng, N. L., Herndon, S. C., Trimborn, A., Canagaratna, M. R., Croteau, P. L., Onasch, T. B., Sueper, D., Worsnop, D. R., Zhang, Q., Sun, Y. L., and Jayne, J. T.: An Aerosol Chemical Speciation Monitor (ACSM) for Routine Monitoring of the Composition and Mass Concentrations of Ambient Aerosol, Aerosol Science and Technology, 45, 780–794, https://doi.org/10.1080/02786826.2011.560211, 2011.

Parworth, C., Fast, J., Mei, F., Shippert, T., Sivaraman, C., Tilp, A., Watson, T., and Zhang, Q.: Long-term measurements of submicrometer aerosol chemistry at the Southern Great Plains (SGP) using an Aerosol Chemical Speciation Monitor (ACSM), Atmospheric Environment, 106, 43–55, https://doi.org/https://doi.org/10.1016/j.atmosenv.2015.01.060, 2015.

Parworth, C. L., Young, D. E., Kim, H., Zhang, X., Cappa, C. D., Collier, S., and Zhang, Q.: Wintertime water-soluble aerosol composition and particle water content in Fresno, California, Journal of Geophysical Research: Atmospheres, 122, 3155–3170, https://doi.org/https://doi.org/10.1002/2016JD026173, 2017.

Peck, J., Gonzalez, L. A., Williams, L. R., Xu, W., Croteau, P. L., Timko, M. T., Jayne, J. T., Worsnop, D. R., Miake-Lye, R. C., and Smith, K. A.: Development of an aerosol mass spectrometer lens system for PM2.5, Aerosol Science and Technology, 50, 781–789, https://doi.org/10.1080/02786826.2016.1190444, 2016.

Prabhakar, G., Parworth, C. L., Zhang, X., Kim, H., Young, D. E., Beyersdorf, A. J., Ziemba, L.

D., Nowak, J. B., Bertram, T. H., Faloona, I. C., Zhang, Q., and Cappa, C. D.: Observational assessment of the role of nocturnal residual-layer chemistry in determining daytime surface particulate nitrate concentrations, Atmospheric Chemistry and Physics, 17, 14747–14770, https://doi.org/10.5194/acp-17-14747-2017, 2017.

Pusede, S. E., Duffey, K. C., Shusterman, A. A., Saleh, A., Laughner, J. L., Wooldridge, P. J., Zhang, Q., Parworth, C. L., Kim, H., Capps, S. L., Valin, L. C., Cappa, C. D., Fried, A., Walega, J., Nowak, J. B., Weinheimer, A. J., Hoff, R. M., Berkoff, T. A., Beyersdorf, A. J., Olson, J., Crawford, J. H., and Cohen, R. C.: On the effectiveness of nitrogen oxide reductions as a control over ammonium nitrate aerosol, Atmos. Chem. Phys., 16, 2575–2596, https://doi.org/10.5194/acp-16-2575-2016, 2016.

Ramanathan, V. and Carmichael, G.: Global and regional climate changes due to black carbon, Nature Geoscience, 1, 221–227, https://doi.org/10.1038/ngeo156, 2008.

Setyan, A., Zhang, Q., Merkel, M., Knighton, W. B., Sun, Y., Song, C., Shilling, J. E., Onasch, T. B., Herndon, S. C., Worsnop, D. R., Fast, J. D., Zaveri, R. A., Berg, L. K., Wiedensohler, A., Flowers, B. A., Dubey, M. K., and Subramanian, R.: Characterization of submicron particles influenced by mixed biogenic and anthropogenic emissions using high-resolution aerosol mass spectrometry: results from CARES, Atmos. Chem. Phys., 12, 8131–8156, https://doi.org/10.5194/acp-12-8131-2012, 2012.

SJVAPCD: Executive Summary: 2024 Plan for the 2012 Annual PM2.5 Standard, San Joaquin Valley Air Pollution Control District, 2024.

Sun, P., Farley, R. N., Li, L., Srivastava, D., Niedek, C. R., Li, J., Wang, N., Cappa, C. D., Pusede, S. E., Yu, Z., Croteau, P., and Zhang, Q.: PM2.5 composition and sources in the San Joaquin Valley of California: A long-term study using ToF-ACSM with the capture vaporizer, Environmental Pollution, 292, 118254, https://doi.org/10.1016/j.envpol.2021.118254, 2022.

Sun, Y. L., Wang, Z. F., Du, W., Zhang, Q., Wang, Q. Q., Fu, P. Q., Pan, X. L., Li, J., Jayne, J., and Worsnop, D. R.: Long-term real-time measurements of aerosol particle composition in Beijing, China: seasonal variations, meteorological effects, and source analysis, Atmos. Chem. Phys., 15, 10149–10165, https://doi.org/10.5194/acp-15-10149-2015, 2015.

Turpin, B. J. and Lim, H.-J.: Species Contributions to PM2.5 Mass Concentrations: Revisiting Common Assumptions for Estimating Organic Mass, Aerosol Science and Technology, 35, 602–610, https://doi.org/10.1080/02786820119445, 2001.

Williams, L. R., Gonzalez, L. A., Peck, J., Trimborn, D., McInnis, J., Farrar, M. R., Moore, K. D., Jayne, J. T., Robinson, W. A., Lewis, D. K., Onasch, T. B., Canagaratna, M. R., Trimborn, A., Timko, M. T., Magoon, G., Deng, R., Tang, D., de la Rosa Blanco, E., Prévôt, A. S. H., Smith, K. A., and Worsnop, D. R.: Characterization of an aerodynamic lens for transmitting particles greater than 1 micrometer in diameter into the Aerodyne aerosol mass spectrometer, Atmos. Meas. Tech., 6, 3271–3280, https://doi.org/10.5194/amt-6-3271-2013, 2013.

Xu, W., Croteau, P., Williams, L., Canagaratna, M., Onasch, T., Cross, E., Zhang, X., Robinson, W., Worsnop, D., and Jayne, J.: Laboratory characterization of an aerosol chemical speciation monitor with PM2.5 measurement capability, Aerosol Science and Technology, 51, 69–83, https://doi.org/10.1080/02786826.2016.1241859, 2017.

Xue, H., Liu, G., Zhang, H., Hu, R., and Wang, X.: Similarities and differences in PM10 and

PM2.5 concentrations, chemical compositions and sources in Hefei City, China, Chemosphere, 220, 760–765, https://doi.org/https://doi.org/10.1016/j.chemosphere.2018.12.123, 2019.

Young, D. E., Kim, H., Parworth, C., Zhou, S., Zhang, X., Cappa, C. D., Seco, R., Kim, S., and Zhang, Q.: Influences of emission sources and meteorology on aerosol chemistry in a polluted urban environment: results from DISCOVER-AQ California, Atmos. Chem. Phys., 16, 5427–5451, https://doi.org/10.5194/acp-16-5427-2016, 2016.

Young, D. E., Collier, S., Sun, X., Wei, H., Pinkerton, K. E., Bein, K. J., and Zhang, Q.: Investigating the Links between Chemical Composition of Atmospheric Particulates and Adverse Health Effects, Environmental Science & Technology, (in prepar, 2017.

Zhang, Q., Worsnop, D. R., Canagaratna, M. R., and Jimenez, J. L.: Hydrocarbon-like and oxygenated organic aerosols in Pittsburgh: Insights into sources and processes of organic aerosols, Atmospheric Chemistry and Physics, 5, 3289–3311, https://doi.org/10.5194/acp-5-3289-2005, 2005.

Zhang, Q., Zhou, S., Collier, S., Jaffe, D., Onasch, T., Shilling, J., Kleinman, L., and Sedlacek, A.: Understanding Composition, Formation, and Aging of Organic Aerosols in Wildfire Emissions via Combined Mountain Top and Airborne Measurements, in: Multiphase Environmental Chemistry in the Atmosphere, vol. 1299, American Chemical Society, 18–363, https://doi.org/doi:10.1021/bk-2018-1299.ch018, 2018.

Zhang, X., Smith, K., Worsnop, D., Jimenez, J., Jayne, J., and Kolb, C.: A Numerical Characterization of Particle Beam Collimation by an Aerodynamic Lens-Nozzle System: Part I. An Individual Lens or Nozzle, Aerosol Science and Technology, 36, 617–631, https://doi.org/10.1080/02786820252883856, 2002.

Zhang, X., Smith, K. A., Worsnop, D. R., Jimenez, J. L., Jayne, J. T., Kolb, C. E., Morris, J., and Davidovits, P.: Numerical characterization of particle beam collimation: Part II integrated aerodynamic-lens-nozzle system, Aerosol Science and Technology, 38, 619–638, https://doi.org/10.1080/02786820490479833, 2004.

Zhang, X., Kim, H., Parworth, C. L., Young, D. E., Zhang, Q., Metcalf, A. R., and Cappa, C. D.: Optical Properties of Wintertime Aerosols from Residential Wood Burning in Fresno, CA: Results from DISCOVER-AQ 2013, Environmental Science & Technology, 50, 1681–1690, https://doi.org/10.1021/acs.est.5b04134, 2016.

Zhang, Y., Tang, L., Croteau, P. L., Favez, O., Sun, Y., Canagaratna, M. R., Wang, Z., Couvidat, F., Albinet, A., Zhang, H., Sciare, J., Prévôt, A. S. H., Jayne, J. T., and Worsnop, D. R.: Field characterization of the PM2.5 Aerosol Chemical Speciation Monitor: insights into the composition, sources, and processes of fine particles in eastern China, Atmos. Chem. Phys., 17, 14501–14517, https://doi.org/10.5194/acp-17-14501-2017, 2017.

Zheng, Y., Cheng, X., Liao, K., Li, Y., Li, Y. J., Huang, R.-J., Hu, W., Liu, Y., Zhu, T., Chen, S., Zeng, L., Worsnop, D. R., and Chen, Q.: Characterization of anthropogenic organic aerosols by TOF-ACSM with the new capture vaporizer, Atmos. Meas. Tech., 13, 2457–2472, https://doi.org/10.5194/amt-13-2457-2020, 2020.

2.6 Figures

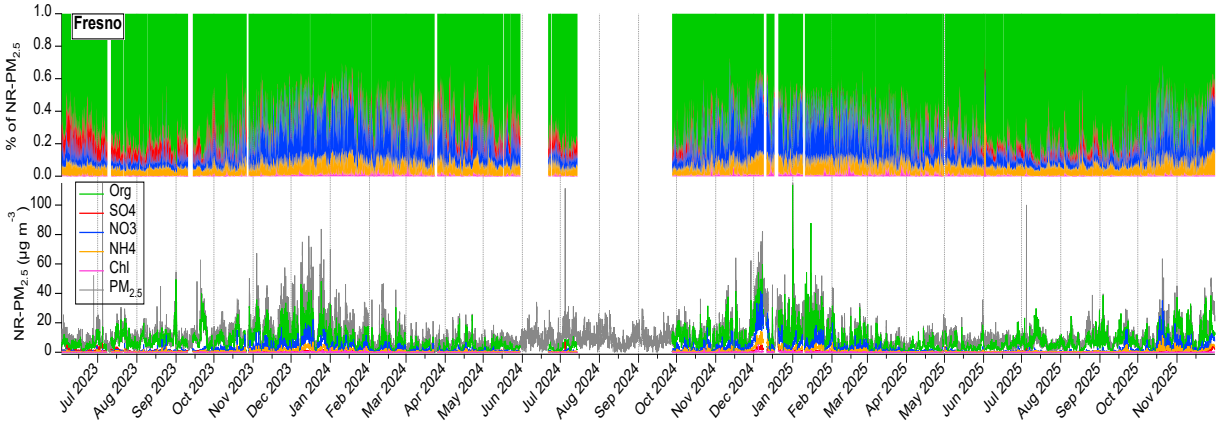

Figure 2-1: Time-series of ACSM-measured NR-$PM_{2.5}$ species and co-located BAM $PM_{2.5}$ concentrations at Fresno at 1-hour resolution from August 2023 to December 2025. Absolute concentrations are shown in the lower panel and fractional contributions in the upper panel. In the lower panel, the individual NR-$PM_{2.5}$ species (organic aerosol, nitrate, sulfate, ammonium, and chloride) are stacked to represent total NR-$PM_{2.5}$, allowing direct visual comparison with the BAM $PM_{2.5}$ measurements.

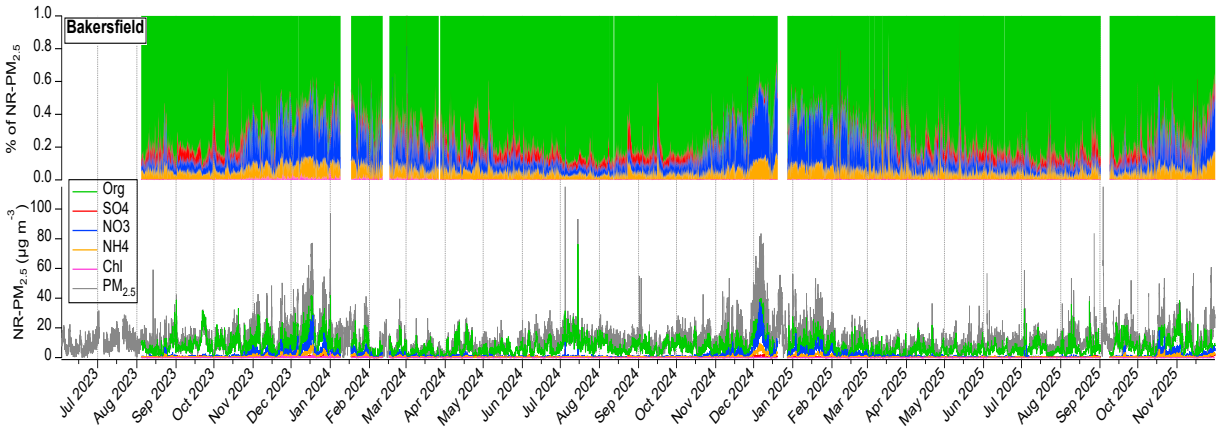

Figure 2-2: Time-series of ACSM-measured NR-$PM_{2.5}$ species and co-located BAM $PM_{2.5}$ concentrations at Bakersfield at 1-hour resolution from August 2023 to December 2025. Absolute concentrations are shown in the lower panel and fractional contributions in the upper panel. In the lower panel, the individual NR-$PM_{2.5}$ species (organic aerosol, nitrate, sulfate, ammonium, and chloride) are stacked to represent total NR-$PM_{2.5}$, allowing direct visual comparison with the BAM $PM_{2.5}$ measurements.

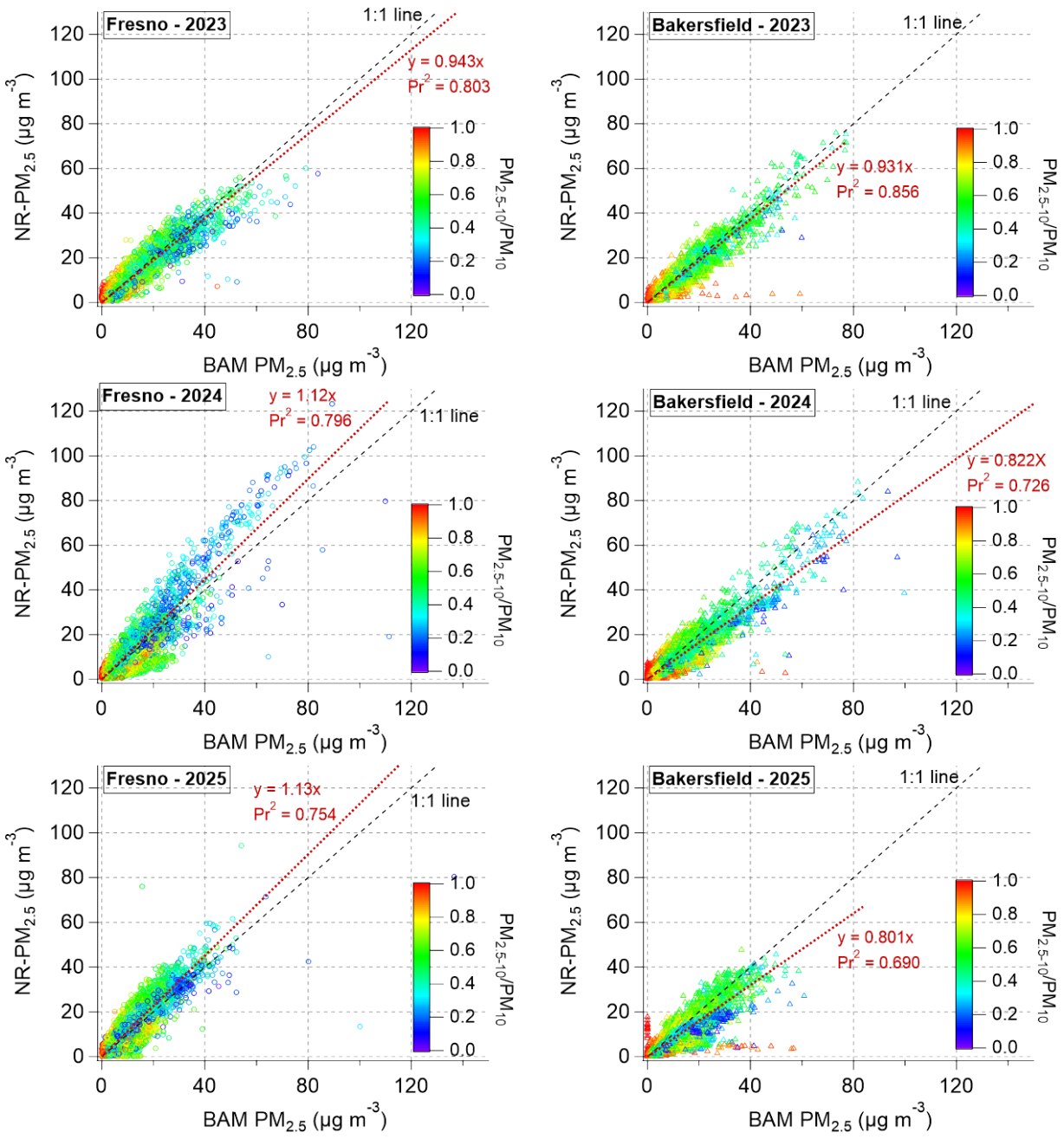

Figure 2-3: Scatter plots comparing ACSM-measured NR-$PM_{2.5}$ with co-located hourly BAM $PM_{2.5}$ measurements from Fresno (left column) and Bakersfield (right column). Panels show annual comparisons for 2023 - 2025 (from top to bottom). Data points are colored by the mass ratio of $PM_{2.5\text{-}10}$ to PM_{10} to illustrate impacts of coarse-mode particles. Red lines indicate orthogonal regression fits constrained through the origin. Fitting equations are provided alongside the r^2 calculated from Pearson's r (Pr^2). Zero values from BAM $PM_{2.5}$ data are omitted from the regression analysis but retained in the scatter plots for visualization.

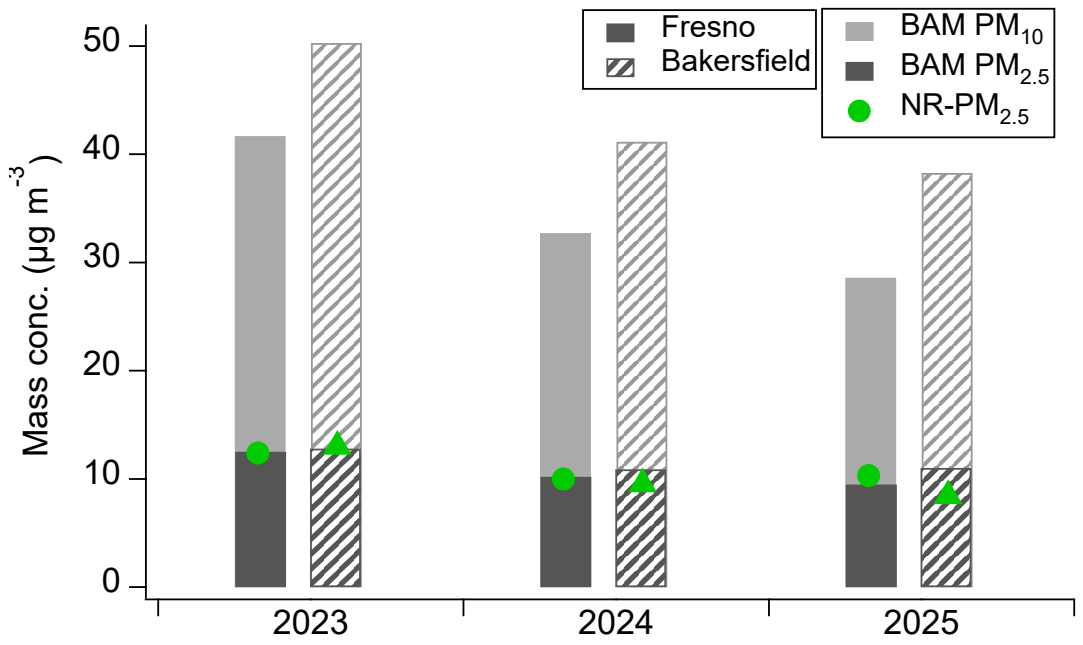

Figure 2-4: Annual-average BAM PM_{10}, BAM $PM_{2.5}$, and ACSM-measured NR-$PM_{2.5}$ concentrations for Fresno and Bakersfield.

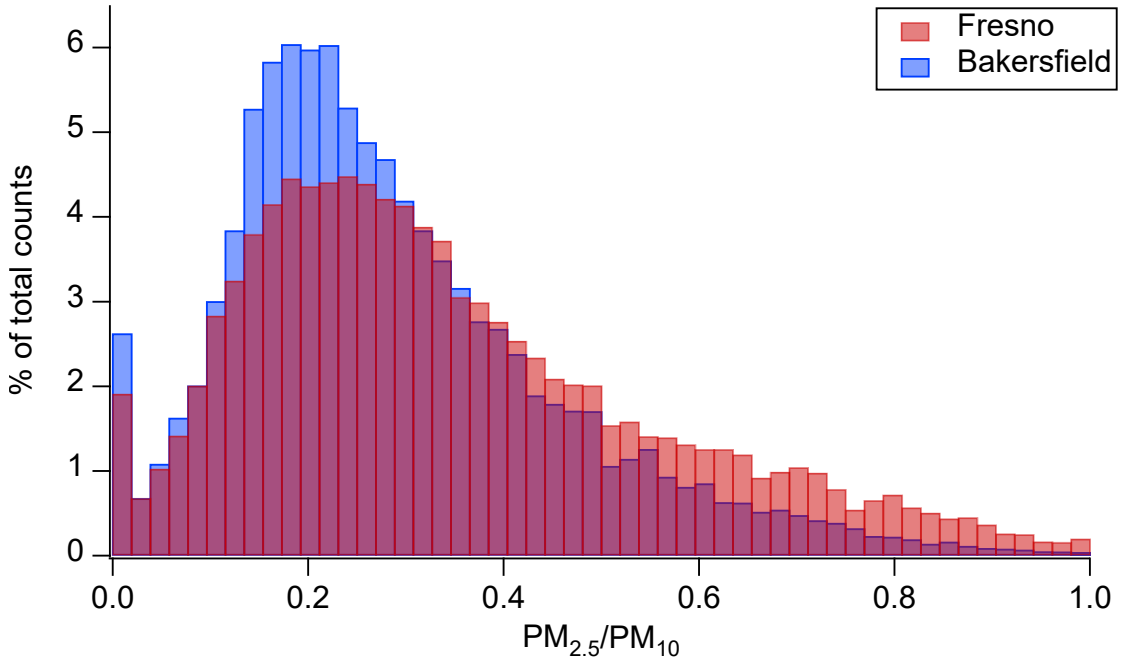

Figure 2-5: Normalized histograms of $PM_{2.5}/PM_{10}$ mass ratios measured by BAM instruments in Fresno and Bakersfield during 2023-2025. Data are normalized to enable direct comparison of

distribution shapes independent of total sample size. The $PM_{2.5}/PM_{10}$ ratio represents the relative contribution of fine particles to PM_{10} based on hourly measurements at each site.

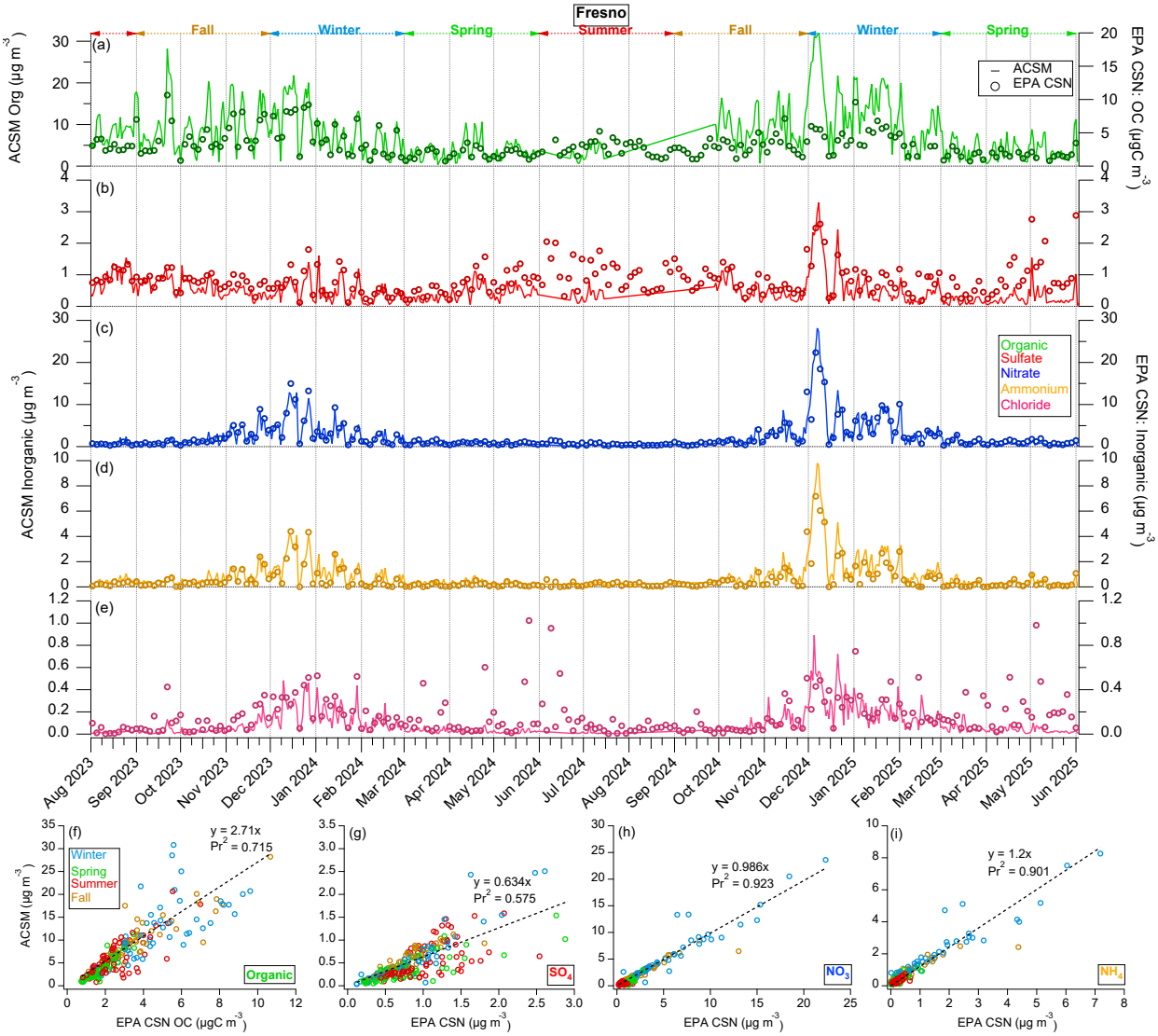

Figure 2-6: Comparison of the ACSM-measured speciated NR-$PM_{2.5}$ to EPA CSN measurements for Fresno. Panels (a-e) show 24-h averaged time series of each NR-$PM_{2.5}$ component. Panels (f – i) show scatter plots of the same data with orthogonal regression fits constrained through the origin. Zero values from the EPA CSN data were excluded from the regression analysis but retained in the scatter plots for visualization. The corresponding regression equations and Pearson correlation coefficients (r^2) are displayed in each panel (f – i).

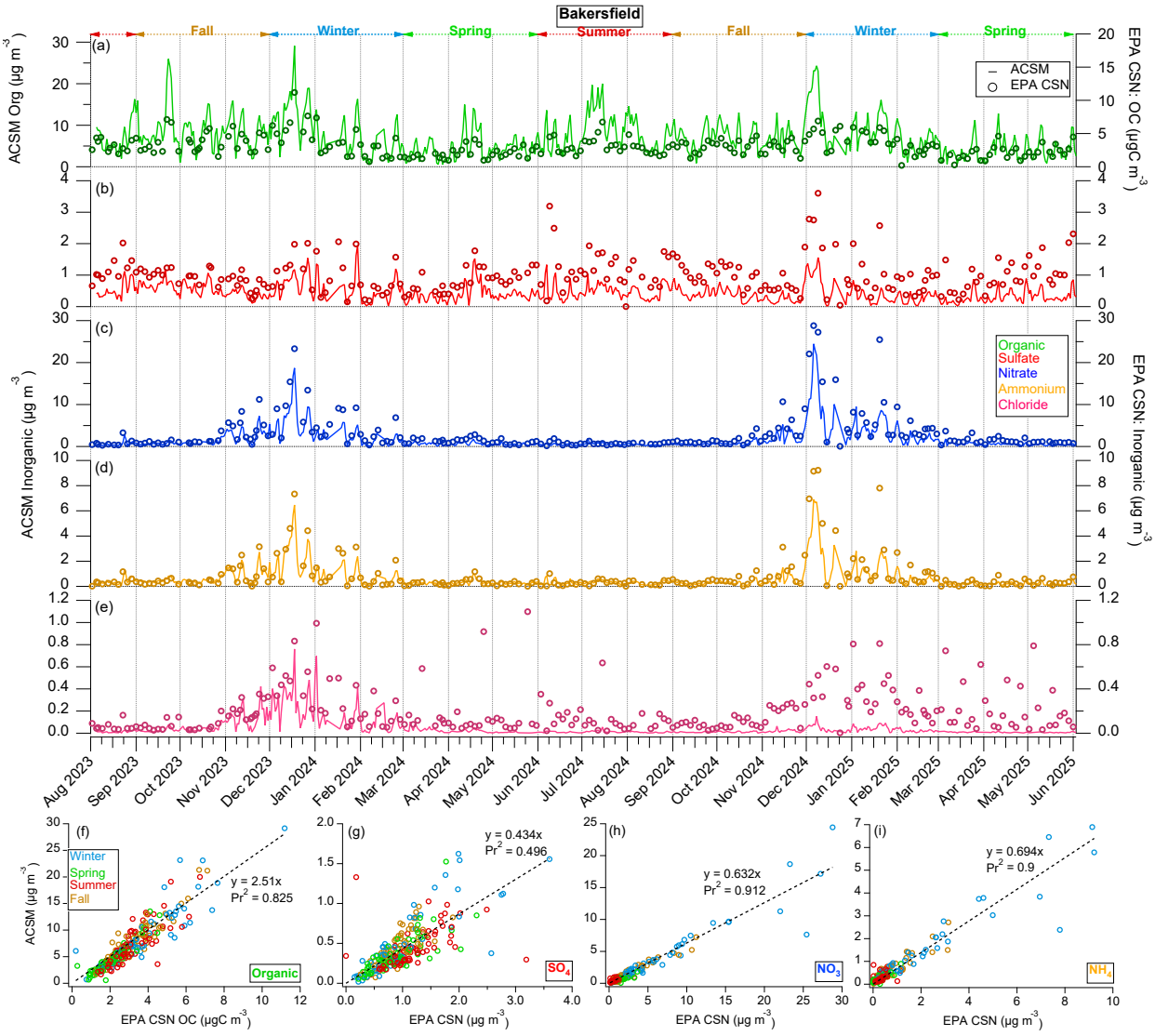

Figure 2-7: Comparison of the ACSM-measured speciated NR-$PM_{2.5}$ to EPA CSN measurements for Bakersfield. Panels (a-e) show 24-h averaged time series of each NR-$PM_{2.5}$ component. Panels (f – i) show scatter plots of the same data with orthogonal regression fits constrained through the origin. Zero values from the EPA CSN data were excluded from the regression analysis but retained in the scatter plots for visualization. The corresponding regression equations and Pearson correlation coefficients (r^2) are displayed in each panel (f – i).

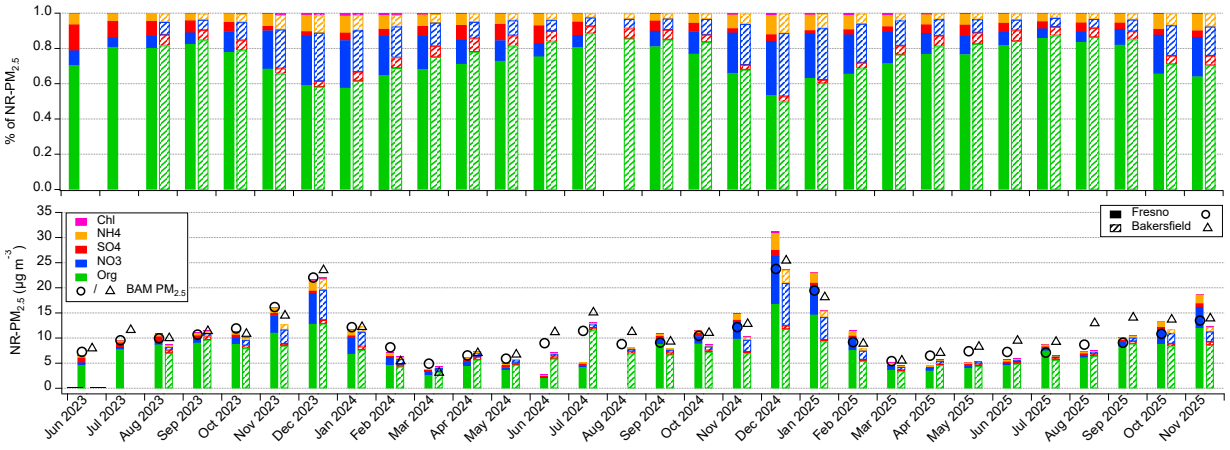

Figure 2-8: Monthly average NR-$PM_{2.5}$ segregated by species. Bottom panel shows the absolute mass concentrations and the top panel shows the fractional contribution of each species.

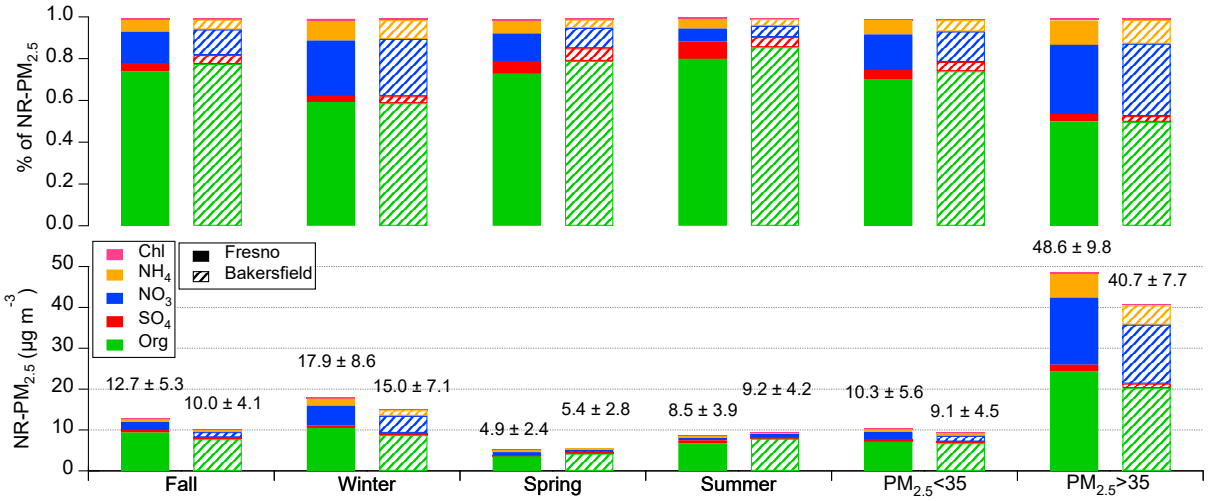

Figure 2-9: Seasonal average mass concentration and composition for NR-$PM_{2.5}$ for Fresno and Bakersfield. The two rightmost sets of bars show the average composition of NR-$PM_{2.5}$ when $PM_{2.5}$ is below and above the EPA 24-hour limit of 35 μg m^{-3}.

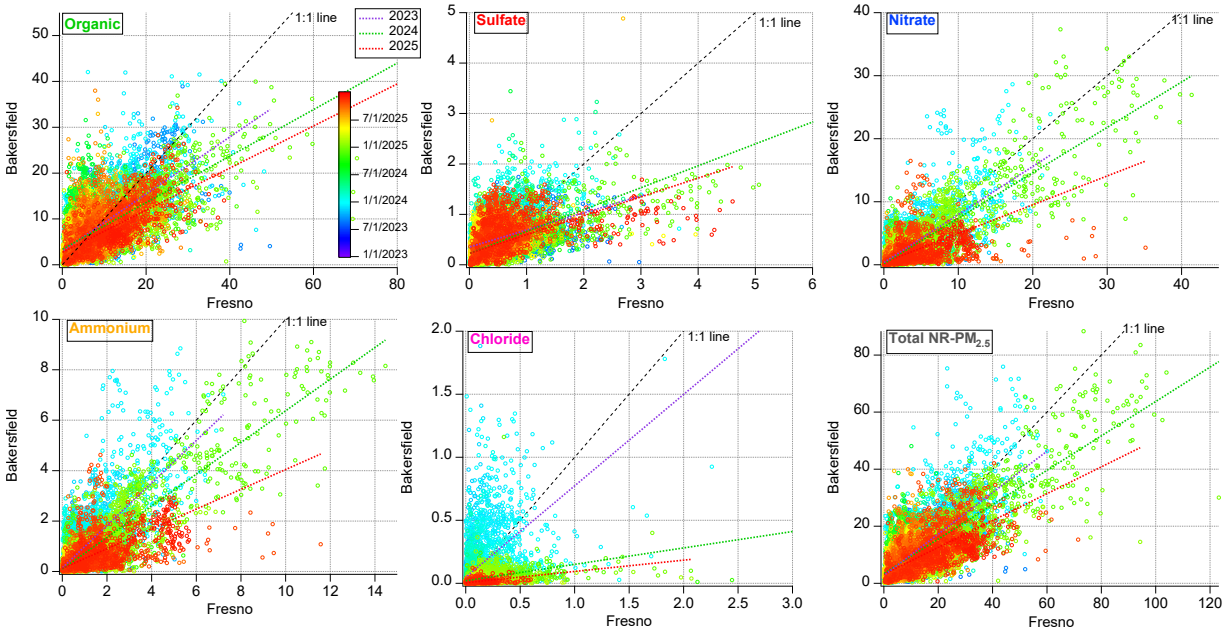

Figure 2-10: Speciated NR-$PM_{2.5}$ comparison between Fresno and Bakersfield. All units are µg m^{-3}. All yearly fits were done from the beginning and end periods of each year in the campaign.

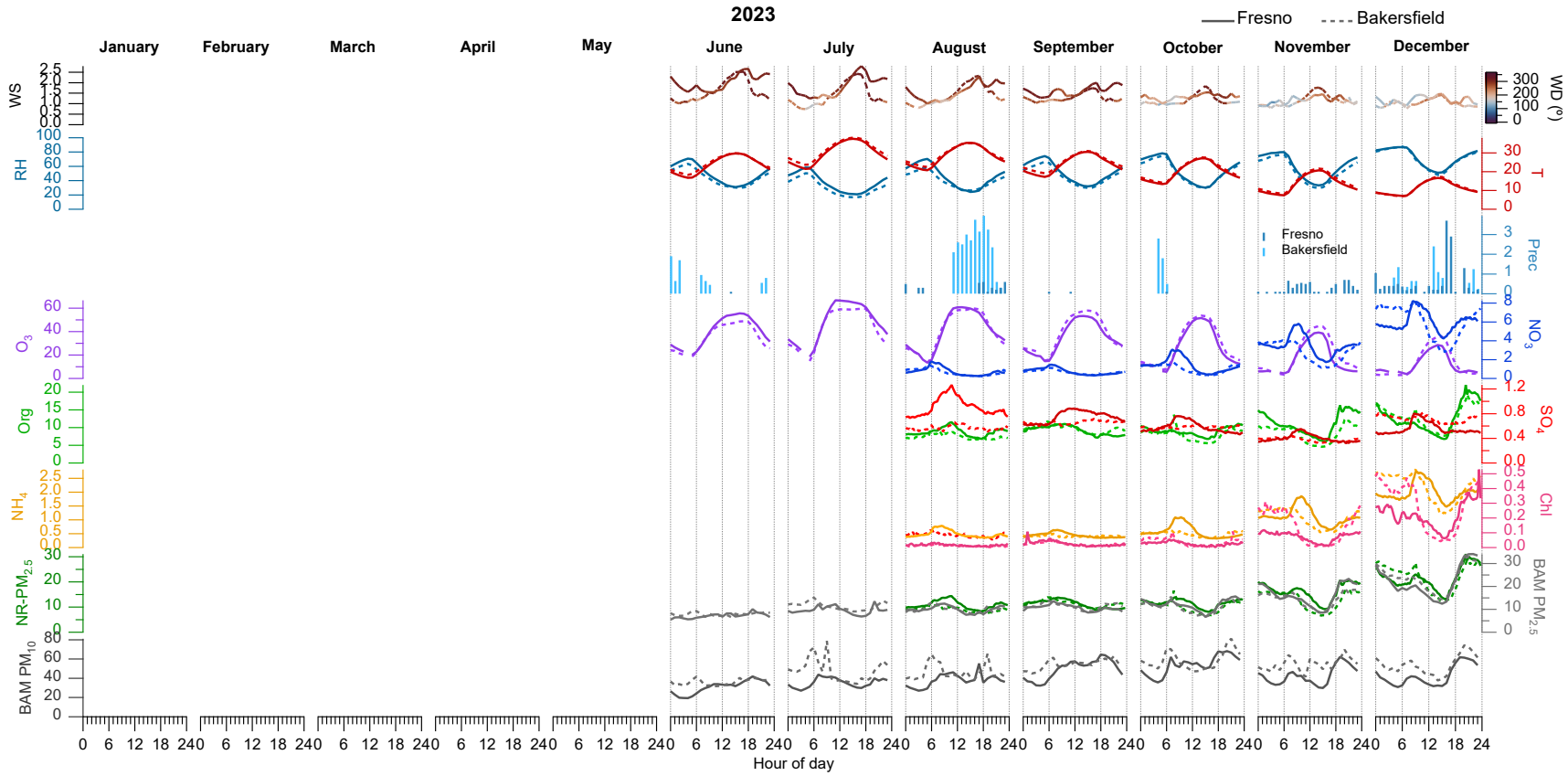
2023
Fresno
Bakersfield
January
February
March
April
May
June
July
August
September
October
November
December
WS
RH
WD (°)
T
Prec
Fresno
Bakersfield
O3
NO3
Org
SO4
NH4
Chl
NR-PM2.5
BAM PM2.5
BAM PM10
Hour of day

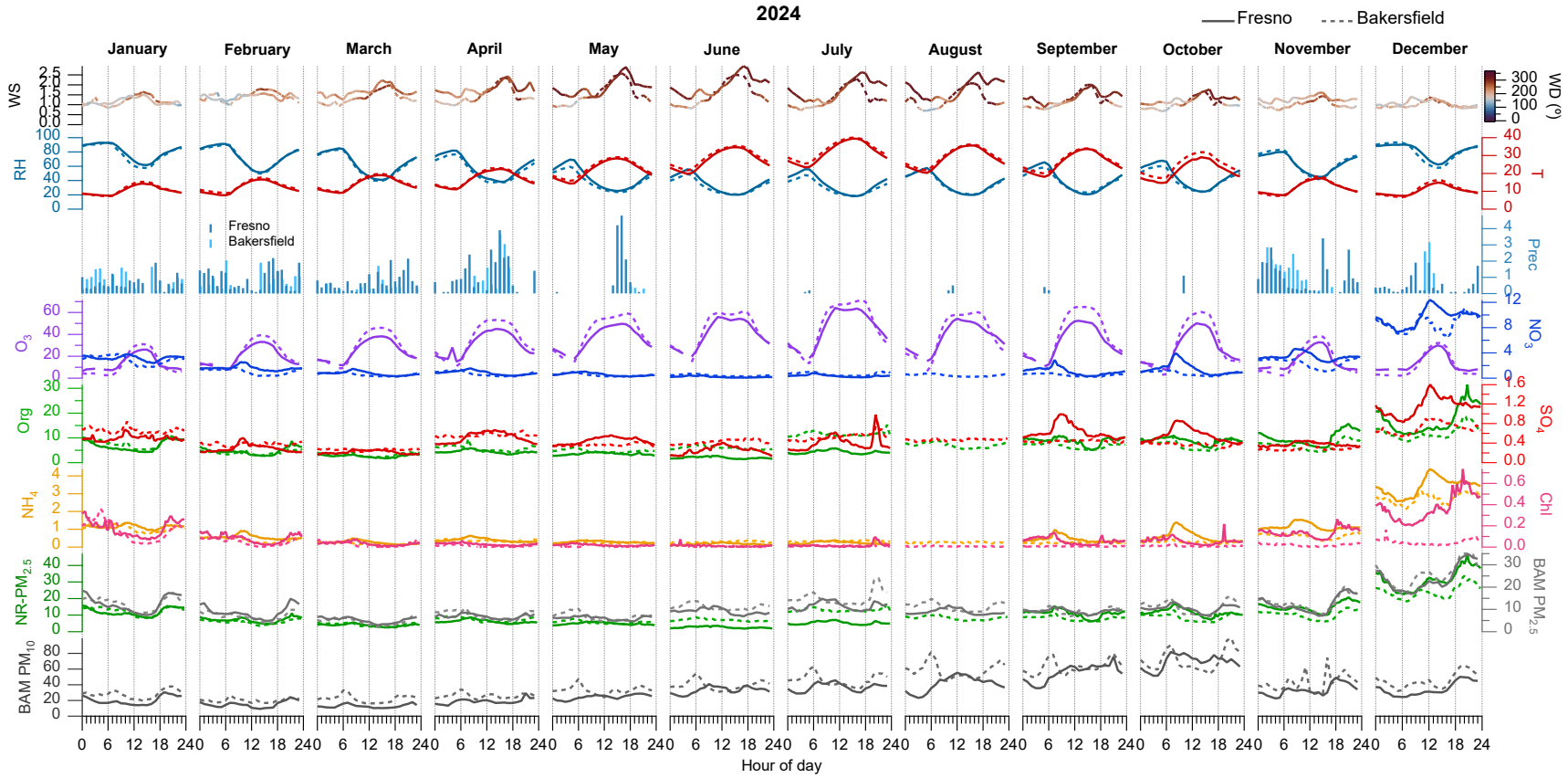
2024
Fresno
Bakersfield
January
February
March
April
May
June
July
August
September
October
November
December
WS
RH
Fresno
Bakersfield
Prec
WD (°)
T
O3
NO3
Org
SO4
NH4
Chl
NR-PM2.5
BAM PM2.5
BAM PM10
Hour of day

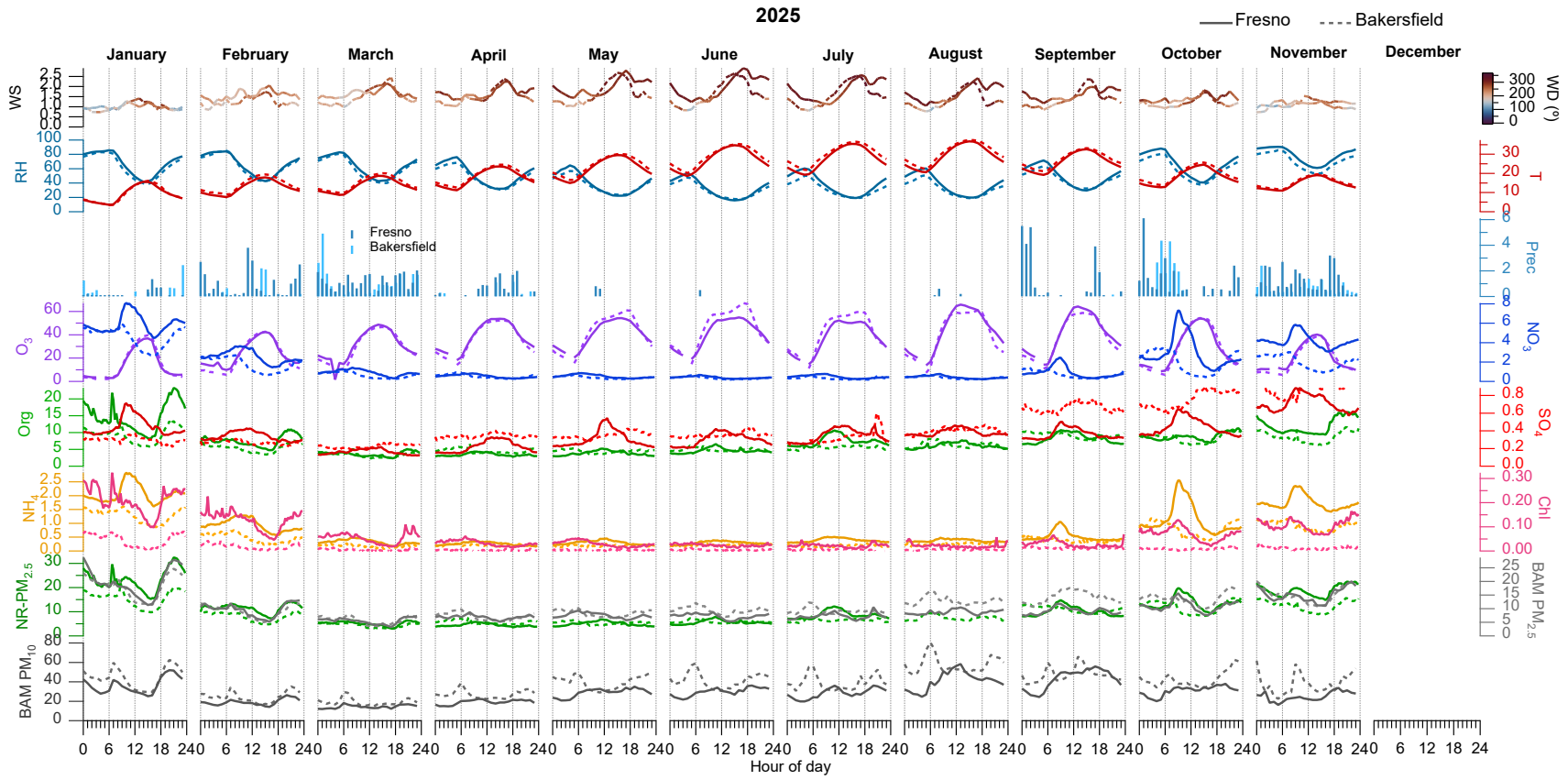

Figure 2-11: Average diel behavior of the major NR-$PM_{2.5}$ components measured by the ACSM, segregated by year

3. SOURCE APPORTIONMENT OF LONG-TERM ACSM NR-$PM_{2.5}$ MEASUREMENTS IN FRESNO AND BAKERSFIELD (SAN JOAQUIN VALLEY)

3.1 Introduction

The ACSM provides time-resolved concentration measurements of NR-$PM_{2.5}$ species along with corresponding matrix of mass spectra of OA and inorganic components. This matrix consists of ensemble mass spectra of NR-$PM_{2.5}$ collected over defined time intervals, where each column represents the concentration of ions at a specific mass-to-charge ratio (m/z) measured throughout the time series (Zhang et al., 2005). The ensemble spectra are linear superpositions of the mass spectra from multiple organic and inorganic aerosol species, weighted by their respective concentrations. Consequently, the signal observed at each m/z reflects a linear combination of contributions from the various sources that generate that ion in the ACSM.

This linearity enables the decomposition of the ACSM mass spectral matrix into its contributing components using matrix factorization techniques. Specifically, the observed matrix can be expressed as the product of two matrices: one representing the mass spectral profiles of individual sources and the other describing their temporal contributions to the particle mass (Zhang et al., 2011). This approach facilitates both the identification and quantification of the sources contributing to the organic and inorganic aerosol fractions measured by the ACSM.

The characteristics of the ACSM mass spectral matrix make it well suited for source apportionment using bilinear factor analytical models such as positive matrix factorization (PMF; (Paatero & Tapper, 1994)). PMF identifies distinct sources or aerosol types by grouping variables into factors based on one of their covariance structure and associated error estimates. By resolving factor-specific mass spectral profiles, PMF enables attribution of individual m/z signals in the ACSM data to specific sources, thereby supporting source identification and quantification (Ulbrich et al., 2009; Zhang et al., 2011).

Mathematically, PMF represents the measured data matrix as the sum of factor contributions and residuals:

$$X = GF + E \qquad \text{Eq. 1}$$

where X is the m × n matrix of measured ACSM mass spectra of NR-$PM_{2.5}$,

G is the m × p matrix of time-dependent factor contributions (source strengths),

F is the p × n matrix of factor mass spectral profiles, and

E is the m × n matrix of residuals not explained by the p factors,

PMF solves this bilinear model by minimizing the weighted least-squares objective function Q:

$$Q = \left\| (X - GF)./\sigma \right\|_F^2 \qquad \text{Eq. 2}$$

Where σ is the matrix of standard deviations of the errors associated with each element of X,

./ denotes element-by-element division, and $||B||_F$ represents the Frobenius Norm, =

The objective function Q explicitly incorporates $\sqrt{\sum_i \sum_j B_{ij}^2}$ measurement uncertainties, thereby down-weighting data points affected by higher uncertainty, proximity to detection limits, missing values, or outliers. The PMF solution is constrained to non-negative values, consistent with the physical requirement that source contributions and mass concentrations cannot be negative. The resulting factors are interpreted as physically meaningful aerosol sources and their corresponding temporal contributions.

In practice, the user specifies the number of factors, p, and PMF determines the optimal solution by minimizing Q subject to these constraints. By incorporating error estimates directly into the factorization, PMF establishes a statistically robust relationship between the measured data and the underlying sources, yielding source-resolved aerosol chemical profiles and time series that can be linked to atmospheric processes and emission sources.

PMF solution can be obtained using either the PMF-2 (Paatero & Tapper, 1994) or the more flexible multilinear engine (ME-2) algorithm (Paatero, 1999). While PMF-2 has been widely applied to aerosol mass spectrometer datasets (Zhang et al., 2011), it can produce mixed or rotationally ambiguous solutions when sources exhibit strong temporal covariance, such as when variability is dominated by meteorological processes such as boundary layer dynamics, or when source chemical profiles are highly similar (Paatero & Hopke, 2009). Under these conditions, ME-2 provides improved source separation by allowing the incorporation of a priori information to better constrain the factorization.

ME-2 extends the PMF framework by enabling partial or full constraints on factor profiles and/or time series, thereby bridging unconstrained PMF and chemical mass balance (CMB) approaches (Paatero, 1999). This flexibility allows ME-2 to resolve factors that may not be separable using unconstrained PMF alone. In addition, ME-2 can incorporate external information, such as wind direction, time-of-day indicators, or seasonal patterns, to better represent nonlinear influences on aerosol concentrations associated with source plumes, diurnal activity cycles, and seasonal variability (Paatero et al., 2002; Paatero & Tapper, 1993).

The application of ME-2 is particularly important for source apportionment of the ACSM datasets in this project because the instruments were equipped with capture vaporizer (CVs) rather than the standard cone-shaped vaporizers (SVs) (Sun et al., 2022). While the CV improves particle collection efficiency and mass quantification by minimizing particle bounce (Hu et al., 2017), the longer particle residence time within the vaporizer results in increased thermal decomposition and fragmentation during ionization. As a result, CV-ACSM mass spectra exhibits reduced chemical resolution, enhanced signals at lower m/z values, and greater spectral similarity among OA sources (Hu et al., 2017; Hu et al., 2018).

Despite these limitations, CV-ACSM mass spectra retain identifiable features associated with major OA sources, including vehicular emissions, biomass burning, and secondary formation, albeit with weaker source specificity than observed using SV instruments. Consequently, meaningful PMF source apportionment can still be achieved, particularly when ME-2 is used to constrain well-characterized primary OA factors such as biomass burning OA (BBOA) and hydrocarbon-like OA (HOA). Applying such constraints reduces rotational ambiguity and improves separation of chemically similar sources. Previous studies have demonstrated the effectiveness of this approach in resolving source-identifiable OA factors, including BBOA, HOA, and oxygenated OA (OOA) with varying degree of oxidation (Hu et al., 2020; Joo et al., 2021; Zheng et al., 2020). In particular, Sun et al. (2022) demonstrated that constraining BBOA and HOA profiles was essential for separating vehicle emissions from local and regional biomass burning in CV-ACSM measurements collected in Fresno.

Source apportionment of long-term ACSM datasets requires considerations beyond conventional PMF or ME-2 applications. In urban valley environments such as Fresno and Bakersfield, strong temporal variability in emissions, meteorology, and atmospheric processing, particularly across seasons and between pollution regimes, means that a single, static PMF or ME-2 solution applied to multi-year datasets is insufficient to resolve evolving OA sources and formation pathways. Over extended time scales, both primary source profiles and secondary OA characteristics can change substantially in response to precursor emissions, oxidant chemistry, and multiphase processing.

To account for this variability, a rolling-window PMF framework is required, in which factorization is performed over successive, overlapping time windows (Parworth et al., 2015). This approach allows source profiles and contributions to evolve over time while retaining constraints on well-characterized primary sources such as HOA and BBOA. As a result, rolling-window ME-2 improves separation of chemically distinct SOA processes, reduces rotational ambiguity in long-term CV-ACSM datasets, and provides a more physically realistic representation of OA sources and processes across multiple years of observations in the SJV (Chazeau et al., 2022; Parworth et al., 2015).

In this project, ME-2 was applied in a rolling-window configuration to the long-term NR-$PM_{2.5}$ OA mass spectral datasets from Fresno and Bakersfield to identify OA sources and quantify their seasonal contributions to $PM_{2.5}$. Incorporation of a priori constraints within ME-2 further reduces rotational uncertainty, while the rolling-window approach captures temporal evolution in OA chemical properties driven by seasonality in emissions, changes in solar insolation, temperature, relative humidity (RH), and source characteristics. Previous studies have shown that rolling-window PMF outperforms seasonal or static approaches by improving correlations with external tracers and minimizing model residuals, making it particularly well suited for multi-year ACSM datasets (Via et al., 2022).

3.2 Methods

3.2.1 Monitoring site and instrumentation

Site description. For the long-term field observations, we deployed two ACSMs, one at Fresno (3727 N. 1st Street, Suite 104, Fresno CA 93726; 36.78538ºN, 119.77321ºW; 97m above sea level) and one at Bakersfield (5558 California Ave, Bakersfield CA 93309, 35.35662ºN, 119.06261ºW; 119 m above sea level). Both instruments have been operated and maintained continuously since Summer 2023 to summer 2025 as part of this project. The Fresno site is surrounded by residential neighborhoods and commercial areas and is close to several major highways, representative of urban basins that are influenced by shallow nocturnal inversions, weak ventilation, frequent radiation fog, and strong residential wood burning. Bakersfield site is surrounded by a high density of chain restaurants and commercial establishments, with additional regional emissions from oil extraction and agriculture. Particulate matter was sampled continuously through a $PM_{2.5}$ cyclone and Nafion dryer mounted approximately 1.5 m above the roofline. The inlet flow was maintained at 0.1 L/min to the ACSM. Routine meteorological and air-quality data collected at these stations include temperature, RH, wind speed and direction, solar radiation, O_3, NO, NO_2, CO, NH_3, SO_2, black carbon, $PM_{2.5}$, and PM_{10}, which provide the environmental context alongside the ACSM measurements.

ACSM. The ACSM measures aerosol mass concentration and chemical composition by sampling particles through an aerodynamic lens into a high-vacuum chamber (Zhang et al., 2002, 2004). Where non-refractory particulate matter is flash vaporized on a heated surface. The resulting gaseous molecules are ionized using 70 eV electron impact ionization and analyzed by mass spectrometry (Fröhlich et al., 2013). In this project, both ACSMs were equipped with a $PM_{2.5}$ aerodynamic lens (Peck et al., 2016) and a capture vaporizer (CV) maintained at approximately 500 ºC. The CV minimizes particle bounce and achieves near-unity collection efficiency for NR-$PM_{2.5}$ (Hu et al., 2017). The configuration enables quantitative measurement of organic aerosol, nitrate, sulfate, ammonium, and chloride in $PM_{2.5}$ (Sun et al., 2022; Zhang et al., 2017; Zheng et al., 2020)

The ACSM deployed at Fresno was equipped with a time-of-flight mass spectrometer (ToF-ACSM), while the instrument deployed at Bakersfield uses a quadrupole mass spectrometer (Q-ACSM). Because the ToF-ACSM provides higher sensitivity than the Q-ACSM (Ng et al., 2011a; Frohlich et al., 2013), NR-$PM_{2.5}$ data at Fresno were collected at higher time resolution than at Bakersfield (10 min vs. 20 min). Such time resolution is substantially higher than the typical hourly resolution used for long-term monitoring, improving the ability to capture short-term variability in $PM_{2.5}$ concentration and composition and enhancing subsequent source apportionment analyses.

Instrument performance was monitored daily using remote-access software (e.g., Teamviewer), and routine on-site calibrations were conducted to determine the ionization efficiency (IE) and relative ionization efficiencies (RIEs) for ammonium and sulfate. Calibrations for IE and ammonium RIE were performed using size-selected ammonium nitrate particles (Canagaratna et

al., 2007) while pure ammonium sulfate particles were used to determine the sulfate RIE (Setyan et al., 2012). These procedures ensured stable instrument performance and improved accuracy of the reported concentrations of NR-$PM_{2.5}$ species.

3.2.2 PMF approach

In this study due to the long-term ACSM time series, a static PMF solution over the full dataset is not assumed to be appropriate. OA source profiles and the composition of secondary OA can evolve with emission regimes and atmospheric processing over time (Canonaco et al., 2015; Paatero et al., 2014). Therefore, we implemented a rolling-window PMF (RPMF) framework following the standardized protocol described by Chen et al. (2022) and Canonaco et al. (2021), building on earlier rolling approaches (Parworth et al., 2015) (Figure 3-1). RPMF was coupled with bootstrap resampling (Davison & Hinkley, 1997) and a random a-value (ME-2) strategy to quantify both statistical and rotational uncertainties and to minimize user subjectivity via automated selection criteria.

Method development, sensitivity testing, and reference profile refinement were initially conducted using ACSM data from Fresno, where additional co-located measurements were available to support methodological evaluation (Figure 3-2). Once finalized, the same RPMF configuration and selection framework were uniformly applied to the full two-year ACSM datasets from both Fresno and Bakersfield.

3.2.3 Rolling-window PMF

Positive Matrix Factorization (Paatero and Tapper, 1994) was performed on the $PM_{2.5}$-ACSM OA mass spectral matrix to investigate aerosol sources and processes using a rolling window strategy to capture seasonal variations within the factor profiles. Rolling-window PMF was applied by running ME-2/PMF repeatedly on successive, overlapping subsets ("windows") of the OA matrix. For each window, constrained and unconstrained factors were resolved, and the ensemble of solutions was then filtered using objective criteria prior to averaging. This approach allows factor profiles and contributions to evolve gradually through time while retaining physically meaningful constraints on primary sources. PMF analysis was conducted using the Multilinear Engine-2 (ME-2) algorithm within the Source Finder software (SoFi Pro V6.B, Datalystica LTD.) within Igor Pro v6.37 (Canonaco et al., 2013; Paatero, 1999).

3.2.3.1 PMF Pre-tests

Dec 2023 Pre-tests. To establish environmentally reasonable base-case solutions (especially POAs to act as a reference profile for final RPMF on longer data) and finalize ME-2 constraint and RPMF parameters (window length and shift size) settings prior to rolling-window PMF analysis on full two-year datasets, we conducted structured pre-tests on selected one-month subsets from Fresno representing winter season (December 2023) following the stepwise workflow recommended by Chen et al. (2022). We first performed a series of unconstrained conventional PMF runs with the

number of factors varied from 2 to 6 to explore the feasible solution space and identify the possible primary factors that can be used further to use as constraint for ME-2. Solutions were evaluated using Q/Q_{exp} together with inspection of factor time series, diel patterns, mass spectral features, and residual structure. Where evidence of source mixing was present, we introduced priori constraints for primary organic aerosol factors using clean HOA and BBOA reference profiles from earlier Fresno studies and tested multiple cases by systematically varying a-values. This included applying previously used Fresno-based settings, scanning HOA constraint tightness over a broad range (a-value of 0 to 1 with a step-size of 0.1), while keeping BBOA fixed, and performing a more comprehensive sensitivity analysis in which both HOA and BBOA a-values were varied from 0 to 1 with a step size of 0.1 to assess rotational behavior, factor stability, and residual response. Across these sensitivity runs, we compared factor interpretability using spectral markers, diurnal behavior, external tracer relationships, and residual diagnostics, and selected a consistent ME-2 constraint strength (a = 0.4 for both HOA and BBOA) for subsequent analyses.

June 2023 Pre-tests. After finalizing the RPMF parameters (window length = 7 days and shift size = 6 hours) and ME-2 constraint strength (a = 0.4 for both HOA and BBOA) , we wanted a pre-test exercise on a month (June 2023) from other season to evaluate the transferability of the December-derived reference information under a different seasonal regime and to explicitly assess the feasibility of resolving cooking-related OA within the ACSM data. Like December, we ran unconstrained PMF (2–6 factors) to characterize the seasonal based factors and then applied constrained solutions using the HOA and BBOA profiles derived from the December with a bootstrap run with a-value=0.4. In additional sensitivity tests, COA was included as a constrained primary factor (COA reference profile from Hu et al. (2017) and for the COA, a-value was systematically varied within a defined range (a-value from 0 to 0.4 with a step of 0.1) while maintaining the HOA and BBOA constraints. Collectively, these pre-tests were used to define a consistent factor framework suitable for rolling-window implementation, while maintaining a static number of OOA factors when environmentally reasonable, consistent with the protocol guidance that objective determination of factor-number transition periods over time remains challenging.

Refined Dec 2023 RPMF with insights from June Pre-test (COA included) and validation using CIMS. Following the June 2023 pre-tests, which demonstrated that cooking organic aerosol (COA) could be consistently resolved under constrained conditions, we returned to the December 2023 Fresno dataset to reassess and refine the COA constraint strategy within the rolling-window PMF framework. December 2023 period was uniquely suited for this refinement because ACSM measurements were co-deployed with both AMS and CIMS at the same site, enabling the use of independent, molecular-level tracers to evaluate the robustness of COA identification (Figure 3-3.

The resulting averaged COA reference profile discussed in detail in section 3.2.2.3 was then used as the COA constraint in subsequent rolling-window PMF analyses of the full 2-year ACSM datasets at Fresno and Bakersfield, together with the finalized HOA and BBOA constraints and the rolling-window parameters established earlier. This refinement step ensured that the COA

constraint applied in the long-term RPMF analysis was informed by both seasonal testing and independent tracer validation, while remaining compatible with the ACSM measurement characteristics.

3.2.2.3 ME-2 Constraint

HOA and BBOA constraints. The final ME-2 constraint was set to a-value = 0.4 for both HOA and BBOA, based on the December 2023 pre-test sensitivity analyses and bootstrap evaluation described above. Reference mass spectra used for PMF pre-tests and subsequent rolling analyses were taken from the December bootstrapped solutions and then used as fixed reference inputs for June and other periods to maintain consistency.

COA constraint. Unlike HOA and BBOA, a site-specific ACSM COA reference spectrum was not available at the start of the analysis. Therefore, an initial COA constraint was derived from (Hu et al., 2017) using an AMS database profile acquired with a capture vaporizer and a $PM_{2.5}$ lens. The Hu et al. (2017) profile was originally high-resolution and was averaged to unit-mass resolution (UMR) to match the ACSM organic matrix and then used as the COA reference spectrum for constrained RPMF runs during the initial pre-test PMF analysis on Dec 2023 ACSM data.

To test the consistency of COA constraints in ACSM RPMF, we performed a series of sensitivity analyses on the December ACSM dataset in which ME-2 was applied using alternative COA constraint strategies. These included constraining ACSM RPMF with (i) The published AMS-derived COA profile adapted from Hu et al. (2017), (ii) ACSM-compatible COA reference profiles generated by constraining AMS-derived cooking-related time series within the ACSM rolling PMF, resulting in a site-specific UMR COA reference profile., and (iii) Averaged COA profile by combining Hu et al., 2017 and ACSM-compatible COA profiles generated by constraining AMS-derived cooking time series. These tests were designed to evaluate the stability of the resulting COA mass spectral profiles and to assess the sensitivity of ACSM PMF to differences in instrument configuration, size cut (PM_1 vs $PM_{2.5}$), and vaporizer type (SV vs CV).

The sensitivity analyses indicated that COA profiles derived solely from AMS-based time-series constraints were strongly influenced by instrument-specific characteristics, while reliance on the published Hu et al. profile alone did not fully capture the site-specific cooking signal observed during December 2023. This limitation is not solely due to the lack of high-resolution mass spectra from the ACSM, but also reflects differences in instrument configuration (e.g., unit-mass resolution, vaporizer type, and size cut) and site-specific variability in cooking emissions. To balance these effects and to develop a COA constraint appropriate for long-term ACSM RPMF, we adopted a hybrid approach in which the final COA reference spectrum was constructed by averaging the Hu et al. (2017) COA profile with ACSM-compatible profile derived from ME-2 analyses constrained by AMS-based cooking time series under moderate a-value settings. This approach was chosen to preserve consistency with the ACSM $PM_{2.5}$ measurement configuration

while incorporating site-specific information from co-located high-resolution and molecular-level observations.

Because only Fresno had co-deployed advanced instrumentation (ACSM + AMS + CIMS) and only during December 2023, additional COA constraint refinement was performed using the Fresno December subset. Specifically, AMS-derived cooking-related OA time series were used within ME-2 (and in sensitivity runs) to generate ACSM-compatible UMR COA profiles for evaluation against the initial Hu et al. constraint. These COA profile-development steps were conducted as method development to improve the constraint robustness for long-term ACSM rolling PMF analysis.

3.2.2.4 Bootstrapping for uncertainty in Base solutions from Pre-Test PMF

Bootstrap analysis was conducted to quantify uncertainty and evaluate the repeatability of constrained solutions following the pre-test PMF (Davison & Hinkley, 1997). Using the selected constraint settings (HOA, BBOA and COA), we performed 100 bootstrap runs in which random a-values were drawn for constrained factors within 0 to 0.4 using a step size of 0.1. Each bootstrap resample yields a PMF solution that reflects both sampling variability and rotational flexibility (Tobler et al., 2020).

To minimize manual screening and user subjectivity, bootstrap solutions were processed using a criteria-based selection framework (Canonaco et al., 2021; Chen et al., 2022). This framework automatically accepts/rejects candidate solutions based on pre-defined, environmentally reasonable criteria (Figure 3-4) and includes statistical testing using a double-tailed Welch's t-test ($p \leq 0.05$) for time-series-based discrimination and/or thresholds derived from Pre-test seasonal bootstrap runs. The accepted bootstrap solutions were used to (i) assess the stability of constrained factors, (ii) identify suitable reference profiles for rolling analysis, and (iii) provide internally consistent input spectra for the rolling-window PMF for full 2-year ACSM data.

PMF uncertainty for each factor was evaluated using the variability across repeated time points obtained from the selected rolling-window solutions. This uncertainty reflects contributions from both bootstrap resampling and the ensemble of solutions generated using different a-value constraints. Figure 3-5 and Figure 3-6 show the probability density functions (pdfs) of the ratio between the standard deviation and the mean concentration for each PMF time point. Following approaches commonly adopted in previous rolling PMF studies (e.g., (Canonaco et al., 2021; A. K. Tobler et al., 2021), the uncertainty of each PMF factor is quantified using the center of the fitted lognormal distribution (x_0).

3.2.2.5 Criteria-based selection for PMF runs

Rolling-window PMF generates a large number of PMF runs, making manual inspection impractical. Therefore, an automated, criteria-based selection framework was implemented in SoFi Pro to objectively evaluate solution quality and to ensure consistent factor identification. (Figure 3-4), following the methodology described by Canonaco et al. (2021) and Chen et al. (2022). This

approach serves two purposes: (i) filtering out environmentally unreasonable PMF solutions and (ii) systematically sorting factors prior to averaging, thereby minimizing subjective user intervention.

Selection criteria were defined using a combination of time-series-based diagnostics, mass-spectral and explained-variation metrics, and statistical significance testing. Time-series and correlation-based criteria were evaluated using Welch's t-test, with a significant threshold of $p \leq 0.05$, to ensure that the base-case met the specified criterion more strongly than other factors within the same PMF solution. This statistical screening reduces ambiguity associated with factor swapping and rotational variability inherent to rolling analyses.

For the long-term ACSM datasets, primary organic aerosol factors were identified using site-specific external and mass spectral criteria. HOA was selected based on its correlation with NO_x (Chen et al., 2022), reflecting traffic-related emissions, while BBOA was identified using the explained variation of m/z 60, a well-established biomass burning marker (Alfarra et al., 2007). These criteria were applied consistently across all rolling windows to reject non-physical solutions and to maintain consistent factor labeling prior to averaging. Unconstrained secondary organic aerosol factors were sorted using representative mass-spectral characteristics to prevent mixing in factors across iterations, consistent with recommendations for rolling-window PMF analyses. The same selection criteria and thresholds were applied uniformly to all tested rolling-window configurations to ensure comparability and robustness of the final average solutions at both Fresno and Bakersfield.

3.2.2.6 Final RPMF for full 2-year ACSM data

Based on the December 2023 pre-tests and bootstrap analyses, final rolling-window PMF (RPMF) parameters were selected to ensure stable factor separation while capturing temporal variability in the ACSM datasets. Following the standardized framework of Canonaco et al. (2021) and Chen et al. (2022), mass spectral profiles derived from Dec pre-test PMF bootstrap solutions were used as reference constraints for primary organic aerosol (POA) factors during rolling PMF analysis. In this study, HOA, BBOA, and COA were all treated as constrained POA factors within the ME-2 framework.

RPMF was implemented using ME-2 with a random a-value approach to account for rotational uncertainty. For each rolling window, a-values for constrained factors were randomly selected within predefined ranges, with an upper limit of 0.4 applied to all constrained POA factors based on bootstrap sensitivity analyses. Several rolling configurations were evaluated during method development, and a 7-day rolling window with a 6-hour step size was selected as the final configuration, balancing temporal resolution and statistical stability. The number of factors was consistently tested within a narrow range of 5 to 6 factors, reflecting the structure identified during the pre-tests. Final RPMF solutions for Fresno and Bakersfield were obtained by applying a criteria-based selection framework prior to averaging.

3.3 Results and Discussion

3.3.1 ME-2 based RPMF OA source apportionment on ACSM data

Rolling-window ME-2 analysis of the long-term ACSM datasets resolved six organic aerosol (OA) factors at both Fresno and Bakersfield: hydrocarbon-like organic aerosol (HOA), cooking organic aerosol (COA), two biomass burning factors (BBOA1 and BBOA2), and oxygenated organic aerosol separated into more-oxidized (MOOA) and less-oxidized (LOOA) factors. The resolved factor mass spectra, diurnal cycles, time series, and average contributions are shown in Figures 3-7 (Fresno) and Figure 3-8 (Bakersfield).

Hydrocarbon-like Organic Aerosol (HOA). HOA is characterized by a mass spectral profile dominated by m/z 41 ($C_3H_5^+$), 43 ($C_3H_7^+$), 55 ($C_4H_7^+$), 57 ($C_4H_9^+$), 69 ($C_5H_9^+$) and 71 ($C_5H_{11}^+$), consistent with freshly emitted vehicular and fossil fuel combustion aerosols (Figure 3-7a and 3-8a) (Zhang et al., 2011). At both sites, HOA exhibits pronounced diurnal variability with elevated concentrations during morning and evening periods, reflecting traffic activity, and enhanced nighttime levels associated with reduced boundary layer height (Figure 3-7b and 3-8b). Temporal behavior and spectral characteristics support attribution of HOA to traffic-related emissions in both Fresno and Bakersfield. HOA contributes a smaller but consistent fraction of the total OA mass (7%) over the analysis period at both sites (Figure 3-7d and 3-8d).

Cooking Organic Aerosol (COA)

Although the COA mass spectrum shows similarities to HOA due to overlapping hydrocarbon fragments, it maintains key features of the cooking OA reference spectrum (Mohr et al., 2012), with comparatively higher m/z 41 to 43 and m/z 55 to 57 ratios that are characteristic of cooking emissions (Pikmann et al., 2024). While the temporal structure is broadly similar between Fresno and Bakersfield, slight differences in relative contribution, reflecting site-specific cooking activity patterns. COA represents a distinct primary OA component and contributes a significant fraction (10 to 11%) to total OA across the study period (Figure 3-7d and 3-8d). Independent validation is further supported by strong correlations between ACSM COA and AMS cooking tracers, including AMS $C_6H_{10}O^+$ (r=0.87; Fig. 3.15) and AMS-resolved COA (r=0.85; Fig. 3.15), confirming consistent identification of cooking emissions across the two collocated instruments.

Biomass Burning Organic Aerosol (BBOA1 and BBOA2)

Two biomass burning OA factors were resolved at both sites (Figure 3-7 and 3-8). BBOA1 exhibits prominent peaks at m/z 60 and 73, well-established tracers of biomass combustion (Alfarra et al., 2007). While BBOA2 is dominated by m/z 29 (CHO, widely used as a marker for wood combustion (Goetz et al., 2022)) and has more oxidized ion signal (Figure 3-7a and 3-8a). The two factors differ in relative spectral features and temporal behavior, supporting their separation into distinct components. Both factors show enhanced nighttime concentrations, consistent with residential burning and nocturnal accumulation. The presence of two BBOA factors indicates

contributions from different biomass burning emissions or combustion conditions (residential wood burning, wildfires etc.) captured by the rolling-window analysis.

Oxidized Organic Aerosol (OOA). The oxidized organic aerosol resolved by the rolling-window ME-2 analysis is represented by two factors indicating sequential oxidation: more-oxidized OA (MOOA) and less-oxidized OA (LOOA). Together, these factors account for a major fraction of the OA mass at both Fresno and Bakersfield, underscoring the importance of secondary aerosol formation in the region. MOOA is characterized by a dominant signal at m/z 44 (CO_2^+) and a high f44/f43 ratio, indicative of highly oxidized organic source (Chazeau et al., 2022; Zhang et al., 2011) (Figure 3-7a and 3-8a). Its temporal behavior is relatively smooth, with weak diurnal variability compared to primary OA factors, consistent with regional secondary formation and atmospheric aging (Figure 3-7c and 3-8c). A modest afternoon enhancement is occasionally observed, particularly during periods of higher solar insolation, reflecting photochemical production (Figure 3-7b and 3-8b).

LOOA exhibits comparatively enhanced contributions at other m/z values and a higher f43/f44 ratio relative to MOOA, indicative of less-oxidized organic source (Chazeau et al., 2022; Zhang et al., 2011). While its temporal variability remains smoother than that of primary OA components, LOOA shows more pronounced diurnal structure than MOOA. During warmer periods, LOOA displays diurnal patterns like MOOA, suggesting increased photochemical processing and convergence toward more oxidized states. In contrast, during colder months, LOOA exhibits semi-volatile behavior, with enhanced nighttime concentrations and afternoon minima, consistent with temperature-driven gas–particle partitioning and dilution effects. Together, MOOA and LOOA capture the evolving oxidation stages of secondary organic aerosol across seasons and sites.

3.3.2 Comparison of OA sources in Fresno and Bakersfield

The daily averaged time series further supports these compositional differences (Figure 3-9). Fresno shows more frequent short-term enhancements in BBOA and COA, which coincide with elevated CO and NOx, indicating stronger coupling with local combustion-related activities. In contrast, Bakersfield displays smoother time series, with MOOA contributing persistently and showing periods of co-variation with O_x and O_3, consistent with a stronger influence of regional secondary aerosol formation. HOA remains a minor factor but consistently contributed to total OA mass at both sites, with slightly greater variability at Fresno reflected in its time series behavior.

Monthly-averaged NR-$PM_{2.5}$ shows clear variability between Fresno and Bakersfield (Figure 3-10). Both sites exhibit their highest monthly mean concentrations in December, followed by January, with Fresno reaching ~27 $\mu g.m^{-3}$ in December compared to ~23 $\mu g.m^{-3}$ at Bakersfield. Several intermediate months show comparable or slightly higher NR-$PM_{2.5}$ at Bakersfield, indicating periods of reversed site dominance. Across all months, organic aerosols remain the dominant NR-$PM_{2.5}$ component at both sites, accounting for most of the total mass.

The OA composition is consistently dominated by secondary components (MOOA and LOOA), which together contribute the largest fraction in most months at both locations. MOOA shows relatively stable monthly contributions, whereas LOOA exhibits larger month-to-month variability, consistent with its more dynamic temporal behavior observed in the time series. Biomass burning OA (BBOA1 and BBOA2) contributes to a noticeably larger fraction at Fresno than at Bakersfield, particularly in months with elevated NR-$PM_{2.5}$, while Bakersfield generally exhibits a more balanced distribution among OA components.

3.3.3 Seasonal variation of OA sources

Seasonal averages of NR-$PM_{2.5}$ and its chemical composition reveal strong contrasts across seasons at both Fresno and Bakersfield (Fig. 3-11). Winter exhibits the highest NR-$PM_{2.5}$ concentrations (18.3 ± 6.3 $\mu g.m^{-3}$) in Fresno and 15.3 ± 5.5 $\mu g.m^{-3}$ in Bakersfield, followed by fall, whereas spring shows substantially lower concentrations (≈5-6 $\mu g.m^{-3}$) and summer moderate levels (≈9-10 $\mu g.m^{-3}$)). These seasonal differences are consistently reflected in both sites, although Fresno maintains higher absolute concentrations throughout the year.

Organic aerosol dominates NR-$PM_{2.5}$ mass in all seasons, with secondary OA (MOOA and LOOA) contributing the largest fraction year-round. During spring and summer, OOA accounts for up to ~55% of NR-$PM_{2.5}$, despite lower total PM levels. This is supported by the diurnal profiles, where MOOA exhibits pronounced daytime enhancements that coincide with elevated O_x and O_3, reflecting active photochemical production under higher temperatures and stronger solar radiation (Hayes et al., 2013). Even as primary emissions and inorganic components decrease, the persistence of OOA indicates that secondary formation remains an important contributor to $PM_{2.5}$ across all seasons.

In contrast, wintertime NR-$PM_{2.5}$ enhancements are driven by increased contributions from primary OA and nitrate. Biomass burning OA contributes substantially during winter and fall (≈10-15% of OA), as seen in both the seasonal composition and the diurnal profiles showing nighttime BBOA maxima (Figure 3-12). These enhancements coincide with elevated CO and NO_x, low wind speeds, and higher relative humidity, indicating accumulation of combustion-related emissions under stagnant conditions (Hu et al., 2017). The diurnal structure of BBOA, with sustained nighttime elevations, contrasts sharply with its minimal contribution in spring, when higher wind speeds and deeper boundary layers promote dilution.

Nitrate exhibits its largest fractional contribution during winter, consistent with low temperatures favoring gas–particle partitioning (Guo et al., 2016). This behavior is reflected in the nighttime and early-morning nitrate peaks, which weaken in warmer seasons as temperatures increase, wintertime enhancement likely reflects the combined effect of lower temperatures and higher cumulative NOx emissions from anthropogenic combustion, with biomass burning providing an additional, but comparatively smaller, NOx source. O_x-driven photochemistry shifts the aerosol composition toward sulfate and MOOA (Guo et al., 2016; Shah et al., 2018). During summer,

sulfate and highly oxidized OA become relatively more important, consistent with enhanced oxidation and regional transport processes.

Overall, the seasonal evolution of $PM_{2.5}$ at both Fresno and Bakersfield reflects a transition from wintertime accumulation of primary emissions and semi-volatile inorganic aerosol under stagnant meteorology to warmer-season conditions dominated by photochemically produced secondary organic aerosol, as supported by the combined seasonal composition, diurnal behavior, gas-phase tracers, and meteorological parameters.

Weekend/weekday Analysis. Figure 3-13 and 3-14 shows Seasonal weekday and weekend diurnal profiles of NR-$PM_{2.5}$ species and OA factors at Bakersfield and Fresno, showing broadly similar shapes with modest weekend reductions in traffic-related HOA but persistent evening COA and wintertime nitrate enhancements. The diurnal variability in NR-$PM_{2.5}$ components and sources is strongest during winter and weakest during spring & summer at both Fresno and Bakersfield, with consistently larger concentrations in Fresno.

HOA shows slightly higher early-morning peaks on weekdays compared with weekends, especially in winter and autumn, consistent with enhanced commuter traffic emissions during weekday rush hours. On weekends, the HOA morning peak appears damped and shifted later in the day, indicating reduced and temporally redistributed traffic activity. MOOA and LOOA show broadly similar diurnal shapes on weekdays and weekends, with daytime enhancements reflecting photochemical production that depends more on radiation and regional precursor fields than on local weekday traffic differences. For most species and factors (nitrate, sulfate, MOOA, LOOA), weekday and weekend diurnal cycles are very similar in shape and magnitude in all seasons, implying that large-scale regional processes dominate their variability rather than local weekday-specific emissions. This similarity suggests that any weekend effect in total $PM_{2.5}$ mass is modest compared to the strong seasonal contrast, especially for nitrate and secondary OA.

3.3.4 Diurnal variations of PM2.5 composition and sources

Figure 3-15 and 3-16 summarizes how NR-$PM_{2.5}$ composition (including inorganics and OA factor) changes with $PM_{2.5}$ loading, shown separately for daytime (08:00–16:00) and nighttime (18:00–06:00) for Fresno and Bakersfield. In both cities, NR-$PM_{2.5}$ increases to much higher loadings at night than during the day (black triangles) (Figure 3-15 and 3-16), and the accompanying stacked bars show that this nighttime enhancement is associated with a larger primary OA fraction. In Fresno, the night panel extends into the highest loading bins (100 $\mu g.m^{-3}$), while the daytime bins reach similar loadings but occur far less frequently (shown by the rapidly decreasing "fraction of data points" curve at higher bins). Bakersfield reaches slightly lower maximum loading bins overall, and high-loading bins similarly represent a small fraction of observations.

Across both sites, nitrate (NO_3) increases strongly with NR-$PM_{2.5}$ in both day and night, but its behavior diverges at the highest loadings. In Fresno nighttime, NO_3 rises with PM loading up to the mid–high bins and then tends to decrease (the blue curve flattens at the uppermost bins), while

OA components continue to increase, particularly MOOA and biomass-burning-related OA (BBOA1+BBOA2). This shift is also visible in the fraction bars: under high nighttime loadings in Fresno, the combined BBOA fraction becomes distinctly larger than during daytime at comparable loadings, indicating that severe nighttime pollution is increasingly associated with combustion-related primary OA in addition to secondary mass. Bakersfield shows a similar qualitative pattern (higher primary OA fractions at night than day), but the fractional enhancement of BBOA at the highest nighttime loadings is less pronounced than Fresno, and NO_3 continues to increase more steadily across the nighttime loading range.

The day and night contrast is clearest for primary OA. At both sites, BBOA1 and BBOA2 remain a relatively small fraction during daytime across bins, while at night their fractions increase with loading, especially in Fresno. HOA and COA also increase with NR-$PM_{2.5}$ at night (their concentration curves rise with loading), but their fractional contributions remain comparatively smaller than those of NO_3 and OOA across most bins, indicating that the largest changes driving high NR-$PM_{2.5}$ conditions are tied to secondary nitrate + secondary OA plus an increasing primary combustion OA contribution at night. The accompanying gas-phase context from earlier sections is consistent with this interpretation: periods with elevated NOx and CO align with enhanced primary components (especially at night), whereas higher O_x/O_3 conditions support the persistence of oxidized OA (MOOA), which increases more smoothly with loading and remains a major contributor in both Fresno and Bakersfield.

Finally, comparing both sites with similar loading bins, Fresno exhibits a clearer transition toward primary-OA-enriched composition at night, while Bakersfield retains a composition that remains more consistently dominated by secondary mass (NO_3 + OOA) even under elevated loadings. This site contrast, combined with the stronger nighttime primary OA enrichment in Fresno, is consistent with the broader two-year rolling PMF results showing greater influence of variable primary OA components in Fresno relative to Bakersfield.

3.3.5 ACSM OA sources comparison with SP-AMS OA sources for Dec 2023 at Fresno

Comparison of ACSM rolling PMF (RPMF) OA factors with co-located AMS PMF results during the December 2023 overlap period demonstrate strong consistency in both factor contribution and temporal behavior (Figure 3-17 and 3-18). All AMS MOOA-type factors (MOOA1–3 and MZ43OA1–2) were summed and compared with ACSM MOOA; AMS LOOA factors were similarly aggregated and compared with ACSM LOOA; all AMS COA and BBOA factors; HOA factor were summed and compared with their ACSM Corresponding factors. The resulting time series show close temporal agreement across all major OA components, with synchronized enhancements during pollution episodes and consistent relative magnitudes, indicating that the ACSM resolves the same dominant OA sources and processes as the AMS despite differences in instrumental configuration.

Quantitatively, ACSM reproduces AMS OA source contributions within expected uncertainty, with secondary OA (MOOA + LOOA) dominating total OA in both datasets and primary OA components (BBOA, COA, HOA) exhibiting comparable episodic behavior. Minor differences in absolute magnitude are attributable to known instrumental factors, including the ACSM capture vaporizer versus the AMS standard vaporizer and differences in particle transmission and PM lens efficiency. Independent validation is further supported by strong correlations between ACSM COA and AMS cooking tracers, including AMS $C_6H_{10}O^+$ and AMS-resolved COA ($r=0.8$; Figure 3-19), confirming consistent identification of cooking emissions across the two collocated instruments. Together, the factor-to-factor correspondence, aligned time series, and robust tracer correlations demonstrate that ACSM RPMF provides a reliable and internally consistent representation of OA sources, closely tracking the co-located AMS and supporting its use for long-term source apportionment in regulatory applications.

3.4. Conclusions and Implications

This study provides a two-year, process-resolved characterization of organic aerosol sources in the southern San Joaquin Valley using rolling-window ME-2 PMF applied to long-term ACSM measurements in Fresno and Bakersfield. Six OA factors; HOA, COA, BBOA1, BBOA2, MOOA, and LOOA were resolved at both sites, demonstrating that the rolling ME-2 framework can reliably separate multiple primary and secondary OA components in chemically complex, multi-year datasets. Across both cities, secondary OA dominates the OA mass throughout the year, with MOOA and LOOA together contributing the largest fraction in all seasons, highlighting the persistent role of secondary formation processes in regional $PM_{2.5}$.

Wintertime $PM_{2.5}$ pollution is driven by the combined effects of enhanced primary emissions and unfavorable meteorology, particularly at night. Diurnal and seasonal analyses show strong nighttime enhancements of BBOA, HOA, COA, and nitrate under shallow boundary layers, with this behavior more pronounced in Fresno than Bakersfield. In warmer seasons, diurnal concentrations weaken, primary OA contributions decrease, and OA compositions become dominated by secondary components with smoother temporal behavior. Across all analyses, Fresno consistently shows stronger nighttime enrichment of primary OA, whereas Bakersfield exhibits a more stable OA composition dominated by regionally influenced secondary aerosol. Bin-wise PM loading analysis further indicates that as NR-$PM_{2.5}$ increases, nighttime composition shifts toward larger contributions from primary OA, especially biomass burning OA, while nitrate increases tend to level off at the highest loadings, particularly in Fresno. This transition demonstrates that the most severe PM episodes are increasingly influenced by combustion-related primary OA in addition to secondary mass, whereas daytime PM remains dominated by secondary factors across PM loading bins.

These results have direct implications for air quality management in the San Joaquin Valley. The strong enrichment of primary OA during high-loading nighttime conditions indicates that targeted controls on residential wood burning and other evening combustion activities can be especially

effective in reducing extreme $PM_{2.5}$ events, particularly in Fresno. At the same time, the persistence of secondary OA across all seasons and PM loading levels underscores the importance of coordinated reductions in precursor gases (NOx, VOCs, and NH_3) to achieve sustained improvements in air quality. Finally, the observed differences between Fresno and Bakersfield emphasize the need for location-specific strategies: Fresno requires greater emphasis on mitigating variable primary sources and nocturnal accumulation, while Bakersfield benefits more from regional approaches aimed at limiting secondary aerosol formation.

3.5. References

Alfarra, M. R., Prevot, A. S. H., Szidat, S., Sandradewi, J., Weimer, S., Lanz, V. A., Schreiber, D., Mohr, M., & Baltensperger, U. (2007). Identification of the mass spectral signature of organic aerosols from wood burning emissions. *Environmental Science and Technology*, *41*(16), 5770–5777. https://doi.org/10.1021/es062289b

Canagaratna, M. R., Jayne, J. T., Jimenez, J. L., Allan, J. D., Alfarra, M. R., Zhang, Q., Onasch, T. B., Drewnick, F., Coe, H., Middlebrook, A., Delia, A., Williams, L. R., Trimborn, A. M., Northway, M. J., DeCarlo, P. F., Kolb, C. E., Davidovits, P., & Worsnop, D. R. (2007). Chemical and microphysical characterization of ambient aerosols with the aerodyne aerosol mass spectrometer. *Mass Spectrometry Reviews*, *26*(2), 185–222. https://doi.org/10.1002/MAS.20115

Canonaco, F., Crippa, M., Slowik, J. G., Baltensperger, U., & Prévôt, A. S. H. (2013). SoFi, an IGOR-based interface for the efficient use of the generalized multilinear engine (ME-2) for the source apportionment: ME-2 application to aerosol mass spectrometer data. *Atmospheric Measurement Techniques*, *6*(12), 3649–3661. https://doi.org/10.5194/amt-6-3649-2013

Canonaco, F., Slowik, J. G., Baltensperger, U., & Prévôt, A. S. H. (2015). Seasonal differences in oxygenated organic aerosol composition: Implications for emissions sources and factor analysis. *Atmospheric Chemistry and Physics*, *15*(12), 6993–7002. https://doi.org/10.5194/acp-15-6993-2015

Canonaco, F., Tobler, A., Chen, G., Sosedova, Y., Gates Slowik, J., Bozzetti, C., Rudolf Daellenbach, K., El Haddad, I., Crippa, M., Huang, R. J., Furger, M., Baltensperger, U., & Prévôt, A. S. H. (2021). A new method for long-term source apportionment with time-dependent factor profiles and uncertainty assessment using SoFi Pro: Application to 1 year of organic aerosol data. *Atmospheric Measurement Techniques*, *14*(2), 923–943. https://doi.org/10.5194/AMT-14-923-2021

Chazeau, B., El Haddad, I., Canonaco, F., Temime-Roussel, B., D'Anna, B., Gille, G., Mesbah, B., Prévôt, A. S. H., Wortham, H., & Marchand, N. (2022). Organic aerosol source apportionment by using rolling positive matrix factorization: Application to a Mediterranean

coastal city. *Atmospheric Environment: X*, *14*, 100176. https://doi.org/10.1016/J.AEAOA.2022.100176

Chen, G., Canonaco, F., Tobler, A., Aas, W., Alastuey, A., Allan, J., Atabakhsh, S., Aurela, M., Baltensperger, U., Bougiatioti, A., De Brito, J. F., Ceburnis, D., Chazeau, B., Chebaicheb, H., Daellenbach, K. R., Ehn, M., El Haddad, I., Eleftheriadis, K., Favez, O., … Prévôt, A. S. H. (2022). European aerosol phenomenology − 8: Harmonised source apportionment of organic aerosol using 22 Year-long ACSM/AMS datasets. *Environment International*, *166*, 107325. https://doi.org/10.1016/J.ENVINT.2022.107325

Davison, A. C., & Hinkley, D. V. (1997). Bootstrap Methods and their Application. *Bootstrap Methods and Their Application*. https://doi.org/10.1017/CBO9780511802843

Fröhlich, R., Cubison, M. J., Slowik, J. G., Bukowiecki, N., Prévôt, A. S. H., Baltensperger, U., Schneider, J., Kimmel, J. R., Gonin, M., Rohner, U., Worsnop, D. R., & Jayne, J. T. (2013). The ToF-ACSM: A portable aerosol chemical speciation monitor with TOFMS detection. *Atmospheric Measurement Techniques*, *6*(11), 3225–3241. https://doi.org/10.5194/amt-6-3225-2013

Goetz, J. D., Giordano, M. R., Stockwell, C. E., Bhave, P. V., Puppala, P. S., Panday, A. K., Jayarathne, T., Stone, E. A., Yokelson, R. J., & Decarlo, P. F. (2022). Aerosol Mass Spectral Profiles from NAMaSTE Field-Sampled South Asian Combustion Sources. *ACS Earth & Space Chemistry*, *6*(11), 2619. https://doi.org/10.1021/ACSEARTHSPACECHEM.2C00173

Guo, H., Sullivan, A. P., Campuzano-Jost, P., Schroder, J. C., Lopez-Hilfiker, F. D., Dibb, J. E., Jimenez, J. L., Thornton, J. A., Brown, S. S., Nenes, A., & Weber, R. J. (2016). Fine particle pH and the partitioning of nitric acid during winter in the northeastern United States. *Journal of Geophysical Research*, *121*(17), 10355–10376. https://doi.org/10.1002/2016JD025311

Hayes, P. L., Ortega, A. M., Cubison, M. J., Froyd, K. D., Zhao, Y., Cliff, S. S., Hu, W. W., Toohey, D. W., Flynn, J. H., Lefer, B. L., Grossberg, N., Alvarez, S., Rappenglück, B., Taylor, J. W., Allan, J. D., Holloway, J. S., Gilman, J. B., Kuster, W. C., De Gouw, J. A., … Jimenez, J. L. (2013). Organic aerosol composition and sources in Pasadena, California, during the 2010 CalNex campaign. *Journal of Geophysical Research Atmospheres*, *118*(16), 9233–9257. https://doi.org/10.1002/jgrd.50530

Hu, W., Campuzano-Jost, P., Day, D. A., Croteau, P., Canagaratna, M. R., Jayne, J. T., Worsnop, D. R., & Jimenez, J. L. (2017). Evaluation of the new capture vapourizer for aerosol mass spectrometers (AMS) through laboratory studies of inorganic species. *Atmospheric Measurement Techniques*, *10*(8), 2897–2921. https://doi.org/10.5194/amt-10-2897-2017

Hu, W., Campuzano-Jost, P., Day, D. A., Nault, B. A., Park, T., Lee, T., Pajunoja, A., Virtanen, A., Croteau, P., Canagaratna, M. R., Jayne, J. T., Worsnop, D. R., & Jimenez, J. L. (2020). Ambient Quantification and Size Distributions for Organic Aerosol in Aerosol Mass

Spectrometers with the New Capture Vaporizer. *ACS Earth and Space Chemistry*, *4*(5), 676–689. https://doi.org/10.1021/ACSEARTHSPACECHEM.9B00310

Hu, W., Day, D. A., Campuzano-Jost, P., Nault, B. A., Park, T., Lee, T., Croteau, P., Canagaratna, M. R., Jayne, J. T., Worsnop, D. R., & Jimenez, J. L. (2018). Evaluation of the new capture vaporizer for aerosol mass spectrometers: Characterization of organic aerosol mass spectra. *Aerosol Science and Technology*, *52*(7), 725–739. https://doi.org/10.1080/02786826.2018.1454584;JOURNAL:JOURNAL:UAST20;REQUESTEDJOURNAL:JOURNAL:UAST20;WGROUP:STRING:PUBLICATION

Hu, W., Hu, M., Hu, W.-W., Zheng, J., Chen, C., Wu, Y., & Guo, S. (2017). Seasonal variations in high time-resolved chemical compositions, sources, and evolution of atmospheric submicron aerosols in the megacity Beijing. *Atmos. Chem. Phys*, *17*, 9979–10000. https://doi.org/10.5194/acp-17-9979-2017

Joo, T., Chen, Y., Xu, W., Croteau, P., Canagaratna, M. R., Gao, D., Guo, H., Saavedra, G., Kim, S. S., Sun, Y., Weber, R., Jayne, J., & Ng, N. L. (2021). Evaluation of a New Aerosol Chemical Speciation Monitor (ACSM) System at an Urban Site in Atlanta, GA: The Use of Capture Vaporizer and PM2.5 Inlet. *ACS Earth and Space Chemistry*, *5*(10), 2565–2576. https://doi.org/10.1021/ACSEARTHSPACECHEM.1C00173

Mohr, C., DeCarlo, P. F., Heringa, M. F., Chirico, R., Slowik, J. G., Richter, R., Reche, C., Alastuey, A., Querol, X., Seco, R., Peñuelas, J., Jiḿenez, J. L., Crippa, M., Zimmermann, R., Baltensperger, U., & Prévôt, A. S. H. (2012). Identification and quantification of organic aerosol from cooking and other sources in Barcelona using aerosol mass spectrometer data. *Atmospheric Chemistry and Physics*, *12*(4), 1649–1665. https://doi.org/10.5194/acp-12-1649-2012

Paatero, P. (1999). The Multilinear Engine: A Table-Driven, Least Squares Program for Solving Multilinear Problems, including the n-Way Parallel Factor Analysis Model. *Journal of Computational and Graphical Statistics*, *8*(4), 854. https://doi.org/10.2307/1390831

Paatero, P., Eberly, S., Brown, S. G., & Norris, G. A. (2014). Methods for estimating uncertainty in factor analytic solutions. *Atmospheric Measurement Techniques*, *7*(3), 781–797. https://doi.org/10.5194/amt-7-781-2014

Paatero, P., & Hopke, P. K. (2009). Rotational tools for factor analytic models. *Journal of Chemometrics*, *23*(2), 91–100. https://doi.org/10.1002/cem.1197

Paatero, P., Hopke, P. K., Song, X. H., & Ramadan, Z. (2002). Understanding and controlling rotations in factor analytic models. *Chemometrics and Intelligent Laboratory Systems*, *60*(1–2), 253–264. https://doi.org/10.1016/S0169-7439(01)00200-3

Paatero, P., & Tapper, U. (1993). Analysis of different modes of factor analysis as least squares fit problems. *Chemometrics and Intelligent Laboratory Systems*, *18*(2), 183–194. https://doi.org/10.1016/0169-7439(93)80055-M

Paatero, P., & Tapper, U. (1994). Positive matrix factorization: A non-negative factor model with optimal utilization of error estimates of data values. *Environmetrics*, *5*(2), 111–126. https://doi.org/10.1002/env.3170050203

Parworth, C., Fast, J., Mei, F., Shippert, T., Sivaraman, C., Tilp, A., Watson, T., & Zhang, Q. (2015). Long-term measurements of submicrometer aerosol chemistry at the Southern Great Plains (SGP) using an Aerosol Chemical Speciation Monitor (ACSM). *Atmospheric Environment*, *106*, 43–55. https://doi.org/10.1016/J.ATMOSENV.2015.01.060

Peck, J., Gonzalez, L. A., Williams, L. R., Xu, W., Croteau, P. L., Timko, M. T., Jayne, J. T., Worsnop, D. R., Miake-Lye, R. C., & Smith, K. A. (2016). Development of an aerosol mass spectrometer lens system for PM2.5. *Aerosol Science and Technology*, *50*(8), 781–789. https://doi.org/10.1080/02786826.2016.1190444

Pikmann, J., Drewnick, F., Fachinger, F., & Borrmann, S. (2024). Particulate emissions from cooking: emission factors, emission dynamics, and mass spectrometric analysis for different cooking methods. *Atmos. Chem. Phys*, *24*, 12295–12321. https://doi.org/10.5194/acp-24-12295-2024

Setyan, A., Zhang, Q., Merkel, M., Knighton, W. B., Sun, Y., Song, C., Shilling, J. E., Onasch, T. B., Herndon, S. C., Worsnop, D. R., Fast, J. D., Zaveri, R. A., Berg, L. K., Wiedensohler, A., Flowers, B. A., Dubey, M. K., & Subramanian, R. (2012). Characterization of submicron particles influenced by mixed biogenic and anthropogenic emissions using high-resolution aerosol mass spectrometry: Results from CARES. *Atmospheric Chemistry and Physics*, *12*(17), 8131–8156. https://doi.org/10.5194/ACP-12-8131-2012

Shah, V., Jaeglé, L., Thornton, J. A., Lopez-Hilfiker, F. D., Lee, B. H., Schroder, J. C., Campuzano-Jost, P., Jimenez, J. L., Guo, H., Sullivan, A. P., Weber, R. J., Green, J. R., Fiddler, M. N., Bililign, S., Campos, T. L., Stell, M., Weinheimer, A. J., Montzka, D. D., & Brown, S. S. (2018). Chemical feedbacks weaken the wintertime response of particulate sulfate and nitrate to emissions reductions over the eastern United States. *Proceedings of the National Academy of Sciences*, *115*(32), 8110–8115. https://doi.org/10.1073/PNAS.1803295115

Sun, P., Farley, R. N., Li, L., Srivastava, D., Niedek, C. R., Li, J., Wang, N., Cappa, C. D., Pusede, S. E., Yu, Z., Croteau, P., & Zhang, Q. (2022). PM2.5 composition and sources in the San Joaquin Valley of California: A long-term study using ToF-ACSM with the capture vaporizer. *Environmental Pollution*, *292*, 118254. https://doi.org/10.1016/J.ENVPOL.2021.118254

Tobler, A., Bhattu, D., Canonaco, F., Lalchandani, V., Shukla, A., Thamban, N. M., Mishra, S., Srivastava, A. K., Bisht, D. S., Tiwari, S., Singh, S., Močnik, G., Baltensperger, U., Tripathi, S. N., Slowik, J. G., & Prévôt, A. S. H. (2020). Chemical characterization of PM2.5 and source apportionment of organic aerosol in New Delhi, India. *Science of The Total Environment*, *745*, 140924. https://doi.org/10.1016/j.scitotenv.2020.140924

Tobler, A. K., Skiba, A., Canonaco, F., Močnik, G., Rai, P., Chen, G., Bartyzel, J., Zimnoch, M., Styszko, K., Nęcki, J., Furger, M., Rózański, K., Baltensperger, U., Slowik, J. G., & Prevot, A. S. H. (2021). Characterization of non-refractory (NR) PM1and source apportionment of organic aerosol in Kraków, Poland. *Atmospheric Chemistry and Physics*, *21*(19), 14893–14906. https://doi.org/10.5194/ACP-21-14893-2021

Ulbrich, I. M., Canagaratna, M. R., Zhang, Q., Worsnop, D. R., & Jimenez, J. L. (2009). Interpretation of organic components from Positive Matrix Factorization of aerosol mass spectrometric data. *Atmospheric Chemistry and Physics*, *9*(9), 2891–2918. https://doi.org/10.5194/acp-9-2891-2009

Via, M., Chen, G., Canonaco, F., Daellenbach, K. R., Chazeau, B., Chebaicheb, H., Jiang, J., Keernik, H., Lin, C., Marchand, N., Marin, C., O'dowd, C., Ovadnevaite, J., Petit, J. E., Pikridas, M., Riffault, V., Sciare, J., Slowik, J. G., Simon, L., … Cruz Minguillón, M. (2022). Rolling vs. seasonal PMF: Real-world multi-site and synthetic dataset comparison. *Atmospheric Measurement Techniques*, *15*(18), 5479–5495. https://doi.org/10.5194/AMT-15-5479-2022

Zhang, Q., Jimenez, J. L., Canagaratna, M. R., Ulbrich, I. M., Ng, N. L., Worsnop, D. R., & Sun, Y. (2011). Understanding atmospheric organic aerosols via factor analysis of aerosol mass spectrometry: A review. *Analytical and Bioanalytical Chemistry*, *401*(10), 3045–3067. https://doi.org/10.1007/s00216-011-5355-y

Zhang, Q., Rami Alfarra, M., Worsnop, D. R., Allan, J. D., Coe, H., Canagaratna, M. R., & Jimenez, J. L. (2005). Deconvolution and quantification of hydrocarbon-like and oxygenated organic aerosols based on aerosol mass spectrometry. *Environmental Science and Technology*, *39*(13), 4938–4952. https://doi.org/10.1021/es0485681

Zhang, X., Smith, K. A., Worsnop, D. R., Jimenez, J., Jayne, J. T., & Kolb, C. E. (2002). A Numerical Characterization of Particle Beam Collimation by an Aerodynamic Lens-Nozzle System: Part I. An Individual Lens or Nozzle. *Aerosol Science & Technology*, *36*(5), 617–631. https://doi.org/10.1080/02786820252883856

Zhang, X., Smith, K. A., Worsnop, D. R., Jimenez, J. L., Jayne, J. T., Kolb, C. E., Morris, J., & Davidovits, P. (2004). Numerical characterization of particle beam collimation: Part II integrated aerodynamic-lens-nozzle system. *Aerosol Science and Technology*, *38*(6), 619–638. https://doi.org/10.1080/02786820490479833;CTYPE:STRING:JOURNAL

Zhang, Y., Tang, L., Croteau, P. L., Favez, O., Sun, Y., Canagaratna, M. R., Wang, Z., Couvidat, F., Albinet, A., Zhang, H., Sciare, J., Prévôt, A. S. H., Jayne, J. T., & Worsnop, D. R. (2017). Field characterization of the PM2.5 Aerosol Chemical Speciation Monitor: Insights into the composition, sources, and processes of fine particles in eastern China. *Atmospheric Chemistry and Physics*, *17*(23), 14501–14517. https://doi.org/10.5194/ACP-17-14501-2017

Zheng, Y., Cheng, X., Liao, K., Li, Y., Jie Li, Y., Huang, R. J., Hu, W., Liu, Y., Zhu, T., Chen, S., Zeng, L., Worsnop, D. R., & Chen, Q. (2020). Characterization of anthropogenic organic aerosols by TOF-ACSM with the new capture vaporizer. *Atmospheric Measurement Techniques*, *13*(5), 2457–2472. https://doi.org/10.5194/amt-13-2457-2020

3. 6 Figures

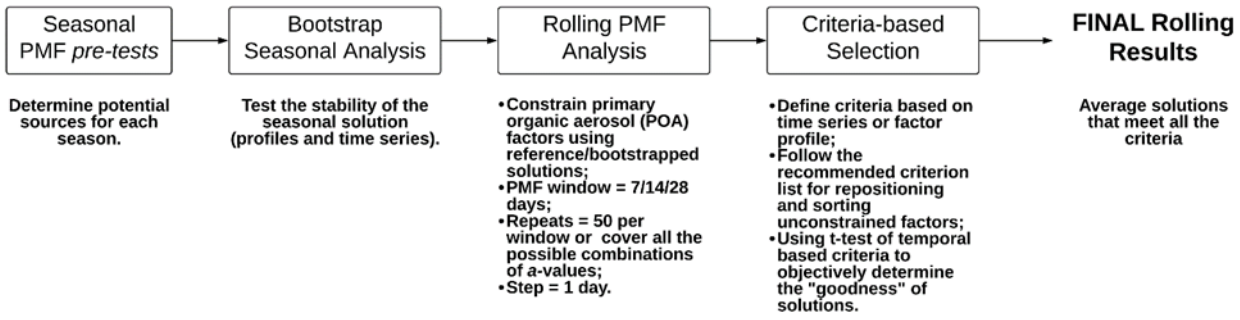

Figure 3-1: Flow diagram of the standardized procedure for rolling PMF (Figure reproduced from Chen et al., 2022).

Step-by-Step Procedure followed using Rolling PMF analysis on ACSM data for Fresno and Bakersfield in SJV

1.Test PMF Analysis on Dec data: **a) Pre-tests:** a) Run unconstrained PMF (2-6 factors). b) Test for specific OA factors (HOA, BBOA, COA, OOA). c) Perform residual analysis (check diel profiles, time series, spectra). d) Conduct a-value sensitivity analysis for constrained factors (POAs). **b) Bootstrap Analysis:** a) Constrain POAs from pre-tests. b) Use bootstrap resampling with random a-values (From 0 to 0.4,step size=0.1). c) Filter environmentally unreasonable PMF runs. d) Criterion based selection*; Quality check the bootstrapped solution. **c) Rolling PMF on Dec datsets:** a) Constrain primary factors & apply random a-values (From 0 to 0.4,step size=0.1). b) Enable bootstrap; **Test for Rolling PMF parameters:** window length (7 days) and shift size (6 hrs).	**2. Test the Dec RPMF settings on June data** a) Constrain POAs from pre-tests. b) Determine factor range based on seasonal analysis. c) Tested for cooking factor d) Criterion based selection*; Quality check the solutions **3. For Cooking source tested on Dec-Feb data** a) Constrain POAs from pre-tests. b) Check for quality of the solution based on results from pre-tests **c) Comparison of Cooking timeseries and diurnal results with CIMS** d) Criterion based selection*; Quality check the solutions **4. Final Rolling PMF on the full year data** a) Constrain POAs from pre-tests. b) Perform residual analysis (check diel profiles, time series, spectra). c) Criterion based selection*; Quality check the solutions

Figure 3-2: Detailed step-by-step procedure followed in this study to perform the ME-2 rolling PMF on ACSM datasets.

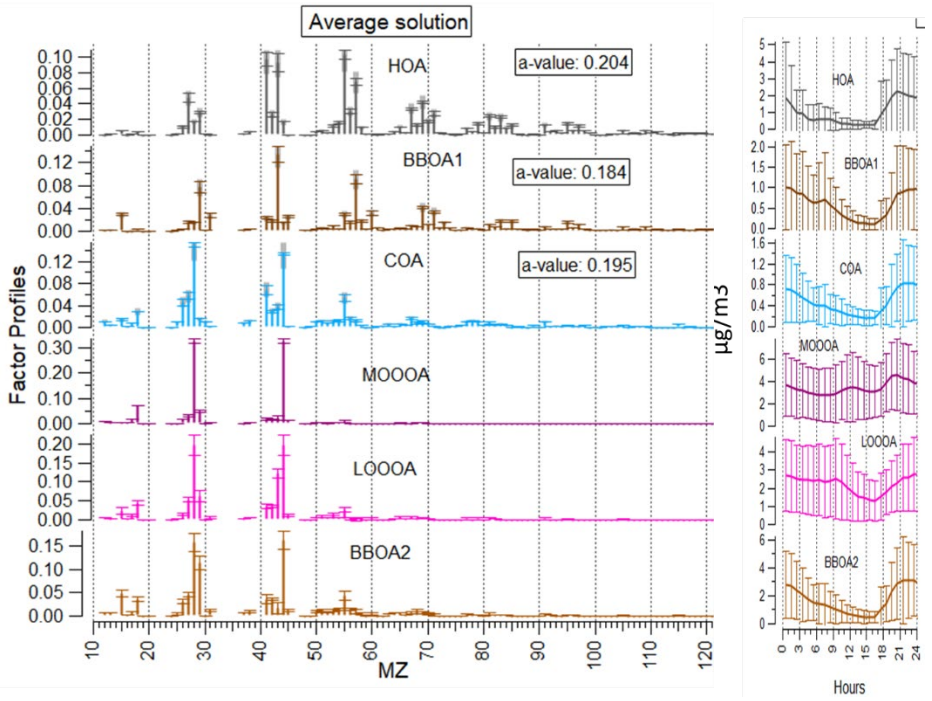

Figure 3-3: Factor profile (left) and diurnal variation (right) of **Pre-test PMF** on the December 2023 ACSM data at Fresno.

#	Criterion	Type	Threshold
0	HOA vs NO_x	R^2, normal time series	p-value ≤ 0.05
1	factor_1[55]'/ factor_1[57]'	Profiles, fraction	p-value ≤ 0.05
2	Explained Variation [60] by BBOA	Average, normal time series	to-factor (p-value ≤ 0.05)
3	factor_3[44]	Profiles, fraction, Sorting criterion	>0
4	factor_4[43]	Profiles, fraction, Sorting criterion	>0
5	factor_5[29]	Profiles, fraction	>0

Figure 3-4: List of objective quantitative criteria applied to assess PMF run quality and to systematically order unconstrained factors for averaging in the ACSM RPMF analysis.

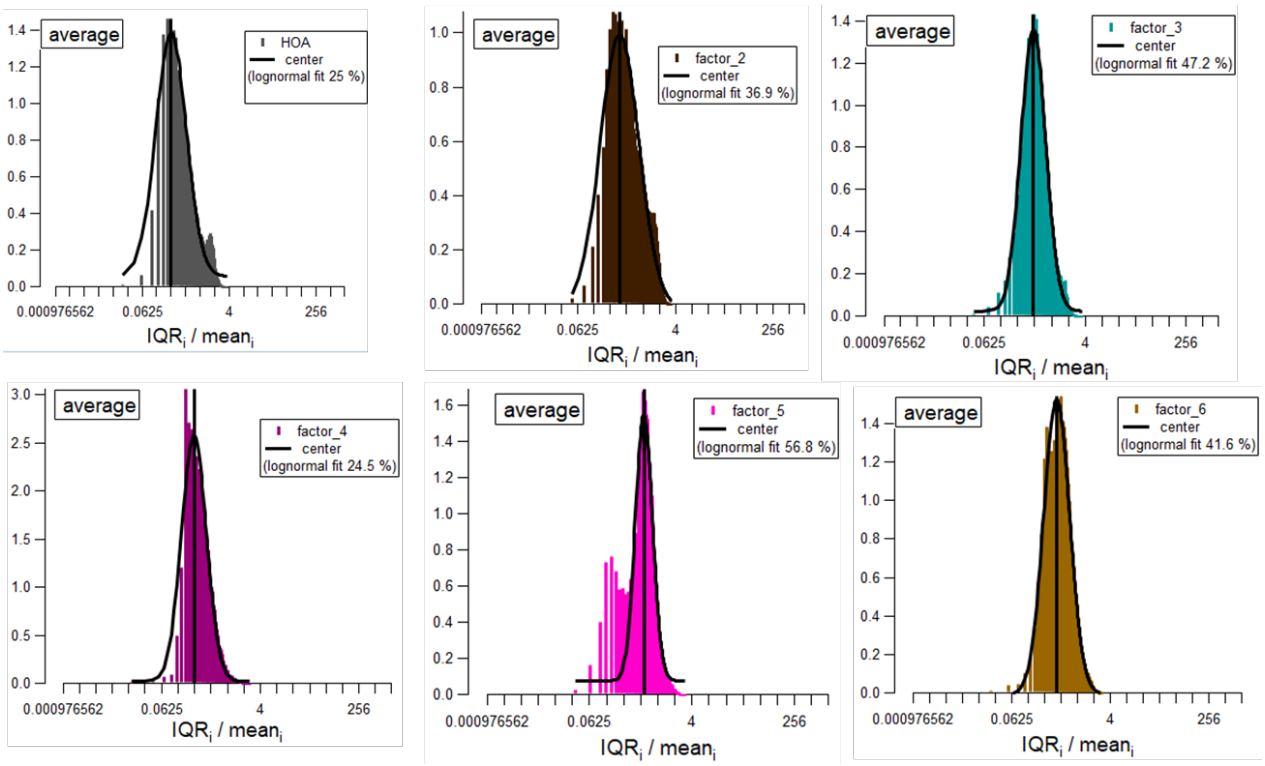

Figure 3-5: Fresno: PMF uncertainty characterization for the six resolved OA factors from long-term RPMF on ACSM data. The ratio of the standard deviation to the mean concentration at each PMF time point is shown as log-probability density functions, with X_0 denoting the centers of the corresponding lognormal fits.

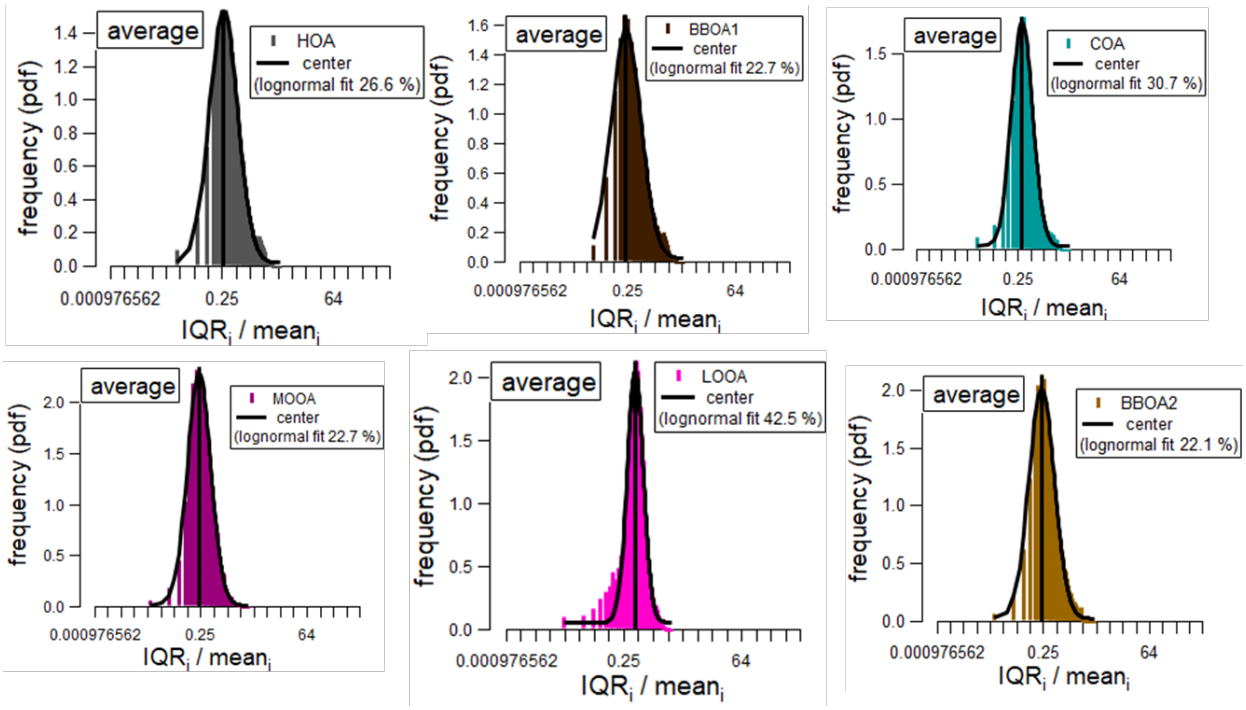

Figure 3-6: Bakersfield: PMF uncertainty characterization for the six resolved OA factors from long-term RPMF on ACSM data. The ratio of the standard deviation to the mean concentration at each PMF time point is shown as log-probability density functions, with X_0 denoting the centers of the corresponding lognormal fits.

Fresno

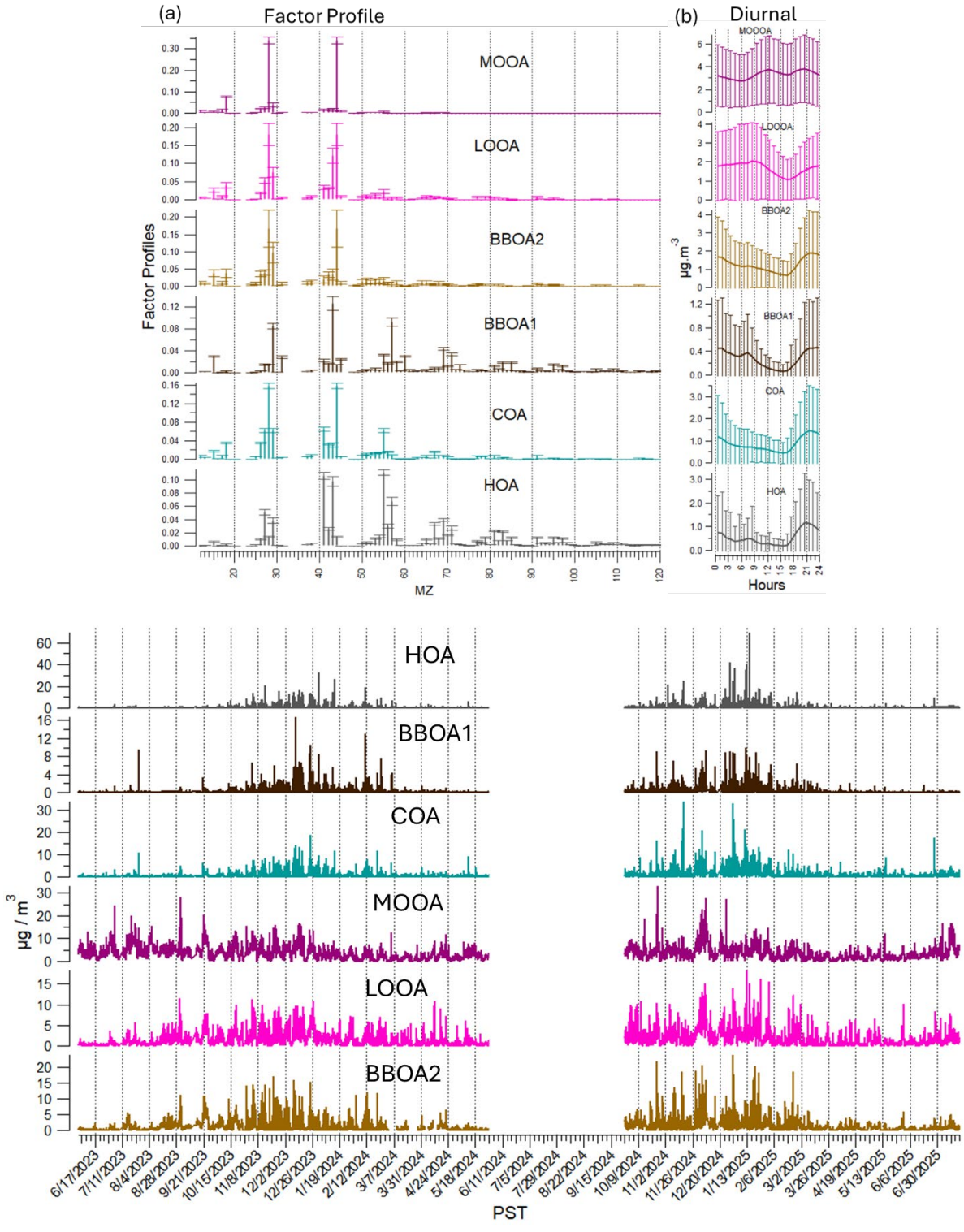
(a)
Factor Profile
MOOA
LOOA
BBOA2
BBOA1
COA
HOA
Factor Profiles
MZ
(b)
Diurnal
µg.m-3
Hours
µg / m3
PST

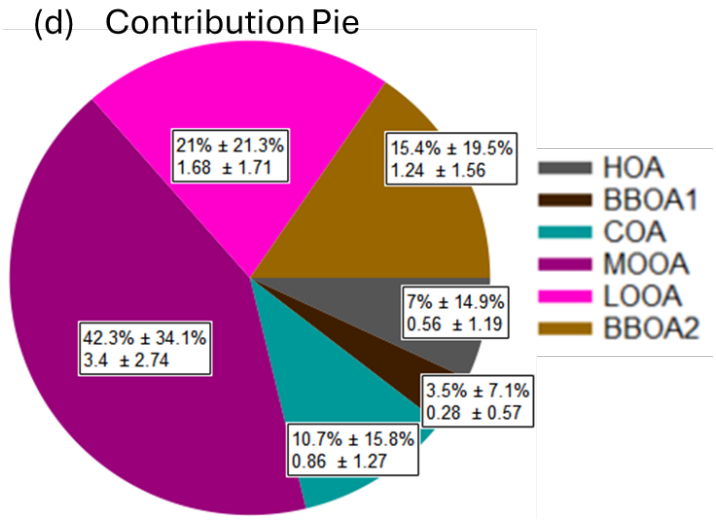

Figure 3-7: RPMF results on 2-year ACSM data. (a) factor profile (b) diurnal cycles, (c) time series, and (d) Relative contribution of resolved OA factors at Fresno.

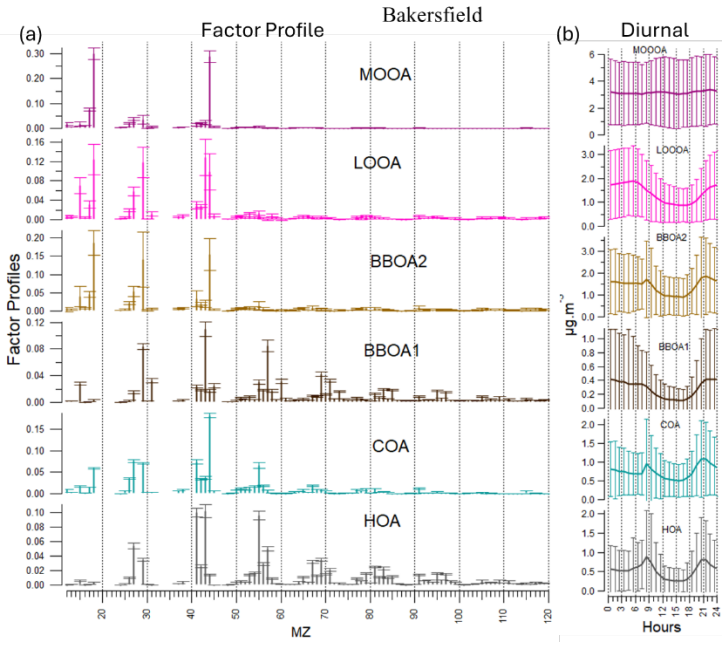

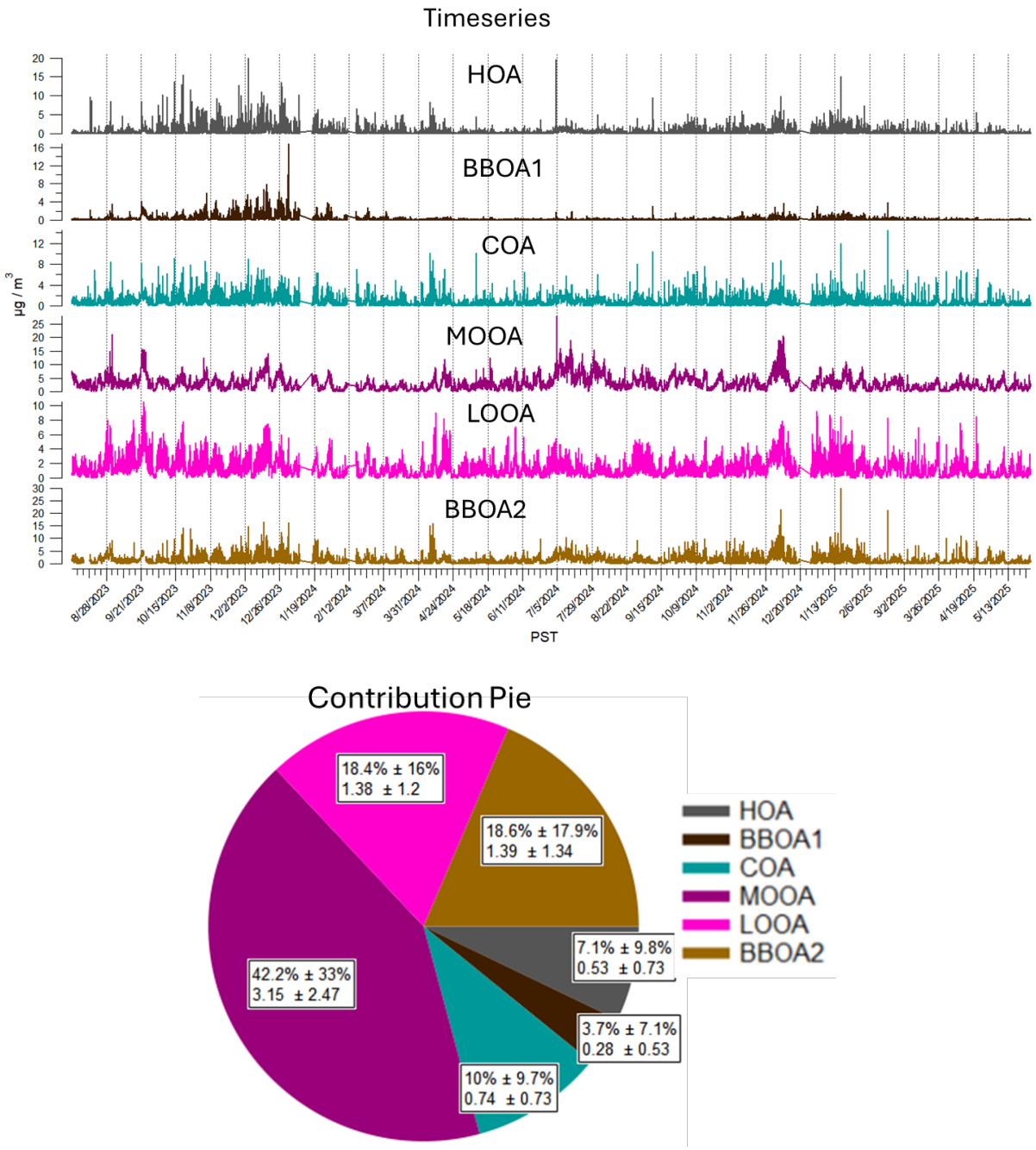

Figure 3-8: RPMF results on 2-year ACSM data. (a) factor profile (b) diurnal cycles, (c) time series, and (d) Relative contribution of resolved OA factors at Bakersfield.

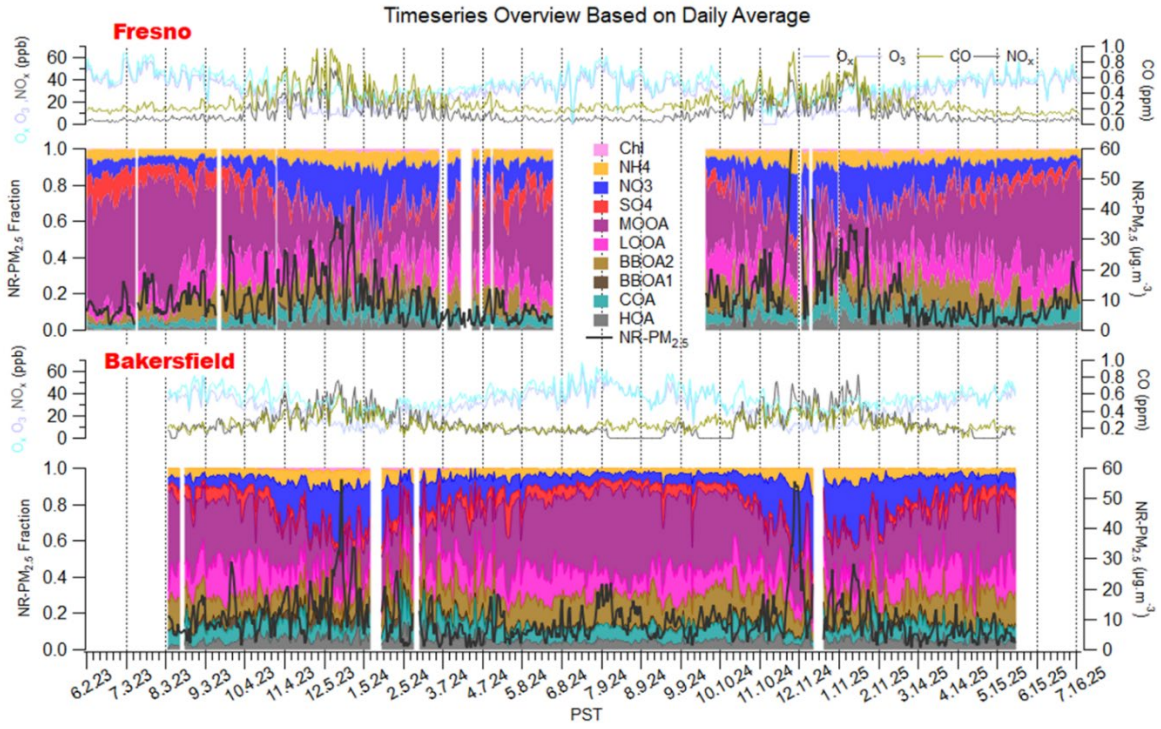

Figure 3-9: Daily average time series of NR-$PM_{2.5}$ (black) and its resolved chemical composition (stacked fractions: inorganics (SO4+NO3+NH4+Chl) + OA factors) plotted with Ox, O_3, CO, and NOx for Fresno (top) and Bakersfield (bottom).

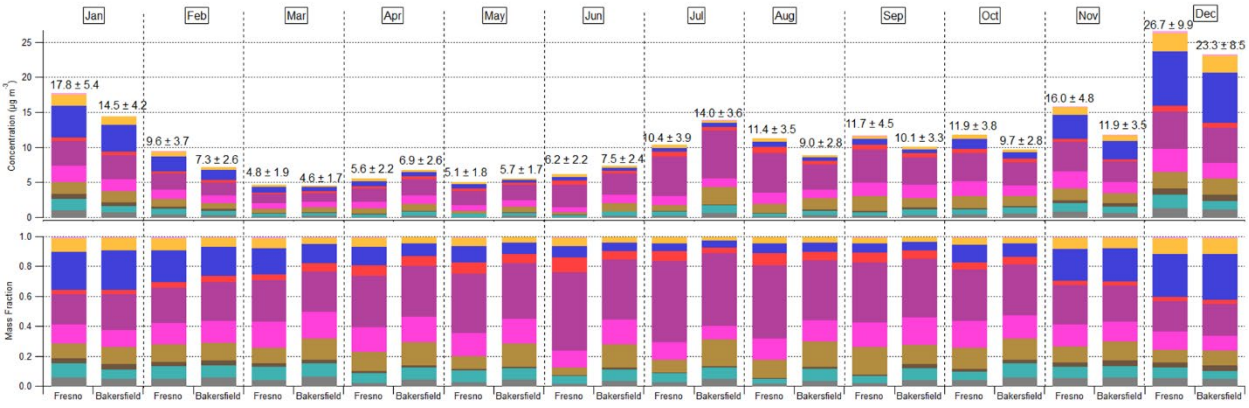

Figure 3-10: Monthly average NR-PM2.5 segregated by species. The top panel shows the absolute mass concentration, and the Bottom panel shows the fractional contribution of each species.

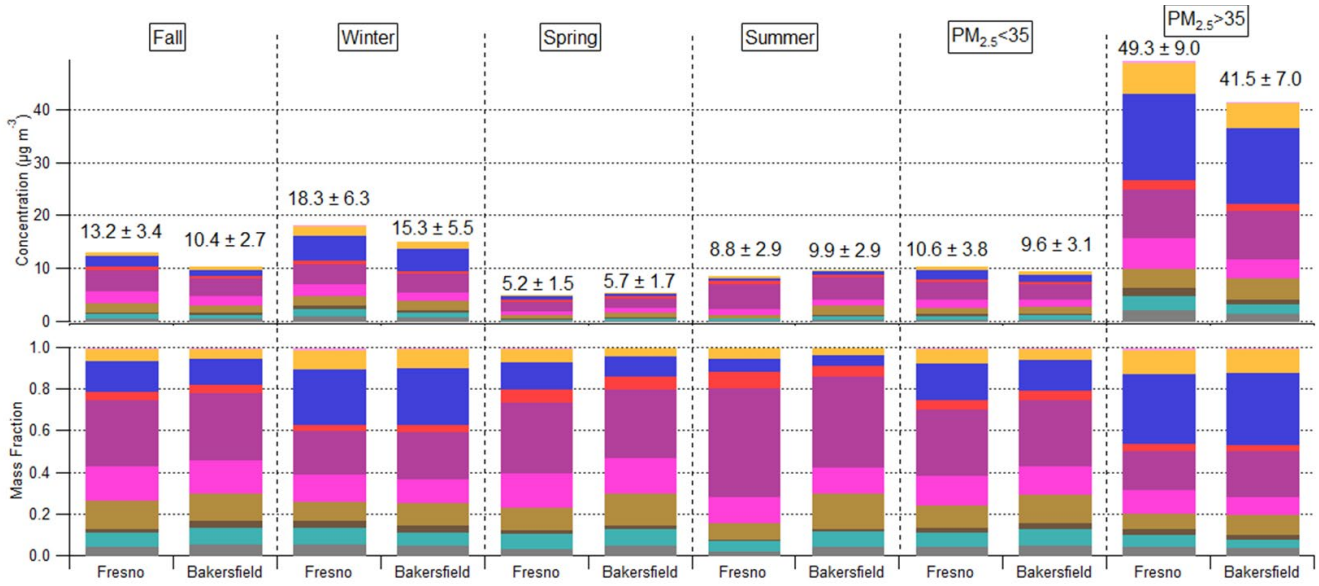

Figure 3-11: Seasonal average NR-PM2.5 segregated by species. Top panel shows the absolute mass concentration and the bottom panel shows the fractional contribution of each species.

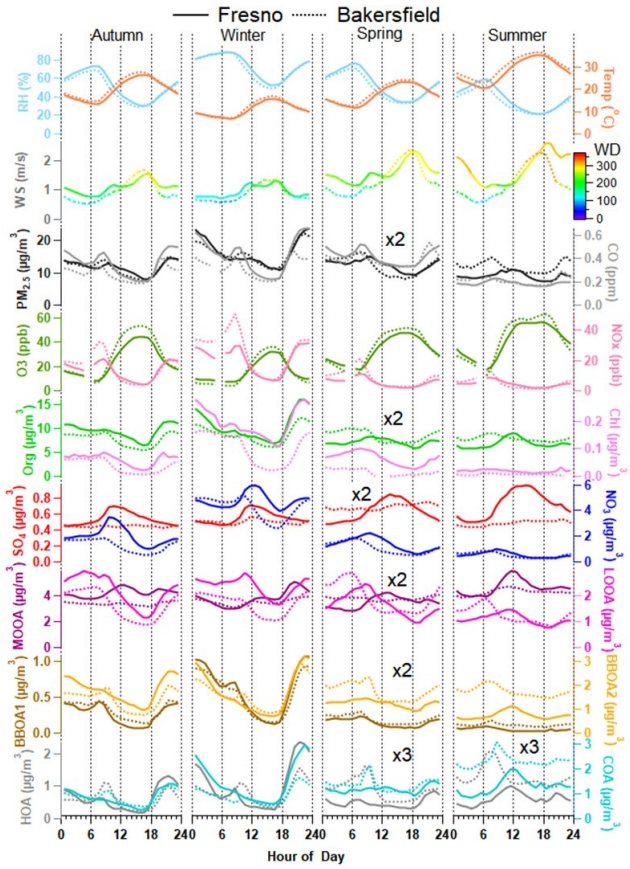

Figure 3-12: Comparison of average diel behavior of the OA sources from the RPMF on ACSM data, along with other meteorological and gas parameters between Fresno and Bakersfield.

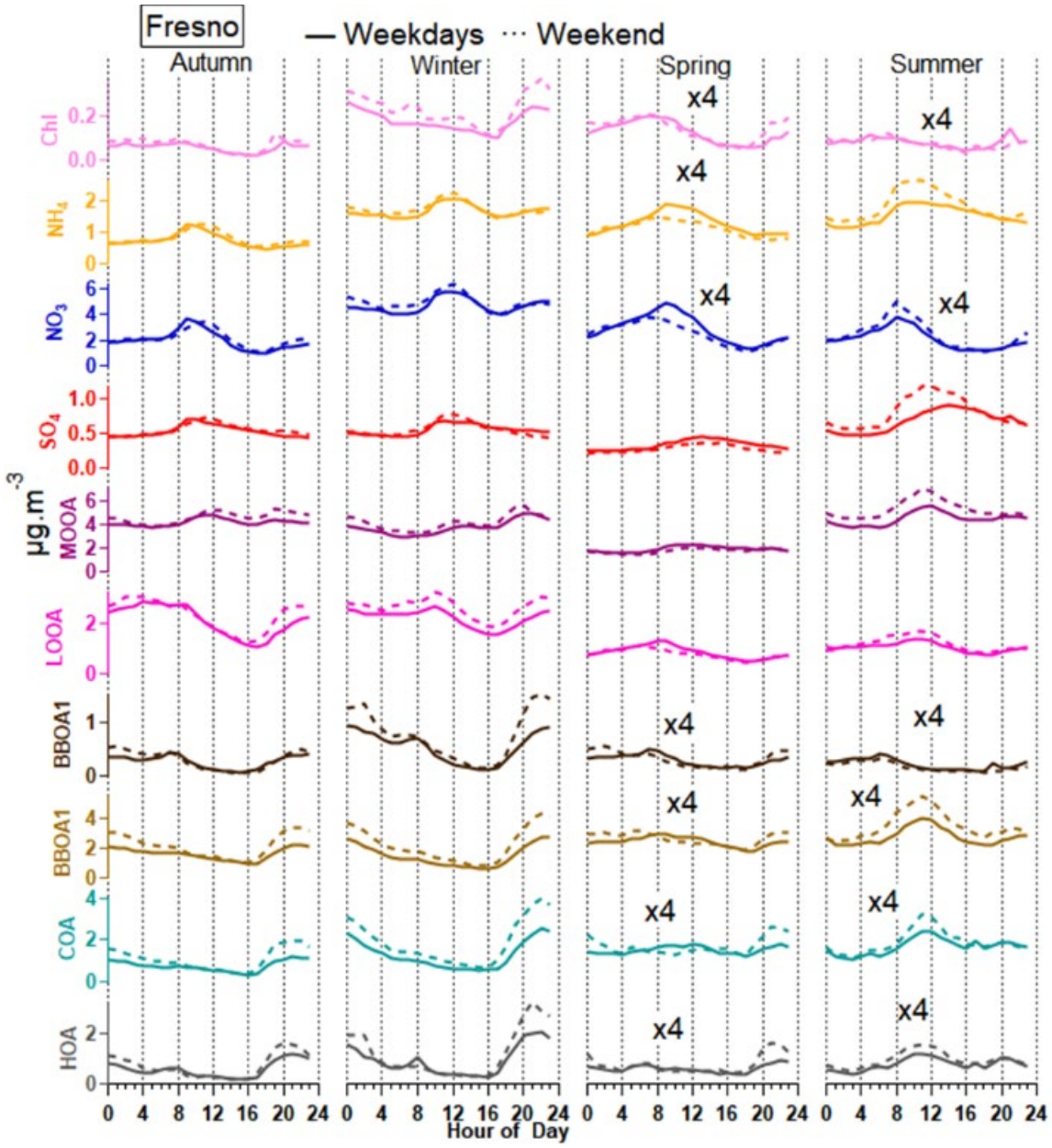

Figure 3-13: Comparison of average diel behavior of the OA sources from the RPMF on ACSM data, along with other meteorological and gas parameters between Weekdays ((Wkd) = Mon-Fri) and Weekend ((Wke)=Sat+Sun) at Fresno.

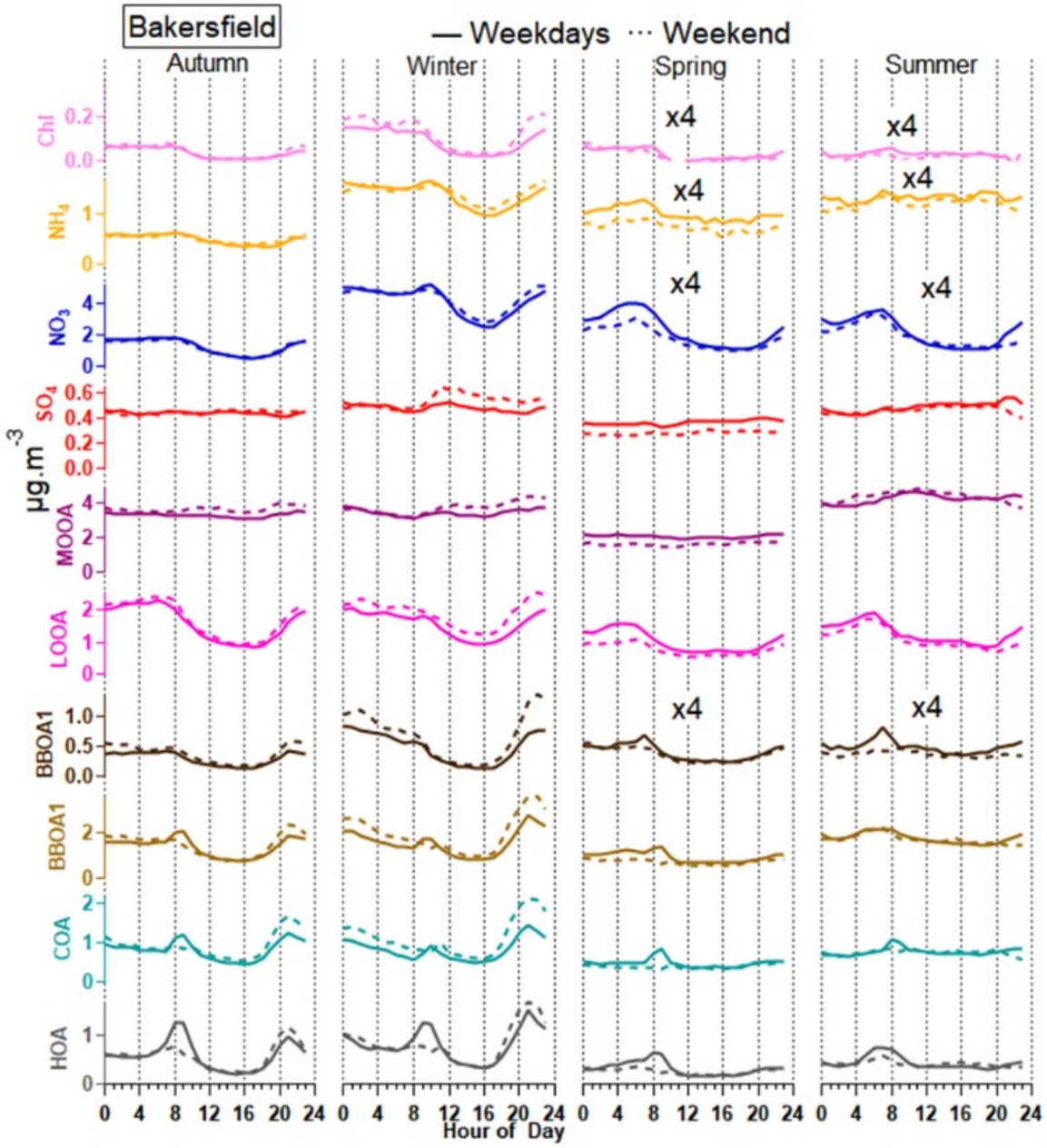

Figure 3-14: Comparison of average diel behavior of the OA sources from the RPMF on ACSM data, along with other meteorological and gas parameters between Weekdays ((Wkd) = Mon-Fri) and Weekend ((Wke)=Sat+Sun) at Bakersfield.

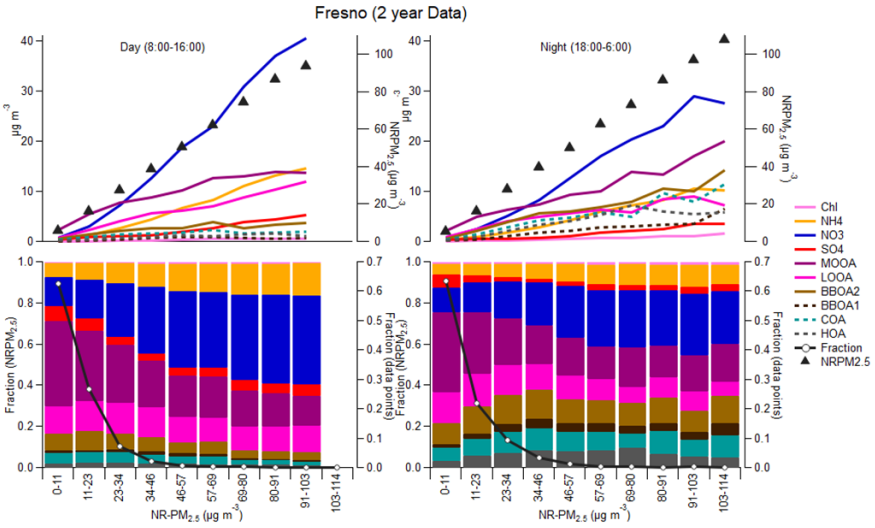

Figure 3-15: Fresno: Variations in aerosol species mass concentrations (top panel) and mass fractions (bottom panel) as a function of total $PM_{2.5}$ loading during June 2023–July 2025 for daytime (left) and nighttime (right) conditions. The right axes of the bottom panel indicate the cumulative frequency. The right axis of top panel indicates the NR-PM2.5 concentration (indicated by black triangle).

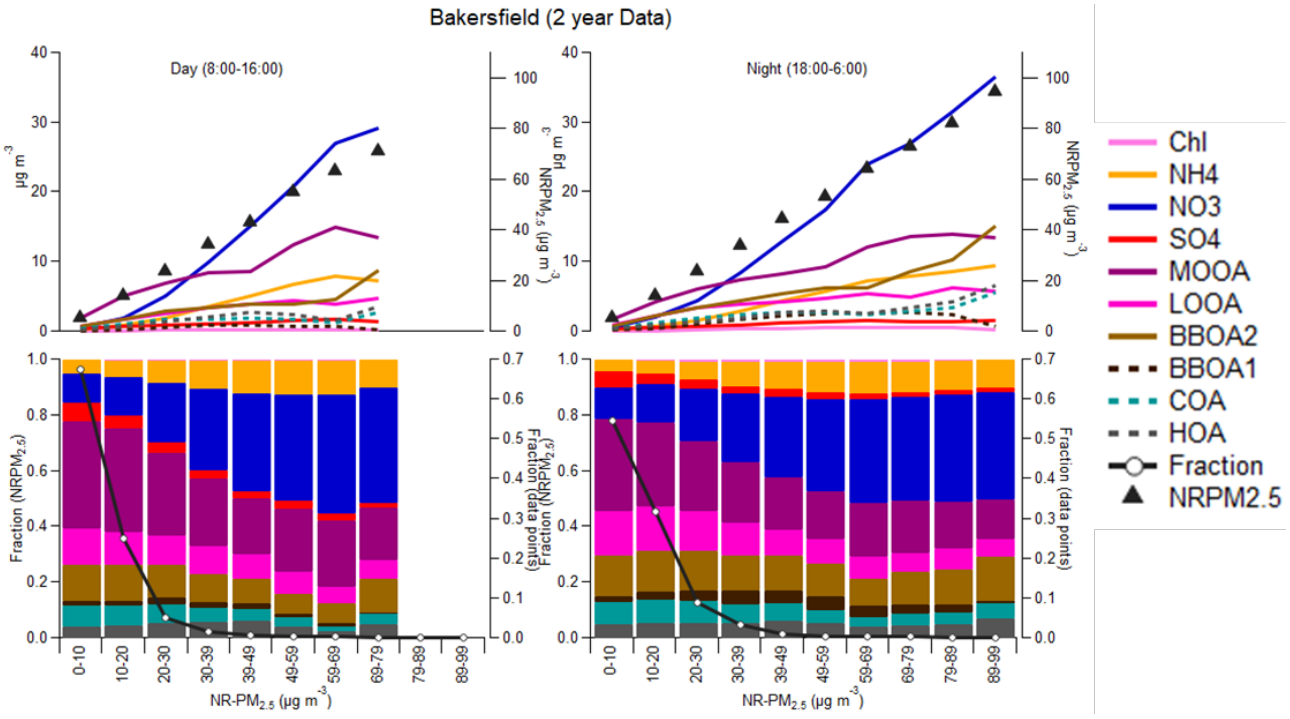

Figure 3-16: (a) Bakersfield: Variations in aerosol species mass concentrations (top panel) and mass fractions (bottom panel) as a function of total $PM_{2.5}$ loading during June 2023–July 2025 for daytime (left) and nighttime (right) conditions. The right axes of the bottom panel indicate

the cumulative frequency. The right axis of top panel indicates the NR-PM2.5 concentration (indicated by black triangle).

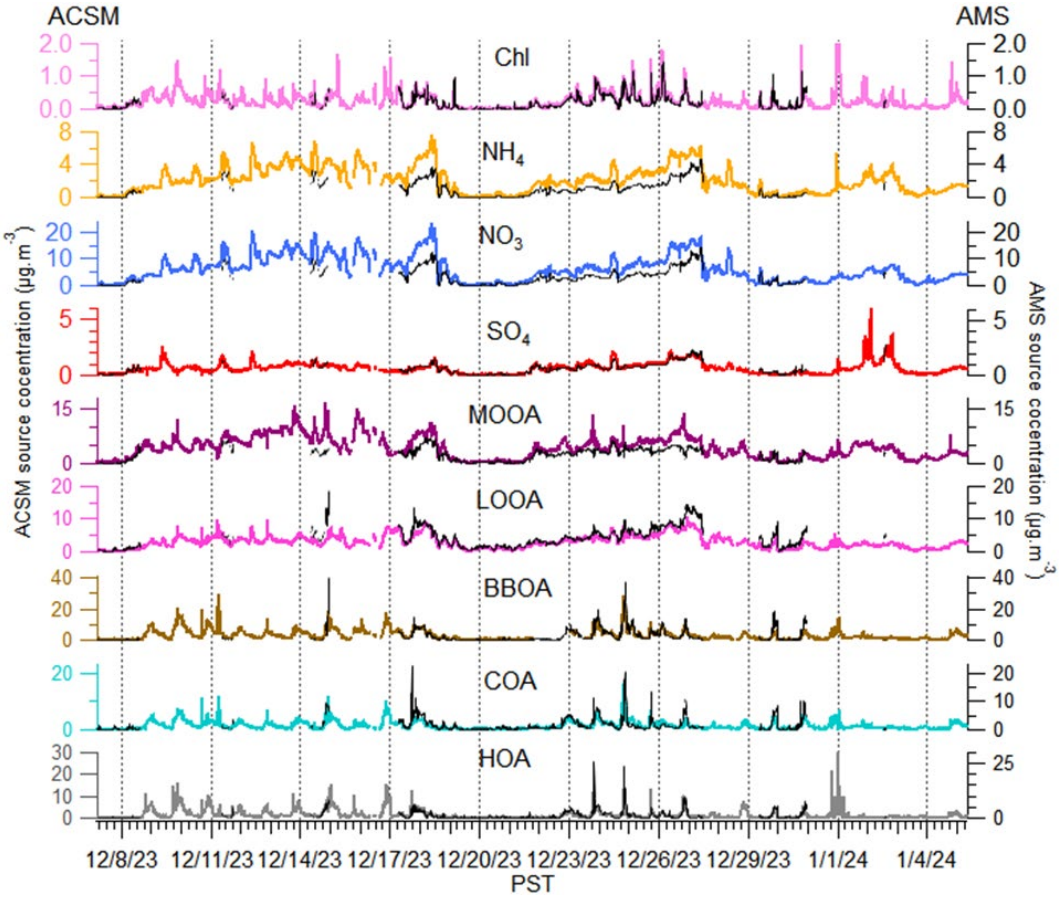

Figure 3-17: Excellent agreement between the ACSM OA factor timeseries and AMS OA factor timeseries for the collocated measurements in Fresno during December 2023.

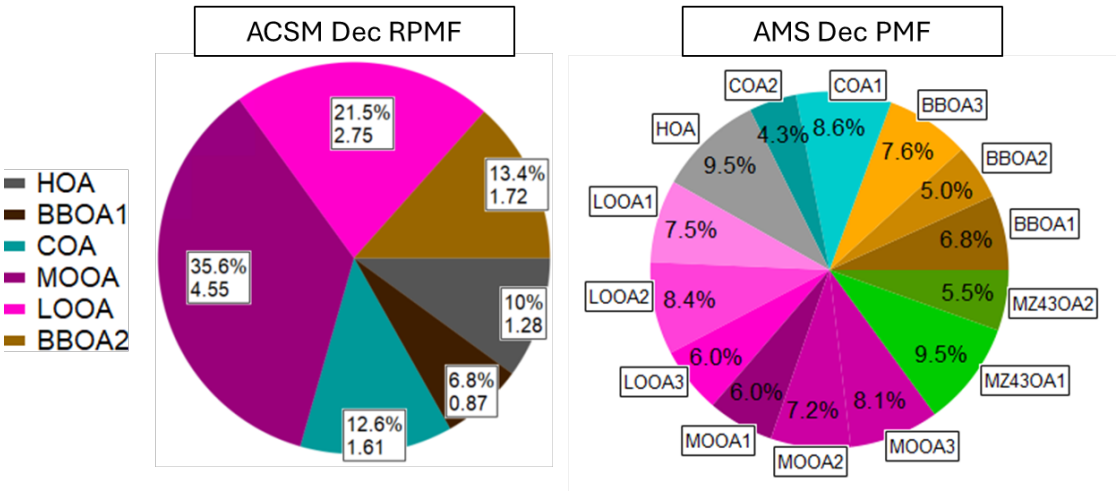

Figure 3-18: Comparison of source contribution between the ACSM OA factor timeseries and AMS OA factor timeseries for the collocated measurements in Fresno during December 2023.

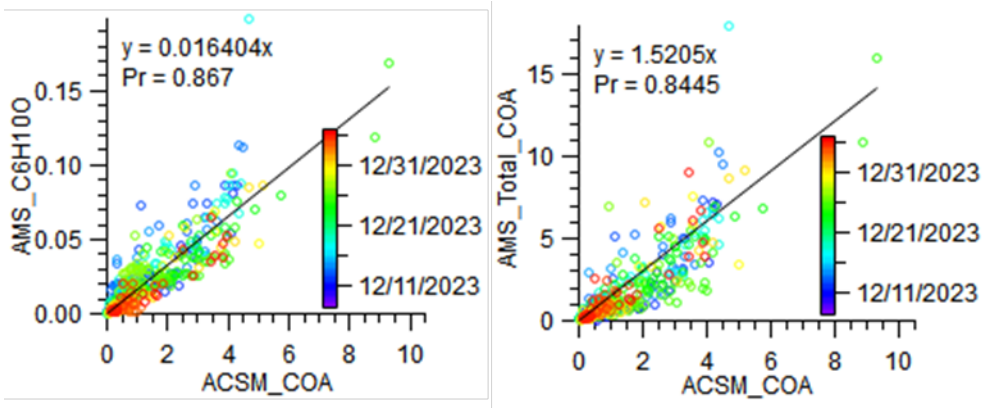

Figure 3-19: Scatter plots showing the relationship between ACSM COA (for Dec 2023) and corresponding AMS cooking-related tracers ($C_6H_{10}O^+$) and total AMS COA factor (discussed in section 5), with points colored by collocated time period (December 2023).

4 RESOLVING WINTERTIME ORGANIC AEROSOL SOURCES AND FORMATION PROCESSES IN FRESNO USING COMBINED POSITIVE MATRIX FACTORIZATION (cPMF) OF SP-AMS AND FIGAERO-CIMS MEASUREMENTS

4.1 Introduction

Particulate matter pollution in the San Joaquin Valley (SJV) remains among the most severe in the United States, with frequent exceedances of the 24-hour $PM_{2.5}$ National Ambient Air Quality Standards (NAAQS). These exceedances occur most often during late fall and winter, when enhanced emissions combined with unfavorable meteorological conditions lead to persistent, multi-day pollution episodes. During winter, $PM_{2.5}$ burden in the SJV is dominated by ammonium nitrate and organic aerosol (OA) (Sun et al., 2022; Young et al., 2016). Ammonium nitrate forms through secondary reactions involving nitrogen oxides (NO_x) and ammonia (NH_3), while OA comprises a complex mixture of both primary organic aerosol (POA) directly emitted from sources such as traffic, cooking, and biomass burning, and secondary organic aerosol (SOA) formed through atmospheric reactions of volatile organic compounds (VOCs).

Wintertime SOA formation is highly sensitive to precursor composition, oxidant chemistry, and multiphase partitioning (He et al., 2024; Jimenez et al., 2009; Wang et al., 2021; Yazdani et al., 2023). In urban valley basins such as the SJV, persistent stagnation, shallow boundary layers, and cold temperatures create conditions that strongly favor multiphase and heterogenous chemistry (Collier et al., 2018; Ge et al., 2012b; Gilardoni et al., 2016) and promote SOA accumulation, even as reduced solar radiation suppresses daytime photochemical processing (Liu et al., 2024; Peng et al., 2021; Xu et al., 2024). Despite its central contribution to winter $PM_{2.5}$, process-level attribution of SOA remains challenging, limiting identification of dominant pathways and constraining the development of effective air-quality management and public health protection strategies.

The SJV exemplifies these challenges. During the cold season, emissions in the region shift toward anthropogenic combustion sources, increasing inputs of NO_x, NH_3, and VOCs from residential heating and other winter activities (Chen et al., 2018; Farley et al., 2023; Ge et al., 2012b, a; Young et al., 2016). Nocturnal formation of a stable boundary layer isolates a chemically active residual layer aloft, enabling nighttime nitrate formation through nitrate radical ($NO_3\cdot$) and N_2O_5 chemistry and the accumulation of oxidants and gaseous organic precursors that can be entrained into the surface layer the following day (Prabhakar et al., 2017; Pusede et al., 2016; Young et al., 2016). Combined with stagnant and humid conditions, this vertical decoupling enhances SOA production through multiphase and heterogeneous pathways. As a result, wintertime SOA in the SJV is both substantial and chemically distinct from summer conditions, with aqueous processing and nocturnal chemistry emerging as key but insufficiently constrained drivers of $PM_{2.5}$ pollution.

Aqueous-phase processing occurs in fog and aerosol waters under conditions of high relative humidity (RH) and frequent radiation fog. Water-soluble organic compounds, including small carbonyls (e.g., glyoxal and methylglyoxal) and phenolic species, readily partition into the aqueous

phase, where they undergo rapid oxidation by a range of oxidants, including hydroxyl radical ($\cdot OH$), O_3, nitrate radical ($NO_3\cdot$), triplet excited states of organic carbon ($^3C^*$), and singlet oxygen ($^1O_2^*$) (Arciva et al., 2022, 2025; Herrmann et al., 2015; Jiang et al., 2021; Lamkaddam et al., 2025; Wang et al., 2024). Laboratory studies demonstrate that these multiphase reactions efficiently generate aqueous SOA (aqSOA) with high mass yields and enhanced formation of oligomers, organic acids, and highly oxidized species compared to gas-phase reactions (Go et al., 2024; Huang et al., 2018; Jiang et al., 2024). Field observations in fog-prone regions, such as the Po Valley in northern Italy and SJV, further indicate substantial aqSOA contributions linked to biomass-burning-derived phenols and enriched in small dicarboxylic acids and brown carbon chromophores (Collier et al., 2018; Farley et al., 2023; Ge et al., 2012b; Gilardoni et al., 2016; Paglione et al., 2020). Together, these studies indicate fog and aerosol water as active chemical reactors in winter basins, however, the magnitude, molecular composition, precursor diversity, and persistence of aqSOA following fog dissipation remain poorly understood.

Nocturnal chemistry represents a second major pathway shaping winter SOA formation. At night, $NO_3\cdot$, generated from reactions between NO_2 and O_3, rapidly oxidize unsaturated VOCs such as alkenes and monoterpenes, to produce low-volatility products and organic nitrates that contribute to SOA (Brown and Stutz, 2012). Laboratory studies show efficient dark oxidation of biomass-burning and biogenic emissions by $NO_3\cdot$, producing highly oxidized OA and mixed organic-inorganic nitrate species (Bates et al., 2022; Kodros et al., 2020; Zhang et al., 2025). In parallel, heterogeneous uptake of N_2O_5 forms particulate nitrate (pNO_3) and, in the presence of chloride, $ClNO_2$, which photolyzes quickly after sunrise to release chlorine atoms ($Cl\cdot$) and NO_2, thereby influencing morning oxidant budgets (Bannan et al., 2017; Brown and Stutz, 2012; Chen et al., 2023). In aqueous media, N_2O_5 can further dissociate to NO_2^+, promoting electrophilic nitration of phenols and formation of nitrophenols and nitrosophenols (Heal et al., 2007; Kroflič et al., 2021; Wang et al., 2023b). Aircraft and surface observations indicate that much of this chemistry occurs in the decoupled nocturnal residual layer (NRL), with subsequent morning entrainment leading to sharp increases in surface pNO_3 concentrations (Pusede et al., 2016; Sun et al., 2025; Young et al., 2016). Modeling studies further suggest that NRL production dominates morning surface nitrate budgets (Prabhakar et al., 2017; Sun et al., 2025). While nighttime SOA formation in polluted NRLs can be substantial (Zaveri et al., 2020; Zhou et al., 2023), its quantitative contribution and chemical signatures remain challenging to isolate because of mixed precursors and potential influence from transported air.

Disentangling distinct SOA formation processes is essential for advancing process-level understanding and informing effective air-quality management strategies. Source apportionment using aerosol mass spectrometry (AMS) has played a central role in advancing our understanding of SOA by providing time-resolved, quantitative insights into organic aerosol composition and evolution (Canagaratna et al., 2007; Jimenez et al., 2009; Zhang et al., 2007, 2011). However, source apportionment approaches based on AMS data alone often struggle to resolve these processes. Positive matrix factorization (PMF) applied to AMS data robustly separates primary

OA (POA) components, such as hydrocarbonlike OA (HOA), cooking OA (COA), and biomass burning OA (BBOA), but resolving SOA remains challenging. The combination of high-temperature (600 °C) vaporization and 70 eV electron-ionization, combined with the chemical complexity of OA and substantial overlap among formation pathways, causes extensive fragmentation that compresses molecular information. As a result, diverse secondary processes are frequently collapsed into a small number of bulk oxygenated OA (OOA) factors, obscuring mechanistic distinctions and masking the roles of key precursors (Crippa et al., 2014; Ng et al., 2010; Ulbrich et al., 2009; Zhang et al., 2007, 2011).

In contrast, soft ionization mass spectrometry provides enhanced molecular specificity and improved differentiation among secondary products, but the instrument sensitivities vary across compounds, limiting their quantitative utility when applied alone (Kumar et al., 2022; Qi et al., 2019; Stefenelli et al., 2019). Recent advances in combined PMF (cPMF), which integrates hard- and soft-ionization mass spectrometry datasets within a unified factorization framework, offer a promising pathway to overcomes these limitations by enabling improved factor separation while maintaining quantitative mass closure (Simon et al., 2025; Tong et al., 2022).

In this study, to better understand OA emission sources and formation pathways in the SJV, we conducted an intensive winter field campaign in Fresno, California, deploying a high-resolution soot-particle aerosol mass spectrometer (SP-AMS) alongside a chemical ionization mass spectrometer (CIMS) coupled with a Filter Inlet for Gases and AEROsols (FIGAERO). By applying a cPMF framework to the merged SP-AMS and FIGAERO-CIMS datasets, we resolved primary emissions and process-specific SOA factors. Nineteen distinct OA factors were resolved, spanning primary emissions (HOA, COA, and multiple BBOAs) and process specific SOA factors, including four aqSOA factors and three SOA factors associated with nocturnal reactions in the residual layer followed by morning entrainment (RL-SOA). Aqueous processing, involving diverse precursors and different oxidation levels, is a leading contributor to SOA. RL-SOA factors, with daily morning peaks aligned with nitrate and $ClNO_2$, indicate that nocturnal chemistry in the RL supplies a reproducible surface OA source. Our analysis highlights distinct SOA formation pathways that are often underrepresented in models, and the results provide a strong basis for more targeted and actionable air quality management in winter basins.

4.2 Methods

4.2.1 Monitoring site and instrumentation

Site description. The winter field observations were conducted from 8 December 2023 to 6 January 2024 at the California Air Resources Board's Fresno-Garland station (36° 47' 12'' N, 119° 46' 25'' W; 97 m a.s.l.) in Fresno, CA. The site is surrounded by residential neighborhoods and commercial areas and is close to several major highways, representative of urban basins that are influenced by shallow nocturnal inversions, weak ventilation, frequent radiation fog, and strong residential wood burning. Particulate matter was sampled continuously through a $PM_{2.5}$ cyclone and Nafion dryer mounted approximately 1.5 m above the roofline. The inlet flow was maintained

at 4.5 L/min, split as 0.1 L/min to the SPAMS, 4.3 L/min to the FIGAERO polytetrafluoroethylene (PTFE) filter, and 0.1 L/min to the ACSM. Routine meteorological and air-quality data collected at this station include temperature, RH, wind speed and direction, solar radiation, O_3, NO, NO_2, CO, NH_3, SO_2, black carbon, $PM_{2.5}$, and PM_{10}, which provide the environmental context alongside the mass spectrometric measurements.

SP-AMS. A soot particle aerosol mass spectrometer (SP-AMS) was used to characterize the composition of PM_1 species at 2min time resolution (DeCarlo et al., 2006; Onasch et al., 2012). The instrument was operated under "V" ion optical mode. AMS data were processed and analyzed using the standard data analysis toolkits SQUIRREL and PIKA within Igor Pro. Organic aerosol elemental ratios, including the molar ratios of oxygen to carbon (O/C) and hydrogen to carbon (H/C), were calculated using the improved ambient method (Canagaratna et al., 2015).

FIGAERO-I-CIMS. A FIGAERO-I-CIMS was used to characterize particle-phase oxygenated organic compounds. A detailed description of FIGAERO-CIMS has been reported (Lopez-Hilfiker et al., 2014), and the iodide ionization mechanisms have been illustrated previously (Lee et al., 2014). The instrument alternated hourly between a 20-min gas mode, during which particles were collected on a PTFE filter, and a 40min particle desorption mode, during which 2 L/min of heated N_2 gas was passed through the PTFE filter to volatilize the sampled particles. The thermal desorption comprised a 15-min ramp from ambient temperature to ~ 200 °C, a 10-min soak at ~ 200 °C, and a 15-min cool-down to room temperature (Figure 4-1). Background measurements were conducted by placing a HEPA filter at the inlet entrance while sampling ambient air. Raw data were saved at 1 Hz and were pre-averaged to 5 s for further data processing. Tofware (v4.0.0) was used to process the FIGAERO-CIMS data, handling mass calibration, peak shape and width optimization, and high-resolution ion peak fitting for the mass spectra (Stark et al., 2015). Ion signals were normalized to total reagent ions (i.e., I^-, IH_2O^-, and $IC_2H_3N^-$) at 10E6 ions/s. To obtain an ambient particle-phase abundance ($I_{CIMS\_ambient}$, ions/m^3), ions signals were integrated over the thermal desorption period (i.e., ramp and soak) and converted via:

$$I_{CIMS\_ambient} = \frac{I_{CIMS\_integrated}}{Q_{FIGAERO} \times T} \qquad \text{(Eq1)}$$

where $I_{CIMS\_integrated}$ is the integrated ion signal, $Q_{FIGAERO}$ is the particle sampling flow through the FIGAERO filter, and T is the particle collection time. In the following discussion, the particle-phase CIMS signals reported are $I_{CIMS\_ambient}$ unless noted. Here, since no sensitivity conversion is applied, this expression implicitly assumes a uniform response for all the detected compounds. Given the iodide reagent's higher sensitivity towards oxygenated compounds (Lee et al., 2014), the importance of more oxidized compounds can be overestimated, while the less oxidized compounds are likely underestimated. Nevertheless, total OA concentration measured by AMS correlates well with total particle phase CIMS signal (R=0.995; Figure 4-2), supporting the use of CIMS data as a semi-quantitative approach.

4.2.2 PMF approach

Source apportionment was performed on the FIGAERO-I-CIMS and SP-AMS data both separately and in combination using positive matrix factorization (PMF) (Paatero and Tapper, 1994). We began with applying PMF to each instrument individually. Single instrument PMF established instrument specific factor structures and identified artifacts and backgrounds. Next, we analyzed a single, merged matrix comprising both instruments. The combined PMF (cPMF) ensured a balanced representation for each instrument, leveraging the quantitative capability of AMS and the molecular specificity of CIMS.

4.2.2.1 PMF principles

PMF is a bilinear receptor-only model broadly used in atmospheric studies (Ng et al., 2010; Ulbrich et al., 2009; Zhang et al., 2011), which represents the input data matrix as the product of static factor profiles and their time variations, such that

$$X = G \times F + E \qquad \text{(Eq2)}$$

where X (dimension of m*n) is the input data matrix containing m measurements of n variables, F (dimension of p*n) is a matrix of factor profiles, G (dimension of m*p) is a matrix of factor time series, and E (dimension of m*n) is the residual matrix. Here, p is the number of factors in the PMF solution selected by the user.

PMF solves Eq 2 using a least-squares algorithm that iteratively fits the values of G and F to the input data, minimizing parameter Q, which is the sum of squared uncertainty-weighted residuals (Eq 3).

$$Q = \sum_{i=1}^{m} \sum_{j=1}^{n} \left(\frac{e_{ij}}{s_{ij}}\right)^2 \qquad \text{(Eq3)}$$

where e_{ij} is an element in the residual matrix E, and s_{ij} is the corresponding element in the uncertainty matrix. The theoretical expectation of Q, denoted Q_{exp}, should equal the degrees of freedom of the fitted data:

$$Q_{exp} = m \times n - p \times (m + n) \qquad \text{(Eq4)}$$

If the model is appropriate and errors are well characterized, the optimal solution would yield a Q/Q_{exp} near unity. In practice, atmospheric datasets rarely meet all idealized assumptions, so Q/Q_{exp} is typically higher than 1.

4.2.2.2. PMF on single-instrument measurements

SP-AMS PMF. For the PMF analysis performed on SP-AMS data (amsPMF), the input high-resolution organic mass spectral and uncertainty matrices were prepared following Ulbrich (2009). In total, 227 ions were included between m/z 12-400. Isotopic ions whose signals were scaled from their parents were removed. Ions with signal-to-noise (S/N) ratio < 0.2 were excluded, and ions

with S/N between 0.2 and 2 were downweighed by increasing their uncertainties by a factor of 2. The CO_2^+ ion and related CO^+, H_2O^+, HO^+, and O^+ ions were also downweighed as recommended by Ulbrich (2009). The PMF solution was evaluated using a PMF Evaluation Toolkit (PET v3.08) following the procedures described in Zhang (2011). A 14-factor solution was selected after careful evaluation. The rotational ambiguity of the solution was explored by varying the fPeak from -1 to 1, and fPeak=0 was chosen. The identified factors include HOA, COA, POA, three BBOA, and eight OOA factors. Figure 4-3 summarizes the MS profiles, time series, and diurnal variations of the optimal amsPMF solution, while detailed interpretation is presented in a companion paper (Shukla et al., in preparation).

FIGAERO-I-CIMS PMF. For the PMF analysis performed on FIGAERO-I-CIMS data (cimsPMF), the $I_{CIMS\_ambient}$ (as described in Section 4.2.1) was used as the input data. The uncertainties (S_{cims}) of the signals were initially estimated using Poison statistics:

$$S_{CIMS} = \sqrt{I_{CIMS\_ambient}} \qquad \text{(Eq5)}$$

However, this estimation only provides a lower limit for the actual noise, while thermogram integration and ambient abundance conversion can add variance not captured by Poisson statistics. With the initial uncertainty values, the Q/Q_{exp} was >> 1, indicating an underestimation of the uncertainties (Ulbrich et al., 2009). Given the complexity of uncertainties associated with thermal desorption and ambient conversion and a lack of well-developed methods to estimate these uncertainties, we scaled uncertainties empirically by a uniform factor of 40 to reflect additional variance, which yields more reasonable Q/Q_{exp} values. In total, 685 ion formulas were included for cimsPMF analysis. Since ICIMS shows significantly stronger response to anhydrosugars ($C_6H_{10}O_5$; e.g., levoglucosan, mannosan, and galactosan) (Gaston et al., 2016; Lee et al., 2014; Ye et al., 2021), we further downweighed the corresponding ion $IC_6H_{10}O_5^-$ by increasing its uncertainty by a factor of 10 to avoid having a single, highly responsive marker dominate the fit. A 14-factor solution was selected, which resolved three BBOA, two residual layer SOA, three aqSOA, two biogenic SOA, two background, and one artifact factor. A summary of the cimsPMF factors is provided in -Figure 4-4.

4.2.2.3 Combined PMF (cPMF) on merged CIMS and AMS data

To prepare the input for the cPMF, we time-aligned the AMS data (originally at 2-min resolution) to the FIGAERO-CIMS collection cycle. AMS signals were averaged over each 20min FIGAERO particle collection window per hour, with uncertainties propagated accordingly. Subsequently, the AMS and CIMS data were merged to generate a unified data matrix that contains 912 variables (227 AMS ions and 685 CIMS formulas) (Figure 4-5). The associated uncertainty matrix is constructed similarly.

Since the two instruments differ in variable count, response, and noise, a weighting factor (C_{CIMS}) was applied to the error matrix of the CIMS to balance the relative contributions of the two instruments and to ensure both instruments are well represented:

$$s'_{ij} = \begin{cases} \frac{s_{ij}}{C_{CIMS}}, & j \in \text{CIMS data} \\ s_{ij}, & j \in \text{AMS data} \end{cases} \quad \text{(Eq6)}$$

To determine the optimal weighting factor, the scaled residuals of both instruments were monitored following previously reported approaches (Simon et al., 2025; Tong et al., 2022). First, for the selected single-instrument solutions (the 14-factor amsPMF and the 14-factor cimsPMF), we calculated the probability distribution of the scaled residuals and quantified their similarity via the overlap ($F_{overlap}$) between the two distributions (Figure 4-6):

$$F_{overlap} = \int \min(P_{AMS}, P_{CIMS}) \quad \text{(Eq7)}$$

where P_{AMS} and P_{CIMS} are scaled residual probability distributions for the amsPMF and the cimsPMF solutions. Next, we calculated the scaled residual distributions overlap ($F_{overlap}$') for the cPMF solution:

$$F'_{overlap} = \int \min(P_{AMS\_cPMF}, P_{CIMS\_cPMF}) \quad \text{(Eq8)}$$

where P_{AMS_cPMF} and P_{CIMS_cPMF} are the scaled residual probability distributions for the AMS and CIMS data from the cPMF solution. Ideally, an $F_{overlap}$' value similar to $F_{overlap}$ is desired (Tong et al., 2022). However, in practice, we did not necessarily try to produce the exact same $F_{overlap}$' with $F_{overlap}$ but rather use it as an important diagnostic, in combination with other metrics (e.g, Q/Q_{exp} and environmental interpretability) to determine the optimal cPMF solution.

We explored a broad range of C_{CIMS} and p (number of factors) values. Figure 4-7 summarizes the explored C_{CIMS}-p space in terms of Q/Q_{exp} and $F_{overlap}$'. For a C_{CIMS} value higher than 3 or lower than 0.5, the Q/Q_{exp} value increases significantly and the $F_{overlap}$' value deviates significantly from $F_{overlap}$. For a factor number lower than 14, the Q/Q_{exp} also increases significantly. We therefore rejected these solutions and focused further evaluation on the remaining candidates ($0.5 \leq C_{CIMS} \leq 3$ and $p \geq 14$).

Among the candidates, we sought an environmentally reasonable case. The selection criteria include appropriate Q/Q_{exp} and $F_{overlap}$' values, interpretable diurnal cycles and event responses, reasonable correlation with external tracers, and crossmethod coherence assessed by correlating the cPMF factor time series with that from the single instrument PMF and by verifying expected spectral signatures. The 22-factor cPMF solution with C_{CIMS} =3 appears to be the optimal as it captured the largest set of key factors resolved by single instrument PMFs (Figure 4-8). Among the 22 factors, one factor shows a repeating time pattern synchronized with FIGAERO filter changes and is interpreted as an artifact linked to incomplete desorption and particle accumulation on the filter. Two factors show minimal AMS signal and similar CIMS profiles with background CIMS spectra, so they are treated as background factors. Excluding these three factors, the final cPMF comprises 19 chemically interpretable OA factors, including a HOA, a COA, five BBOA, four aqSOA, three residual layer SOA, four biogenic SOA, and an OOA (Figure 4-9).

4.3 Results and Discussion

4.3.1 Drivers of winter organic aerosol pollution in the SJV

The cPMF performed on FIGAERO-I-CIMS and SPAMS datasets resolved 19 chemically interpretable OA factors, with POA and SOA contributing comparably during the campaign. POA, including HOA (11.3%), COA (9.3%), and BBOAs (30.4%), accounted for 51% of the total OA mass (Figure 4-9). All POA factors peaked at night (Figure 4-9) when evening traffic, dinner cooking, and residential heating intensify and a shallow nocturnal boundary layer traps emissions near the surface. These primary emissions are consistent with prior winter Fresno observations which highlight wood burning, vehicles, and cooking as dominant primary sources (Farley et al., 2023; Ge et al., 2012b; Sun et al., 2022; Young et al., 2016).

SOA accounted for 49% of the OA mass (Figure 4-9). Aqueous phase processing in fog and aerosol water was the leading secondary formation pathway (~22.3%), followed by nocturnal chemistry in the residual layer (~12.9%) and oxidation of biogenic VOCs (~8.9%). The comparable contributions of POA and SOA suggest that, even in winter, when sunlight, oxidant levels (e.g., ozone and •OH), and biogenic VOC emissions (e.g., isoprene and monoterpenes) are lower, secondary formation remains a major contributor to OA mass. High humidity and frequent radiation fog promote aqueous reactions, while active nocturnal reactions in the residual layer primes a morning surface OA increase as mixing layer expands. These secondary processes are critical to understanding the persistence and severity of winter PM episodes in Fresno.

4.3.2 SOA from fog and aerosol water processing

Two multiday fog episodes (Dec 22-27 and Jan 1-3) were identified, featured by RH > 85% and dew-point depression < 2.5 °C from night through late morning (Figure 4-10). The cold and humid conditions favored aqueous phase reactions and provided us an opportunity to investigate how fog water affects winter OA composition.

During the fog episodes, OA and $PM_{2.5}$ did not decrease (Figures 4-10 and 4-11), indicating that wet scavenging was limited or that SOA production in fog water outweighed removal. Multiple observations evidenced efficient aqueous processing. Sulfate increased from 0.5 to 1.1 $\mu g/m^3$, the sulfur oxidation ratio (SOR) increased from 0.2 to 0.6, oxalic acid concentration increased, and the fraction of aqSOA factors increased from 14% to 40% of total OA mass (Figure 4-11). These changes are consistent with fog-driven uptake of water-soluble gases (e.g., SO_2, glyoxal/methylglyoxal, and phenols) into fog droplets and water-rich particles, followed by rapid aqueous-phase reactions with oxidants (e.g., OH, O_3, $^3C^*$, and $^1O_2{}^*$) that produce sulfate and low volatility organics such as oligomers and small dicarboxylic acids (Herrmann et al., 2015; Jiang et al., 2021; Lim et al., 2010; McNeill, 2015; Volkamer et al., 2007; Wang et al., 2016, 2020; Yu et al., 2016).

The aqSOA continued to grow for hours after fog dissipated, remaining a substantial fraction into early afternoon even as RH and ALWC declined. This observation suggests that the low volatility species formed in fog water were retained in residual particles and continued to affect OA composition after fog dissipation. Additionally, the post-fog enhancement may also indicate SOA production during fog water evaporation. As water evaporates, the solute concentrations and the ionic strength of the particle phase increase, which can accelerate accretion and oligomerization and favor low-volatility products formation (Galloway et al., 2014; Loeffler et al., 2006; McNeill, 2015; Nguyen et al., 2012). Laboratory studies have reported evaporation-driven oligomer formation from glyoxal/methylglyoxal (Loeffler et al., 2006) and acid-catalyzed aldol chemistry that yields N/S-containing brown carbon species (Nguyen et al., 2012), both consistent with continued aerosol-phase reactions as fog water evaporates.

In this study, cPMF resolved four aqSOA factors (AQ1-4) with O/C ratios from 0.46 to 0.69 (Figure 4-12). At the molecular level, these factors are enriched in C_2–C_4 dicarboxylic acids, such as oxalic, malonic, malic, and succinic acids. These diacids can be formed through aqueous phase oxidation of water-soluble small carbonyls (e.g., glyoxal and methylglyoxal) and phenols. Longer diacids are converted to smaller ones through oxidative decarboxylation and fragmentation during aging. For example, aqueous oxidation of succinic acid yields malonic acid with malic acid as an intermediate, and hydroxylation of succinic acid also produces malic acid (Sorooshian et al., 2007). Oxalic acid represents the endpoint of extensive aqueous oxidation (Ervens et al., 2011). The correlation between oxalate and sulfate, along with the ratio of oxalate to sulfate, has been widely used as a marker for aqueous processing across campaigns (Hilario et al., 2021). In the AMS spectra the aqSOA factors, CO_2^+ and CHO_2^+ are strongly enhanced (Figure 4-12). The four aqSOA factors together account for 40% and 50% of CO_2^+ and CHO_2^+ signals, respectively (Figure 4-12), consistent with significant carboxylic acid formation. The combined AMS markers (CO_2^+ and CHO_2^+) and CIMS dicarboxylic acid tracers provide coherent, cross instrument evidence that AQ1-4 arise from aqueous-phase reactions. Additionally, the time series of total AQ1-4 tracks sulfate (Figure 4-12), further confirming the aqueous pathways.

Among the aqSOA factors, AQ3 and AQ4 show higher O/C, higher f_{CO2+}, and lower f_{C2H3O+} than AQ1 and AQ2 (Figure 4-12 and 4-13), indicating that they experienced more extensive aging. The different oxidation levels of the aqSOA factors correspond to different chemical composition, meteorology and source conditions discussed below.

AQ1 is dominated by malonic acid ($C_3H_4O_4$, ~14% of the CIMS signal) (Figure 4-12), a product of succinic acid photodegradation. A high malonic/succinic ratio indicates ongoing aqueous aging, yet the lack of oxalic acid suggests incomplete oxidation (Kawamura and Bikkina, 2016), consistent with the lower O/C and smaller f_{CO2+} of AQ1. Wind analysis ties AQ1 to influence from southeast (Figure 4-13).

AQ2 is characterized by oxalic ($C_2H_2O_4$) and malonic ($C_3H_4O_4$) acids alongside methanesulfonic acid (MSA, CH_4SO_3) and nitrophenols (e.g., $C_6H_5NO_4$ and $C_7H_7NO_4$) (Figure 4-12). MSA can be

formed from aqueous-phase reactions of sulfur-containing organics, such as dimethyl sulfide (DMS) (Novak et al., 2021; Tashmim et al., 2024). The presence of nitrophenols likely indicates aqueous-phase nitration of phenols by NO_2^+ (Heal et al., 2007; Kroflič et al., 2021; Wang et al., 2023b). Several observations suggest that AQ2 likely captures biomass burning influenced aqueous processing. AQ2 is significantly enhanced during a BB-rich period (Dec 22-27). Compared to other aqSOA factors, AQ2 shows higher contributions to aromatic products, such as highly hydroxylated phenols and phenolic oligomers (Figure 4-12), which are typical aqueous oxidation products of BB-derived phenols. Prior studies have demonstrated that BB-emitted water-soluble phenols readily partition to atmospheric waters and undergo rapid aqueous-phase reactions with multiple oxidants to generate aqSOA through functionalization, oligomerization, and fragmentation (Jiang et al., 2021; Sun et al., 2010; Yu et al., 2016).

AQ3 features high fractions of malonic ($C_3H_4O_4$) and glycolic ($C_2H_4O_3$) acids (Figure 4-12). Prior work has reported glycolic acid formation from aqueous OH oxidation of glycolaldehyde (Perri et al., 2009). Like AQ2, AQ3 intensifies during a BB-rich period (Dec 22-27) and shows a higher aromatic fraction than AQ1&4. Additionally, both AQ2 and AQ3 show high correlations with low wind speeds (Figure 4-14), indicating strong local influence, consistent with nearby residential wood burning as a key precursor source.

AQ4 is the most oxidized factor and is dominated by oxalic acid (23% of the CIMS signal), alongside prominent maleic ($C_4H_4O_4$) and succinic ($C_4H_6O_4$) acids (Figure 4-12). AQ4 peaks during Jan 1-3, a period of sustained high aerosol liquid water content (ALWC) that extends into midday (and RH > 80% the whole day) (Figure 4-15). The long duration of highly humid conditions allows extensive aqueous aging and enhanced partitioning of small acids (Hennigan et al., 2009). The polar plot of AQ4 shows a broader footprint, with a strong southeast influence but contributions from other directions as well (Figure 4-14). This pattern suggests that the deeply aged aqSOA (AQ4) may reflect regional processing rather than purely local influence.

Our observations suggest that, in the SJV, fog-driven aqueous processing reconfigures the winter OA toward more acid- and sulfur-rich composition, with strong influence that persist for hours even after fog dissipation. The four distinct aqSOA factors revealed that precursor availability, liquid water duration, and transport scale all affect the aqueous phase chemistry and aqSOA formation. Due to extensive residential wood burning, aqueous-phase reactions of BB emissions are a major aqSOA source in winter SJV. Practically, reductions in BB emissions and co-controls on $SO_2/NO_x/NH_3$ during humid stagnation events would efficiently suppress SOA growth.

4.3.3 Nocturnal residual layer chemistry and morning entrainment

Prior work in the San Joaquin Valley has shown that chemistry in the nocturnal residual layer strongly influence daytime surface PM. Field studies have observed sharp morning increases in surface nitrate that track the growth of the mixing layer, and models have demonstrated that residual layer NO_3/N_2O_5 chemistry dominates morning nitrate burden (Prabhakar et al., 2017;

Pusede et al., 2016; Young et al., 2016). We observed the same pattern in this campaign. Ground-level nitrate starts to increase near 7 am as the mixing layer expands, and $ClNO_2$ rises in parallel (Figure 4-16). The $ClNO_2$ increase suggests nighttime heterogeneous reactions of N_2O_5 with Cl-containing particles in the residual layer (McDuffie et al., 2018). Based on these observations, we expect that residual layer chemistry can affect the surface aerosol, not only by boosting nitrate but also by modifying the OA composition.

The cPMF resolved three OA factors associated with residual layer processing (RL1–3) (Figure 4-16). All the RL factors show a pronounced morning increase that aligned with the mixing layer expansion as well as the concurrent increases in nitrate and $ClNO_2$ beginning around 7 am. The consistent timing of the morning increases indicates that the RL factors are produced in the residual layer overnight and mixed to the surface during boundary layer growth.

Although the AMS features of the three RL factors are generally similar, with bulk O/C ratios between 0.47-0.50, their molecular fingerprints are distinct. These molecular characteristics allow the cPMF to separate different RL-SOA types that would otherwise be difficult to distinguish using AMS data alone.

RL1 is enriched in small carboxylic acids such as glycolic, oxalic, and malonic acids (Figure 4-16), indicating dark aqueous reactions in the residual layer (Herrmann et al., 2015). Prior Fresno winter studies have shown that heterogeneous uptake and hydrolysis of N_2O_5 aloft is substantial, implying that despite lower RH, the particle water in the residual layer is sufficient to host meaningful aqueous and heterogeneous reactions. Hygroscopic nitrate maintains aerosol liquid water (Hodas et al., 2014), and elevated acidity further promotes multiple condensed-phase pathways (Pye et al., 2020; Surratt et al., 2010). RL1 also contains nitrophenols, likely indicating heterogeneous NO_3 oxidation (Rana and Guzman, 2022) and/or aqueous-phase NO_2^+-mediated nitration of BB-derived phenols (Kroflič et al., 2021; Wang et al., 2023b).

RL2 features organonitrates together with CHO species from monoterpene oxidation (Figure 4-16). Molecular markers (e.g., $C_8H_{11}NO_7$, $C_{10}H_{15}NO_6$, $C_{10}H_{18}N_2O_8$, and $C_8H_{12}O_5$) point to nighttime NO3 reactions of monoterpenes. Similar observations of organonitrate and SOA formation have been reported in the polluted residual layer over Sacramento, CA, where anthropogenic nitrate radicals reacted with BVOCs efficiently in the residual layer, with SOA mass yields up to 0.55, comparable to that of daytime oxidation (Zaveri et al., 2020). RL2 also contains slightly elevated levoglucosan ($C_6H_{10}O_5$), indicating some influence from biomass burning emissions. Both RL1 and RL2 show enhanced $C_9H_{13}NO_2S$, likely representing an aromatic sulfonamide compound. Aromatic sulfonamides are widely used as industrial plasticizers and veterinary antibiotics and have been observed in various environmental media including groundwater, surface water, soil, manure, and PM (Baran et al., 2011; De Groote et al., 2002; Grung et al., 2017; Maceira et al., 2018; Sarmah et al., 2006). Sulfonamides can also be produced through reactions of sulfonyl halides with amines, which provides a plausible secondary formation pathway in polluted air (Das et al., 2018; Pedersen et al., 2023). The RL2 molecular composition

therefore suggests nighttime NO_3 oxidation of monoterpenes with a modest biomass burning imprint and a potential contribution from sulfonamide chemistry.

RL3 shows a high fraction of MSA, together with elevated malonic and oxalic acids (Figure 4-16). MSA can be generated in the dark through multiphase reactions of sulfur-containing gases (e.g., DMS) initiated by various oxidants (e.g., NO_3, O_3, and •OH) (Berndt, 2025; Fung et al., 2022; Van Rooy et al., 2021). The dominance of MSA in RL3 suggests the important role of organosulfur chemistry in nighttime OA growth in the residual layer.

Wind analysis further differentiates the three RL factors (Figure 4-14). RL1 is consistent with local influence, whereas RL2 and RL3 show stronger correlations with air from the southeast of the site. This pattern suggests that the air masses associated with monoterpene oxidation and organosulfur processing may be transported from the southeast.

Our observations highlight a clear mechanism linking residual layer chemistry to surface OA. Overnight, the residual layer decouples from the surface but still holds oxidants, precursors, and aerosol liquid water to support active nighttime chemistry. With ozone largely untitrated aloft, NO_2 reacts with O_3 to form NO_3, leading to significant NO_3 oxidation of VOCs. NO_3 also combines with NO_2 to produce N_2O_5, which heterogeneously taken up by particle water and yields nitrate. In parallel, aqueous-phase reactions, likely involving Fenton chemistry, and organosulfur reactions, can drive additional SOA formation. After sunrise, growth of the mixing layer entrains this processed air to the surface, modifying ground-level aerosol composition. This cycle recurs in Fresno winters, governed by stable nocturnal stratification and complex aloft precursors.

4.3.4 Other OA sources/processes

4.3.4.1 HOA

Hydrocarbon-like organic aerosol composed 9.3% of the average OA mass during the campaign. The time series of HOA followed NO_x and is primarily related to vehicular emissions. The diurnal cycle showed a morning increase around 8 am and a larger evening maximum near 9 pm (Figure 4-17). The morning peak aligns with traffic emissions during rush hours, and the stronger nighttime increase reflects both evening traffic activity and the shallow nocturnal boundary layer that concentrates emissions near the surface. The monitoring site is close to several major highways, consistent with the strong HOA signal and the predominantly local character indicated by the wind analysis (Figure 4-14).

The AMS spectrum of HOA is dominated by aliphatic C_nH_{2n-1} and C_nH_{2n+1} ions, with prominent signals at m/z 27 ($C_2H_3^+$), 29 ($C_2H_5^+$), 41 ($C_3H_5^+$), 43 ($C_3H_7^+$), 55 ($C_4H_7^+$), 57 ($C_4H_9^+$), 69 ($C_5H_9^+$), and 71 ($C_5H_{11}^+$), typical fragments of long-chain alkanes, cycloalkanes, and aromatics associated with fuel and lubricating oil (Presto et al., 2014; Price et al., 2017; Zhang et al., 2005). HOA is the least oxidized OA factor, with O/C ratio of 0.07 and H/C of 1.95, similar to the values previously reported by Young et al. (2016). Additionally, HOA explains large fractions of the $C_4H_7^+$ and $C_4H_9^+$ signals, with an f_{55}/f_{57} ratio of 0.9. These features confirm the identification of HOA and its

association with traffic-related fossil fuel combustion. Since I-CIMS is more sensitive to oxygenated molecules rather than hydrocarbons, HOA accounts for only 2.1% of the total CIMS signal. Even so, cPMF resolved a set of oxygenated molecules associated with HOA (e.g., C_5H_8O4, $C_2H_2O_4$, and $C_6H_{10}O_5$), which likely reflect a mixture of slight traffic emission aging and co-emissions of BBOAs with HOA.

4.3.4.2 COA

Cooking-related organic aerosol accounted for 11.3% of the OA mass during the campaign. The diurnal pattern shows that COA increased in late afternoon near 4 pm, reached a first maximum around 5 pm, and climbed again to a broader peak near 8 pm (Figure 4-17). The timing aligns with local dinner preparation. High COA concentrations correlated with low wind speeds from the northeast and northwest, indicating nearby sources on both directions of the site (Figure 4-14).

The AMS spectrum of COA shares the hydrocarbon ions common to HOA and shows low oxidation degree (O/C = 0.11). Compared with HOA, COA shows more enhanced $C_xH_yO_1^+$ ions, including $C_2H_3O^+$ (m/z 43), $C_3H_3O^+$ (m/z 55), $C_3H_5O^+$ (m/z 57), $C_5H_8O^+$ (m/z 84), $C_6H_{10}O^+$ (m/z 98), and $C_7H_{12}O^+$ (m/z 112), which have been proposed as tracer ions for cooking emissions (Sun et al., 2016). The COA shows an f_{55}/f_{57} ratio of 1.4, higher than HOA, but slightly lower than the value commonly reported for COA (2.6-3.0) (Huang et al., 2021; Mohr et al., 2012). The CIMS spectrum of COA is characterized by a family of fatty acids and their oxidation products, including $C_{18}H_{34}O_2$ (oleic acid), $C_{18}H_{32}O_2$ (linoleic acid), $C_{18}H_{36}O_2$ (stearic acid), $C_{16}H_{32}O_2$ (palmitic acid), and $C_9H_{16}O_3$ (9-oxononanoic acid), which are major constituents of culinary oils and are emitted during cooking (Abdullahi et al., 2013; Reyes-Villegas et al., 2018). COA accounts for large fractions of these fatty acid signals, contributing 20% of $C_{18}H_{34}O_2$, 18% of $C_{18}H_{32}O_2$, and 17% of $C_{18}H_{36}O_2$, which chemically links this factor to cooking activities.

4.3.4.3 BBOAs

Five biomass burning factors (BBOA1-5) were resolved, together accounting for 29.7% of the OA mass. The high contribution of BBOAs is consistent with prior studies that show prevalent residual wood burning in winter Fresno (Chen et al., 2018; Chow et al., 2008; Ge et al., 2012b; Sun et al., 2022; Young et al., 2016). The multiple BBOA factors likely reflect the diversity of burning practices.

The AMS spectra provide evidence for the BBOA assignments. The O/C ratio of BBOAs spans from 0.25 to 0.31, and f_{60} ranges from 0.007 to 0.068, well above the 0.003 background threshold for nonBB aerosol (Cubison et al., 2011) (Figure 4-18). In the triangle plot, the BBOAs cluster at low f_{44} (0.01-0.05) and moderately high f_{43} (0.05- 0.13), consistent with fresh BB emissions (Figure 4-13). Four of the BBOAs show strong levoglucosan-related ions (e.g., $C_2H_4O_2^+$ and $C_3H_5O_2^+$) that are established tracers for biomass burning emissions (Avery et al., 2023; Cubison et al., 2011; Simoneit et al., 1999). The CIMS spectra add molecular speciation to the BBOA assignments. All BBOAs show enhanced $C_6H_{10}O_5$, consistent with anhydrosugars (e.g., levoglucosan, mannosan, and galactosan) from cellulose and hemicellulose pyrolysis. BBOA2 and

BBOA3 are dominated by CHO species, whereas BBOA1, BBOA4, and BBOA5 contain higher fractions of nitrophenols such as $C_6H_5NO_4$ and $C_7H_7NO_4$. Nitrophenols are emitted directly from biomass burning and are also produced secondarily through nighttime NO_3 oxidation of phenols or daytime photooxidation under high NO_x conditions (Finewax et al., 2018; Mohr et al., 2013; Wang et al., 2023a). BBOA3 shows enhanced $C_5H_8O_4$, likely glutaric or methylsuccinic acid (Jen et al., 2019). These features agree with previously reported CIMS signatures for biomass burning emissions (Gaston et al., 2016; Ye et al., 2021). Quantitatively, the BBOAs contribute 65% of $C_6H_{10}O_5$, 40%-60% of phenols (e.g., $C_7H_8O_3$, $C_8H_{10}O_2$, and $C_8H_8O_3$) and up to 78% of nitrophenols (e.g., $C_6H_5NO_4$, $C_7H_7NO_4$, and $C_8H_9NO_4$), indicating biomass burning as the dominant source of these compounds.

The BBOAs show clear nighttime enhancements with local origins (Figures 4-18 and 4-14). All five factors were lowest in the afternoon, increased after 5 pm, and peaked at night, consistent with increased residential heating, a shallow nocturnal boundary layer that traps emissions, and low temperatures that favor partitioning of semivolatile BB components during night. BBOA3, BBOA4, and BBOA5 tend to peak earlier (8-9 pm), whereas BBOA2 peaked near midnight and BBOA1 was elevated from late evening until ~3 am. The polar plots indicate local origins for all five factors, with BBOA1 and BBOA2 associated with nearby sources from the northeast and BBOA3–5 receiving additional contributions from the northwest.

The five distinct BBOA factors likely capture different biomass burning emission sources with variations in fuel types, appliance technologies, burn phases, and aging degrees. Although we are not able to unambiguously assign each factor to a specific fuel or device, the results suggest that biomass burning in winter Fresno is neither chemically monolithic nor temporally uniform, and that multiple BB source types contribute to the winter OA.

4.3.4.4 Biogenic SOAs

Four SOA factors (BIO1-4) related to oxidation of biogenic VOCs (e.g., monoterpenes and isoprene) were resolved, with O/C ratios in the range of 0.27 to 0.40. In the AMS spectra, all BIO factors show prominent signals at m/z 27, 29, 43, and 44, consistent with previously reported spectra for biogenic SOA (Kiendler-Scharr et al., 2009).

CIMS provides molecular differences among the BIO factors, enabling their separation (Figure 4-19). BIO1 is characterized by CHO compounds generated from monoterpene oxidation, including $C_7H_{10\text{-}14}O_{4\text{-}8}$, $C_8H_{12\text{-}16}O_{4\text{-}8}$, $C_9H_{14\text{-}18}O_{4\text{-}8}$, and $C_{10}H_{16}O_z$. BIO3 shows a similar CHO pattern with BIO1, while BIO2 diverges from this template, showing enhanced $C_6H_{10}O_5$ but significantly lower $C_8H_{12}O_5$, $C_8H_{14}O_4$, and $C_9H_{14}O_5$, likely indicating interplay between biogenic and biomass burning emissions. A defining feature of BIO2 and BIO3 is the presence of abundant CHON species associated with organonitrate formation from monoterpenes. These organonitrates (e.g., $C_8H_{11}NO_7$, $C_9H_{15}NO_{6\text{-}7}$, $C_{10}H_{15,17,19}NO_{5\text{-}8}$, and $C_{10}H_{16,18}N_2O_{7\text{-}8}$) can be produced through both nighttime NO_3 chemistry and OH photooxidation under high NO_x conditions (Lee et al., 2016; Ng et al., 2017). In BIO3, CHON signals skew toward high molecular weight (primarily C_8–C_{10}),

whereas BIO2 contains a larger fraction of small C_3–C_5 CHON compounds (e.g., $C_3H_5NO_3$ and $C_3H_7NO_3$).

The diurnal patterns of the BIO factors agree with their chemical compositions (Figure 4-19). BIO3 increased after sunset, built steadily through the night, and peaked before sunrise, a pattern consistent with nocturnal NO_3 chemistry coupled with cooler temperatures that favor partitioning to the particle phase. BIO2 shows a modest increase overnight but surged sharply around 7 am and peaked near 9 am. This morning peak reflects two possible processes: (i) morning entrainment brought the organonitrates formed in the nocturnal residual layer to the surface; and (ii) rush hour NO_x emission enhanced organonitrate formation from monoterpene photooxidation. Both BIO2 and BIO3 dropped quickly after 9 am, consistent with daytime losses of organonitrates through photolysis, hydrolysis, and further oxidation (Zare et al., 2018). In contrast, BIO1, dominated by monoterpene-derived CHO species, shows no pronounced diurnal cycle.

Despite some variations among the three monoterpene-related factors (BIO1-3), the composition of BIO4 differs more substantially. The CIMS spectrum of BIO4 is characterized by $C_5H_{12}O_5$ (Figure 4-19), a well-known product of isoprene OH oxidation (D'Ambro et al., 2017). BIO4 concentration increased during a clean, post-storm period (Dec 20-23) with moderate rainfall. Wind analysis links high BIO4 concentrations to air masses from the southwest (Figure 4-14). These observations imply that BIO4 is likely associated with regional transport and extended aging that allow oxidized isoprene products to accumulate despite low local biogenic emissions.

4.3.5 Clean vs. polluted periods

Winter Fresno is characterized by stagnant conditions that allow local emissions and in situ chemistry to accumulate, while this stagnation is occasionally interrupted by westerly marine-influenced air, easterly downslope flow from the Sierra Nevada Mountains, and regionally transported air from the southeast. In this study, we observed several transitions between polluted and clean periods, coinciding with air mass changes, dilution, and wet scavenging during rainfall. HYSPLIT back trajectory cluster analysis (Figure 4-20) shows that the clean intervals are associated with oceanic flow from the northwest and southwest (primarily Cluster 1&4), confirming that severe PM episodes are largely locally generated and that external ventilation flushes the basin air.

To investigate the variations in OA chemistry between clean and polluted conditions, we define clean periods as times when $PM_{2.5}$ below 10 μg/m^3. Compared with polluted conditions, clean periods are generally warmer (12±3.7 °C vs. 10.5±3.6 °C) and show higher wind speeds (1.3±0.7 vs. 0.7±0.5 m/s) and stronger ventilation (Figure 4-21). The average PM concentration is 3.8±2.7 μg/m^3 in clean conditions and 28±12.6 μg/m^3 in polluted conditions. Organics remain the largest PM component in both regimes, contributing 59% and 54% in clean and polluted conditions (Figure 4-21). During clean conditions, biogenic SOA and BBOA are the greatest OA contributors, accounting for 21.1% and 19.5%. In polluted conditions, the absolute concentrations of all OA

types increase, with HOA increasing from 0.2 to 1.7 μg/m^3, COA from 0.36 to 2.0 μg/m^3, the ensemble of BBOAs from 0.67 to 5.4 μg/m^3, and the total SOA and OOA from 2.2 to 8.2 μg/m^3. The most significant fractional gains occur for BBOA and aqSOA factors, which increase from 19.5% to 31% and from 15% to 23%, respectively (Figure 4-21). In contrast, the contribution of biogenic SOA factors decreases from 21.1% to 7.3%. The results suggest that local residential wood burning emissions and aqueous-phase processing are the principal drivers of winter PM pollution formation, and thus the most direct targets for effective control in SJV.

4.3.6 Comparison of cPMF with single instrument PMF

The combined PMF applied to merged FIGAERO-I-CIMS and SP-AMS data resolved 19 chemically interpretable factors, a separation neither instrument can achieve alone. In AMS, 600 °C thermal vaporization followed by 70 eV EI leads to extensive fragmentation that sacrifices chemical diversity, whereas I-CIMS emphasizes oxygenated species with variable sensitivities across compounds. Due to the instrument limitations, each single-instrument PMF analysis (i.e., amsPMF and cimsPMF) only resolved 14 factors (Figures 4-3 and 4-4), and the solutions did not map one-to-one, with several sources and processes either merged or missing. Comparison of the amsPMF and cimsPMF factor time series (Figure 4-22) revealed seven pairs of highly correlated factors (Pearsons $r \geq 0.7$), indicating that these likely represent common sources and processes that can be resolved by PMF applied to either instrument individually. These matched pairs include one COA factor (cimsPMF COA with amsPMF COA), two BBOA factors (cimsPMF BBOA1 with amsPMF LOOA1, and cimsPMF BBOA3 with amsPMF BBOA1), two aqSOA factors (cimsPMF AQ1 with amsPMF MZ43O_1, and cimsPMF AQ4 with amsPMF MOOA1), one residual-layer SOA factor (cimsPMF RL1 with amsPMF MOOA4), and one biogenic SOA factor (cimsPMF BIO3 with amsPMF MZ43O_2). However, several SOA factors that were clearly resolved by cimsPMF (e.g., AQ3, RL3, BIO1, and OOA) were not distinctly separated by amsPMF, whereas cimsPMF was relatively insensitive to less oxidized primary factors such as HOA. Integrating the two datasets can preserve the quantitative strengths of AMS while adding molecular characterization from CIMS. Incorporating CIMS data clearly improves factor separation. As shown in Figure 4-23, the AMS spectra of many cPMF factors show high similarity (r = 0.4-0.9) due to extensive fragmentation during high-temperature vaporization and electron ionization in AMS measurements, whereas the corresponding CIMS spectra are highly distinct (r= 0.02-0.2) and chemically informative. This additional chemical specificity provides stronger constraints in the PMF analysis and enables improved separation of factors that are difficult to distinguish using AMS data alone.

Compared with the single-instrument PMF solutions, cPMF refines rather than reinvents the source apportionment. For the factors resolved by both approaches, their time series correlate well (Figure 4-24), providing an important validity check. In the cimsPMF, three BBOAs, three aqSOAs, two residual layer SOAs, and two biogenic SOAs are retrieved, and their time series align closely with the corresponding cPMF factors (r = 0.75-0.99). In the amsPMF, HOA, COA, four BBOAs, three

aqSOAs, one residual layer SOA, and one biogenic SOA are resolved with good correlations to the corresponding cPMF factors (r=0.73-0.98). The cross-approach consistency extends to fractional contributions. For example, the HOA and COA mass fractions from cPMF closely match the amsPMF estimates, indicating that the AMS quantification is retained.

The added scientific value of the cPMF analysis lies in the factors that single instrument PMF could not separate. For example, HOA and COA were not resolved by cimsPMF, because I-CIMS is not sensitive towards nonoxygenated hydrocarbons. On the other hand, amsPMF tended to merge chemically distinct SOA factors due to extensive fragmentation. By integrating the two, cPMF was able to resolve a complete set of primary and secondary factors that differ in oxidation state, molecular composition, diurnal behavior, and meteorological dependencies. Overall, cPMF yields a detailed and defensible picture of winter Fresno OA, providing the most reliable source apportionment for this complex winter basin.

4.4. Conclusions and Implications

This study provides a process-resolved view of wintertime OA in an urban basin environment by applying combined PMF (cPMF) to merged FIGAERO-I-CIMS and SP-AMS datasets. The cPMF resolves 19 distinct OA factors, linking molecular markers to mass-quantitative factors and capturing sources and pathways that single instrument PMF not able to isolate.

Secondary production remains substantial despite reduced daytime photochemistry in winter. Fog-driven aqueous processing and nocturnal chemistry in the residual layer are two key secondary pathways, while biomass burning is the largest primary source. All aqSOA factors are enriched in dicarboxylic acid but reflect different precursors and oxidation levels. With biomass-burning prevalent at the site, aqueous reactions of BB emissions make a significant contribution to aqSOA. SOA production in the residual layer involves NO_3 oxidation of monoterpenes, organosulfur chemistry, and dark aqueous reactions. RL-SOAs show repeated morning peaks that coincide with nitrate and nitryl chloride, indicating that overnight processing in the residual layer seeds a consistent surface OA source. These findings generalize to winter basins with shallow nocturnal inversions, weak ventilation, frequent fog and high humidity and substantial nighttime wood burning–conditions common across mid-latitude valley cities.

Policy implications follow directly. Since local biomass burning is the largest primary source and dominates at night, limiting nighttime wood burning can significantly reduce POA and the precursor supply to SOA. During stagnant, foggy days, cocontrolling VOCs, NO_x, and NH_3 may further suppress aqueous reactions and NO_3/N_2O_5driven nocturnal chemistry. The findings in this work also guide modeling work. Incorporating aqueous SOA formation, nocturnal chemistry in the residual layer, and boundary layer dynamics should improve winter OA predictions in models and guide more effective air quality management.

4.5. References

Abdullahi, K. L., Delgado-Saborit, J. M., and Harrison, R. M.: Emissions and indoor

concentrations of particulate matter and its specific chemical components from cooking: A review, Atmos. Environ., 71, 260–294, https://doi.org/https://doi.org/10.1016/j.atmosenv.2013.01.061, 2013.

Arciva, S., Niedek, C., Mavis, C., Yoon, M., Sanchez, M. E., Zhang, Q., and Anastasio, C.: Aqueous ·OH Oxidation of Highly Substituted Phenols as a Source of Secondary Organic Aerosol, Environ. Sci. Technol., 56, 9959–9967, https://doi.org/10.1021/acs.est.2c02225, 2022.

Arciva, S., Zhou, Y., Jiang, W., Ross, A., Zhang, Q., and Anastasio, C.: Aqueous Oxidation of Biomass-Burning Furans by Singlet Molecular Oxygen (1O2*), Environ. Sci. Technol., 59, 10357–10367, https://doi.org/10.1021/acs.est.4c10778, 2025.

Avery, A. M., Fawaz, M., Williams, L. R., Bond, T., and Onasch, T. B.: Chemically distinct particle-phase emissions from highly controlled pyrolysis of three wood types, Atmos. Chem. Phys., 23, 8837–8854, https://doi.org/10.5194/acp-23-8837-2023, 2023.

Bannan, T. J., Bacak, A., Le Breton, M., Flynn, M., Ouyang, B., McLeod, M., Jones, R., Malkin, T. L., Whalley, L. K., Heard, D. E., Bandy, B., Khan, M. A. H., Shallcross, D. E., and Percival, C. J.: Ground and Airborne U.K. Measurements of Nitryl Chloride: An Investigation of the Role of Cl Atom Oxidation at Weybourne Atmospheric Observatory, J. Geophys. Res. Atmos., 122, 11,111-154,165, https://doi.org/https://doi.org/10.1002/2017JD026624, 2017.

Baran, W., Adamek, E., Ziemiańska, J., and Sobczak, A.: Effects of the presence of sulfonamides in the environment and their influence on human health, J. Hazard. Mater., 196, 1–15, https://doi.org/https://doi.org/10.1016/j.jhazmat.2011.08.082, 2011.

Bates, K. H., Burke, G. J. P., Cope, J. D., and Nguyen, T. B.: Secondary organic aerosol and organic nitrogen yields from the nitrate radical (NO3) oxidation of alpha-pinene from various RO2 fates, Atmos. Chem. Phys., 22, 1467–1482, https://doi.org/10.5194/acp-22-1467-2022, 2022.

Berndt, T.: Methanesulfonic acid (MSA) and SO3 formation from the addition channel of atmospheric dimethyl sulfide oxidation, Chem. Commun., 61, 1443–1446, https://doi.org/10.1039/D4CC05913A, 2025.

Brown, S. S. and Stutz, J.: Nighttime radical observations and chemistry, Chem. Soc. Rev., 41, 6405–6447, https://doi.org/10.1039/C2CS35181A, 2012.

Canagaratna, M. R., Jayne, J. T., Jimenez, J. L., Allan, J. D., Alfarra, M. R., Zhang, Q., Onasch, T. B., Drewnick, F., Coe, H., Middlebrook, A., Delia, A., Williams, L. R., Trimborn, A. M., Northway, M. J., DeCarlo, P. F., Kolb, C. E., Davidovits, P., and Worsnop, D. R.: Chemical and microphysical characterization of ambient aerosols with the aerodyne aerosol mass spectrometer, Mass Spectrom. Rev., 26, 185–222, https://doi.org/10.1002/mas.20115, 2007.

Canagaratna, M. R., Jimenez, J. L., Kroll, J. H., Chen, Q., Kessler, S. H., Massoli, P., Hildebrandt Ruiz, L., Fortner, E., Williams, L. R., Wilson, K. R., Surratt, J. D., Donahue, N. M., Jayne, J. T., and Worsnop, D. R.: Elemental ratio measurements of organic compounds using aerosol mass spectrometry: characterization, improved calibration, and implications, Atmos. Chem. Phys., 15, 253–272, https://doi.org/10.5194/acp-15-253-2015, 2015.

Chen, C.-L., Chen, S., Russell, L. M., Liu, J., Price, D. J., Betha, R., Sanchez, K. J., Lee, A. K. Y., Williams, L., Collier, S. C., Zhang, Q., Kumar, A., Kleeman, M. J., Zhang, X., and Cappa, C. D.: Organic Aerosol Particle Chemical Properties Associated With Residential Burning and Fog in Wintertime San Joaquin Valley (Fresno) and With Vehicle and Firework Emissions in Summertime South Coast Air Basin (Fontana), J. Geophys. Res. Atmos., 123, 10,707-710,731, https://doi.org/10.1029/2018JD028374, 2018.

Chen, X., Xia, M., Wang, W., Yun, H., Yue, D., and Wang, T.: Fast near-surface ClNO2 production and its impact on O3 formation during a heavy pollution event in South China, Sci. Total Environ., 858, 159998, https://doi.org/https://doi.org/10.1016/j.scitotenv.2022.159998, 2023.

Chow, J. C., Watson, J. G., Lowenthal, D. H., Park, K., Doraiswamy, P., Bowers, K., and Bode, R.: Continuous and filter-based measurements of PM2.5 nitrate and sulfate at the Fresno Supersite, Environ. Monit. Assess., 144, 179–189, https://doi.org/10.1007/s10661-007-9987-5, 2008.

Collier, S., Williams, L. R., Onasch, T. B., Cappa, C. D., Zhang, X., Russell, L. M., Chen, C.-L., Sanchez, K. J., Worsnop, D. R., and Zhang, Q.: Influence of Emissions and Aqueous Processing on Particles Containing Black Carbon in a Polluted Urban Environment: Insights From a Soot Particle-Aerosol Mass Spectrometer, J. Geophys. Res. Atmos., 123, 6648–6666, https://doi.org/https://doi.org/10.1002/2017JD027851, 2018.

Crippa, M., Canonaco, F., Lanz, V. A., Äijälä, M., Allan, J. D., Carbone, S., Capes, G., Ceburnis, D., Dall'Osto, M., Day, D. A., DeCarlo, P. F., Ehn, M., Eriksson, A., Freney, E., Hildebrandt Ruiz, L., Hillamo, R., Jimenez, J. L., Junninen, H., Kiendler-Scharr, A., Kortelainen, A.-M., Kulmala, M., Laaksonen, A., Mensah, A. A., Mohr, C., Nemitz, E., O'Dowd, C., Ovadnevaite, J., Pandis, S. N., Petäjä, T., Poulain, L., Saarikoski, S., Sellegri, K., Swietlicki, E., Tiitta, P., Worsnop, D. R., Baltensperger, U., and Prévôt, A. S. H.: Organic aerosol components derived from 25 AMS data sets across Europe using a consistent ME-2 based source apportionment approach, Atmos. Chem. Phys., 14, 6159–6176, https://doi.org/10.5194/acp-14-6159-2014, 2014.

Cubison, M. J., Ortega, A. M., Hayes, P. L., Farmer, D. K., Day, D., Lechner, M. J., Brune, W. H., Apel, E., Diskin, G. S., Fisher, J. A., Fuelberg, H. E., Hecobian, A., Knapp, D. J., Mikoviny, T., Riemer, D., Sachse, G. W., Sessions, W., Weber, R. J., Weinheimer, A. J., Wisthaler, A., and Jimenez, J. L.: Effects of aging on organic aerosol from open biomass burning smoke in aircraft and laboratory studies, Atmos. Chem. Phys., 11, 12049–12064, https://doi.org/10.5194/acp-11-12049-2011, 2011.

D'Ambro, E. L., Lee, B. H., Liu, J., Shilling, J. E., Gaston, C. J., Lopez-Hilfiker, F. D., Schobesberger, S., Zaveri, R. A., Mohr, C., Lutz, A., Zhang, Z., Gold, A., Surratt, J. D., Rivera-Rios, J. C., Keutsch, F. N., and Thornton, J. A.: Molecular composition and volatility of isoprene photochemical oxidation secondary organic aerosol under low- and high-NOx conditions, Atmos. Chem. Phys., 17, 159–174, https://doi.org/10.5194/acp-17-159-2017, 2017.

Das, T. C., Quadri, S. A., and Farooqui, M.: Recent advances in synthesis of sulfonamides: A review., Chem. Biol. Interface, 8, 2018.

DeCarlo, P. F., Kimmel, J. R., Trimborn, A., Northway, M. J., Jayne, J. T., Aiken, A. C., Gonin,

M., Fuhrer, K., Horvath, T., Docherty, K. S., Worsnop, D. R., and Jimenez, J. L.: Field-Deployable, High-Resolution, Time-of-Flight Aerosol Mass Spectrometer, Anal. Chem., 78, 8281–8289, https://doi.org/10.1021/ac061249n, 2006.

Ervens, B., Turpin, B. J., and Weber, R. J.: Secondary organic aerosol formation in cloud droplets and aqueous particles (aqSOA): a review of laboratory, field and model studies, Atmos. Chem. Phys., 11, 11069–11102, https://doi.org/10.5194/acp-11-11069-2011, 2011.

Farley, R. N., Collier, S., Cappa, C. D., Williams, L. R., Onasch, T. B., Russell, L. M., Kim, H., and Zhang, Q.: Source apportionment of soot particles and aqueous-phase processing of black carbon coatings in an urban environment, Atmos. Chem. Phys., 23, 15039–15056, https://doi.org/10.5194/acp-23-15039-2023, 2023.

Finewax, Z., de Gouw, J. A., and Ziemann, P. J.: Identification and Quantification of 4-Nitrocatechol Formed from OH and NO3 Radical-Initiated Reactions of Catechol in Air in the Presence of NOx: Implications for Secondary Organic Aerosol Formation from Biomass Burning, Environ. Sci. Technol., 52, 1981–1989, https://doi.org/10.1021/acs.est.7b05864, 2018.

Fung, K. M., Heald, C. L., Kroll, J. H., Wang, S., Jo, D. S., Gettelman, A., Lu, Z., Liu, X., Zaveri, R. A., Apel, E. C., Blake, D. R., Jimenez, J.-L., Campuzano-Jost, P., Veres, P. R., Bates, T. S., Shilling, J. E., and Zawadowicz, M.: Exploring dimethyl sulfide (DMS) oxidation and implications for global aerosol radiative forcing, Atmos. Chem. Phys., 22, 1549–1573, https://doi.org/10.5194/acp-22-1549-2022, 2022.

Galloway, M. M., Powelson, M. H., Sedehi, N., Wood, S. E., Millage, K. D., Kononenko, J. A., Rynaski, A. D., and De Haan, D. O.: Secondary Organic Aerosol Formation during Evaporation of Droplets Containing Atmospheric Aldehydes, Amines, and Ammonium Sulfate, Environ. Sci. Technol., 48, 14417–14425, https://doi.org/10.1021/es5044479, 2014.

Gaston, C. J., Lopez-Hilfiker, F. D., Whybrew, L. E., Hadley, O., McNair, F., Gao, H., Jaffe, D. A., and Thornton, J. A.: Online molecular characterization of fine particulate matter in Port Angeles, WA: Evidence for a major impact from residential wood smoke, Atmos. Environ., 138, 99–107, https://doi.org/https://doi.org/10.1016/j.atmosenv.2016.05.013, 2016.

Ge, X., Zhang, Q., Sun, Y., Ruehl, C. R., and Setyan, A.: Effect of aqueous-phase processing on aerosol chemistry and size distributions in Fresno, California, during wintertime, Environ. Chem., 9, 221–235, 2012a.

Ge, X., Setyan, A., Sun, Y., and Zhang, Q.: Primary and secondary organic aerosols in Fresno, California during wintertime: Results from high resolution aerosol mass spectrometry, J. Geophys. Res. Atmos., 117, https://doi.org/10.1029/2012JD018026, 2012b.

Gilardoni, S., Massoli, P., Paglione, M., Giulianelli, L., Carbone, C., Rinaldi, M., Decesari, S., Sandrini, S., Costabile, F., Gobbi, G. P., Pietrogrande, M. C., Visentin, M., Scotto, F., Fuzzi, S., Facchini, M. C., Stefania, G., Paola, M., Marco, P., Lara, G., Claudio, C., Matteo, R., Stefano, D., Silvia, S., Francesca, C., Paolo, G. G., Chiara, P. M., Marco, V., Fabiana, S., Sandro, F., and Cristina, F. M.: Direct observation of aqueous secondary organic aerosol from biomass-burning emissions, Proc. Natl. Acad. Sci., 113, 10013–10018, https://doi.org/10.1073/pnas.1602212113, 2016.

Go, B. R., Li, Y. J., Huang, D. D., and Chan, C. K.: Aqueous-Phase Photoreactions of Mixed Aromatic Carbonyl Photosensitizers Yield More Oxygenated, Oxidized, and less Light-Absorbing Secondary Organic Aerosol (SOA) than Single Systems, Environ. Sci. Technol., 58, 7924–7936, https://doi.org/10.1021/acs.est.3c10199, 2024.

De Groote, P., Devaux, J., and Godard, P.: Effect of benzenesulfonamide plasticizers on the glass-transition temperature of semicrystalline polydodecamide, J. Polym. Sci. Part B Polym. Phys., 40, 2208–2218, https://doi.org/https://doi.org/10.1002/polb.10281, 2002.

Grung, M., Kringstad, A., Bæk, K., Allan, I. J., Thomas, K. V, Meland, S., and Ranneklev, S. B.: Identification of non-regulated polycyclic aromatic compounds and other markers of urban pollution in road tunnel particulate matter, J. Hazard. Mater., 323, 36–44, https://doi.org/https://doi.org/10.1016/j.jhazmat.2016.05.036, 2017.

He, Y., Zhao, B., Wang, S., Valorso, R., Chang, X., Yin, D., Feng, B., Camredon, M., Aumont, B., Dearden, A., Jathar, S. H., Shrivastava, M., Jiang, Z., Cappa, C. D., Yee, L. D., Seinfeld, J. H., Hao, J., and Donahue, N. M.: Formation of secondary organic aerosol from wildfire emissions enhanced by long-time ageing, Nat. Geosci., 17, 124–129, https://doi.org/10.1038/s41561-023-01355-4, 2024.

Heal, M. R., Harrison, M. A. J., and Neil Cape, J.: Aqueous-phase nitration of phenol by N2O5 and ClNO2, Atmos. Environ., 41, 3515–3520, https://doi.org/https://doi.org/10.1016/j.atmosenv.2007.02.003, 2007.

Hennigan, C. J., Bergin, M. H., Russell, A. G., Nenes, A., and Weber, R. J.: Gas/particle partitioning of water-soluble organic aerosol in Atlanta, Atmos. Chem. Phys., 9, 3613–3628, https://doi.org/10.5194/acp-9-3613-2009, 2009.

Herrmann, H., Schaefer, T., Tilgner, A., Styler, S. A., Weller, C., Teich, M., and Otto, T.: Tropospheric Aqueous-Phase Chemistry: Kinetics, Mechanisms, and Its Coupling to a Changing Gas Phase, Chem. Rev., 115, 4259–4334, https://doi.org/10.1021/cr500447k, 2015.

Hilario, M. R. A., Crosbie, E., Bañaga, P. A., Betito, G., Braun, R. A., Cambaliza, M. O., Corral, A. F., Cruz, M. T., Dibb, J. E., Lorenzo, G. R., MacDonald, A. B., Robinson, C. E., Shook, M. A., Simpas, J. B., Stahl, C., Winstead, E., Ziemba, L. D., and Sorooshian, A.: Particulate Oxalate-To-Sulfate Ratio as an Aqueous Processing Marker: Similarity Across Field Campaigns and Limitations, Geophys. Res. Lett., 48, e2021GL096520, https://doi.org/https://doi.org/10.1029/2021GL096520, 2021.

Hodas, N., Sullivan, A. P., Skog, K., Keutsch, F. N., Collett, J. L. J., Decesari, S., Facchini, M. C., Carlton, A. G., Laaksonen, A., and Turpin, B. J.: Aerosol Liquid Water Driven by Anthropogenic Nitrate: Implications for Lifetimes of Water-Soluble Organic Gases and Potential for Secondary Organic Aerosol Formation, Environ. Sci. Technol., 48, 11127–11136, https://doi.org/10.1021/es5025096, 2014.

Huang, D. D., Zhang, Q., Cheung, H. H. Y., Yu, L., Zhou, S., Anastasio, C., Smith, J. D., and Chan, C. K.: Formation and Evolution of aqSOA from Aqueous-Phase Reactions of Phenolic Carbonyls: Comparison between Ammonium Sulfate and Ammonium Nitrate Solutions, Environ. Sci. Technol., 52, 9215–9224, https://doi.org/10.1021/acs.est.8b03441, 2018.

Huang, D. D., Zhu, S., An, J., Wang, Q., Qiao, L., Zhou, M., He, X., Ma, Y., Sun, Y., Huang, C.,

Yu, J. Z., and Zhang, Q.: Comparative Assessment of Cooking Emission Contributions to Urban Organic Aerosol Using Online Molecular Tracers and Aerosol Mass Spectrometry Measurements, Environ. Sci. Technol., 55, 14526–14535, https://doi.org/10.1021/acs.est.1c03280, 2021.

Jen, C. N., Hatch, L. E., Selimovic, V., Yokelson, R. J., Weber, R., Fernandez, A. E., Kreisberg, N. M., Barsanti, K. C., and Goldstein, A. H.: Speciated and total emission factors of particulate organics from burning western US wildland fuels and their dependence on combustion efficiency, Atmos. Chem. Phys., 19, 1013–1026, https://doi.org/10.5194/acp-19-1013-2019, 2019.

Jiang, W., Misovich, M. V, Hettiyadura, A. P. S., Laskin, A., McFall, A. S., Anastasio, C., and Zhang, Q.: Photosensitized Reactions of a Phenolic Carbonyl from Wood Combustion in the Aqueous Phase—Chemical Evolution and Light Absorption Properties of AqSOA, Environ. Sci. Technol., 55, 5199–5211, https://doi.org/10.1021/acs.est.0c07581, 2021.

Jiang, W., Yu, L., Yee, L., Chhabra, P., Seinfeld, J., Anastasio, C., and Zhang, Q.: Chemical Differences between Phenolic Secondary Organic Aerosol Formed through Gas-Phase and Aqueous-Phase Reactions, ACS Earth Sp. Chem., https://doi.org/10.1021/acsearthspacechem.4c00204, 2024.

Jimenez, J. L., Canagaratna, M. R., Donahue, N. M., Prevot, A. S. H., Zhang, Q., Kroll, J. H., DeCarlo, P. F., Allan, J. D., Coe, H., Ng, N. L., Aiken, A. C., Docherty, K. S., Ulbrich, I. M., Grieshop, A. P., Robinson, A. L., Duplissy, J., Smith, J. D., Wilson, K. R., Lanz, V. A., Hueglin, C., Sun, Y. L., Tian, J., Laaksonen, A., Raatikainen, T., Rautiainen, J., Vaattovaara, P., Ehn, M., Kulmala, M., Tomlinson, J. M., Collins, D. R., Cubison, M. J., Dunlea, J., Huffman, J. A., Onasch, T. B., Alfarra, M. R., Williams, P. I., Bower, K., Kondo, Y., Schneider, J., Drewnick, F., Borrmann, S., Weimer, S., Demerjian, K., Salcedo, D., Cottrell, L., Griffin, R., Takami, A., Miyoshi, T., Hatakeyama, S., Shimono, A., Sun, J. Y., Zhang, Y. M., Dzepina, K., Kimmel, J. R., Sueper, D., Jayne, J. T., Herndon, S. C., Trimborn, A. M., Williams, L. R., Wood, E. C., Middlebrook, A. M., Kolb, C. E., Baltensperger, U., and Worsnop, D. R.: Evolution of Organic Aerosols in the Atmosphere, Science (80-.)., 326, 1525–1529, https://doi.org/10.1126/science.1180353, 2009.

Kawamura, K. and Bikkina, S.: A review of dicarboxylic acids and related compounds in atmospheric aerosols: Molecular distributions, sources and transformation, Atmos. Res., 170, 140–160, https://doi.org/https://doi.org/10.1016/j.atmosres.2015.11.018, 2016.

Kiendler-Scharr, A., Zhang, Q., Hohaus, T., Kleist, E., Mensah, A., Mentel, T. F., Spindler, C., Uerlings, R., Tillmann, R., and Wildt, J.: Aerosol Mass Spectrometric Features of Biogenic SOA: Observations from a Plant Chamber and in Rural Atmospheric Environments, Environ. Sci. Technol., 43, 8166–8172, https://doi.org/10.1021/es901420b, 2009.

Kodros, J. K., Papanastasiou, D. K., Paglione, M., Masiol, M., Squizzato, S., Florou, K., Skyllakou, K., Kaltsonoudis, C., Nenes, A., and Pandis, S. N.: Rapid dark aging of biomass burning as an overlooked source of oxidized organic aerosol, Proc. Natl. Acad. Sci. U. S. A., 117, 33028–33033, https://doi.org/10.1073/PNAS.2010365117, 2020.

Kroflič, A., Anders, J., Drventić, I., Mettke, P., Böge, O., Mutzel, A., Kleffmann, J., and Herrmann, H.: Guaiacol Nitration in a Simulated Atmospheric Aerosol with an Emphasis on Atmospheric

Nitrophenol Formation Mechanisms, ACS Earth Sp. Chem., 5, 1083–1093, https://doi.org/10.1021/acsearthspacechem.1c00014, 2021.

Kumar, V., Giannoukos, S., Haslett, S. L., Tong, Y., Singh, A., Bertrand, A., Lee, C. P., Wang, D. S., Bhattu, D., Stefenelli, G., Dave, J. S., Puthussery, J. V, Qi, L., Vats, P., Rai, P., Casotto, R., Satish, R., Mishra, S., Pospisilova, V., Mohr, C., Bell, D. M., Ganguly, D., Verma, V., Rastogi, N., Baltensperger, U., Tripathi, S. N., Prévôt, A. S. H., and Slowik, J. G.: Highly time-resolved chemical speciation and source apportionment of organic aerosol components in Delhi, India, using extractive electrospray ionization mass spectrometry, Atmos. Chem. Phys., 22, 7739–7761, https://doi.org/10.5194/acp-22-7739-2022, 2022.

Lamkaddam, H., Dommen, J., Ranjithkumar, A., Gordon, H., Wehrle, G., Krechmer, J., Majluf, F., Salionov, D., Schmale, J., Bjelić, S., Carslaw, K. S., El Haddad, I., and Baltensperger, U.: Large contribution to secondary organic aerosol from isoprene cloud chemistry, Sci. Adv., 7, eabe2952, https://doi.org/10.1126/sciadv.abe2952, 2025.

Lee, B. H., Lopez-Hilfiker, F. D., Mohr, C., Kurtén, T., Worsnop, D. R., and Thornton, J. A.: An Iodide-Adduct High-Resolution Time-of-Flight Chemical-Ionization Mass Spectrometer: Application to Atmospheric Inorganic and Organic Compounds, Environ. Sci. Technol., 48, 6309–6317, https://doi.org/10.1021/es500362a, 2014.

Lee, B. H., Mohr, C., Lopez-Hilfiker, F. D., Lutz, A., Hallquist, M., Lee, L., Romer, P., Cohen, R. C., Iyer, S., Kurtén, T., Hu, W., Day, D. A., Campuzano-Jost, P., Jimenez, J. L., Xu, L., Ng, N. L., Guo, H., Weber, R. J., Wild, R. J., Brown, S. S., Koss, A., de Gouw, J., Olson, K., Goldstein, A. H., Seco, R., Kim, S., McAvey, K., Shepson, P. B., Starn, T., Baumann, K., Edgerton, E. S., Liu, J., Shilling, J. E., Miller, D. O., Brune, W., Schobesberger, S., D'Ambro, E. L., and Thornton, J. A.: Highly functionalized organic nitrates in the southeast United States: Contribution to secondary organic aerosol and reactive nitrogen budgets, Proc. Natl. Acad. Sci., 113, 1516–1521, https://doi.org/10.1073/pnas.1508108113, 2016.

Lim, Y. B., Tan, Y., Perri, M. J., Seitzinger, S. P., and Turpin, B. J.: Aqueous chemistry and its role in secondary organic aerosol (SOA) formation, Atmos. Chem. Phys., 10, 10521–10539, https://doi.org/10.5194/acp-10-10521-2010, 2010.

Liu, L., Hohaus, T., Franke, P., Lange, A. C., Tillmann, R., Fuchs, H., Tan, Z., Rohrer, F., Karydis, V., He, Q., Vardhan, V., Andres, S., Bohn, B., Holland, F., Winter, B., Wedel, S., Novelli, A., Hofzumahaus, A., Wahner, A., and Kiendler-Scharr, A.: Observational evidence reveals the significance of nocturnal chemistry in seasonal secondary organic aerosol formation, npj Clim. Atmos. Sci., 7, 207, https://doi.org/10.1038/s41612-024-00747-6, 2024.

Loeffler, K. W., Koehler, C. A., Paul, N. M., and De Haan, D. O.: Oligomer Formation in Evaporating Aqueous Glyoxal and Methyl Glyoxal Solutions, Environ. Sci. Technol., 40, 6318–6323, https://doi.org/10.1021/es060810w, 2006.

Lopez-Hilfiker, F. D., Mohr, C., Ehn, M., Rubach, F., Kleist, E., Wildt, J., Mentel, T. F., Lutz, A., Hallquist, M., Worsnop, D., and Thornton, J. A.: A novel method for online analysis of gas and particle composition: description and evaluation of a Filter Inlet for Gases and AEROsols (FIGAERO), Atmos. Meas. Tech., 7, 983–1001, https://doi.org/10.5194/amt-7-983-2014, 2014.

Maceira, A., Marcé, R. M., and Borrull, F.: Occurrence of benzothiazole, benzotriazole and benzenesulfonamide derivates in outdoor air particulate matter samples and human exposure assessment, Chemosphere, 193, 557–566, https://doi.org/https://doi.org/10.1016/j.chemosphere.2017.11.073, 2018.

McDuffie, E. E., Fibiger, D. L., Dubé, W. P., Lopez-Hilfiker, F., Lee, B. H., Thornton, J. A., Shah, V., Jaeglé, L., Guo, H., Weber, R. J., Michael Reeves, J., Weinheimer, A. J., Schroder, J. C., Campuzano-Jost, P., Jimenez, J. L., Dibb, J. E., Veres, P., Ebben, C., Sparks, T. L., Wooldridge, P. J., Cohen, R. C., Hornbrook, R. S., Apel, E. C., Campos, T., Hall, S. R., Ullmann, K., and Brown, S. S.: Heterogeneous N2O5 Uptake During Winter: Aircraft Measurements During the 2015 WINTER Campaign and Critical Evaluation of Current Parameterizations, J. Geophys. Res. Atmos., 123, 4345–4372, https://doi.org/https://doi.org/10.1002/2018JD028336, 2018.

McNeill, V. F.: Aqueous Organic Chemistry in the Atmosphere: Sources and Chemical Processing of Organic Aerosols, Environ. Sci. Technol., 49, 1237–1244, https://doi.org/10.1021/es5043707, 2015.

Mohr, C., DeCarlo, P. F., Heringa, M. F., Chirico, R., Slowik, J. G., Richter, R., Reche, C., Alastuey, A., Querol, X., Seco, R., Peñuelas, J., Jiménez, J. L., Crippa, M., Zimmermann, R., Baltensperger, U., and Prévôt, A. S. H.: Identification and quantification of organic aerosol from cooking and other sources in Barcelona using aerosol mass spectrometer data, Atmos. Chem. Phys., 12, 1649–1665, https://doi.org/10.5194/acp-12-1649-2012, 2012.

Mohr, C., Lopez-Hilfiker, F. D., Zotter, P., Prévôt, A. S. H., Xu, L., Ng, N. L., Herndon, S. C., Williams, L. R., Franklin, J. P., Zahniser, M. S., Worsnop, D. R., Knighton, W. B., Aiken, A. C., Gorkowski, K. J., Dubey, M. K., Allan, J. D., and Thornton, J. A.: Contribution of Nitrated Phenols to Wood Burning Brown Carbon Light Absorption in Detling, United Kingdom during Winter Time, Environ. Sci. Technol., 47, 6316–6324, https://doi.org/10.1021/es400683v, 2013.

Ng, N. L., Canagaratna, M. R., Zhang, Q., Jimenez, J. L., Tian, J., Ulbrich, I. M., Kroll, J. H., Docherty, K. S., Chhabra, P. S., Bahreini, R., Murphy, S. M., Seinfeld, J. H., Hildebrandt, L., Donahue, N. M., DeCarlo, P. F., Lanz, V. A., Prévôt, A. S. H., Dinar, E., Rudich, Y., and Worsnop, D. R.: Organic aerosol components observed in Northern Hemispheric datasets from Aerosol Mass Spectrometry, Atmos. Chem. Phys., 10, 4625–4641, https://doi.org/10.5194/acp-10-4625-2010, 2010.

Ng, N. L., Brown, S. S., Archibald, A. T., Atlas, E., Cohen, R. C., Crowley, J. N., Day, D. A., Donahue, N. M., Fry, J. L., Fuchs, H., Griffin, R. J., Guzman, M. I., Herrmann, H., Hodzic, A., Iinuma, Y., Jimenez, J. L., Kiendler-Scharr, A., Lee, B. H., Luecken, D. J., Mao, J., McLaren, R., Mutzel, A., Osthoff, H. D., Ouyang, B., Picquet-Varrault, B., Platt, U., Pye, H. O. T., Rudich, Y., Schwantes, R. H., Shiraiwa, M., Stutz, J., Thornton, J. A., Tilgner, A., Williams, B. J., and Zaveri, R. A.: Nitrate radicals and biogenic volatile organic compounds: oxidation, mechanisms, and organic aerosol, Atmos. Chem. Phys., 17, 2103–2162, https://doi.org/10.5194/acp-17-2103-2017, 2017.

Nguyen, T. B., Lee, P. B., Updyke, K. M., Bones, D. L., Laskin, J., Laskin, A., and Nizkorodov, S. A.: Formation of nitrogen- and sulfur-containing light-absorbing compounds accelerated by evaporation of water from secondary organic aerosols, J. Geophys. Res. Atmos., 117, https://doi.org/https://doi.org/10.1029/2011JD016944, 2012.

Novak, G. A., Fite, C. H., Holmes, C. D., Veres, P. R., Neuman, J. A., Faloona, I., Thornton, J. A., Wolfe, G. M., Vermeuel, M. P., Jernigan, C. M., Peischl, J., Ryerson, T. B., Thompson, C. R., Bourgeois, I., Warneke, C., Gkatzelis, G. I., Coggon, M. M., Sekimoto, K., Bui, T. P., Dean-Day, J., Diskin, G. S., DiGangi, J. P., Nowak, J. B., Moore, R. H., Wiggins, E. B., Winstead, E. L., Robinson, C., Thornhill, K. L., Sanchez, K. J., Hall, S. R., Ullmann, K., Dollner, M., Weinzierl, B., Blake, D. R., and Bertram, T. H.: Rapid cloud removal of dimethyl sulfide oxidation products limits SO2 and cloud condensation nuclei production in the marine atmosphere, Proc. Natl. Acad. Sci., 118, e2110472118, https://doi.org/10.1073/pnas.2110472118, 2021.

Onasch, T. B., Trimborn, A., Fortner, E. C., Jayne, J. T., Kok, G. L., Williams, L. R., Davidovits, P., and Worsnop, D. R.: Soot Particle Aerosol Mass Spectrometer: Development, Validation, and Initial Application, Aerosol Sci. Technol., 46, 804–817, https://doi.org/10.1080/02786826.2012.663948, 2012.

Paatero, P. and Tapper, U.: Positive matrix factorization: A non-negative factor model with optimal utilization of error estimates of data values, Environmetrics, 5, 111–126, https://doi.org/https://doi.org/10.1002/env.3170050203, 1994.

Paglione, M., Gilardoni, S., Rinaldi, M., Decesari, S., Zanca, N., Sandrini, S., Giulianelli, L., Bacco, D., Ferrari, S., Poluzzi, V., Scotto, F., Trentini, A., Poulain, L., Herrmann, H., Wiedensohler, A., Canonaco, F., Prévôt, A. S. H., Massoli, P., Carbone, C., Facchini, M. C., and Fuzzi, S.: The impact of biomass burning and aqueous-phase processing on air quality: a multi-year source apportionment study in the Po Valley, Italy, Atmos. Chem. Phys., 20, 1233–1254, https://doi.org/10.5194/acp-20-1233-2020, 2020.

Pedersen, P. S., Blakemore, D. C., Chinigo, G. M., Knauber, T., and MacMillan, D. W. C.: One-Pot Synthesis of Sulfonamides from Unactivated Acids and Amines via Aromatic Decarboxylative Halosulfonylation, J. Am. Chem. Soc., 145, 21189–21196, https://doi.org/10.1021/jacs.3c08218, 2023.

Peng, J., Hu, M., Shang, D., Wu, Z., Du, Z., Tan, T., Wang, Y., Zhang, F., and Zhang, R.: Explosive Secondary Aerosol Formation during Severe Haze in the North China Plain, Environ. Sci. Technol., 55, 2189–2207, https://doi.org/10.1021/acs.est.0c07204, 2021.

Perri, M. J., Seitzinger, S., and Turpin, B. J.: Secondary organic aerosol production from aqueous photooxidation of glycolaldehyde: Laboratory experiments, Atmos. Environ., 43, 1487–1497, https://doi.org/https://doi.org/10.1016/j.atmosenv.2008.11.037, 2009.

Prabhakar, G., Parworth, C. L., Zhang, X., Kim, H., Young, D. E., Beyersdorf, A. J., Ziemba, L. D., Nowak, J. B., Bertram, T. H., Faloona, I. C., Zhang, Q., and Cappa, C. D.: Observational assessment of the role of nocturnal residual-layer chemistry in determining daytime surface particulate nitrate concentrations, Atmos. Chem. Phys., 17, 14747–14770, https://doi.org/10.5194/acp-17-14747-2017, 2017.

Presto, A. A., Gordon, T. D., and Robinson, A. L.: Primary to secondary organic aerosol: evolution of organic emissions from mobile combustion sources, Atmos. Chem. Phys., 14, 5015–5036, https://doi.org/10.5194/acp-14-5015-2014, 2014.

Price, D. J., Chen, C.-L., Russell, L. M., Lamjiri, M. A., Betha, R., Sanchez, K., Liu, J., Lee, A. K.

Y., and Cocker, D. R.: More unsaturated, cooking-type hydrocarbon-like organic aerosol particle emissions from renewable diesel compared to ultra low sulfur diesel in at-sea operations of a research vessel, Aerosol Sci. Technol., 51, 135–146, https://doi.org/10.1080/02786826.2016.1238033, 2017.

Pusede, S. E., Duffey, K. C., Shusterman, A. A., Saleh, A., Laughner, J. L., Wooldridge, P. J., Zhang, Q., Parworth, C. L., Kim, H., Capps, S. L., Valin, L. C., Cappa, C. D., Fried, A., Walega, J., Nowak, J. B., Weinheimer, A. J., Hoff, R. M., Berkoff, T. A., Beyersdorf, A. J., Olson, J., Crawford, J. H., and Cohen, R. C.: On the effectiveness of nitrogen oxide reductions as a control over ammonium nitrate aerosol, Atmos. Chem. Phys., 16, 2575–2596, https://doi.org/10.5194/acp-16-2575-2016, 2016.

Pye, H. O. T., Nenes, A., Alexander, B., Ault, A. P., Barth, M. C., Clegg, S. L., Collett Jr., J. L., Fahey, K. M., Hennigan, C. J., Herrmann, H., Kanakidou, M., Kelly, J. T., Ku, I.-T., McNeill, V. F., Riemer, N., Schaefer, T., Shi, G., Tilgner, A., Walker, J. T., Wang, T., Weber, R., Xing, J., Zaveri, R. A., and Zuend, A.: The acidity of atmospheric particles and clouds, Atmos. Chem. Phys., 20, 4809–4888, https://doi.org/10.5194/acp-20-4809-2020, 2020.

Qi, L., Chen, M., Stefenelli, G., Pospisilova, V., Tong, Y., Bertrand, A., Hueglin, C., Ge, X., Baltensperger, U., Prévôt, A. S. H., and Slowik, J. G.: Organic aerosol source apportionment in Zurich using an extractive electrospray ionization time-of-flight mass spectrometer (EESI-TOF-MS) – Part 2: Biomass burning influences in winter, Atmos. Chem. Phys., 19, 8037–8062, https://doi.org/10.5194/acp-19-8037-2019, 2019.

Rana, M. S. and Guzman, M. I.: Oxidation of Catechols at the Air–Water Interface by Nitrate Radicals, Environ. Sci. Technol., 56, 15437–15448, https://doi.org/10.1021/acs.est.2c05640, 2022.

Reyes-Villegas, E., Bannan, T., Le Breton, M., Mehra, A., Priestley, M., Percival, C., Coe, H., and Allan, J. D.: Online Chemical Characterization of Food-Cooking Organic Aerosols: Implications for Source Apportionment, Environ. Sci. Technol., 52, 5308–5318, https://doi.org/10.1021/acs.est.7b06278, 2018.

Van Rooy, P., Purvis-Roberts, K. L., Silva, P. J., Nee, M. J., and Cocker, D.: Characterization of secondary products formed through oxidation of reduced sulfur compounds, Atmos. Environ., 256, 118148, https://doi.org/https://doi.org/10.1016/j.atmosenv.2020.118148, 2021.

Sarmah, A. K., Meyer, M. T., and Boxall, A. B. A.: A global perspective on the use, sales, exposure pathways, occurrence, fate and effects of veterinary antibiotics (VAs) in the environment, Chemosphere, 65, 725–759, https://doi.org/https://doi.org/10.1016/j.chemosphere.2006.03.026, 2006.

Simon, L., Favez, O., Petit, J.-E., Canonaco, F., Slowik, J. G., Marchand, C., and Gros, V.: Source apportionment of organic gaseous and particulate compounds using a combined positive matrix factorization approach in summer (2020) in the Paris region (France), Atmos. Environ., 354, 121269, https://doi.org/https://doi.org/10.1016/j.atmosenv.2025.121269, 2025.

Simoneit, B. R. T., Schauer, J. J., Nolte, C. G., Oros, D. R., Elias, V. O., Fraser, M. P., Rogge, W. F., and Cass, G. R.: Levoglucosan, a tracer for cellulose in biomass burning and atmospheric particles, Atmos. Environ., 33, 173–182, https://doi.org/https://doi.org/10.1016/S1352-

2310(98)00145-9, 1999.

Sorooshian, A., Ng, N. L., Chan, A. W. H., Feingold, G., Flagan, R. C., and Seinfeld, J. H.: Particulate organic acids and overall water-soluble aerosol composition measurements from the 2006 Gulf of Mexico Atmospheric Composition and Climate Study (GoMACCS), J. Geophys. Res. Atmos., 112, https://doi.org/https://doi.org/10.1029/2007JD008537, 2007.

Stark, H., Yatavelli, R. L. N., Thompson, S. L., Kimmel, J. R., Cubison, M. J., Chhabra, P. S., Canagaratna, M. R., Jayne, J. T., Worsnop, D. R., and Jimenez, J. L.: Methods to extract molecular and bulk chemical information from series of complex mass spectra with limited mass resolution, Int. J. Mass Spectrom., 389, 26–38, https://doi.org/https://doi.org/10.1016/j.ijms.2015.08.011, 2015.

Stefenelli, G., Pospisilova, V., Lopez-Hilfiker, F. D., Daellenbach, K. R., Hüglin, C., Tong, Y., Baltensperger, U., Prévôt, A. S. H., and Slowik, J. G.: Organic aerosol source apportionment in Zurich using an extractive electrospray ionization time-of-flight mass spectrometer (EESI-TOF-MS) – Part 1: Biogenic influences and day–night chemistry in summer, Atmos. Chem. Phys., 19, 14825–14848, https://doi.org/10.5194/acp-19-14825-2019, 2019.

Sun, P., Farley, R. N., Li, L., Srivastava, D., Niedek, C. R., Li, J., Wang, N., Cappa, C. D., Pusede, S. E., Yu, Z., Croteau, P., and Zhang, Q.: PM2.5 composition and sources in the San Joaquin Valley of California: A long-term study using ToF-ACSM with the capture vaporizer, Environ. Pollut., 292, 118254, https://doi.org/10.1016/j.envpol.2021.118254, 2022.

Sun, P., Wang, J., Liu, Y., Nie, W., Chi, X., Xu, Z., Ge, D., Ren, C., Zhu, C., Huang, X., and Ding, A.: Enhanced Particulate Nitrate Formation in Residual Layer Exacerbates Near-Surface Pollution: Insights From Tethered Airship and Long-Term Ground Measurements, J. Geophys. Res. Atmos., 130, e2024JD042672, https://doi.org/https://doi.org/10.1029/2024JD042672, 2025.

Sun, Y., Du, W., Fu, P., Wang, Q., Li, J., Ge, X., Zhang, Q., Zhu, C., Ren, L., Xu, W., Zhao, J., Han, T., Worsnop, D. R., and Wang, Z.: Primary and secondary aerosols in Beijing in winter: sources, variations and processes, Atmos. Chem. Phys., 16, 8309–8329, https://doi.org/10.5194/acp-16-8309-2016, 2016.

Sun, Y. L., Zhang, Q., Anastasio, C., and Sun, J.: Insights into secondary organic aerosol formed via aqueous-phase reactions of phenolic compounds based on high resolution mass spectrometry, Atmos. Chem. Phys., 10, 4809–4822, https://doi.org/10.5194/acp-10-4809-2010, 2010.

Surratt, J. D., Chan, A. W. H., Eddingsaas, N. C., Chan, M., Loza, C. L., Kwan, A. J., Hersey, S. P., Flagan, R. C., Wennberg, P. O., and Seinfeld, J. H.: Reactive intermediates revealed in secondary organic aerosol formation from isoprene, Proc. Natl. Acad. Sci., 107, 6640–6645, https://doi.org/10.1073/pnas.0911114107, 2010.

Tashmim, L., Porter, W. C., Chen, Q., Alexander, B., Fite, C. H., Holmes, C. D., Pierce, J. R., Croft, B., and Ishino, S.: Contribution of expanded marine sulfur chemistry to the seasonal variability of dimethyl sulfide oxidation products and size-resolved sulfate aerosol, Atmos. Chem. Phys., 24, 3379–3403, https://doi.org/10.5194/acp-24-3379-2024, 2024.

Tong, Y., Qi, L., Stefenelli, G., Wang, D. S., Canonaco, F., Baltensperger, U., Prévôt, A. S. H.,

and Slowik, J. G.: Quantification of primary and secondary organic aerosol sources by combined factor analysis of extractive electrospray ionisation and aerosol mass spectrometer measurements (EESI-TOF and AMS), Atmos. Meas. Tech., 15, 7265–7291, https://doi.org/10.5194/amt-15-7265-2022, 2022.

Ulbrich, I. M., Canagaratna, M. R., Zhang, Q., Worsnop, D. R., and Jimenez, J. L.: Interpretation of organic components from Positive Matrix Factorization of aerosol mass spectrometric data, Atmos. Chem. Phys., 9, 2891–2918, https://doi.org/10.5194/acp-9-2891-2009, 2009.

Volkamer, R., San Martini, F., Molina, L. T., Salcedo, D., Jimenez, J. L., and Molina, M. J.: A missing sink for gas-phase glyoxal in Mexico City: Formation of secondary organic aerosol, Geophys. Res. Lett., 34, https://doi.org/https://doi.org/10.1029/2007GL030752, 2007.

Wang, F., Liu, X., Lv, S., Zhang, S., Wu, C., Liu, S., Lei, Y., Chen, Y., Li, R., and Wang, G.: Increasing role of phenolic oxidative branch in daytime oxidation process of aromatics in Chinese haze period, Sci. Total Environ., 857, 159578, https://doi.org/https://doi.org/10.1016/j.scitotenv.2022.159578, 2023a.

Wang, G., Zhang, R., Gomez, M. E., Yang, L., Levy Zamora, M., Hu, M., Lin, Y., Peng, J., Guo, S., Meng, J., Li, J., Cheng, C., Hu, T., Ren, Y., Wang, Y., Gao, J., Cao, J., An, Z., Zhou, W., Li, G., Wang, J., Tian, P., Marrero-Ortiz, W., Secrest, J., Du, Z., Zheng, J., Shang, D., Zeng, L., Shao, M., Wang, W., Huang, Y., Wang, Y., Zhu, Y., Li, Y., Hu, J., Pan, B., Cai, L., Cheng, Y., Ji, Y., Zhang, F., Rosenfeld, D., Liss, P. S., Duce, R. A., Kolb, C. E., and Molina, M. J.: Persistent sulfate formation from London Fog to Chinese haze, Proc. Natl. Acad. Sci., 113, 13630–13635, https://doi.org/10.1073/pnas.1616540113, 2016.

Wang, J., Li, J., Ye, J., Zhao, J., Wu, Y., Hu, J., Liu, D., Nie, D., Shen, F., Huang, X., Huang, D. D., Ji, D., Sun, X., Xu, W., Guo, J., Song, S., Qin, Y., Liu, P., Turner, J. R., Lee, H. C., Hwang, S., Liao, H., Martin, S. T., Zhang, Q., Chen, M., Sun, Y., Ge, X., and Jacob, D. J.: Fast sulfate formation from oxidation of SO2 by NO2 and HONO observed in Beijing haze, Nat. Commun., 11, 2844, https://doi.org/10.1038/s41467-020-16683-x, 2020.

Wang, J., Ye, J., Zhang, Q., Zhao, J., Wu, Y., Li, J., Liu, D., Li, W., Zhang, Y., Wu, C., Xie, C., Qin, Y., Lei, Y., Huang, X., Guo, J., Liu, P., Fu, P., Li, Y., Lee, H. C., Choi, H., Zhang, J., Liao, H., Chen, M., Sun, Y., Ge, X., Martin, S. T., and Jacob, D. J.: Aqueous production of secondary organic aerosol from fossil-fuel emissions in winter Beijing haze, Proc. Natl. Acad. Sci. U. S. A., 118, 1–6, https://doi.org/10.1073/pnas.2022179118, 2021.

Wang, T., Li, K., Bell, D. M., Zhang, J., Cui, T., Surdu, M., Baltensperger, U., Slowik, J. G., Lamkaddam, H., El Haddad, I., and Prevot, A. S. H.: Large contribution of in-cloud production of secondary organic aerosol from biomass burning emissions, npj Clim. Atmos. Sci., 7, 149, https://doi.org/10.1038/s41612-024-00682-6, 2024.

Wang, Y., Jorga, S., and Abbatt, J.: Nitration of Phenols by Reaction with Aqueous Nitrite: A Pathway for the Formation of Atmospheric Brown Carbon, ACS Earth Sp. Chem., 7, 632–641, https://doi.org/10.1021/acsearthspacechem.2c00396, 2023b.

Xu, W., Kuang, Y., Xu, W., Liu, L., Xu, H., Wang, X., Liu, Y., Cheng, H., Zhang, X., Zhai, M., Liu, C., Liang, L., Zhang, G., Luo, B., Tao, J., Liu, J., Zhao, H., Ren, S., Zhou, G., Liu, P., Xu, X., and Sun, Y.: Efficient Nitrate Formation in Fog Events Implicates Fog Interstitial Aerosols

as Significant Drivers of Atmospheric Chemistry, Environ. Sci. Technol., 58, 22298–22311, https://doi.org/10.1021/acs.est.4c09078, 2024.

Yazdani, A., Takahama, S., Kodros, J. K., Paglione, M., Masiol, M., Squizzato, S., Florou, K., Kaltsonoudis, C., Jorga, S. D., Pandis, S. N., and Nenes, A.: Chemical evolution of primary and secondary biomass burning aerosols during daytime and nighttime, Atmos. Chem. Phys., 23, 7461–7477, https://doi.org/10.5194/acp-23-7461-2023, 2023.

Ye, C., Yuan, B., Lin, Y., Wang, Z., Hu, W., Li, T., Chen, W., Wu, C., Wang, C., Huang, S., Qi, J., Wang, B., Wang, C., Song, W., Wang, X., Zheng, E., Krechmer, J. E., Ye, P., Zhang, Z., Wang, X., Worsnop, D. R., and Shao, M.: Chemical characterization of oxygenated organic compounds in the gas phase and particle phase using iodide CIMS with FIGAERO in urban air, Atmos. Chem. Phys., 21, 8455–8478, https://doi.org/10.5194/acp-21-8455-2021, 2021.

Young, D. E., Kim, H., Parworth, C., Zhou, S., Zhang, X., Cappa, C. D., Seco, R., Kim, S., and Zhang, Q.: Influences of emission sources and meteorology on aerosol chemistry in a polluted urban environment: results from DISCOVER-AQ California, Atmos. Chem. Phys., 16, 5427–5451, https://doi.org/10.5194/acp-16-5427-2016, 2016.

Yu, L., Smith, J., Laskin, A., George, K. M., Anastasio, C., Laskin, J., Dillner, A. M., and Zhang, Q.: Molecular transformations of phenolic SOA during photochemical aging in the aqueous phase: competition among oligomerization, functionalization, and fragmentation, Atmos. Chem. Phys., 16, 4511–4527, https://doi.org/10.5194/acp-16-4511-2016, 2016.

Zare, A., Romer, P. S., Nguyen, T., Keutsch, F. N., Skog, K., and Cohen, R. C.: A comprehensive organic nitrate chemistry: insights into the lifetime of atmospheric organic nitrates, Atmos. Chem. Phys., 18, 15419–15436, https://doi.org/10.5194/acp-18-15419-2018, 2018.

Zaveri, R. A., Shilling, J. E., Fast, J. D., and Springston, S. R.: Efficient Nighttime Biogenic SOA Formation in a Polluted Residual Layer, J. Geophys. Res. Atmos., 125, e2019JD031583, https://doi.org/https://doi.org/10.1029/2019JD031583, 2020.

Zhang, Q., Worsnop, D. R., Canagaratna, M. R., and Jimenez, J. L.: Hydrocarbon-like and oxygenated organic aerosols in Pittsburgh: insights into sources and processes of organic aerosols, Atmos. Chem. Phys., 5, 3289–3311, https://doi.org/10.5194/acp-5-3289-2005, 2005.

Zhang, Q., Jimenez, J. L., Canagaratna, M. R., Allan, J. D., Coe, H., Ulbrich, I., Alfarra, M. R., Takami, A., Middlebrook, A. M., Sun, Y. L., Dzepina, K., Dunlea, E., Docherty, K., DeCarlo, P. F., Salcedo, D., Onasch, T., Jayne, J. T., Miyoshi, T., Shimono, A., Hatakeyama, S., Takegawa, N., Kondo, Y., Schneider, J., Drewnick, F., Borrmann, S., Weimer, S., Demerjian, K., Williams, P., Bower, K., Bahreini, R., Cottrell, L., Griffin, R. J., Rautiainen, J., Sun, J. Y., Zhang, Y. M., and Worsnop, D. R.: Ubiquity and dominance of oxygenated species in organic aerosols in anthropogenically-influenced Northern Hemisphere midlatitudes, Geophys. Res. Lett., 34, https://doi.org/https://doi.org/10.1029/2007GL029979, 2007.

Zhang, Q., Jimenez, J. L., Canagaratna, M. R., Ulbrich, I. M., Ng, N. L., Worsnop, D. R., and Sun, Y.: Understanding atmospheric organic aerosols via factor analysis of aerosol mass spectrometry: a review, Anal. Bioanal. Chem., 401, 3045–3067, https://doi.org/10.1007/s00216-011-5355-y, 2011.

Zhang, X., Liu, H., Cheng, J., Song, W., Wang, H., Zhang, Y., and Wang, X.: Gas-Phase Oxidation

of Guaiacol by NO3 Radicals: Kinetic Measurements and Implications, ACS ES&T Air, 2, 903–910, https://doi.org/10.1021/acsestair.4c00353, 2025.

Zhou, X., Huang, X., Sun, P., Chi, X., Ren, C., Lai, S., Wang, Z., Qi, X., Wang, J., Nie, W., Xu, Z., Huo, J., Fu, Q., and Ding, A.: Fast Secondary Aerosol Formation in Residual Layer and Its Impact on Air Pollution Over Eastern China, J. Geophys. Res. Atmos., 128, e2023JD038501, https://doi.org/https://doi.org/10.1029/2023JD038501, 2023.

4.6 Figures

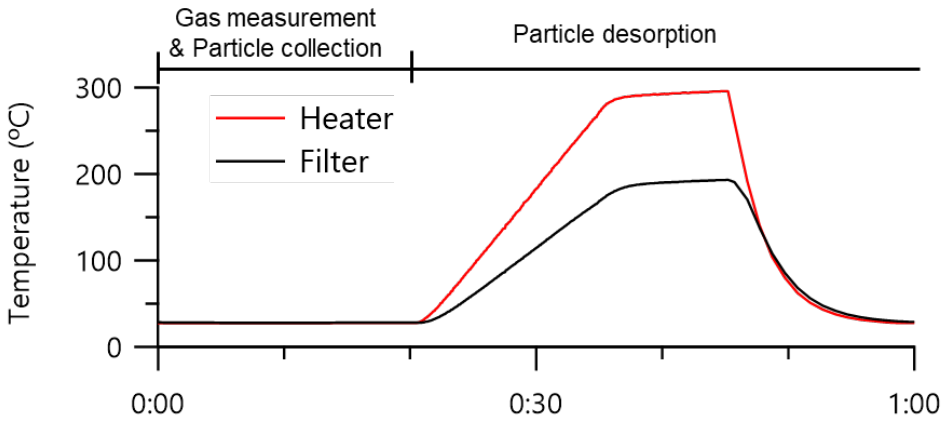

Figure 4-1: Diagram of a FIGAERO cycle and the temperature profile

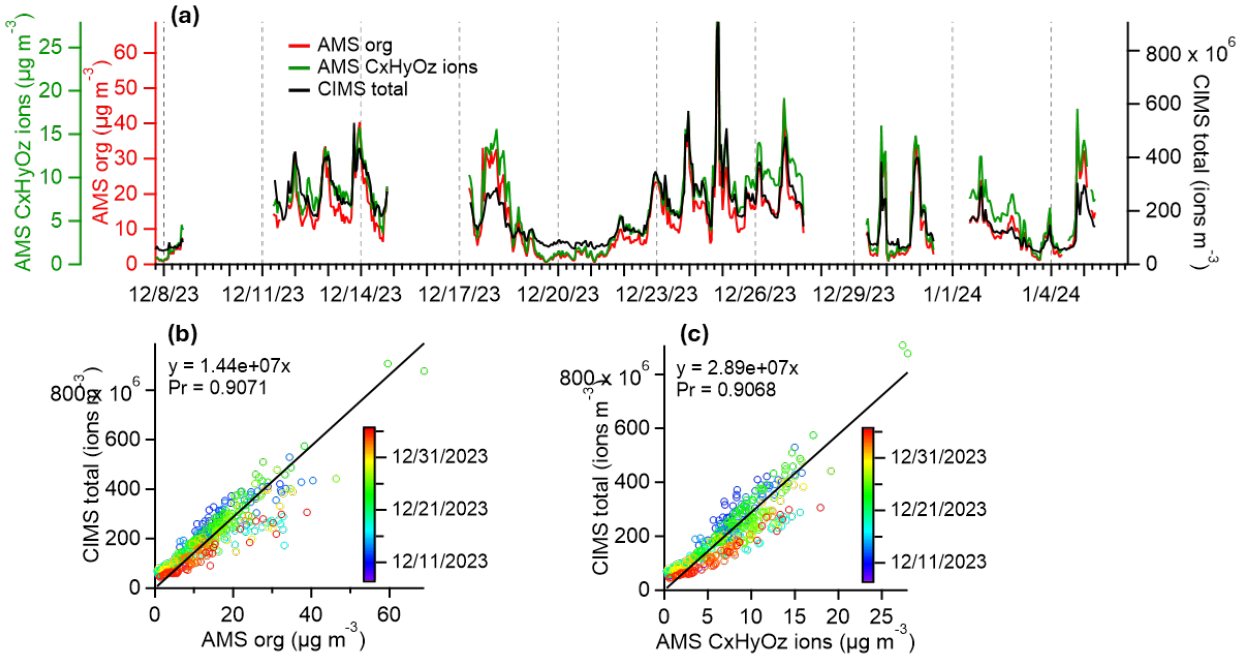

Figure 4-2: (a) Time series of AMS-measured organics and oxygenated organics and total CIMS signal, (b) correlation between CIMS signal and AMS organics, and (c) correlation between CIMS signal and AMS oxygenated organics.

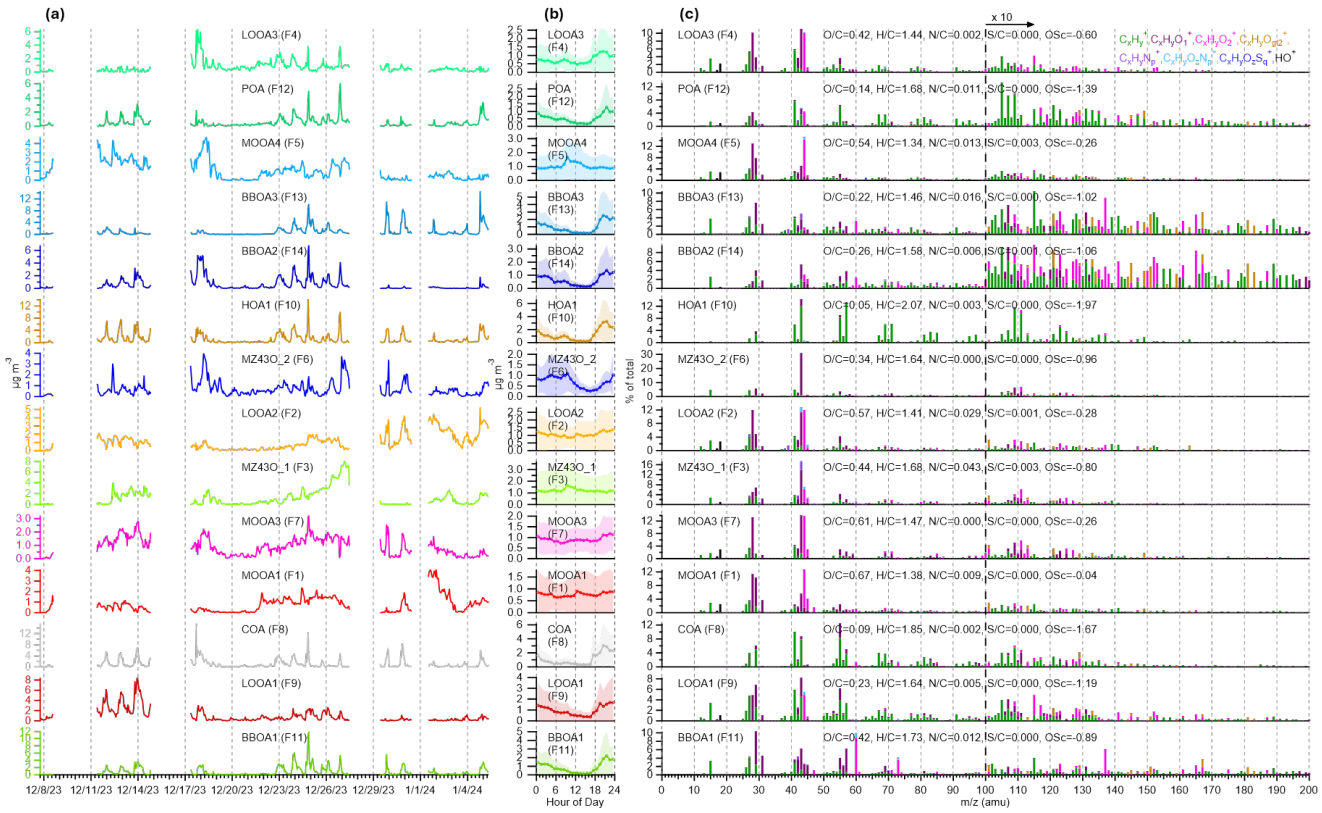

Figure 4-3: 14-factor amsPMF results. (a) time series, (b) diurnal cycles, and (c) AMS profiles of resolved OA factors.

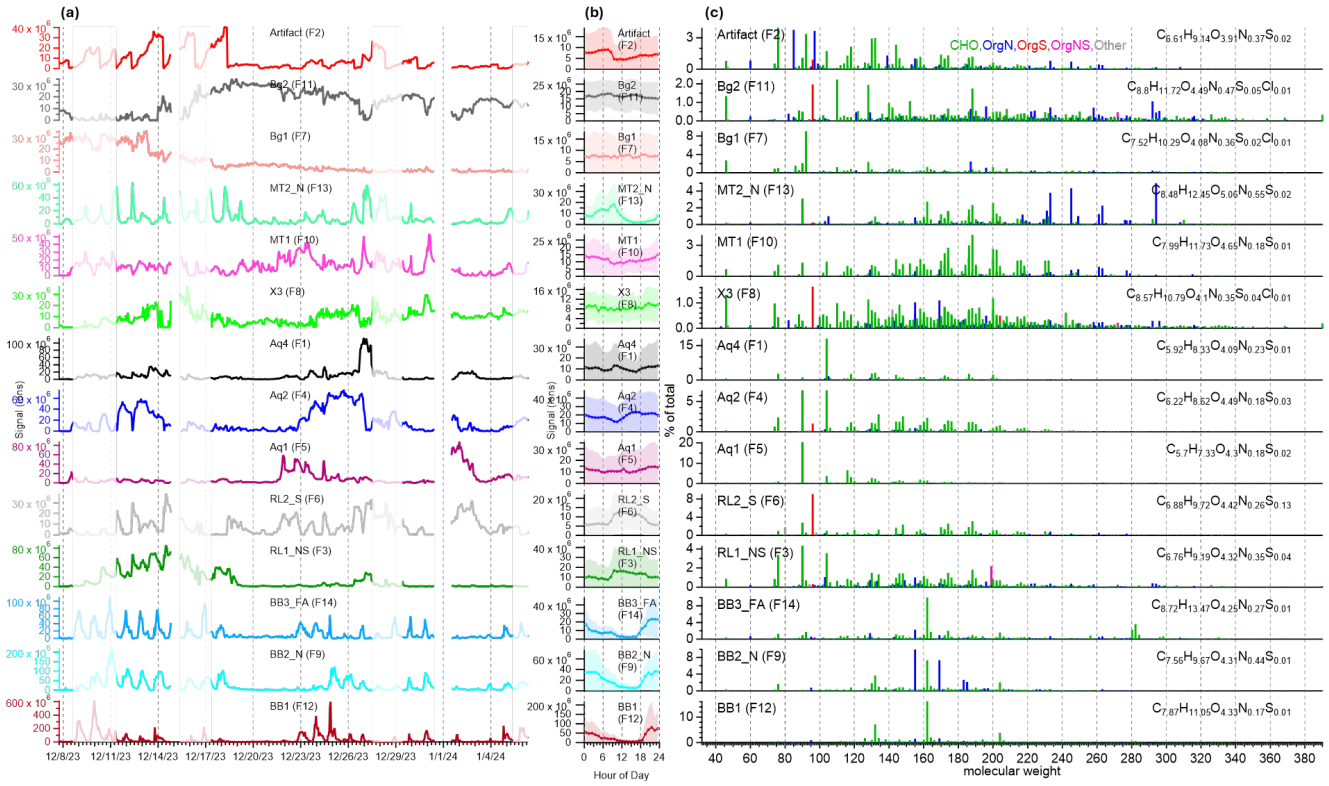

Figure 4-4: 14-factor cimsPMF results. (a) time series, (b) diurnal cycles, and (c) CIMS profiles of resolved OA factors.

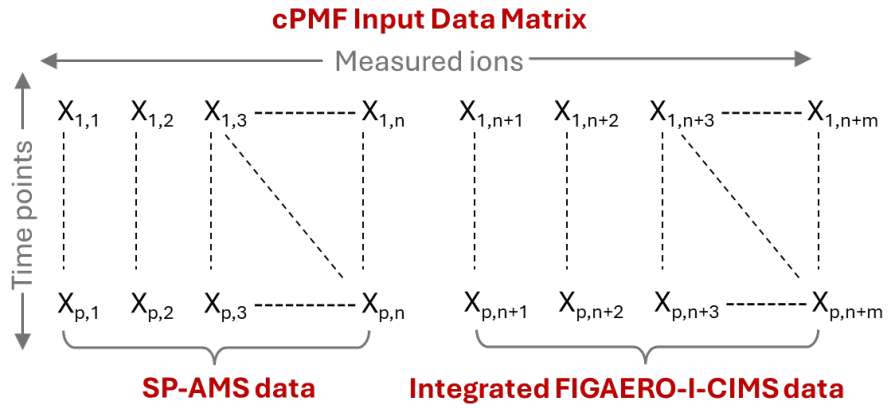

Figure 4-5: Schematics of the combined AMS and CIMS data matrix

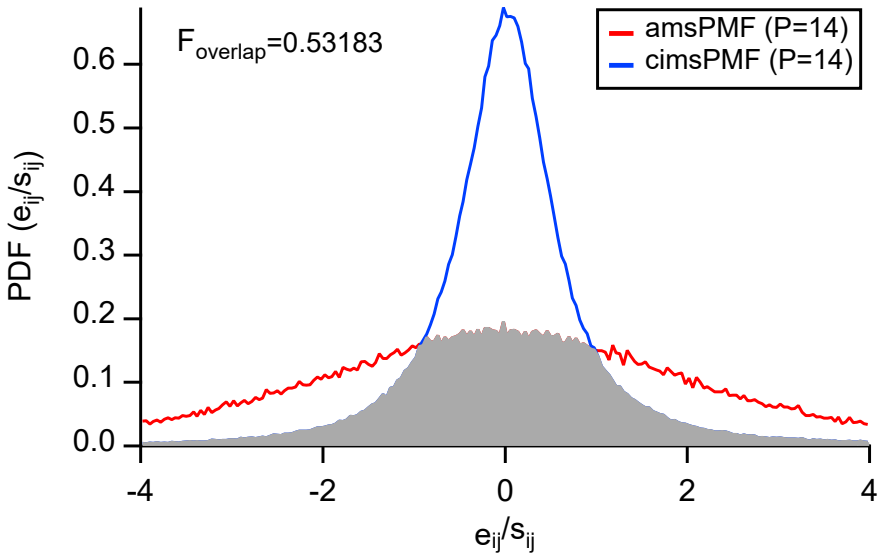

Figure 4-6: Scaled residual probability distributions and region of overlap ($F_{overlap}$) from individual 14-factor amsPMF solution and 14-factor cimsPMF solution.

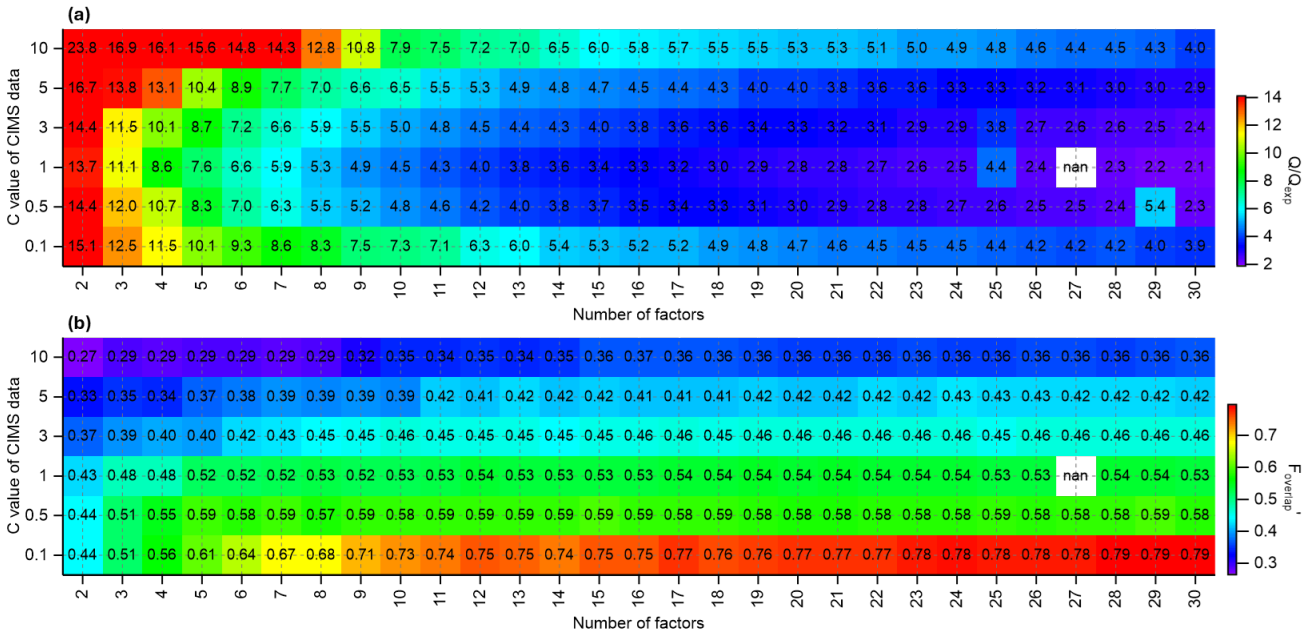

Figure 4-7: (a) Q/Q_{exp} and (b) $F_{overlap}$' obtained from exploratory cPMF runs as a function of C_{CIMS} and number of factors.

	Factors obtained from CIMS-only PMF (P=14)													
	BB1	BB2_N	BB3_FA	RL1_NS	RL2_S	Aq1	Aq2	Aq4	X3	MT1	MT2_N	Bg1	Bg2	Artifact
cPMF (P=18, C_{cims}=1)	✓	✓	✓	✓		✓	✓	✓			✓			
cPMF (P=18, C_{cims}=3)	✓	✓	✓	✓	✓	✓	✓	✓		✓	✓	✓	✓	✓
cPMF (P=19, C_{cims}=1)	✓	✓	✓	✓		✓	✓	✓			✓			
cPMF (P=19, C_{cims}=3)	✓	✓	✓	✓	✓	✓	✓	✓	✓	✓	✓	✓	✓	✓
cPMF (P=20, C_{cims}=1)	✓	✓	✓	✓	✓	✓	✓	✓		✓	✓			
cPMF (P=20, C_{cims}=3)	✓	✓	✓	✓	✓	✓	✓	✓	✓	✓	✓	✓	✓	✓
cPMF (P=21, C_{cims}=1)	✓	✓	✓	✓	✓	✓	✓	✓		✓	✓	✓		✓
cPMF (P=21, C_{cims}=3)	✓	✓	✓	✓	✓	✓	✓	✓	✓	✓	✓	✓	✓	✓
cPMF (P=22, C_{cims}=1)	✓	✓	✓	✓	✓	✓	✓	✓		✓	✓	✓		
cPMF (P=22, C_{cims}=3)	✓	✓	✓	✓	✓	✓	✓	✓	✓	✓	✓	✓	✓	✓
cPMF (P=23, C_{cims}=1)	✓	✓	✓	✓	✓	✓	✓	✓			✓	✓		
cPMF (P=23, C_{cims}=3)	✓	✓	✓	✓	✓	✓	✓	✓	✓	✓	✓	✓	✓	✓
cPMF (P=24, C_{cims}=1)	✓	✓	✓	✓	✓	✓	✓	✓		✓	✓	✓		✓
cPMF (P=24, C_{cims}=3)	✓	✓	✓	✓	✓	✓	✓	✓	✓	✓	✓	✓	✓	✓
cPMF (P=25, C_{cims}=1)	✓	✓	✓	✓	✓	✓	✓	✓		✓	✓	✓		✓
cPMF (P=25, C_{cims}=3)	✓	✓	✓	✓	✓	✓	✓	✓	✓	✓	✓	✓	✓	✓

	Factors obtained from AMS-only PMF (P=14)													
	BBOA1	HOA1	COA	MOOA3	LOOA2	MOOA1	LOOA3	MZ43O_1	LOOA1	MOOA4	MZ43O_2	POA	BBOA3	BBOA2
cPMF (P=18, C_{cims}=1)	✓	✓	✓		✓	✓		✓	✓	✓	✓	✓	✓	✓
cPMF (P=18, C_{cims}=3)	✓	✓				✓		✓	✓	✓	✓		✓	✓
cPMF (P=19, C_{cims}=1)	✓	✓	✓	✓	✓	✓	✓	✓	✓	✓	✓		✓	✓
cPMF (P=19, C_{cims}=3)	✓	✓	✓			✓		✓	✓		✓		✓	✓
cPMF (P=20, C_{cims}=1)	✓	✓	✓		✓	✓		✓	✓	✓	✓		✓	✓
cPMF (P=20, C_{cims}=3)	✓	✓	✓			✓		✓	✓	✓	✓		✓	✓
cPMF (P=21, C_{cims}=1)	✓	✓	✓	✓	✓	✓	✓	✓	✓		✓		✓	✓
cPMF (P=21, C_{cims}=3)	✓	✓	✓			✓		✓	✓	✓	✓		✓	✓
cPMF (P=22, C_{cims}=1)	✓	✓	✓		✓	✓	✓	✓	✓	✓	✓		✓	✓
cPMF (P=22, C_{cims}=3)	✓	✓	✓	✓	✓	✓		✓	✓	✓	✓		✓	✓
cPMF (P=23, C_{cims}=1)	✓	✓	✓		✓	✓		✓	✓	✓	✓	✓	✓	✓
cPMF (P=23, C_{cims}=3)	✓	✓	✓	✓		✓		✓	✓	✓	✓		✓	✓
cPMF (P=24, C_{cims}=1)	✓	✓	✓	✓	✓	✓		✓	✓	✓	✓		✓	✓
cPMF (P=24, C_{cims}=3)	✓	✓	✓			✓		✓	✓		✓		✓	✓
cPMF (P=25, C_{cims}=1)	✓	✓	✓		✓	✓		✓	✓	✓	✓	✓	✓	✓
cPMF (P=25, C_{cims}=3)	✓	✓	✓			✓		✓	✓		✓		✓	✓

Figure 4-8: Identification of amsPMF-resolved and cimsPMF-resolved OA factors in cPMF runs. A check mark indicates that the cPMF factor time series correlates with the corresponding single-instrument factor with Pearson r > 0.70.

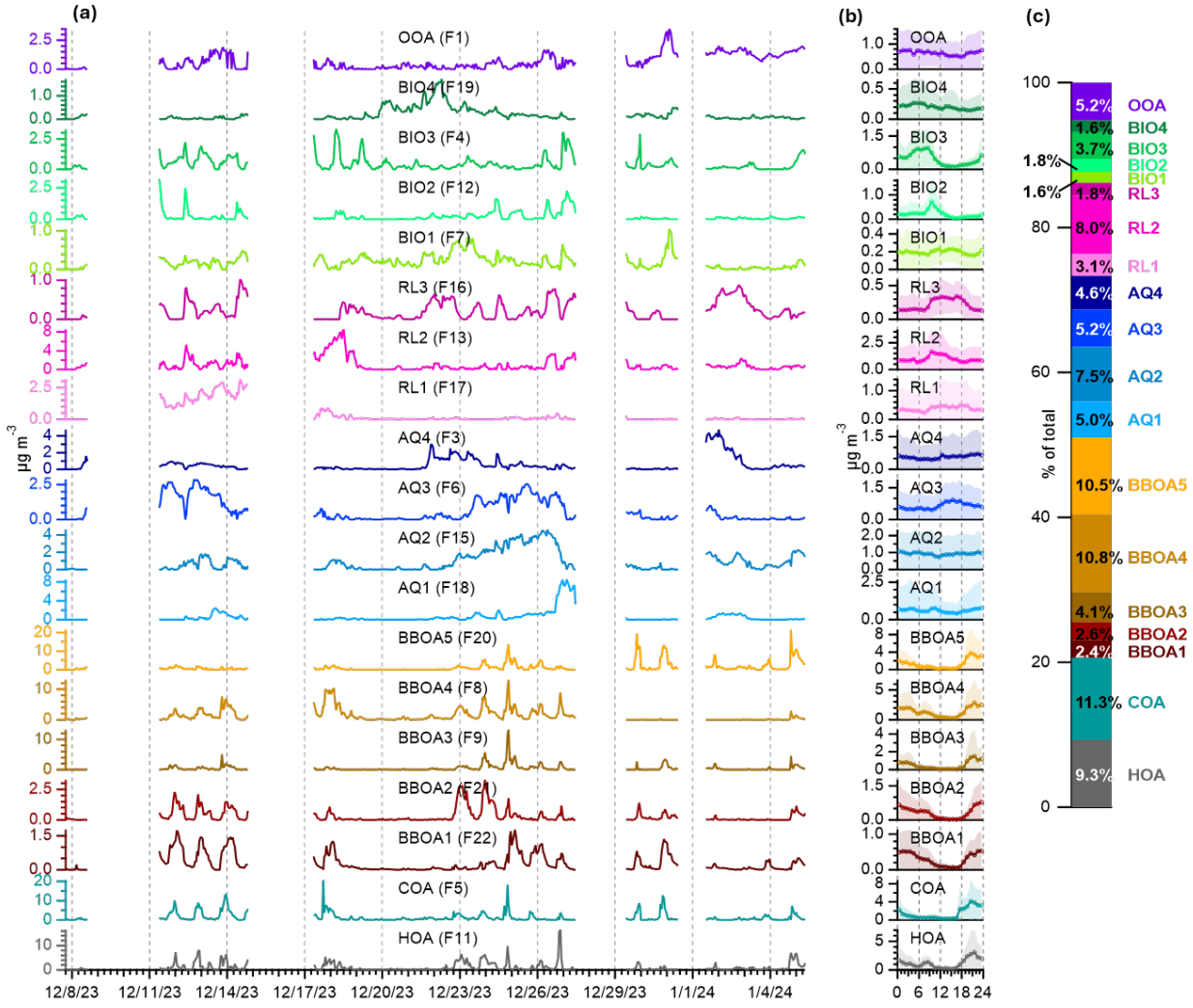
(a)
(b)
(c)
OOA (F1)
BIO4 (F19)
BIO3 (F4)
BIO2 (F12)
BIO1 (F7)
RL3 (F16)
RL2 (F13)
RL1 (F17)
AQ4 (F3)
AQ3 (F6)
AQ2 (F15)
AQ1 (F18)
BBOA5 (F20)
BBOA4 (F8)
BBOA3 (F9)
BBOA2 (F21)
BBOA1 (F22)
COA (F5)
HOA (F11)
μg m-3
12/8/23
12/11/23
12/14/23
12/17/23
12/20/23
12/23/23
12/26/23
12/29/23
1/1/24
1/4/24
0 6 12 18 24
% of total
5.2% OOA
1.6% BIO4
3.7% BIO3
1.8% BIO2
1.6% BIO1
1.8% RL3
8.0% RL2
3.1% RL1
4.6% AQ4
5.2% AQ3
7.5% AQ2
5.0% AQ1
10.5% BBOA5
10.8% BBOA4
4.1% BBOA3
2.6% BBOA2
2.4% BBOA1
11.3% COA
9.3% HOA

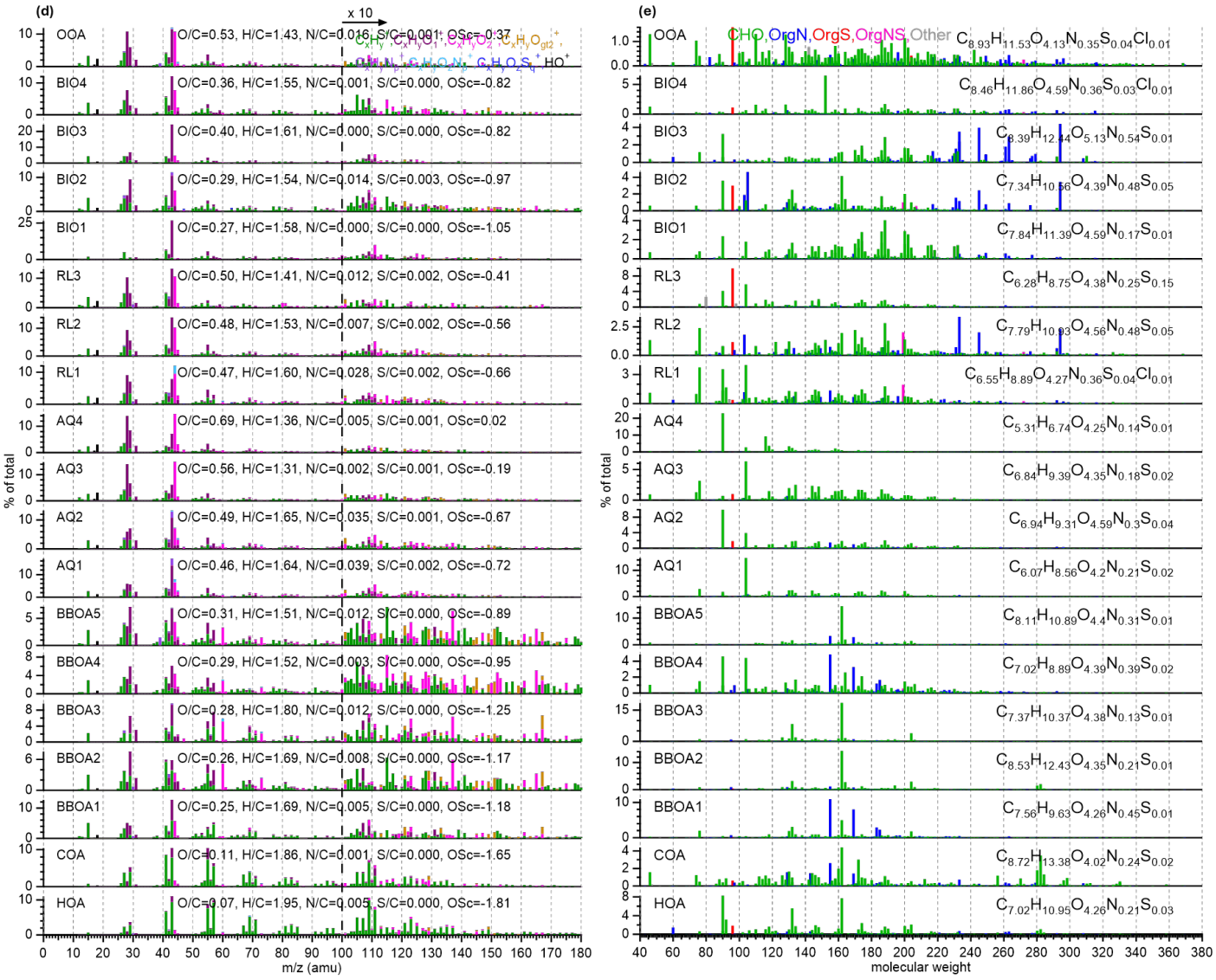

Figure 4-9: cPMF results. (a) Time series, (b) diurnal patterns, (c) factor contributions to total OA concentration, (d) AMS mass spectral profiles, and (e) CIMS mass spectral profiles of all OA factors.

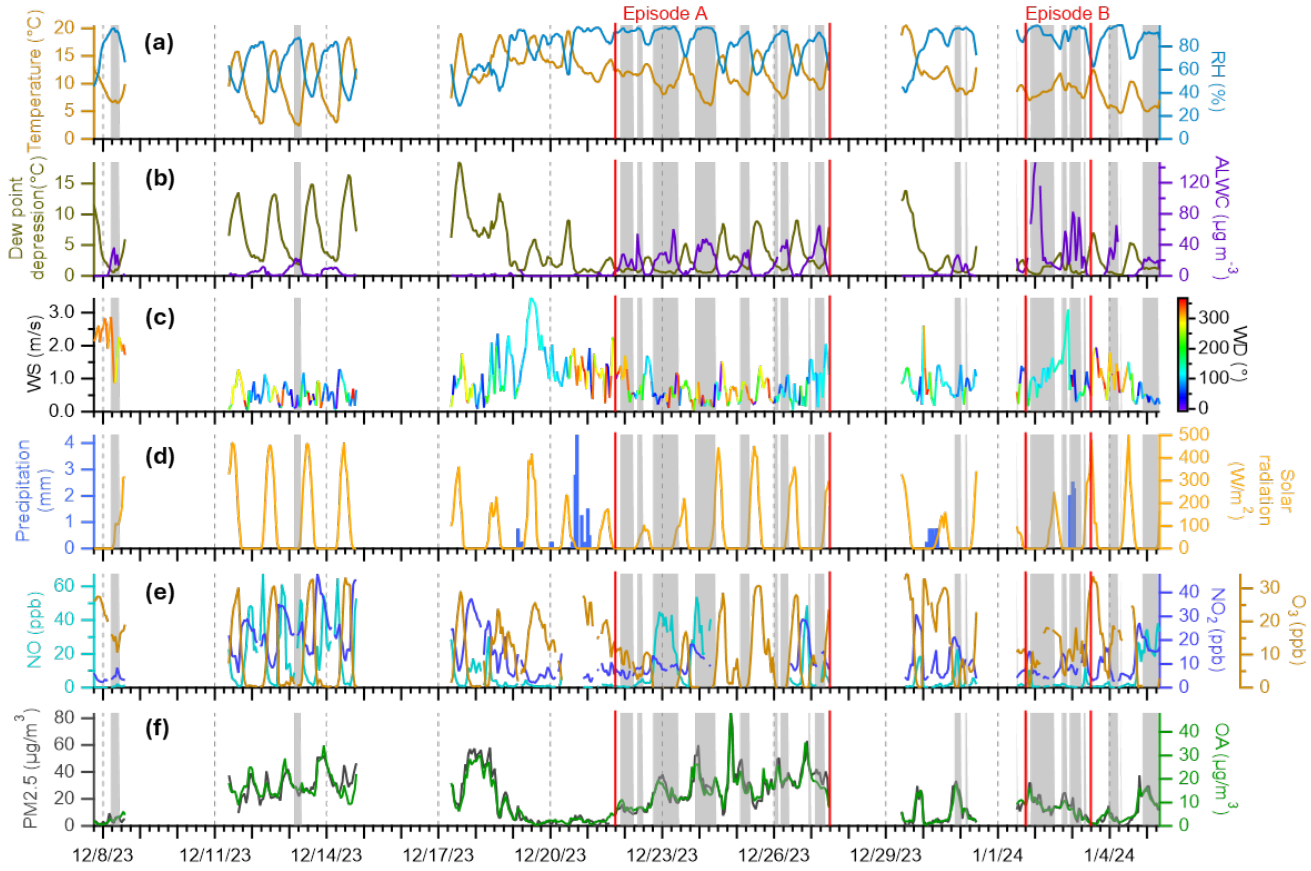

Figure 4-10: Time series of (a) ambient temperature and RH, (b) dew point depression and aerosol liquid water content (ALWC), (c) wind speed colored by wind direction, (d) solar radiation and precipitation, (e) concentrations of NO, NO_2, and O_3, and (e) mass concentrations of $PM_{2.5}$ and AMS-measured organic aerosol (OA). The grey shaded area represents the periods when RH > 85% and dew point depression < 2.5 °C. Episode A and B are the two fog-rich episodes when aqueous processing was enhanced. ALWC was estimated using the Extended Aerosol Inorganic Model (E-AIM) (http://www.aim.env.uea.ac.uk/aim/aim.php) with inputs of ambient temperature, RH, and the concentrations of NH_4^+, NO_3^- and SO_4^{2-} measured by SP-AMS. Because E-AIM model requires neutralized particles, charge balance was achieved by adding H^+ or OH^- as needed. E-AIM Model II was used for RH≤60%, and Model IV was used for RH>60%. Any possible solid formation was disabled in both model calculations.

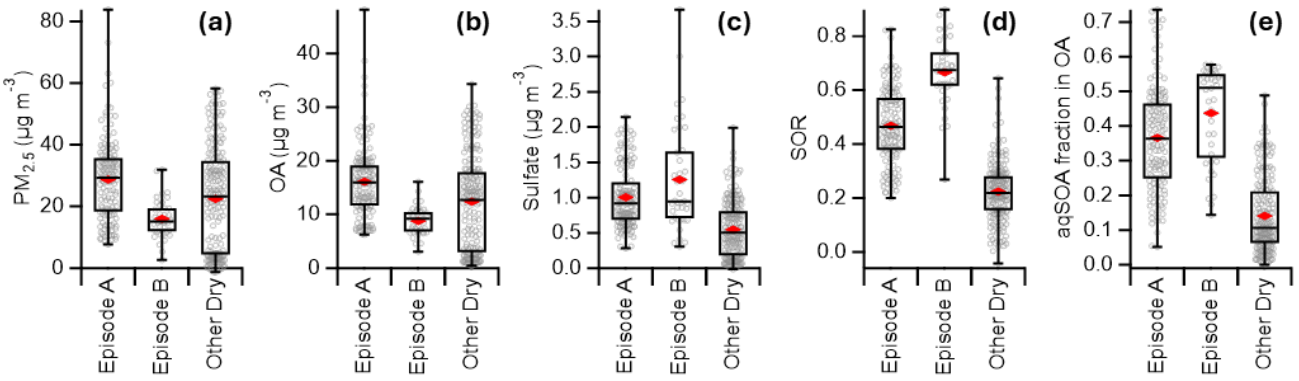

Figure 4-11: Comparison of (a) PM2.5 concentration, (b) organic aerosol concentration, (c) sulfate concentration, (d) sulfur oxidation ratio, and (e) the fractional contribution of aqSOA to the total OA mass between the two foggy episodes and drier periods. Red diamonds indicate the mean for each category.

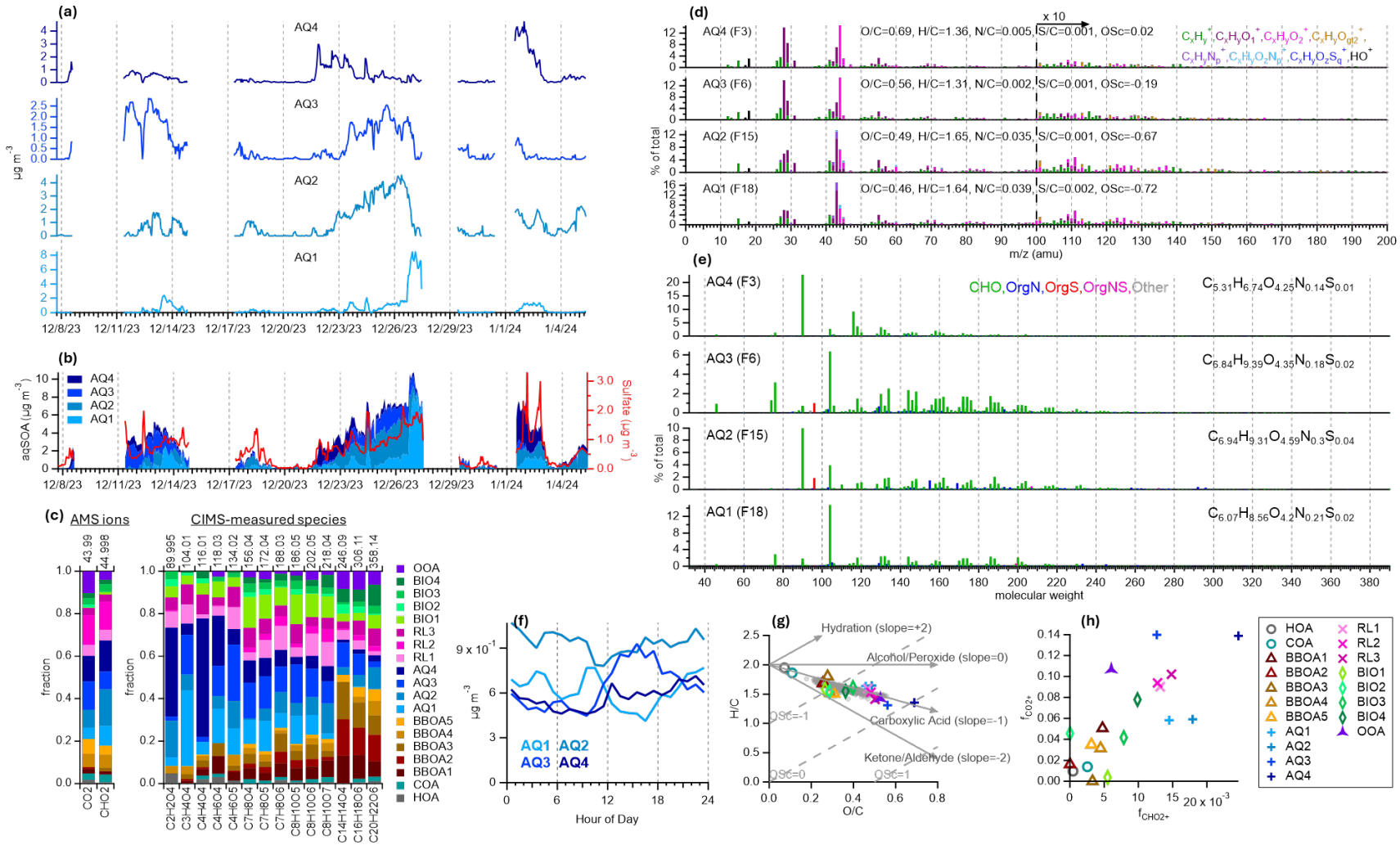

Figure 4-12: cPMF results. (a) Time series of aqSOA factors (AQ1-4), (b) sulfate and stacked aqSOA factors, (c) contributions of all OA factors to selected AMS and CIMS ions, (d) AMS mass spectral profiles of aqSOA factors, (e) CIMS mass spectral profiles of aqSOA factors, (f) diurnal variations of aqSOA factors, (g) Van Krevelen diagram (H/C vs. O/C) for all OA factors, and (h) AMS f_{CO2+} vs. f_{CHO2+} for all OA factors.

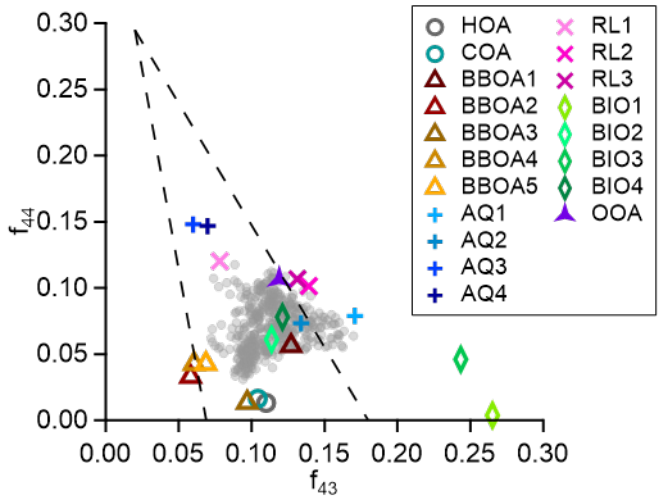

Figure 4-13: Triangle plot (AMS f_{44} vs. f_{43}) for cPMF-resolved OA factors.

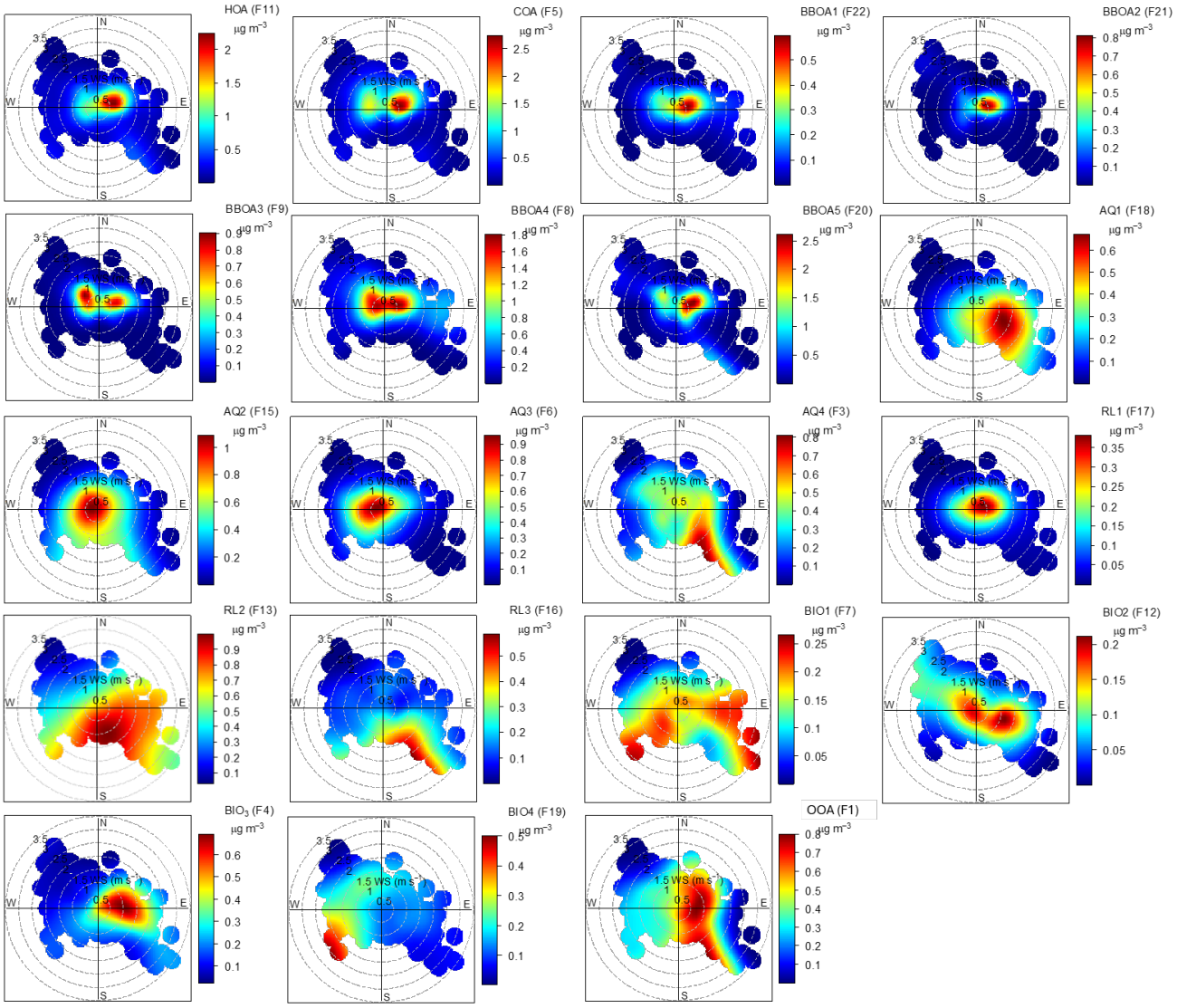

Figure 4-14: Polar plots of cPMF-resolved OA factor concentrations as a function of wind speed and direction.

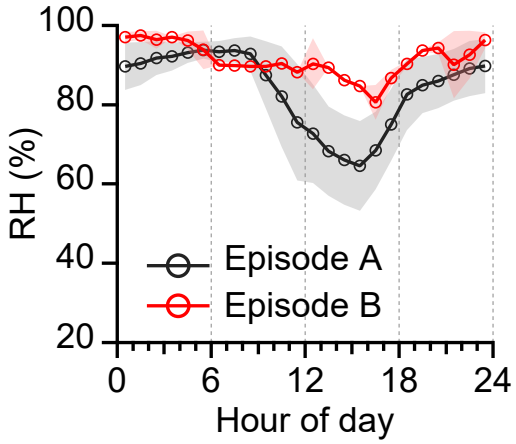

Figure 4-15: Diurnal patterns of RH in fog-rich episodes (e.g., Episode A and B).

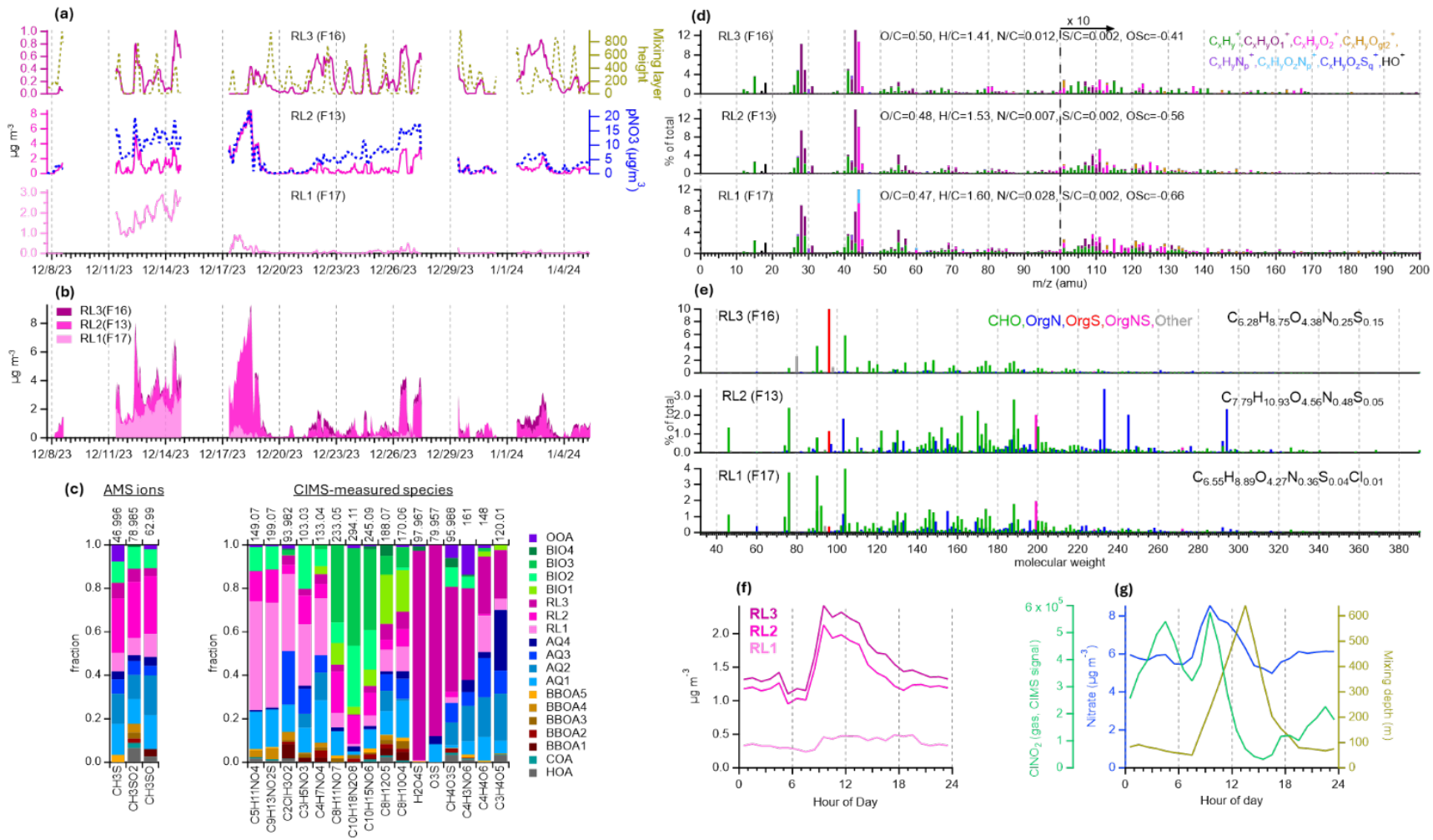

Figure 4-16: cPMF results. (a) Time series of OA factor associated with nocturnal reactions in the residual layer (RL1-3), (b) stacked RL-SOA factors, (c) contributions of all OA factors to selected AMS and CIMS ions, (d) AMS mass spectral profiles of RL-SOA factors, (e) CIMS mass spectral profiles of RL-SOA factors, (f) diurnal variations of RL-SOA factors, and (g) diurnal cycles of nitrate, nitryl chloride, and mixing layer height.

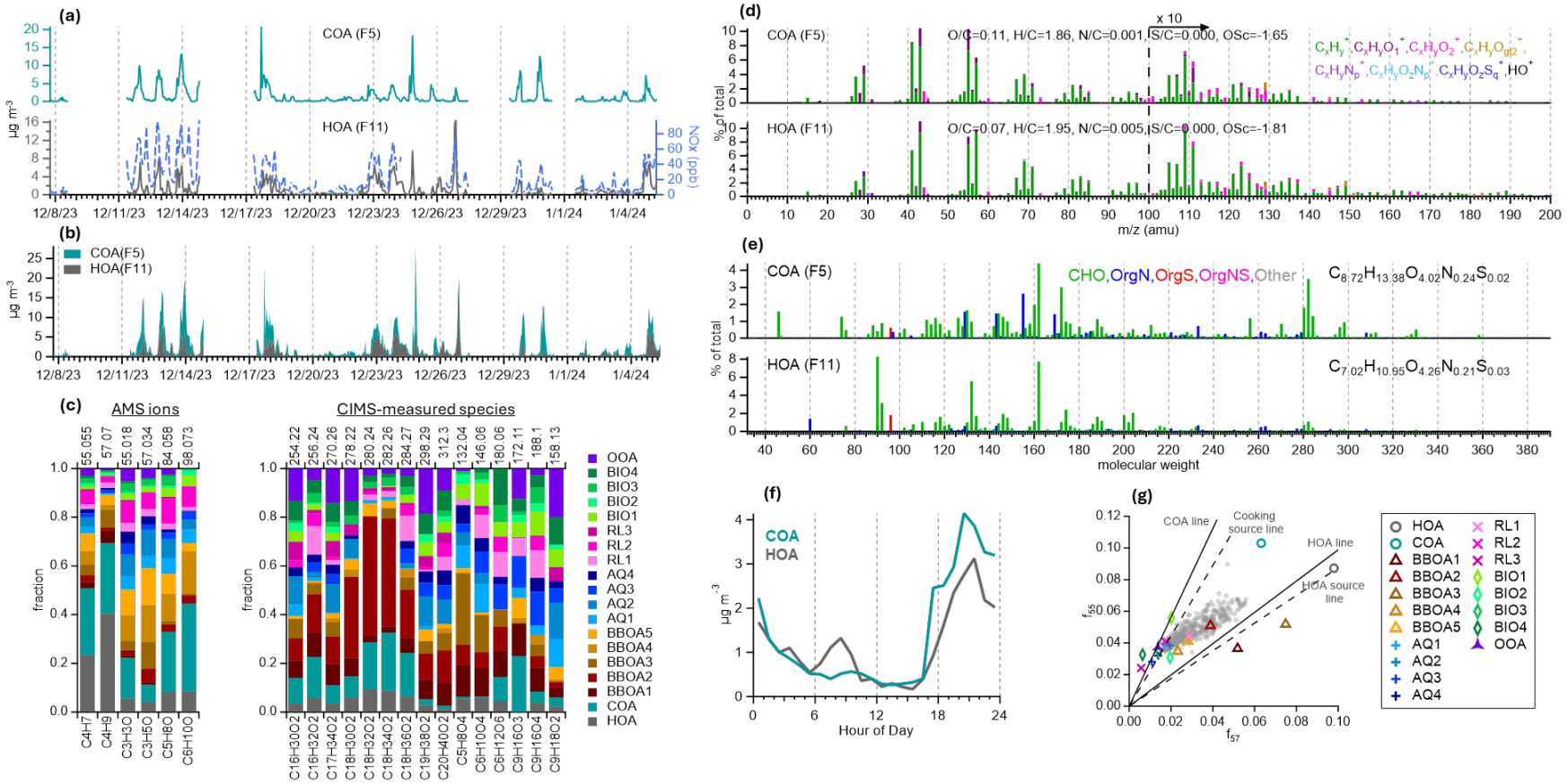

Figure 4-17: cPMF results. (a) Time series of HOA, COA, and NO_x, (b) stacked HOA and COA, (c) contributions of all OA factors to selected AMS and CIMS ions, (d) AMS mass spectral profiles of HOA and COA, (e) CIMS mass spectral profiles of HOA and COA, (f) diurnal variations of HOA and COA, and (g) AMS f_{55} vs. f_{57} for all OA factors.

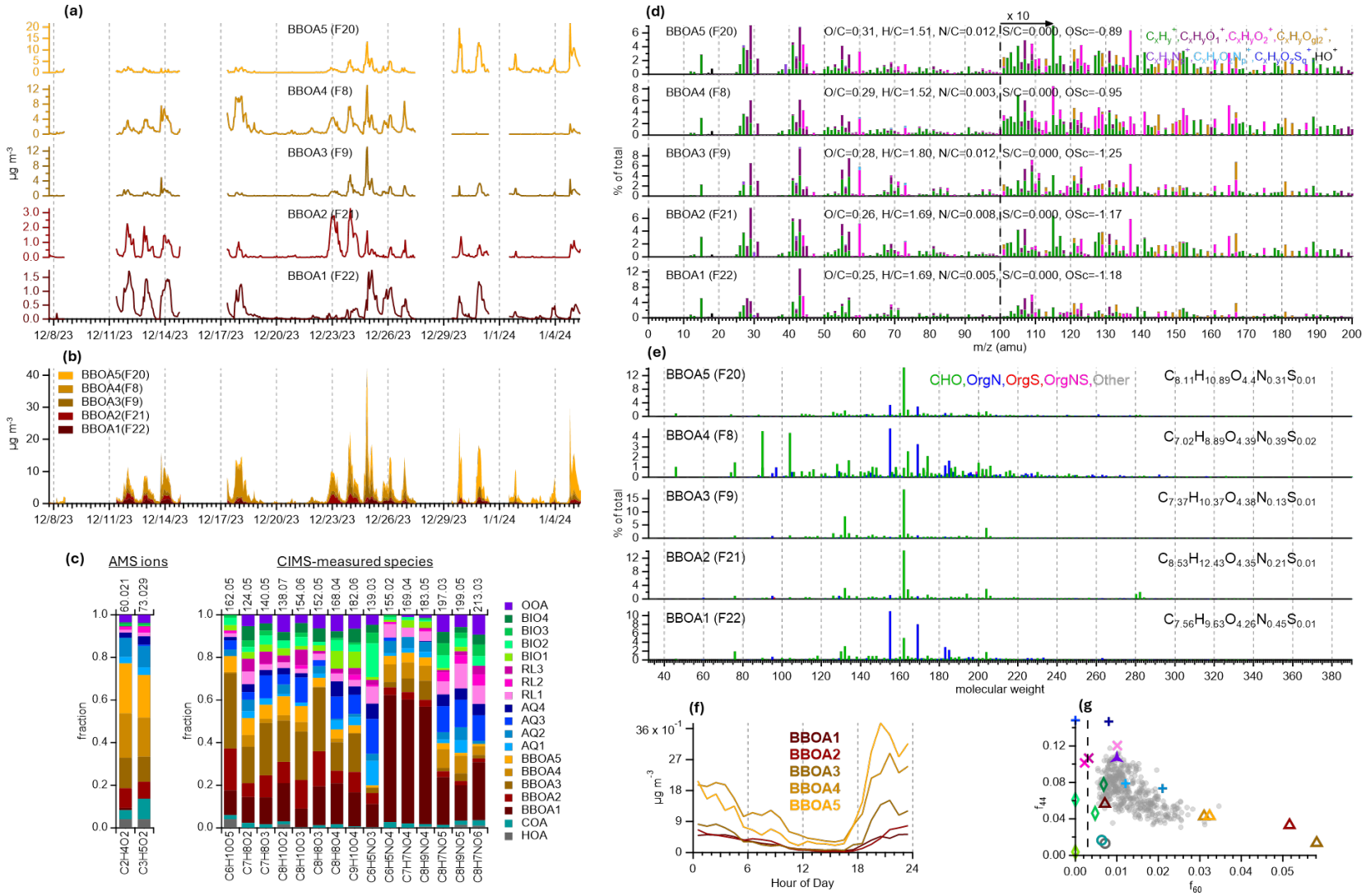

Figure 4-18: cPMF results. (a) Time series of BBOA factors (BBOA1-5), (b) stacked BBOA factors, (c) contributions of all OA factors to selected AMS and CIMS ions, (d) AMS mass spectral profiles of BBOA factors, (e) CIMS mass spectral profiles of BBOA factors, (f) diurnal variations of BBOAs, and (g) AMS f_{44} vs. f_{60} for all OA factors.

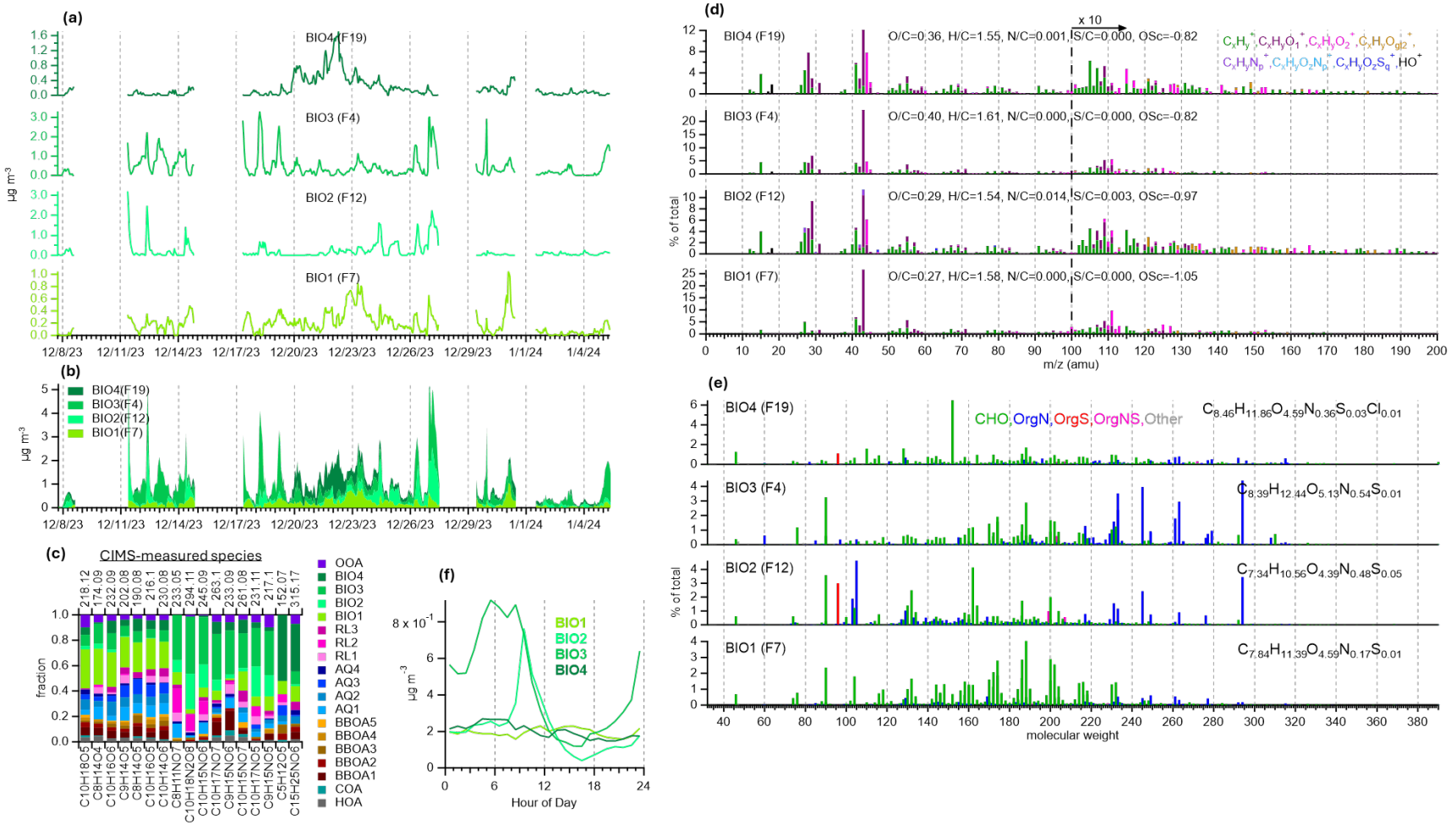

Figure 4-19: cPMF results. (a) Time series of SOA factors related to oxidation of isoprene and monoterpenes (BIO1-4), (b) stacked biogenic SOA factors, (c) contributions of all OA factors to selected AMS and CIMS ions, (d) AMS mass spectral profiles of biogenic SOA factors, (e) CIMS mass spectral profiles of biogenic SOA factors, and (f) diurnal variations of biogenic SOA factors.

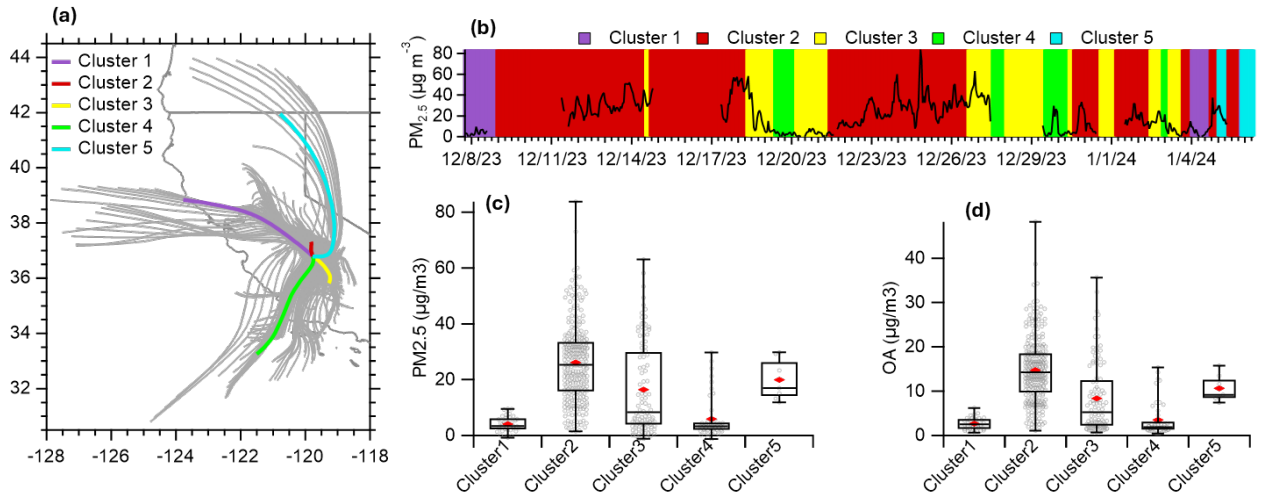

Figure 4-20: (a) 24-h back trajectories arriving at Fresno between 2023-12-7 18:00 and 2024-1-6-8:00. The back trajectories were calculated every 1 h at 100m height using HYSPLIT trajectory model with cluster assignments. (b) Fraction of time dominated by each cluster. (c) $PM_{2.5}$ and (d) OA concentrations associated with different clusters.

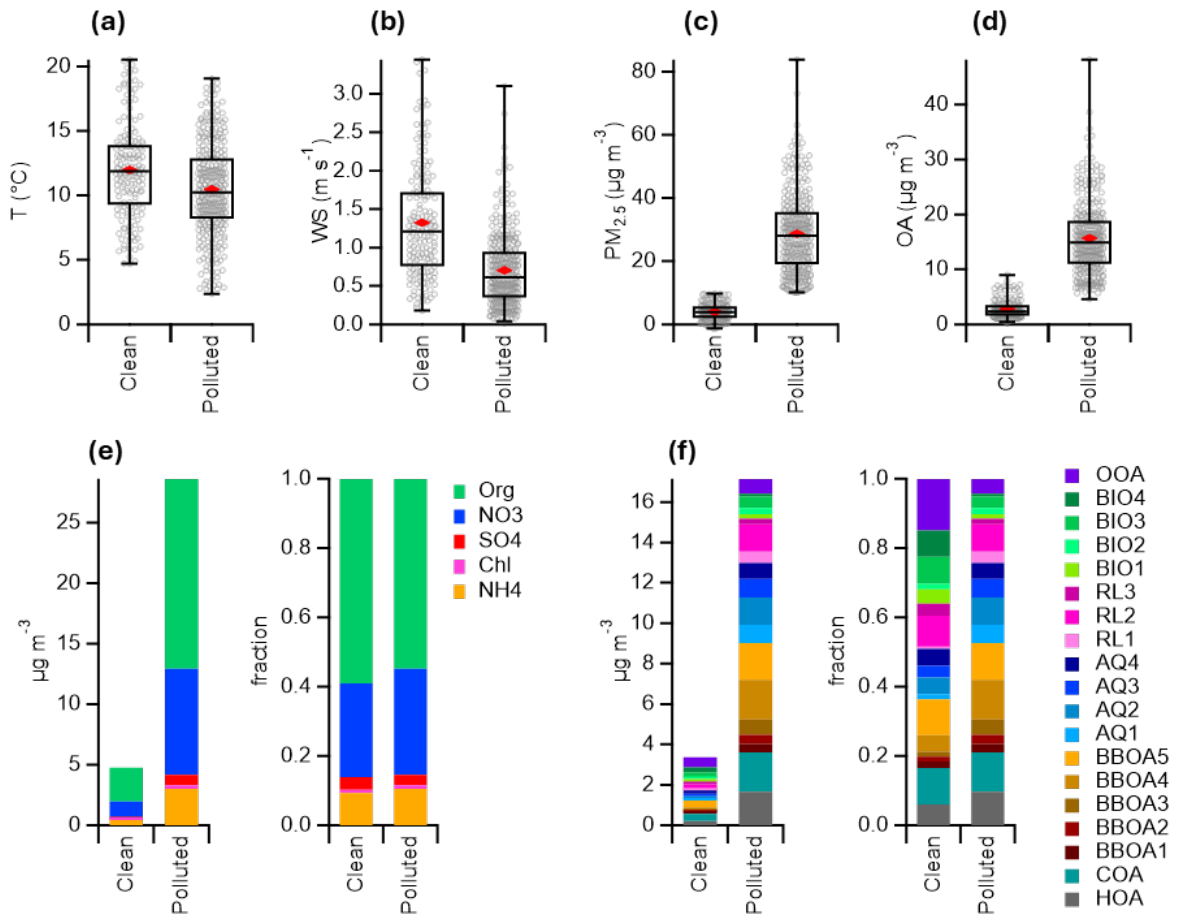

Figure 4-21: Comparison of (a) ambient temperature, (b) wind speed, (c) $PM_{2.5}$ concentration, (d) organic aerosol concentration, (e) aerosol composition (e.g., organics, nitrate, sulfate, chloride, and ammonium), and (f) concentrations and fractional contributions of OA factors between clean and polluted periods.

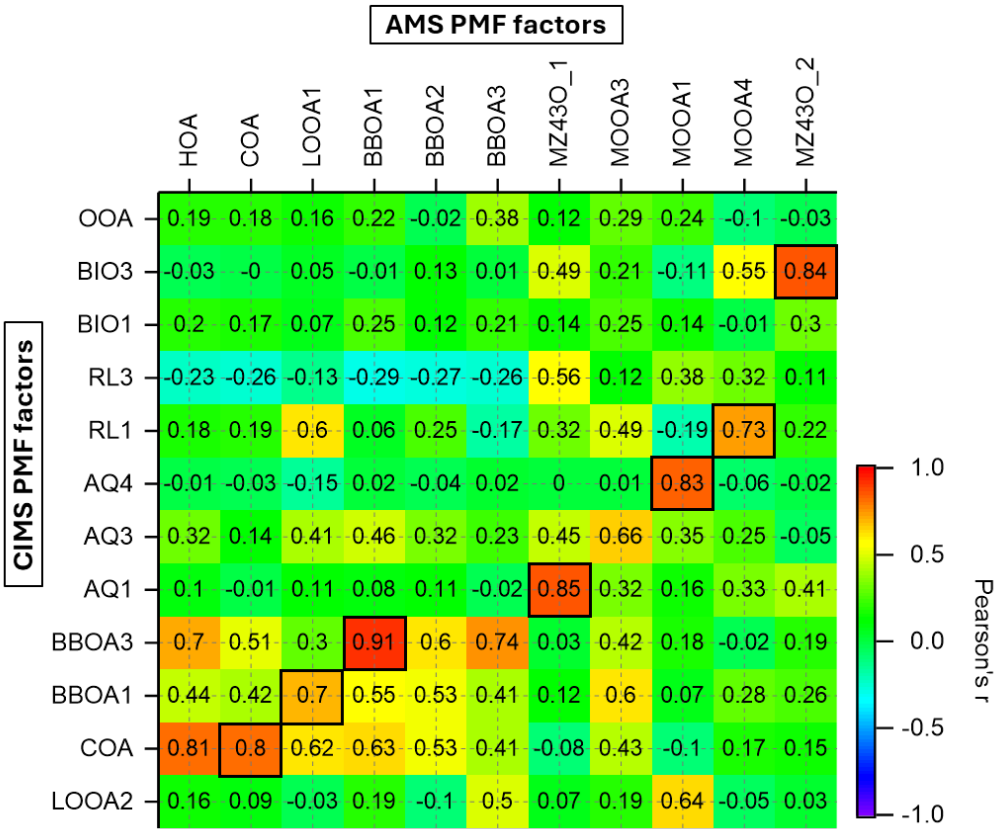

Figure 4-22. Correlations between the time series of amsPMF and cimsPMF resolved factors

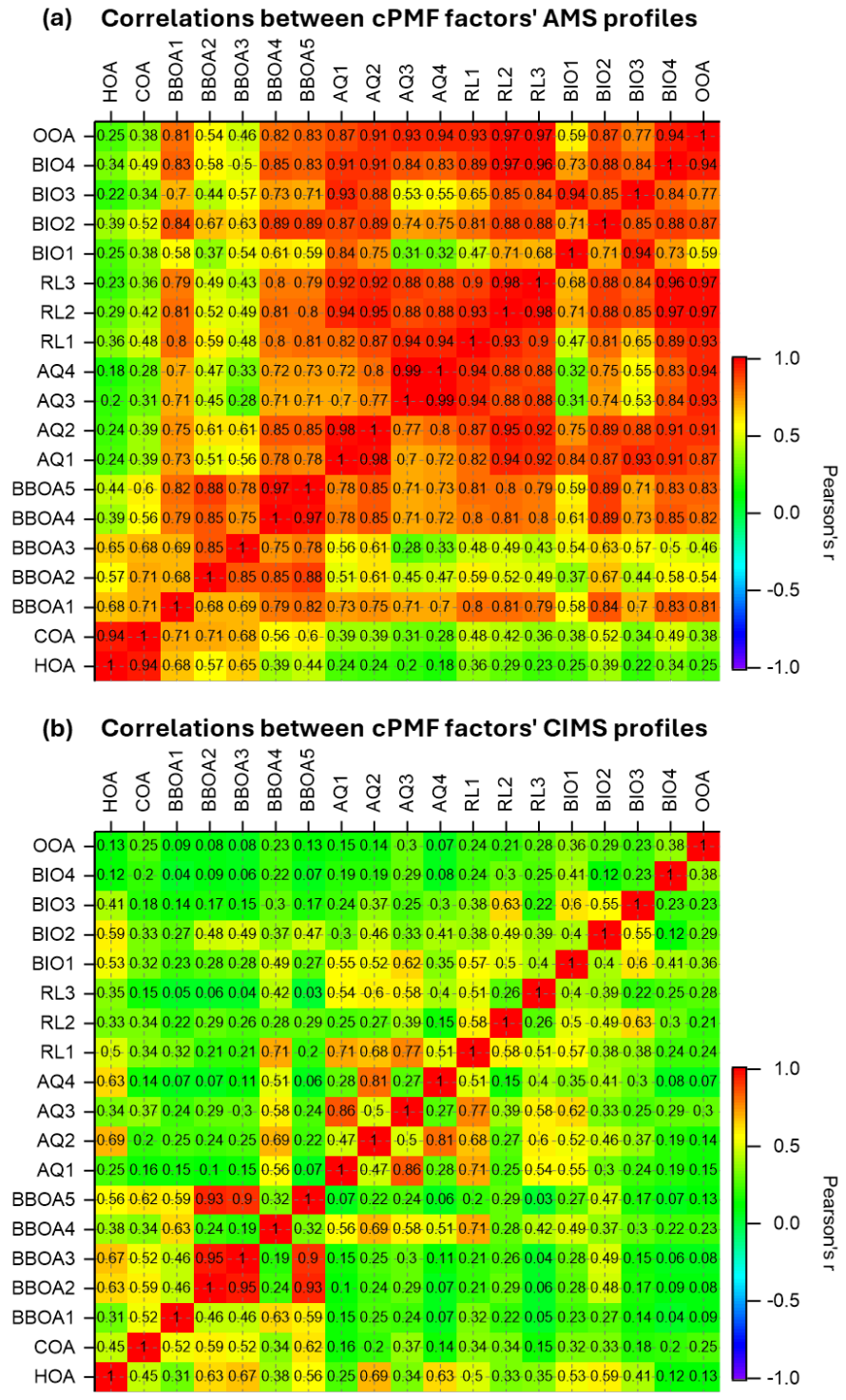

Figure 4-23: Correlations among cPMF factor profiles: (a) AMS profiles and (b) CIMS profiles.

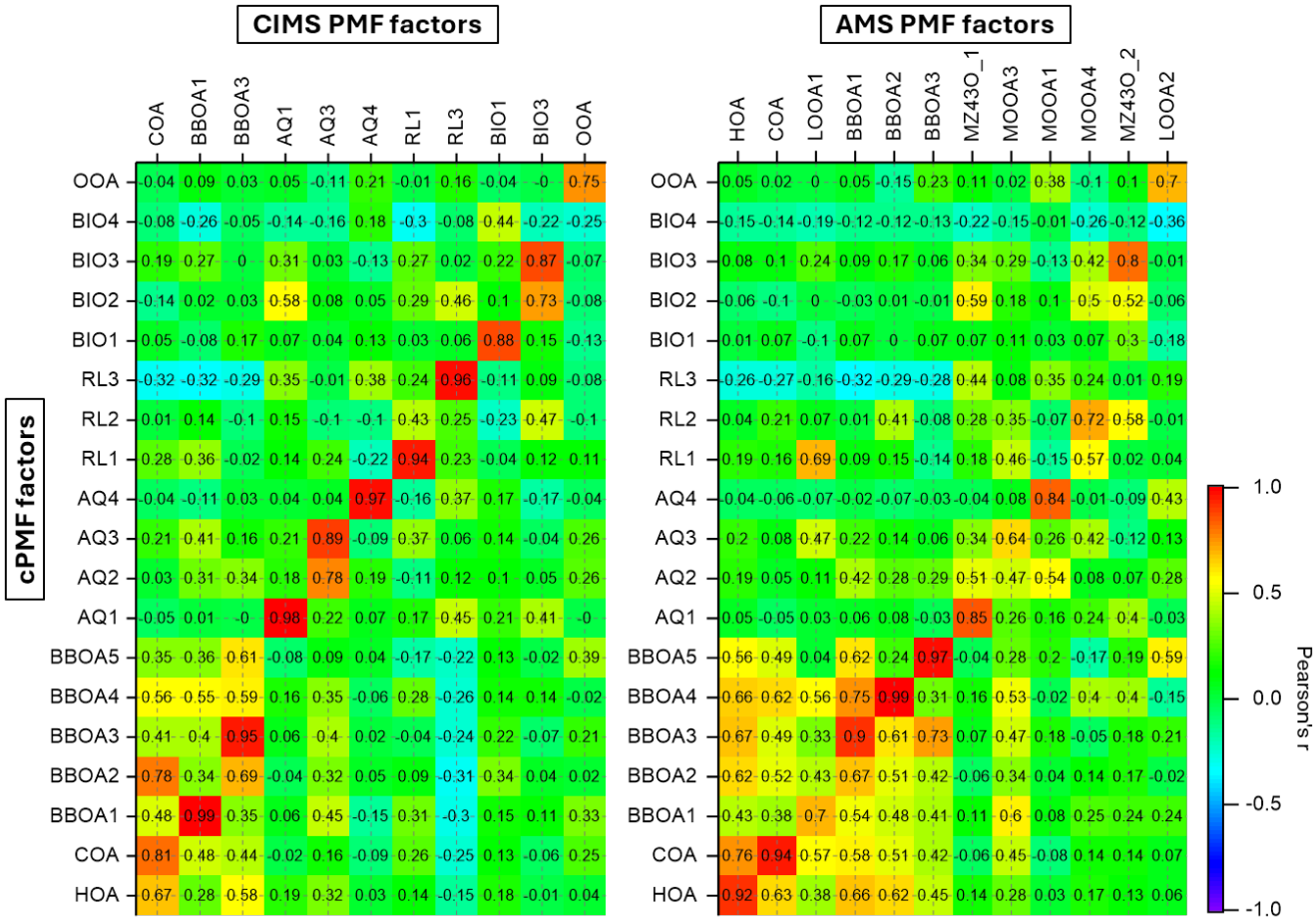

Figure 4-24. Correlations between the time series of cPMF-resolved factors and single-instrument-PMF-resolved factors.

5. IMPROVING WINTERTIME CHARACTERIZATION OF COOKING-RELATED ORGANIC AEROSOL (COA) IN FRESNO USING CHEMICALLY INFORMED SOURCE APPORTIONMENT OF HR-TOF-AMS MEASUREMENTS

5.1 Introduction

Organic aerosol in wintertime urban environments is a complex mixture of primary organic aerosol (POA), directly emitted from sources such as vehicle exhaust, residential and cooking, and biomass burning, and secondary organic aerosol (SOA), formed through atmospheric oxidation of gaseous precursors (Allan et al., 2010; Crippa et al., 2013, 2014; Duan et al., 2004; He et al., 2010; Lanz et al., 2007; Moschos et al., 2016; Ng et al., 2011; Pothier et al., 2023; Shukla et al., 2021; Y. Sun et al., 2016; Zhang et al., 2005, 2011; Zhu et al., 2018). Among POA sources, cooking organic aerosol (COA) has emerged as an increasingly important contributor to urban $PM_{2.5}$, particularly in densely populated regions with extensive residential and commercial cooking activities. Robust quantification of COA is therefore essential for accurate source attribution and for developing effective, source-targeted air quality management strategies.

Previous studies conducted in urban environments worldwide have demonstrated that aerosol mass spectrometry (AMS), combined with positive matrix factorization (PMF), can successfully resolve COA based on its characteristic chemical signature and diurnal behavior (Klein et al., 2019; Liu et al., 2024; Reyes-Villegas et al., 2018; Weitkamp et al., 2008). High-resolution AMS measurements show that COA is enriched in both hydrocarbon fragments and oxygenated ions associated with fatty acids and thermally degraded cooking oils, producing distinctive tracer signals that can differentiate COA from other combustion-related POA sources (Buonanno et al., 2011; Ge, Setyan, et al., 2012; Li et al., 2020; Robinson et al., 2006). In several studies, COA also exhibits pronounced diurnal peaks during meal preparation times, providing a temporal constraint that further aids PMF-based source separation (Mohr et al., 2012). Collectively, these studies suggest that COA can contribute on the order of several to tens of percent of urban submicron OA.

Despite these advances, resolving COA remains challenging in environments due to intense mixing of primary sources and less temporal variability. This challenge is especially pronounced in the SJV during winter. In Fresno, overlapping emissions from vehicle traffic, residential wood burning, agricultural burning, and both residential and commercial cooking occur under conditions of strong nocturnal inversions and suppressed boundary layer heights. These conditions lead to overlapping nighttime concentration increase and substantial covariance among primary sources, reducing the effectiveness of traditional PMF approaches that rely on differences in temporal patterns and chemical profiles to distinguish factors.

As a result, AMS-based source apportionment studies conducted in Fresno have produced inconsistent results with respect to COA. While some winter campaigns successfully resolved substantial COA contributions (Ge, Zhang, et al., 2012; Kim et al., 2019; Young et al., 2016b), other studies conducted at the same location and season were unable to unambiguously identify a

cooking-related factor (Betha et al., 2018; Chen et al., 2018; P. Sun et al., 2022). This inconsistency highlights an important knowledge gap for air quality management in the SJV, where cooking emissions may represent a significant but poorly constrained contributor to wintertime $PM_{2.5}$.

Several factors contribute to this difficulty. First, COA shares substantial spectral overlap with other hydrocarbon-rich POA sources, particularly hydrocarbon-like OA from traffic and certain biomass burning components, reducing spectral contrast in the AMS dataset. Second, atmospheric aging during prolonged stagnation further homogenizes POA chemical signatures, diminishing the distinction between fresh and aged emissions. Third, wintertime nighttime emissions from cooking, traffic, and residential wood burning often peak simultaneously while boundary layer heights collapse, producing nearly identical diurnal profiles that limit PMF's ability to separate sources based on temporal variability alone. Finally, widespread residential cooking emissions, combined with pollutant accumulation under stagnant conditions, yield spatially diffuse and temporally smoothed COA signals that are inherently difficult to isolate.

In this study, we address these challenges by applying a chemically informed, matrix-partitioned PMF framework to high-resolution time-of-flight aerosol mass spectrometer (HR-ToF-AMS) measurements collected during a winter field campaign in Fresno, California. Rather than applying PMF to the full organic mass spectral matrix alone, the AMS organic dataset is separated into two chemically distinct subsets: a hydrocarbon-only matrix composed of $C_xH_y^+$ ions, and a complementary matrix containing oxygen-, nitrogen-, and sulfur-containing organic ions. PMF is performed independently on each subset, enhancing contrast between primary hydrocarbon-rich emissions and more oxidized or aged components and improving the separation of overlapping POA sources.

The insights gained from this partitioned analysis are then integrated with conventional full-matrix PMF results and evaluated using complementary molecular-level measurements from a Filter Inlet for Gases and AEROsols coupled to iodide chemical ionization mass spectrometry (FIGAERO–I-CIMS). This integrated approach provides chemically consistent cross-validation and supports factor interpretation, particularly for cooking-related aerosols.

Using this framework, we successfully resolved two chemically and temporally distinct cooking-related OA factors during winter in Fresno. These results demonstrate that cooking emissions remain a significant contributor to wintertime organic aerosol in the SJV and that their contributions can be robustly identified when chemically targeted source apportionment strategies are employed. Overall, this work improves the characterization of cooking-related $PM_{2.5}$ in a region with persistent air quality challenges and provides a methodological pathway that can support more accurate source attribution and more effective air quality management strategies for the SJV and similar wintertime urban environments.

5.2 Methods

5.2.1 Monitoring site and instrumentation

Site description. The winter field observations were conducted from 8 December 2023 to 6 January 2024 at the California Air Resources Board's Fresno-Garland station (36° 47' 12'' N, 119° 46' 25'' W; 97 m a.s.l.) in Fresno, CA. The site is surrounded by residential neighborhoods and commercial areas and is close to several major highways, representative of urban basins that are influenced by shallow nocturnal inversions, weak ventilation, frequent radiation fog, and strong residential wood burning. Particulate matter was sampled continuously through a $PM_{2.5}$ cyclone and Nafion dryer mounted approximately 1.5 m above the roofline. The inlet flow was maintained at 4.5 L/min, split as 0.1 L/min to the SP-AMS, 4.3 L/min to the FIGAERO perfluorotetrafluoroethylene (PTFE) filter, and 0.1 L/min to the ACSM. Routine meteorological and air-quality data collected at this station include temperature, RH, wind speed and direction, solar radiation, O_3, NO, NO_2, CO, NH_3, SO_2, black carbon, $PM_{2.5}$, and PM_{10}, which provide the environmental context alongside the mass spectrometric measurements.

SP-AMS. A soot particle aerosol mass spectrometer (SP-AMS) was used to characterize the composition of PM_1 species at 2min time resolution (DeCarlo et al., 2006; Onasch et al., 2012). The instrument was operated under "V" ion optical mode. AMS data were processed and analyzed using the standard data analysis toolkits SQUIRREL and PIKA within Igor Pro. Organic aerosol elemental ratios, including the molar ratios of oxygen to carbon (O/C) and hydrogen to carbon (H/C), were calculated using the improved ambient method (Canagaratna et al., 2015).

5.2.2 PMF approach

Source apportionment was performed on the SP-AMS data both separately (CH- and Oxi-PMF) and Full organic matrix (Full-PMF) using positive matrix factorization (PMF) (Paatero and Tapper, 1994). The schematic of the methodology followed for the improved quantification of cooking OA is shown in Figure 5-1. The HR-AMS organic matrix is separated into hydrocarbon-only ($C_xH_y^+$) and oxidized ($C_xH_yO_zN_pS_q^+$) subsets to reduce source overlap and enhance factor separation. The CH- and Oxi-PMF cooking factors were used to guide the Full-PMF especially for quantification of cooking emissions . PMF results are interpreted together with FIGAERO–I-CIMS fatty-acid tracers as well as cPMF factors (described in section 4) to support identification of cooking-related OA .

5.2.2.1 PMF principles

PMF is a bilinear receptor-only model broadly used in atmospheric studies (Ng et al., 2010; Ulbrich et al., 2009; Zhang et al., 2011), which represents the input data matrix as the product of static factor profiles and their time variations, such that

$$X = G \times F + E \qquad \text{(Eq 2)}$$

where X (dimension of m*n) is the input data matrix containing m measurements of n variables, F (dimension of p*n) is a matrix of factor profiles, G (dimension of m*p) is a matrix of factor time series, and E (dimension of m*n) is the residual matrix. Here, p is the number of factors in the PMF solution selected by the user.

PMF solves Eq 2 using a least-squares algorithm that iteratively fits the values of G and F to the input data, minimizing parameter Q, which is the sum of squared uncertainty-weighted residuals (Eq 3).

$$Q = \sum_{i=1}^{m} \sum_{j=1}^{n} \left(\frac{e_{ij}}{s_{ij}}\right)^2 \qquad \text{(Eq 3)}$$

where e_{ij} is an element in the residual matrix E, and s_{ij} is the corresponding element in the uncertainty matrix. The theoretical expectation of Q, denoted Q_{exp}, should equal the degrees of freedom of the fitted data:

$$Q_{exp} = m \times n - p \times (m + n) \qquad \text{(Eq 4)}$$

If the model is appropriate and errors are well characterized, the optimal solution would yield a Q/Q_{exp} near unity. In practice, atmospheric datasets rarely meet all idealized assumptions, so Q/Q_{exp} is typically higher than 1.

For the PMF analysis performed on SP-AMS data, the input high-resolution organic mass spectral and uncertainty matrices were prepared following Ulbrich (2009). Ions with signal-to-noise (S/N) ratio < 0.2 were excluded, and ions with S/N between 0.2 and 2 were downweighed by increasing their uncertainties by a factor of 2. The PMF solution was evaluated using a PMF Evaluation Toolkit (PET v3.08) following the procedures described in Zhang (2011).

5.2.2.2. PMF on partitioned matrices (CH- and Oxi-PMF)

CH-PMF (PMF on $C_xH_y^+$ ions). To reduce the biomass burning interference on cooking factor, we performed PMF on a matrix limited to only $CxHy^+$ ions. BBOA is more strongly influenced by oxidized fragments, while COA is dominated by CH signals. The rotational ambiguity of the solution was explored by varying fPeak values from –0.2 to +0.2. A 12-factor solution was determined to be optimal based on the procedures including physical interpretability of factor profiles, temporal trends, residuals, and diurnal patterns. The CH-PMF solution resolved 2 COA factors, 4 BB factors, 2 HOA factors, 3 MZ41-dominated factors (2 MZ41OA and 1 MOOA1 (Labels are based on correlation with Full-PMF)), and LOOA. Some of the CH-PMF factors were later merged to improve the correlation among the three PMF factor time series. Figure 5-2 summarizes the MS profiles, time series, and diurnal variations of the optimal CH-PMF solution. The CH-PMF helped to resolve two distinct cooking aerosol factors.

Oxi-PMF (PMF on $C_xH_yO^+$, $C_xH_yO_2^+$, $C_xH_yN_p^+$, $C_xH_yS_qO_z^+$ ions). We also performed the PMF on rest of the organic matrix comprising oxygen-, nitrogen-, and sulfur-containing ions (excluding hydrocarbon ions). This Oxi-PMF helped to better isolate secondary and aged OA components and

further combined with CH-PMF to support the selection of final solution in conventional OA PMF (PMF on full organic matrix). A 13-Factor solution was selected based on the procedures including physical interpretability of factor profiles, temporal trends, residuals, and diurnal patterns. The Oxi-PMF solution resolved 1 COA factor, 3 BBOA factors, 2 MZ43OA factors, 3 LOOA and 4 MOOA factors. Some of the Oxi-PMF factors were later merged to improve the correlation among the three PMF factor time series. Figure 5-3 summarizes the MS profiles, time series, and diurnal variations of the optimal Oxi-PMF solution.

5.2.2.3 PMF on full organic matrix (Full-PMF)

To guide the final Full-PMF solution, we followed an extensive framework including: a) The conventional PMF solution selection procedures described by Zhang et al., 2005, b) correlation of factor profiles and timeseries with CH- and Oxi-PMF (shown in Figure 5-4 and 5-5), c) Correlation of factor timeseries with FIGAERO-I-CIMS tracers (shown in Figure 5-6 and 5-7), and d) Correlation analysis with cPMF factors described in section 4 (shown in Figure 5-8 and 5-9). The PMF on SP-AMS organic aerosol (OA) matrix resolved a total of 14 distinct OA factors, comprising six primary and eight secondary factors. The primary factors include one traffic-related factor (HOA), two cooking-related factors (COA1 and COA2), and three biomass burning factors (BBOA1, BBOA2, and BBOA3). The secondary sources consist of three more oxidized organic aerosol factors (MOOA1, MOOA2, and MOOA3) and three less oxidized organic aerosol factors (LOOA1, LOOA2, and LOOA3), and two MZ43-dominated organic aerosol factors (MZ43OA1 and MZ43OA2). These factors exhibit distinct mass spectral signatures, time series, and diurnal behavior, ion series analysis and polar plot-based wind-directional pattern forming a chemically and temporally coherent 14-factor solution (Figure 5-10, 5-11 and 5-12).

5.3 Results and Discussion

5.3.1 Improved COA quantification using CH-PMF and validation from molecular marker measurements

Application of CH-PMF, which isolates hydrocarbon-dominated ions ($C_xH_y^+$), enabled clearer separation of cooking-related organic aerosol from HOA by enhancing contrast between chemically similar primary sources (Figure 5-6), consistent with the approach described by Huang et al. (2021). Within the CH-PMF solution, two distinct cooking factors (COA1 and COA2) were resolved based on differences in their hydrocarbon mass spectral signatures, particularly the m/z 55 to m/z 57 ratio were greater than 1, while HOA it was less than 1, similar ratios were reported in earlier studies, to distinguish between HOA and COA (Figure 5-6a).

External validation using collocated CIMS measurements shows that primary and oxidized cooking tracers from the published literature (Huang et al., 2021) exhibit strong temporal agreement with the two CH-PMF-derived COA factors (Figure 5-6b). Specifically, CIMS fatty acid tracers correlate well with COA1 and COA2 time series, confirming that the CH-PMF framework, supported by molecular-level CIMS information, substantially improves the

quantitative separation of cooking organic aerosols under wintertime conditions. The COA timeseries from the separate PMF (CH- and Oxi-PMF) showed excellent agreement with the total COA (COA1+COA2) from Full-PMF (r=0.99 and slope=1) (Figure 5-13c), indicating the excellent support from CH- and Oxi-PMF to resolve two distinct COA in Full-PMF, overcoming the limitations to resolve cooking.

5.3.2 Conventional Full Organic Matrix PMF (PMFfull) solution

Using this integrated approach, Full-PMF resolved 14 distinct organic aerosol factors, substantially more than typically obtained from conventional AMS-PMF analyses (Figure 5-14), including two cooking organic aerosol (COA) factors (Figure 5.15). The final PMF solutionis constrained by insights from CH-PMF (Figure 5-5), Oxi-PMF (Figure 5-16), CIMS fatty acid tracers (Figure 5-7), and CPMF factors (Figure 5-17). Additional diagnostic analysis, including Van Krevelen analysis (Figure 5-10), carbon-number distributions (Figure 5.11), and polar plots (Figure 5-12), further demonstrate clear chemical, oxidative, and spatial distinctions among the 14 resolved factors by differentiating oxidation pathways, molecular composition, and source influence (Zhang et al., 2005; Mohr et al., 2012) . The characteristics and source apportionment of OA factors will be discussed in brief as they (similar to the CPMF factors) have been already discussed in detail in the previous section 4.

5.3.2.1 Primary organic aerosol factors.

Full-PMF resolved six primary OA factors during wintertime Fresno, including traffic-related HOA, two cooking-related factors (COA1 and COA2), and three biomass-burning-related factors (BBOA1–3) (Figure 5-14).

HOA. The HOA factor is characterized by hydrocarbon-dominated mass spectra, elevated f57 relative to f55 (Figure 5-18), and a pronounced morning rush-hour peak, consistent with fresh vehicular emissions (Presto et al., 2014; Price et al., 2017; Zhang et al., 2005). HOA shows strong agreement with the CPMF HOA factor, with a high time-series correlation (r=0.90) (Figure 5-17), and its detailed chemical composition, diurnal behavior, and source characteristics are discussed extensively in Section 4.3.4.1.

Cooking OA. Cooking emissions are resolved into two Full-PMF factors with similar spectral signatures but differing degrees of oxidation and timing. COA1 exhibits features typical of fresher cooking emissions, while COA2 shows modestly enhanced oxidation and a delayed nighttime maximum (Huang et al., 2021; Mohr et al., 2012). When combined, total Full-PMF COA (COA1 +COA2) shows excellent agreement with the summed CPMF cooking-related contribution (r=0.96) (Figure 5-9). Because cooking aerosol is the primary focus, the detailed chemical and temporal characteristics of COA1 and COA2 are presented separately in the next section, while their CPMF-based interpretation is described in detail in Section 4.3.4.2.

BBOA. Biomass burning emissions are resolved into three distinct Full-PMF factors that show a clear atmospheric processing (Figure 5-10) sequence is consistent with prior studies that show

prevalent residual wood burning in winter Fresno (Chen et al., 2018; Chow et al., 2008; Ge et al., 2012b; Sun et al., 2022; Young et al., 2016). The multiple BBOA factors likely reflect the diversity of burning practices. BBOA1 represents fresher biomass-burning aerosol with strong levoglucosan-related signals and a pronounced nighttime maximum and correlates closely with BBOA3_CPMF (r=0.90) (Figure 5-17). BBOA2 shows reduced levoglucosan influence, a broader diurnal profile, and increased hydrocarbon character, corresponding extremely well with BBOA4_CPMF (r=0.99) (Figure 5-17. BBOA3 is the most processed biomass-burning factor, with minimal levoglucosan signal, enhanced oxidized phenolic fragments, and broader regional influence; it maps robustly to BBOA5_CPMF (r=0.97) (Figure 5-17). The detailed chemical evolution, oxidation pathways, and atmospheric processing of biomass-burning OA are discussed comprehensively in Section 4.3.4.3.

5.3.2.2 Secondary organic aerosol factors.

SPAMS-PMF further resolves eight secondary OA factors reflecting a range of oxidation states and formation pathways, including two m/z 43-dominated OA factors (MZ43OA1–2), three less-oxidized OA factors (LOOA1–3), and three more-oxidized OA factors (MOOA1–3) (Figure 5-14).

M/Z 43-dominated OA. MZ43OA1 is characterized by a highly oxidized but spectrally unique profile and correlates strongly with AQ_CPMF (r=0.90), while MZ43OA2 shows closer association with biogenic-influenced CPMF factors (BIO_CPMF; r=0.83) (Figure 5-8) (Kiendler-Scharr et al., 2009). Although dominated by m/z 43, these factors represent chemically distinct SOA, whose formation mechanisms are discussed in detail in Section 4.3.

LOOA. The three LOOA factors show intermediate oxidation states and semi-volatile behavior. LOOA1 correlates with biomass-burning related CPMF factors (BBOA1_CPMF; r=0.70), indicating partially oxidized combustion influence. LOOA2 aligns with OOA_CPMF (r=0.70) and represents nitrogen-rich oxidized OA formed through sustained secondary processes (Figure 5-17). The atmospheric processing of LOOA1 and LOOA2 is described in detail in Section 4.3. LOOA3 exhibits weaker overall correspondence with CPMF factors but still shows partial agreement with biomass-burning–related CPMF factor, supporting its interpretation as a more aged, regionally influenced oxidized OA derived from combustion emissions (Figure 5-10). Its diurnal cycle peaks in the afternoon, consistent with delayed atmospheric processing relative to LOOA1, and its broad wind-directional pattern suggests transport from multiple source regions. In contrast to LOOA2, nitrogen in LOOA3 is dominated by (m/z 69, $C_3H_3NO^+$), with negligible low m/z CHN or CHNO fragments, indicating incorporation of oxidized heterocyclic nitrogen rather than fresh nitrogenous emissions (Finewax et al., 2018; Mohr et al., 2013). It exhibits broader wind-directional influence and distinct nitrogen speciation, suggesting a more aged, regionally influenced combustion-derived OAFigure 5-12).

MOOA. The three MOOA factors represent more oxidized SOA associated with aqueous-phase processing and residual-layer influenced chemistry. MOOA1 correlates strongly with

AQ4_CPMF (r=0.84) (Figure 5-17) and reflects regionally accumulated aqueous SOA. MOOA2

shows moderate correspondence with AQ3_CPMF (r=0.64) (Figure 5-8), indicating SOA from aqueous OH oxidation of glycolaldehyde (Perri et al., 2009). MOOA3 aligns best with RL2_CPMF (r=0.72) (Figure 5-8). Similar observations of SOA formation have been reported in the polluted residual layer over Sacramento, CA, where anthropogenic nitrate radicals reacted with BVOCs efficiently in the residual layer, comparable to that of daytime oxidation (Zaveri et al., 2020). The chemical composition, formation pathways, and policy-relevant implications of these secondary OA components are discussed extensively in Section 4.3.

5.3.3 Characteristics of two distinct cooking emissions

The two cooking-related organic aerosol (COA) factors resolved in this analysis (COA1 and COA2) display distinct chemical and temporal characteristics that show different types of cooking emissions in the atmosphere. Their mass spectral fingerprints exhibit both overlap and clear divergence; the m/z 55 to m/z 57 ratio (Figure 5-15), a widely used ratio to distinguish between COA and other primary sources such as HOA for distinguishing primary and processed organics (Huang et al., 2021), differ notably between the COA1(~2.5) and COA2(~4.0) (Cash et al., 2021; He et al., 2010; Mohr et al., 2012; Pikmann et al., 2024).

Scatter plots of f55 vs f57 and f67 vs f69 show that the two COA factors are distinct from other primary sources (Figure 5-18) (Pikmann et al., 2024). In the f55 vs f57 scatter plot, COA1 is clearly separated, while COA2 lies closer to other primary factors. In f67 vs f69 space, both COA factors cluster away from HOA and oxygenated factors, indicating different hydrocarbon fragmentation patterns (Klein et al., 2019; Pikmann et al., 2024; Pothier et al., 2023).

Full-PMF COA and CPMF cooking related factors: Comparison of Full-PMF resolved COA factors with cooking-related factors from the Combined PMF (CPMF) shows strong overall consistency (Figure 5-14). In addition, Full-PMF total COA exhibits excellent agreement with the total COA contribution derived from CPMF (COA_CPMF + BBOA2_CPMF), with r=0.95 (Figure 5-9e). Together, these comparisons indicate that both Full-PMF resolved COA factors (COA1 and COA2) are associated with cooking emissions. This is further supported by the strong correlation between COA1_AMS and COA_CPMF (r=0.94) (Figure 5-9c), as well as close agreement in their time series and diurnal profiles, which show similar variation and similar peak timing (Figure 5-8).

In contrast, COA2_AMS shows weaker correlation with BBOA2_CPMF (Figure 5-9d). Time series comparisons indicate partial co-variability, but it is less consistent than for COA1. This behavior likely reflects the mixed nature of BBOA2_CPMF, which is primarily influenced by biomass burning while also containing contributions from fatty acid signals (Figure 4-16), whereas the Full-PMF derived COA factors are more directly associated with cooking emissions. Despite this, the combined COA contribution from Full-PMF closely tracks the summed CPMF cooking-related signal, and diurnal patterns for COA2 still show general consistency with CPMF cooking-related factors, supporting its inclusion as cooking-related emissions in Full-PMF (Figure 5-9).

Full-PMF COA and FIGAERO-I-CIMS tracers: The total cooking organic aerosol (COA) derived from Full-PMF (COA1 + COA2) shows good agreement with the external CIMS total cooking tracer signal, defined as the sum of CIMS cooking tracers ($C_9H_{16}O_4$, $C_{16}H_{32}O_2$, $C_{18}H_{32}O_2$, $C_{18}H_{34}O_2$, $C_{18}H_{36}O_2$), with a correlation coefficient of r=0.81 (Figure 5-7b). This strong correspondence provides independent validation of the SPAMS-derived COA contribution (Huang et al., 2021; Robinson et al., 2006). We investigated the individual fatty acid tracers to further reveal distinct relationships for the two COA factors.

In this study, COA1 exhibits strong temporal agreement with high-molecular-weight fatty acids, particularly oleic acid, supporting its association with primary cooking emissions (Figure 5-7a). In contrast, COA2 shows only weak correlations with azelaic acid, which may partly reflect the higher measurement uncertainties reported for secondary cooking tracers (Huang et al., 2021). Although COA2 displays a higher O:C ratio (Figure 5-10) and a distinct diurnal pattern compared to COA1, it exhibits a delayed peak timing relative to COA1 (Figure 5-19a), consistent with the lagged behavior reported for more processed cooking-related aerosol in Huang et al. (2021). The high m/z 44 signals may be due to rotational ambiguity and the diurnal variation of COA2 does not closely track that of azelaic acid, suggesting that COA2 may reflect a different cooking-related emission pattern rather than a purely secondary cooking aerosol. Polar plot analysis further supports this distinction, with COA2 showing an additional contribution from northwesterly wind directions in addition to the dominant northeasterly influence shared with COA1 (Figure 5-19b) (Pikmann et al., 2024).

5.4. Conclusions and Implications

This study demonstrates that resolving wintertime cooking organic aerosol in a highly polluted urban basin requires an integrated, chemically informed matrix-partitioned PMF based source apportionment framework. By utilizing the matrix-partitioned PMF of HR-AMS data with help from Combined PMF (CPMF) and independent validation using FIGAERO–I-CIMS molecular tracers, we substantially improved separation and interpretation of overlapping primary and secondary OA sources. Partitioning the AMS organic matrix into hydrocarbon-only subsets enhanced contrast among combustion-related emissions and reducing the BBOA interference in cooking emission, while CPMF provided process-level information and CIMS tracers anchored AMS-resolved factors to specific molecular markers.

Within this integrated framework, cooking organic aerosol was robustly resolved into two distinct but related factors that together represent the total cooking contribution in wintertime Fresno. The two COA factors exhibit systematic differences in hydrocarbon fragmentation patterns, m/z 55 to m/z 57 ratios, oxidation state, and diurnal timing, yet remain clearly separated from traffic and other primary sources in diagnostic space. The summed COA timeseries (COA1 + COA2) strongly correlated (r = 0.81) with summed CIMS cooking fatty-acid tracers (including oleic acid, azelaic acid, stearic acid and palmitic acid) supporting both to be associated with cooking emissions. Strong agreement between total SPAMS-derived COA and CPMF cooking-related contributions

(r=0.95), together with independent consistency with CIMS fatty-acid tracers, confirms the cooking origin of both factors despite differences in chemical processing and spatial influence.

Overall, this work shows that integrating chemically targeted PMF, CPMF, and molecular-level CIMS constraints enables robust identification of cooking-related aerosol under conditions of severe source mixing and limited temporal variability. These results highlight cooking emissions as a chemically heterogeneous but significant contributor to wintertime $PM_{2.5}$ in the San Joaquin Valley and provide a methodological pathway for improving OA source attribution in other polluted urban locations, with direct relevance for air quality modeling and management.

5.5. References

Allan, D., Williams, P. I., Morgan, W. T., Martin, C. L., Flynn, M. J., Lee, J., Nemitz, E., Phillips, G. J., Gallagher, M. W., & Coe, H. (2010). Contributions from transport, solid fuel burning and cooking to primary organic aerosols in two UK cities. *Atmospheric Chemistry and Physics*, *10*(2), 647–668. https://doi.org/10.5194/ACP-10-647-2010

Betha, R., Russell, L. M., Chen, C. L., Liu, J., Price, D. J., Sanchez, K. J., Chen, S., Lee, A. K. Y., Collier, S. C., Zhang, Q., Zhang, X., & Cappa, C. D. (2018). Larger Submicron Particles for Emissions With Residential Burning in Wintertime San Joaquin Valley (Fresno) than for Vehicle Combustion in Summertime South Coast Air Basin (Fontana). *Journal of Geophysical Research: Atmospheres*, *123*(18), 10,526-10,545. https://doi.org/10.1029/2017JD026730

Buonanno, G., Johnson, G., Morawska, L., & Stabile, L. (2011). Volatility Characterization of Cooking-Generated Aerosol Particles. *Aerosol Science and Technology*, *45*(9), 1069–1077. https://doi.org/10.1080/02786826.2011.580797

Cash, J. M., Langford, B., Di Marco, C., Mullinger, N. J., Allan, J., Reyes-Villegas, E., Joshi, R., Heal, M. R., Joe Acton, W. F., Nicholas Hewitt, C., Misztal, P. K., Drysdale, W., Mandal, T. K., Gadi, R., Ram Gurjar, B., & Nemitz, E. (2021). Seasonal analysis of submicron aerosol in Old Delhi using high-resolution aerosol mass spectrometry: chemical characterisation, source apportionment and new marker identification. *Atmos. Chem. Phys*, *21*, 10133–10158. https://doi.org/10.5194/acp-21-10133-2021

Chen, C. L., Chen, S., Russell, L. M., Liu, J., Price, D. J., Betha, R., Sanchez, K. J., Lee, A. K. Y., Williams, L., Collier, S. C., Zhang, Q., Kumar, A., Kleeman, M. J., Zhang, X., & Cappa, C. D. (2018). Organic Aerosol Particle Chemical Properties Associated With Residential Burning and Fog in Wintertime San Joaquin Valley (Fresno) and With Vehicle and Firework Emissions in Summertime South Coast Air Basin (Fontana). *Journal of Geophysical Research: Atmospheres*, *123*(18), 10,707-10,731. https://doi.org/10.1029/2018JD028374

Crippa, M., Canonaco, F., Lanz, V. A., Äijälä, M., Allan, J. D., Carbone, S., Capes, G., Ceburnis, D., Dall'Osto, M., Day, D. A., DeCarlo, P. F., Ehn, M., Eriksson, A., Freney, E., Ruiz, L. H.,

Hillamo, R., Jimenez, J. L., Junninen, H., Kiendler-Scharr, A., … Prévôt, A. S. H. (2014). Organic aerosol components derived from 25 AMS data sets across Europe using a consistent ME-2 based source apportionment approach. *Atmospheric Chemistry and Physics*, *14*(12), 6159–6176. https://doi.org/10.5194/acp-14-6159-2014

Crippa, M., Decarlo, P. F., Slowik, J. G., Mohr, C., Heringa, M. F., Chirico, R., Poulain, L., Freutel, F., Sciare, J., Cozic, J., Di Marco, C. F., Elsasser, M., Nicolas, J. B., Marchand, N., Abidi, E., Wiedensohler, A., Drewnick, F., Schneider, J., Borrmann, S., … Baltensperger, U. (2013). Wintertime aerosol chemical composition and source apportionment of the organic fraction in the metropolitan area of Paris. *Atmospheric Chemistry and Physics*, *13*(2), 961–981. https://doi.org/10.5194/acp-13-961-2013

Duan, F., Liu, X., Yu, T., & Cachier, H. (2004). Identification and estimate of biomass burning contribution to the urban aerosol organic carbon concentrations in Beijing. *Atmospheric Environment*, *38*(9), 1275–1282. https://doi.org/10.1016/j.atmosenv.2003.11.037

Ge, X., Setyan, A., Sun, Y., & Zhang, Q. (2012). Primary and secondary organic aerosols in Fresno, California during wintertime: Results from high resolution aerosol mass spectrometry. *Journal of Geophysical Research Atmospheres*, *117*(18). https://doi.org/10.1029/2012JD018026

Ge, X., Zhang, Q., Sun, Y., Ruehl, C. R., & Setyan, A. (2012). Effect of aqueous-phase processing on aerosol chemistry and size distributions in Fresno, California, during wintertime. *Environmental Chemistry*, *9*(3), 221–235. https://doi.org/10.1071/EN11168

He, L. Y., Lin, Y., Huang, X. F., Guo, S., Xue, L., Su, Q., Hu, M., Luan, S. J., & Zhang, Y. H. (2010). Characterization of high-resolution aerosol mass spectra of primary organic aerosol emissions from Chinese cooking and biomass burning. *Atmospheric Chemistry and Physics*, *10*(23), 11535–11543. https://doi.org/10.5194/ACP-10-11535-2010

Huang, D. D., Zhu, S., An, J., Wang, Q., Qiao, L., Zhou, M., He, X., Ma, Y., Sun, Y., Huang, C., Yu, J. Z., & Zhang, Q. (2021). Comparative Assessment of Cooking Emission Contributions to Urban Organic Aerosol Using Online Molecular Tracers and Aerosol Mass Spectrometry Measurements. *Environmental Science and Technology*, *55*(21), 14526–14535. https://doi.org/10.1021/ACS.EST.1C03280/ASSET/IMAGES/LARGE/ES1C03280_0008.JPEG

Kim, H., Collier, S., Ge, X., Xu, J., Sun, Y., Jiang, W., Wang, Y., Herckes, P., & Zhang, Q. (2019). Chemical Processing of Water-Soluble Species and Formation of Secondary Organic Aerosol in Fogs. *Atmospheric Environment*, *200*(August 2018), 158–166. https://doi.org/10.1016/j.atmosenv.2018.11.062

Klein, F., Baltensperger, U., Prévôt, A. S. H., & El Haddad, I. (2019). Quantification of the impact of cooking processes on indoor concentrations of volatile organic species and primary

and secondary organic aerosols. *Indoor Air*, *29*(6), 926–942. https://doi.org/10.1111/INA.12597

Lanz, V. A., Alfarra, M. R., Baltensperger, U., Buchmann, B., Hueglin, C., & Prévôt, A. S. H. (2007). Source apportionment of submicron organic aerosols at an urban site by factor analytical modelling of aerosol mass spectra. *Atmospheric Chemistry and Physics*, *7*(6), 1503–1522. https://doi.org/10.5194/acp-7-1503-2007

Li, J., Forrester, S. M., & Knopf, D. A. (2020). Heterogeneous oxidation of amorphous organic aerosol surrogates by O3, NO3, and OH at typical tropospheric temperatures. *Atmospheric Chemistry and Physics*, *20*(10), 6055–6080. https://doi.org/10.5194/ACP-20-6055-2020

Liu, W., He, L., Liu, Y., Liao, K., Chen, Q., & Kuwata, M. (2024). Suppressed atmospheric chemical aging of cooking organic aerosol particles in wintertime conditions. *Atmos. Chem. Phys*, *24*, 5625–5636. https://doi.org/10.5194/acp-24-5625-2024

Mohr, C., DeCarlo, P. F., Heringa, M. F., Chirico, R., Slowik, J. G., Richter, R., Reche, C., Alastuey, A., Querol, X., Seco, R., Peñuelas, J., Jiḿenez, J. L., Crippa, M., Zimmermann, R., Baltensperger, U., & Prévôt, A. S. H. (2012). Identification and quantification of organic aerosol from cooking and other sources in Barcelona using aerosol mass spectrometer data. *Atmospheric Chemistry and Physics*, *12*(4), 1649–1665. https://doi.org/10.5194/acp-12-1649-2012

Moschos, V., Kumar, N. K., Daellenbach, K. R., Baltensperger, U., Prévôt, A. S. H. H., El Haddad, I., Hayes, P. L., Ortega, A. M., Cubison, M. J., Froyd, K. D., Zhao, Y., Cliff, S. S., Hu, W. W., Toohey, D. W., Flynn, J. H., Lefer, B. L., Grossberg, N., Alvarez, S., Rappenglück, B., … Prévôt, A. S. H. H. (2016). Organic aerosol composition and sources in Pasadena, California, during the 2010 CalNex campaign. *Atmospheric Chemistry and Physics Discussions*, *5*(16), 346–364. https://doi.org/10.5194/acp-2016-621

Ng, N. L., Canagaratna, M. R., Jimenez, J. L., Chhabra, P. S., Seinfeld, J. H., & Worsnop, D. R. (2011). Changes in organic aerosol composition with aging inferred from aerosol mass spectra. *Atmospheric Chemistry and Physics*, *11*(13), 6465–6474. https://doi.org/10.5194/acp-11-6465-2011

Pikmann, J., Drewnick, F., Fachinger, F., & Borrmann, S. (2024). Particulate emissions from cooking: emission factors, emission dynamics, and mass spectrometric analysis for different cooking methods. *Atmos. Chem. Phys*, *24*, 12295–12321. https://doi.org/10.5194/acp-24-12295-2024

Pothier, M. A., Boedicker, E., Pierce, J. R., Vance, M., & Farmer, D. K. (2023). From the HOMEChem frying pan to the outdoor atmosphere: chemical composition, volatility distributions and fate of cooking aerosol. *Environmental Science: Processes & Impacts*, *25*(2), 314–325. https://doi.org/10.1039/D2EM00250G

Reyes-Villegas, E., Bannan, T., Le Breton, M., Mehra, A., Priestley, M., Percival, C., Coe, H., & Allan, J. D. (2018). *Online Chemical Characterization of Food-Cooking Organic Aerosols: Implications for Source Apportionment*. https://doi.org/10.1021/acs.est.7b06278

Robinson, A. L., Subramanian, R., Donahue, N. M., Bernardo-Bricker, A., & Rogge, W. F. (2006). Source apportionment of molecular markers and organic aerosol. 3. Food cooking emissions. *Environmental Science and Technology*, *40*(24), 7820–7827. https://doi.org/10.1021/ES060781P/SUPPL_FILE/ES060781PSI20060912_114127.PDF

Shukla, A. K., Lalchandani, V., Bhattu, D., Dave, J. S., Rai, P., Thamban, N. M., Mishra, S., Gaddamidi, S., Tripathi, N., Vats, P., Rastogi, N., Sahu, L., Ganguly, D., Kumar, M., Singh, V., Gargava, P., & Tripathi, S. N. (2021). Real-time quantification and source apportionment of fine particulate matter including organics and elements in Delhi during summertime. *Atmospheric Environment*, *261*, 118598. https://doi.org/10.1016/J.ATMOSENV.2021.118598

Sun, P., Farley, R. N., Li, L., Srivastava, D., Niedek, C. R., Li, J., Wang, N., Cappa, C. D., Pusede, S. E., Yu, Z., Croteau, P., & Zhang, Q. (2022). PM2.5 composition and sources in the San Joaquin Valley of California: A long-term study using ToF-ACSM with the capture vaporizer. *Environmental Pollution*, *292*, 118254. https://doi.org/10.1016/J.ENVPOL.2021.118254

Sun, Y., Du, W., Fu, P., Wang, Q., Li, J., Ge, X., Zhang, Q., Zhu, C., Ren, L., Xu, W., Zhao, J., Han, T., Worsnop, D. R., & Wang, Z. (2016). Primary and secondary aerosols in Beijing in winter: sources, variations and processes. *Atmospheric Chemistry and Physics*, *16*(13), 8309–8329. https://doi.org/10.5194/acp-16-8309-2016

Weitkamp, E. A., Huff Hartz, K. E., Sage, A. M., Donahue, N. M., & Robinson, A. L. (2008). Laboratory measurements of the heterogeneous oxidation of condensed-phase organic molecular makers for meat cooking emissions. *Environmental Science and Technology*, *42*(14), 5177–5182. https://doi.org/10.1021/ES800181B/SUPPL_FILE/ES800181B-FILE002.PDF

Young, D. E., Kim, H., Parworth, C., Zhou, S., Zhang, X., Cappa, C. D., Seco, R., Kim, S., & Zhang, Q. (2016a). Influences of emission sources and meteorology on aerosol chemistry in a polluted urban environment: results from DISCOVER-AQ California. *Atmos. Chem. Phys*, *16*, 5427–5451. https://doi.org/10.5194/acp-16-5427-2016

Zhang, Q., Jimenez, J. L., Canagaratna, M. R., Ulbrich, I. M., Ng, N. L., Worsnop, D. R., & Sun, Y. (2011). Understanding atmospheric organic aerosols via factor analysis of aerosol mass spectrometry: A review. *Analytical and Bioanalytical Chemistry*, *401*(10), 3045–3067. https://doi.org/10.1007/s00216-011-5355-y

Zhang, Q., Rami Alfarra, M., Worsnop, D. R., Allan, J. D., Coe, H., Canagaratna, M. R., & Jimenez, J. L. (2005). Deconvolution and quantification of hydrocarbon-like and oxygenated

organic aerosols based on aerosol mass spectrometry. *Environmental Science and Technology*, *39*(13), 4938–4952. https://doi.org/10.1021/es0485681

Zhu, Q., Huang, X. F., Cao, L. M., Wei, L. T., Zhang, B., He, L. Y., Elser, M., Canonaco, F., Slowik, J. G., Bozzetti, C., El-Haddad, I., & Prévôt, A. S. H. (2018). Improved source apportionment of organic aerosols in complex urban air pollution using the multilinear engine (ME-2). *Atmospheric Measurement Techniques*, *11*(2), 1049–1060. https://doi.org/10.5194/amt-11-1049-2018

5.6 Figures

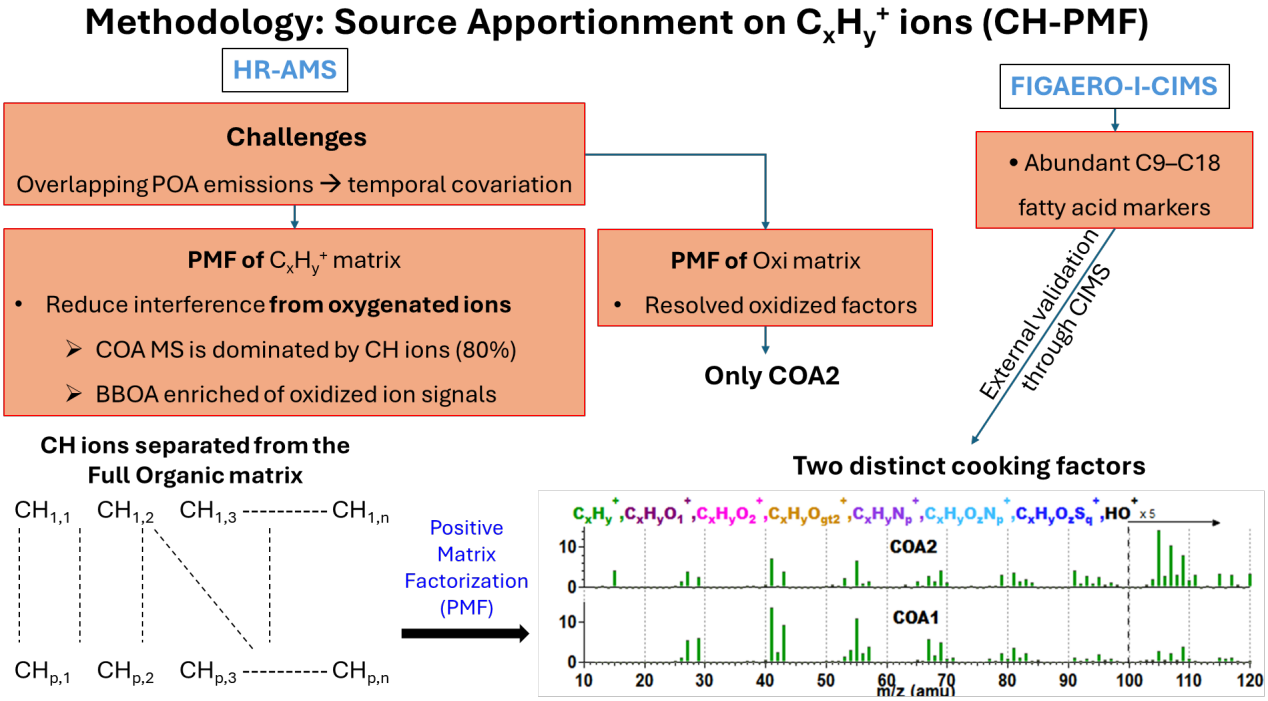

Figure 5-1: Overview of the chemically informed, matrix-partitioned PMF approach used to improve cooking organic aerosol (COA) quantification. The HR-AMS organic matrix is separated into hydrocarbon-only ($C_xH_y^+$) and oxidized ($C_xH_yO_zN_pS_q^+$) subsets to reduce source overlap and enhance factor separation. PMF results are interpreted together with FIGAERO–I-CIMS fatty-acid tracers to support identification of cooking-related OA.

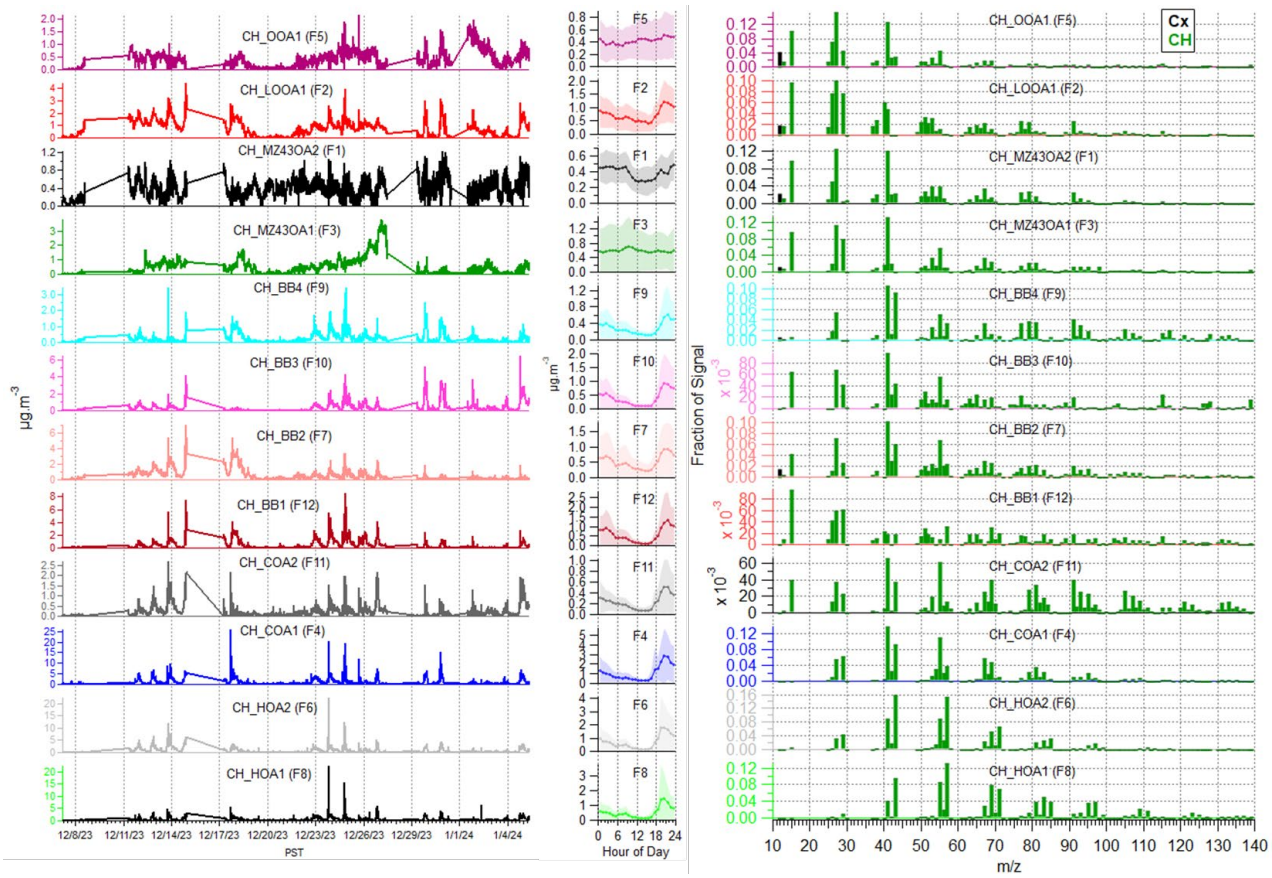

Figure 5-2: Summary data for the CH-PMF solution: time series (left), diurnal variations (middle), and factor profiles (right).

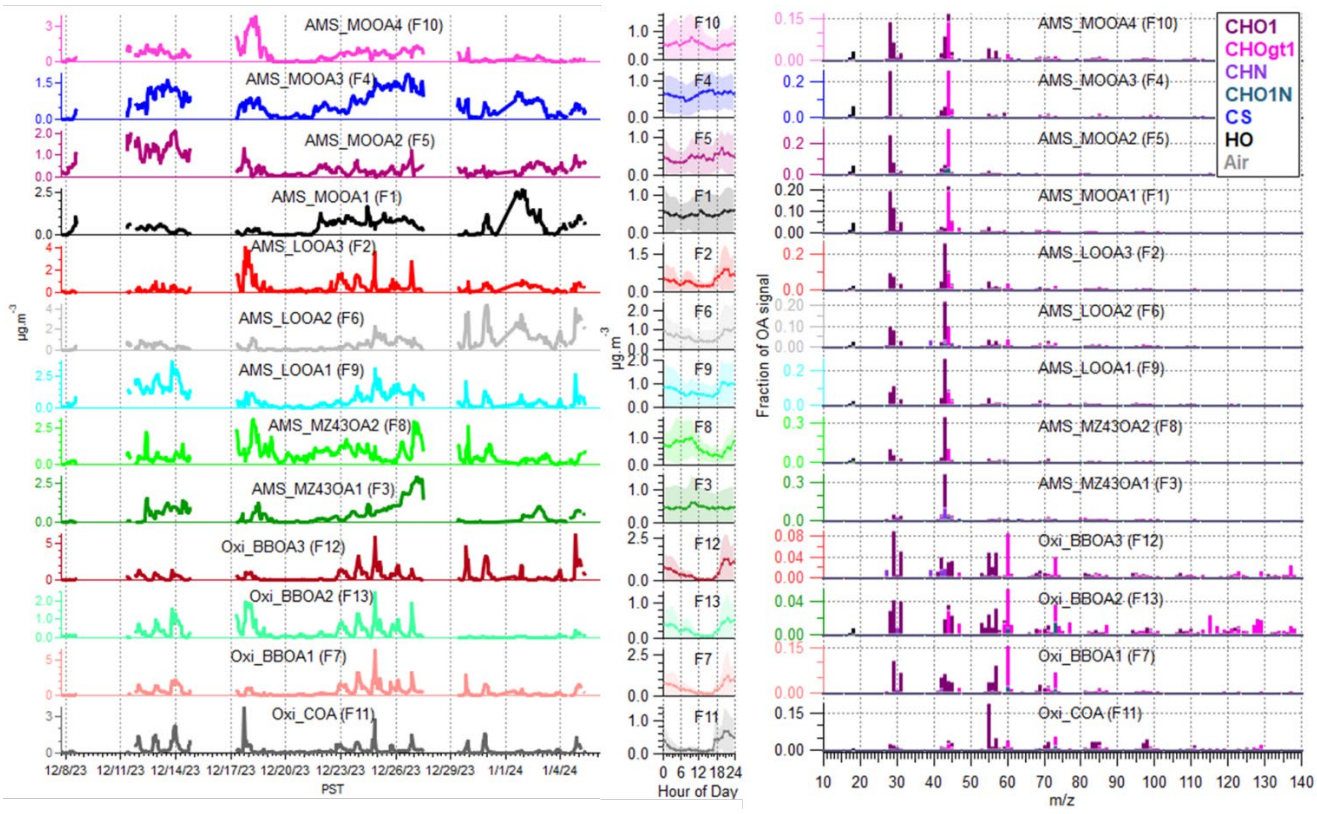

Figure 5-3: Summary data for the Oxi-PMF solution: time series (left), diurnal variations (middle), and factor profiles (right).

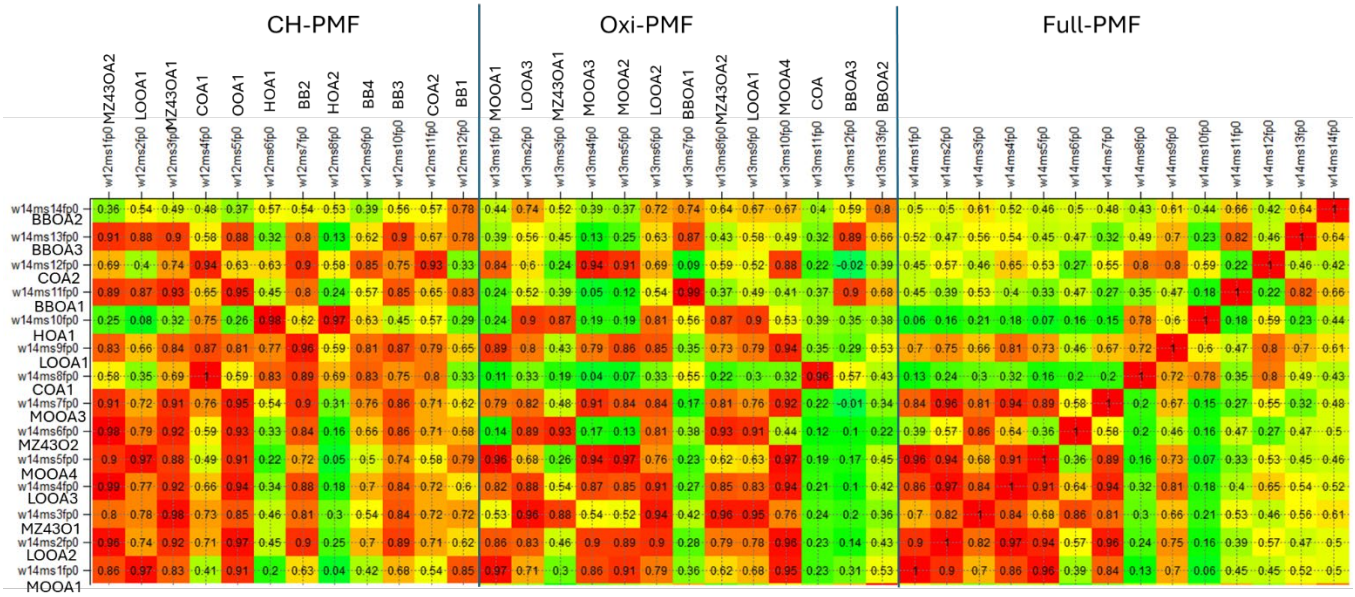

Figure 5-4: Correlation of the Factor profile (mass spectra) of Full-PMF 14-factor solution with factor profile resolved from the three PMFs (CH-PMF, Oxi-PMF and Full-PMF)

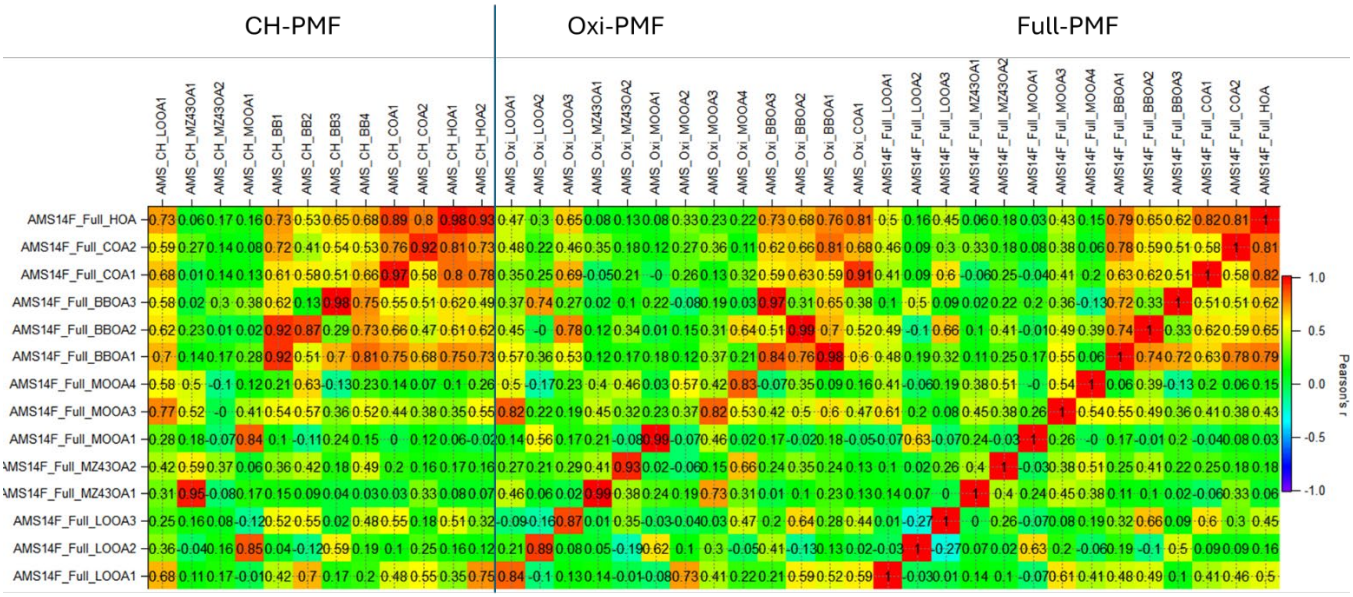

Figure 5-5: Correlation of the timeseries of Full-PMF14-factor solution with factor timeseries resolved from the three PMFs (CH-PMF, Oxi-PMF and Full-PMF)

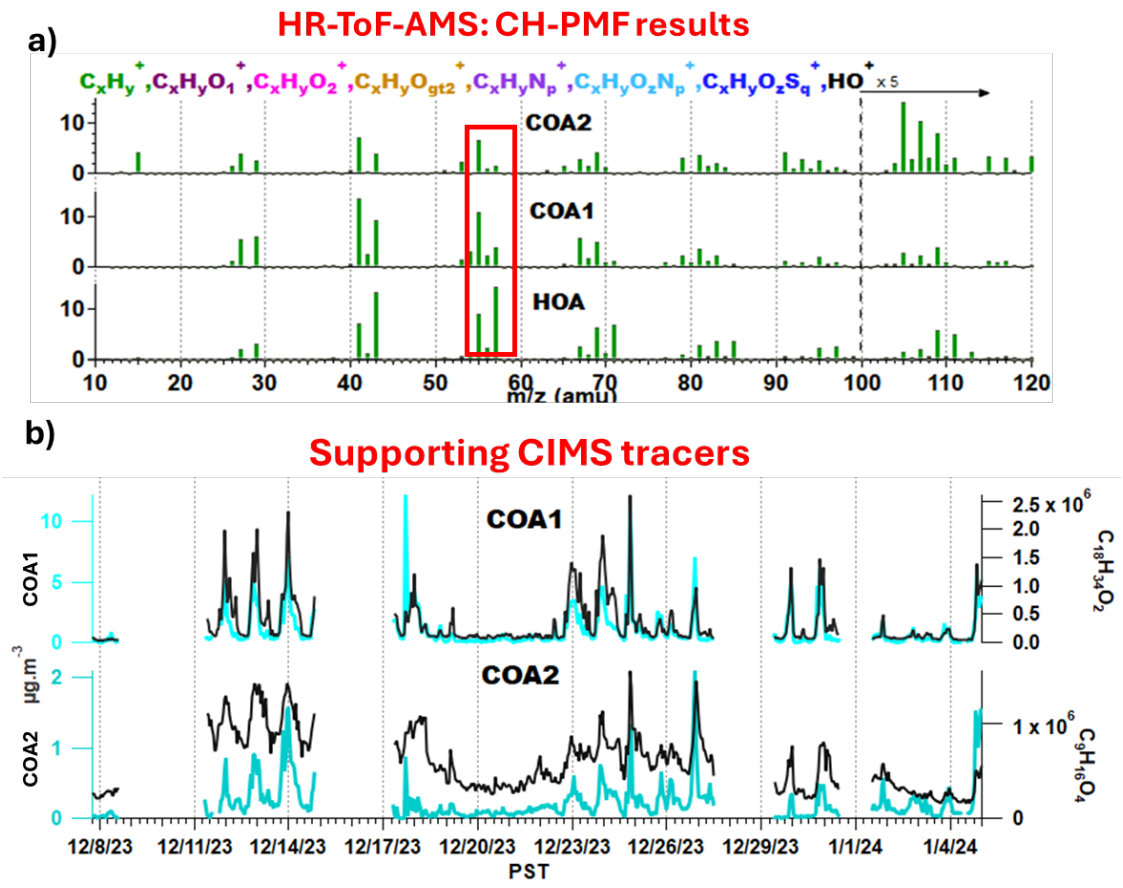

Figure 5-6: (a) HR-ToF-AMS CH-PMF mass spectral profiles for HOA, COA1, and COA2 highlighting hydrocarbon-dominated fragment patterns. (b) Time series of COA1 and COA2 compared with corresponding FIGAERO–I-CIMS fatty-acid tracers ($C_{18}H_{34}O_2$ (oleic acid) & $C_9H_{16}O_4$ (azelaic acid), distinct cooking emissions resolved from CH-PMF.

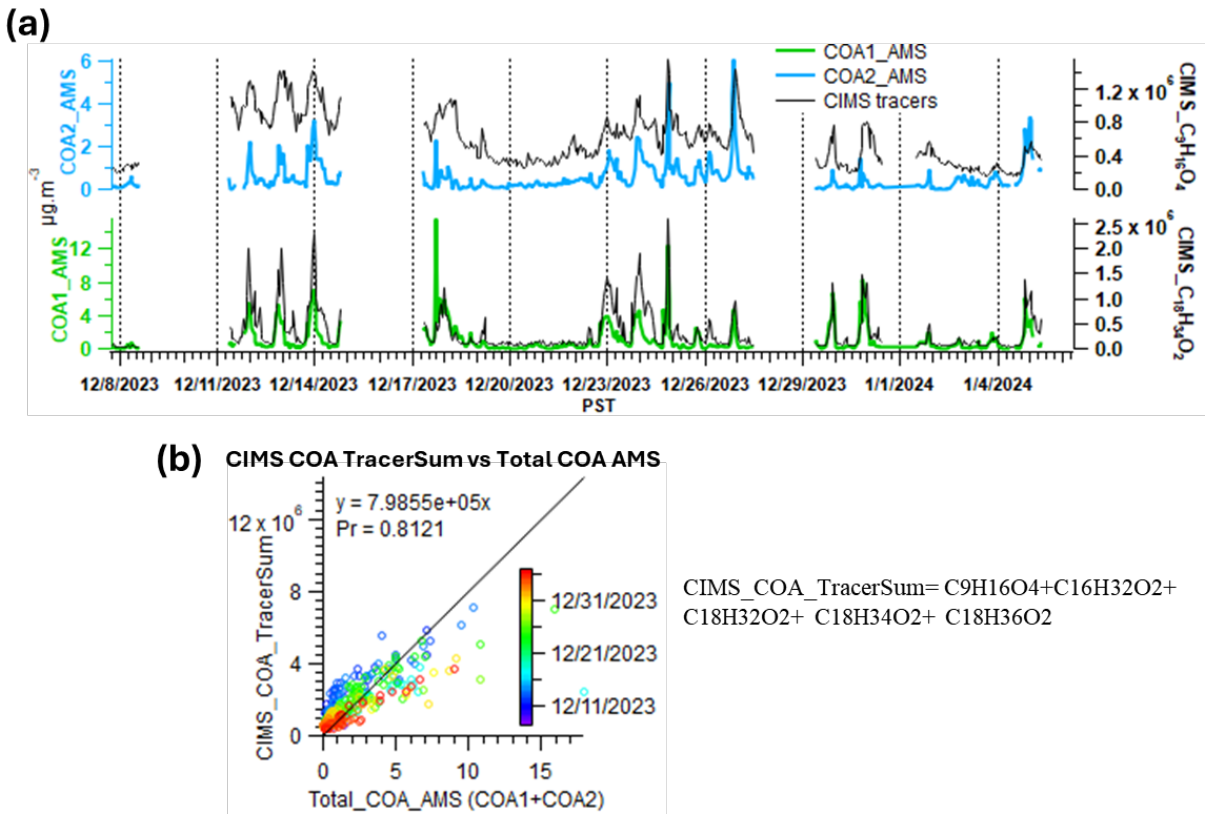

Figure 5-7: Comparison of Full-PMF cooking OA factors (COA1 and COA2) with FIGAERO–I-CIMS cooking tracers ($C_{18}H_{34}O_2$ (oleic acid) & $C_9H_{16}O_4$ (azelaic acid) (a) Timeseries comparison and (b) Scatter plot between total COA from Full-PMF and summed CIMS fatty-acid tracers showing strong agreement.

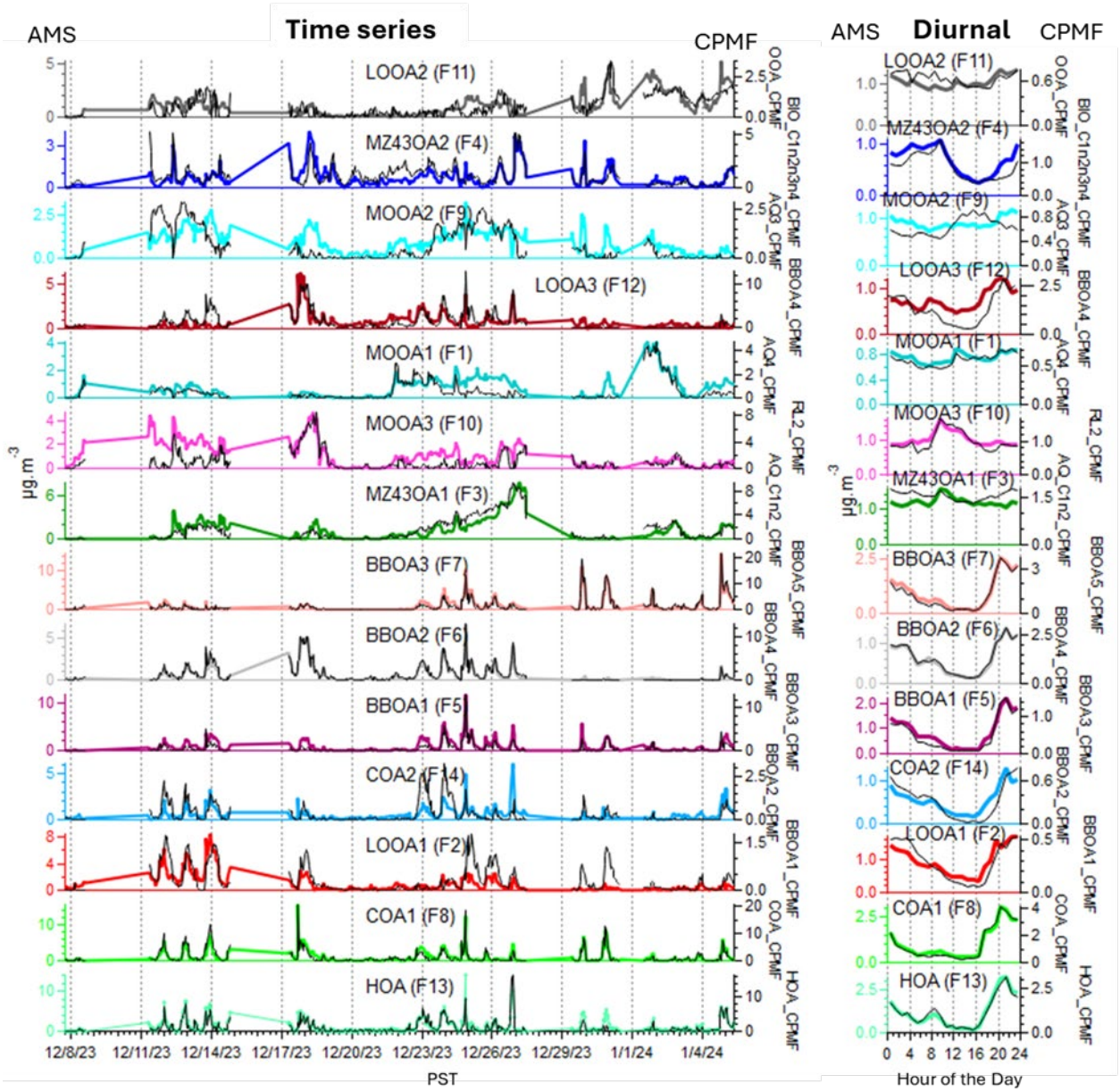

Figure 5-8: Time series and diurnal profiles of the Full-PMF resolved organic aerosol factors, illustrating one-on-one mapping with CPMF factors showing similar temporal evolution and diurnal behavior across primary and secondary OA factors.

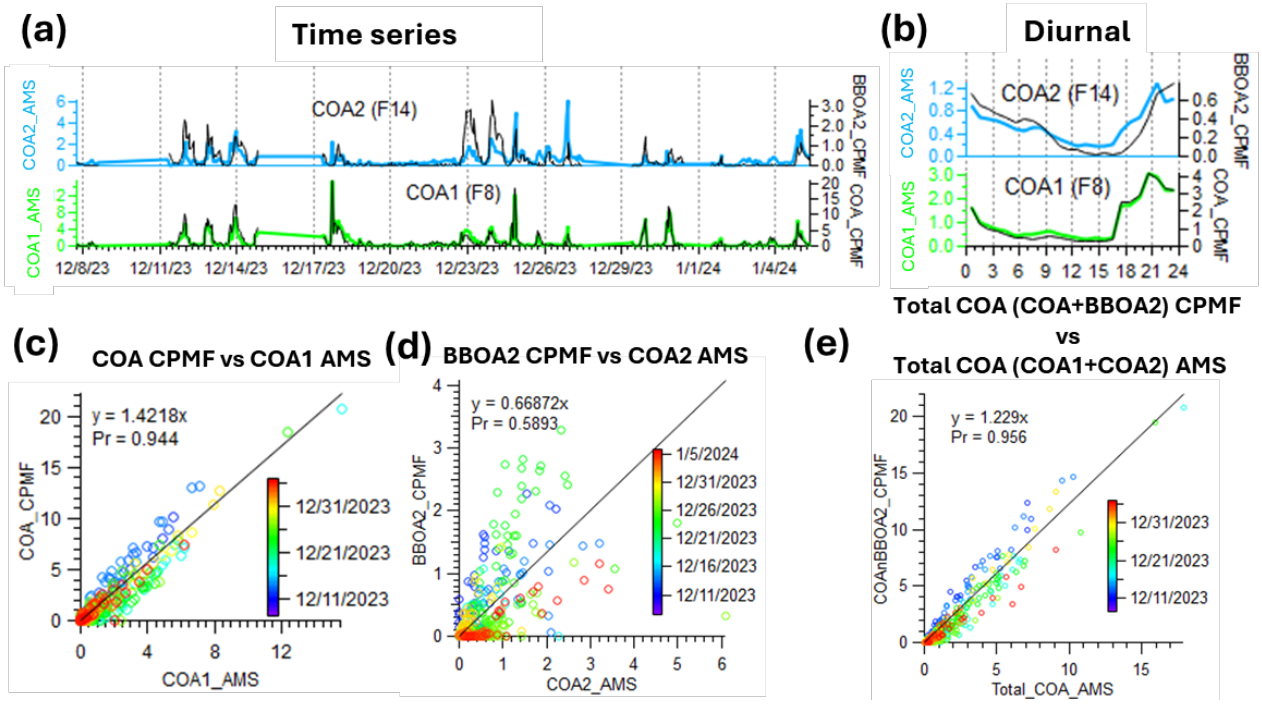

Figure 5-9: Comparison of Full-PMF and CPMF-resolved cooking OA (a) Time series of COA1 and COA2 from Full-PMF shows excellent agreement with CPMF factors, (b) Diurnal profiles of COA1 and COA2 also has excellent agreement with corresponding CPMF factors, (c) COA1 timeseries from Full-PMF correlation with COA_CPMF, (d) COA2 from Full-PMF time-series correlation with BBOA2_CPMF, (e) Total COA correlation between Full-PMF and CPMF.

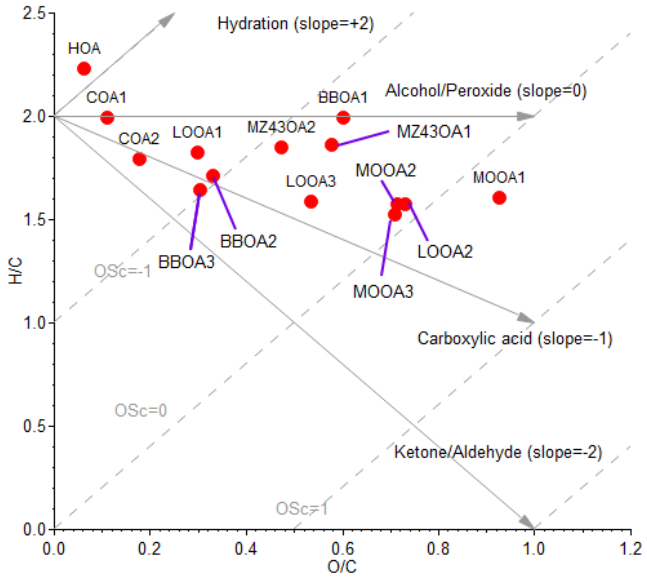

Figure 5-10: Van Krevelen diagram (H/C vs. O/C) for the Full-PMF OA factors, illustrating their chemical diversity and relative oxidation states, with primary factors clustering at lower O/C and secondary factors extending toward more oxidized functionalization

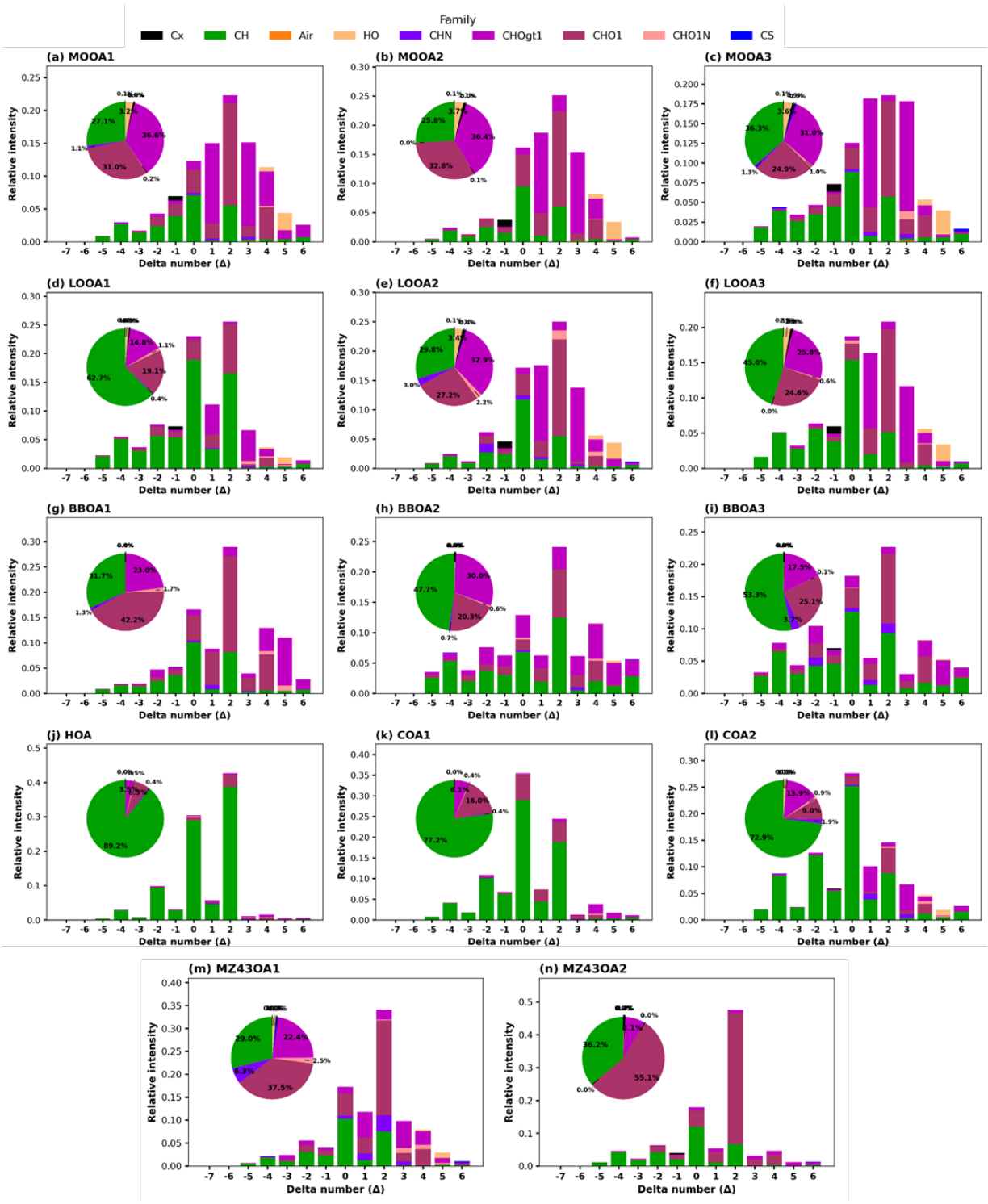

Figure 5-11: Carbon number (Δ) distributions and chemical family contributions for the Full-PMF OA factors, illustrating distinct molecular composition patterns across organic aerosol sources.

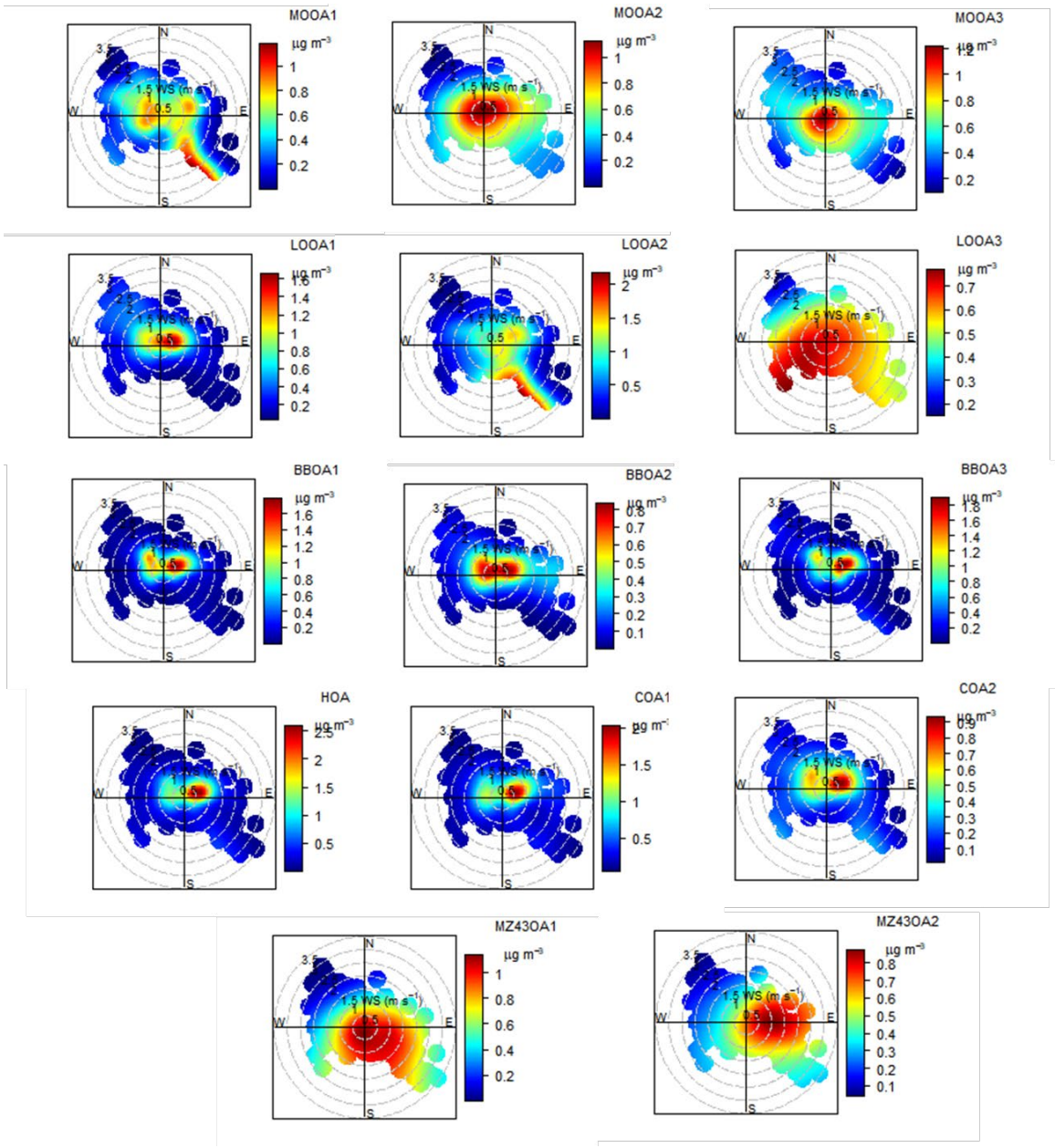

Figure 5-12: Polar plots of Full-PMF OA factor concentrations as a function of wind speed and direction. Local factors (LOOA1, BBOA1, BBOA3, HOA, COA1, COA2) exhibit broadly similar polar patterns due to shared source regions and meteorological influences, but are distinguished by their mass spectral features, temporal behavior, and correlations with external tracers.

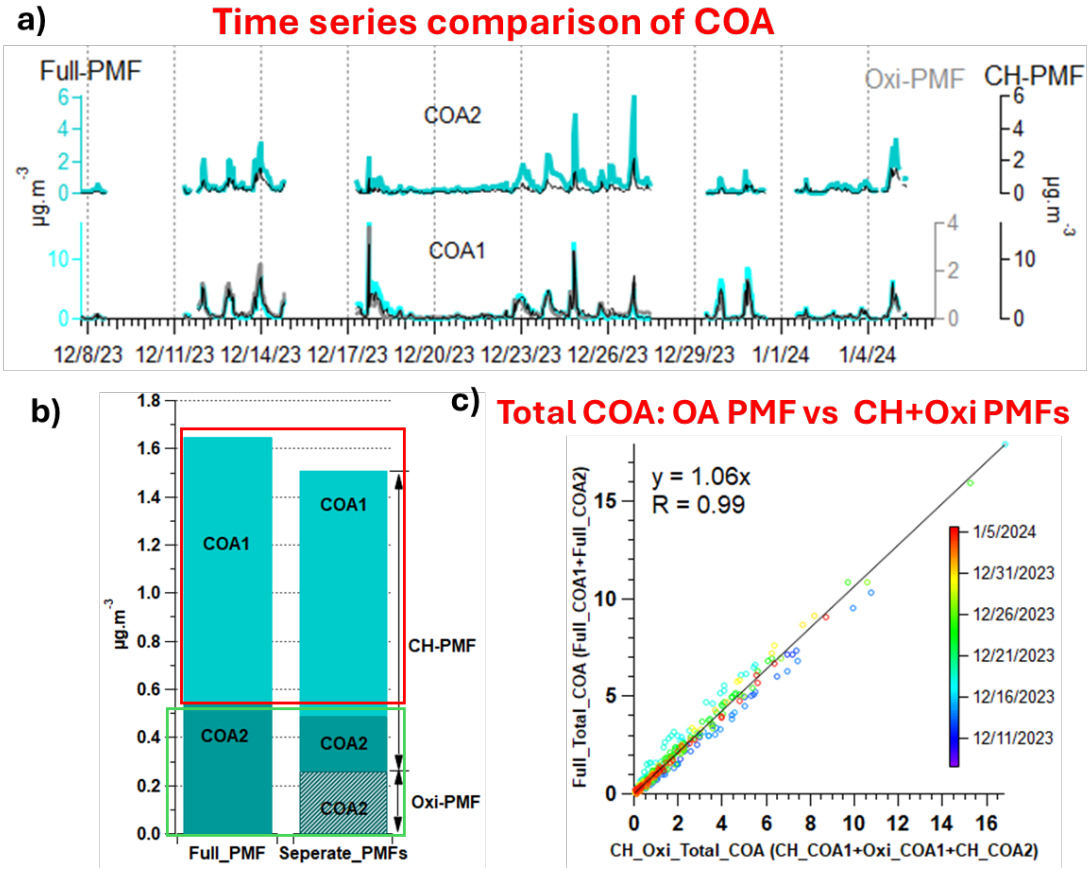

Figure 5-13: CH-PMF and Oxi-PMF helping to improve the quantification of cooking emissions in conventional organic PMF (Full-PMF; PMF on full organic matrix). (a) Time series comparison of COA1 and COA2 resolved by Full-PMF, CH-PMF, and Oxi-PMF, (b) Mean COA contributions from Full-PMF and the combined CH-PMF + Oxi-PMF solutions and (c) Comparison of total COA from Full-PMF and combined CH-PMF + Oxi-PMF, showing strong agreement.

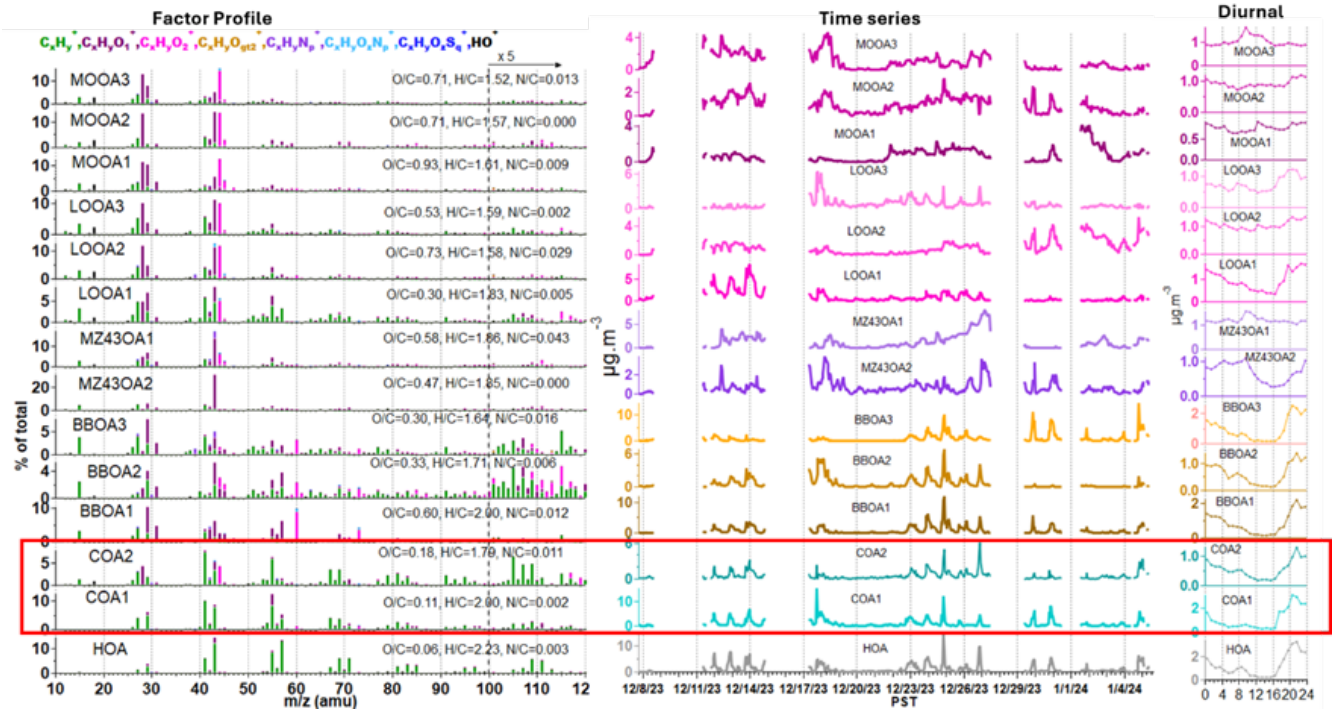

Figure 5-14: Mass spectra, time series, and diurnal patterns of the Full-PMF organic aerosol factors, highlighting distinct chemical composition and temporal behavior across primary and secondary sources.

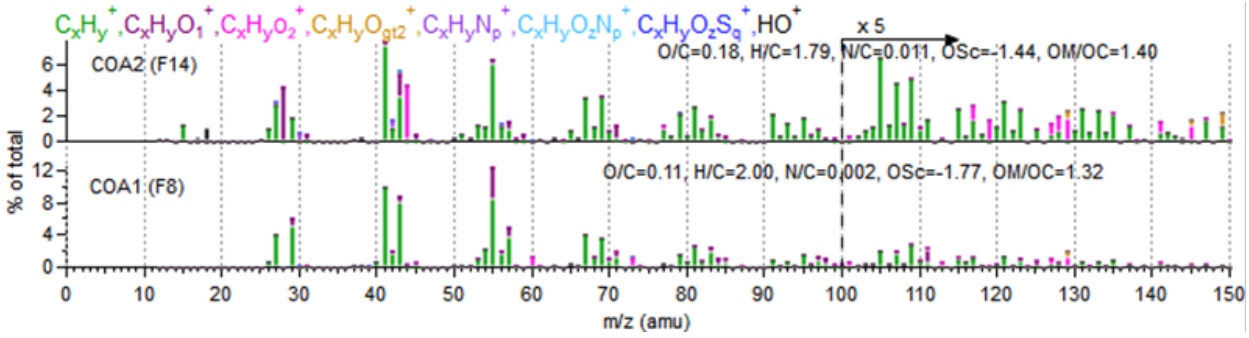

Figure 5-15: Mass spectra of the two cooking organic aerosol factors (COA1 and COA2) from Full-PMF, showing distinct m/z dominating along with variation in elemental ratios.

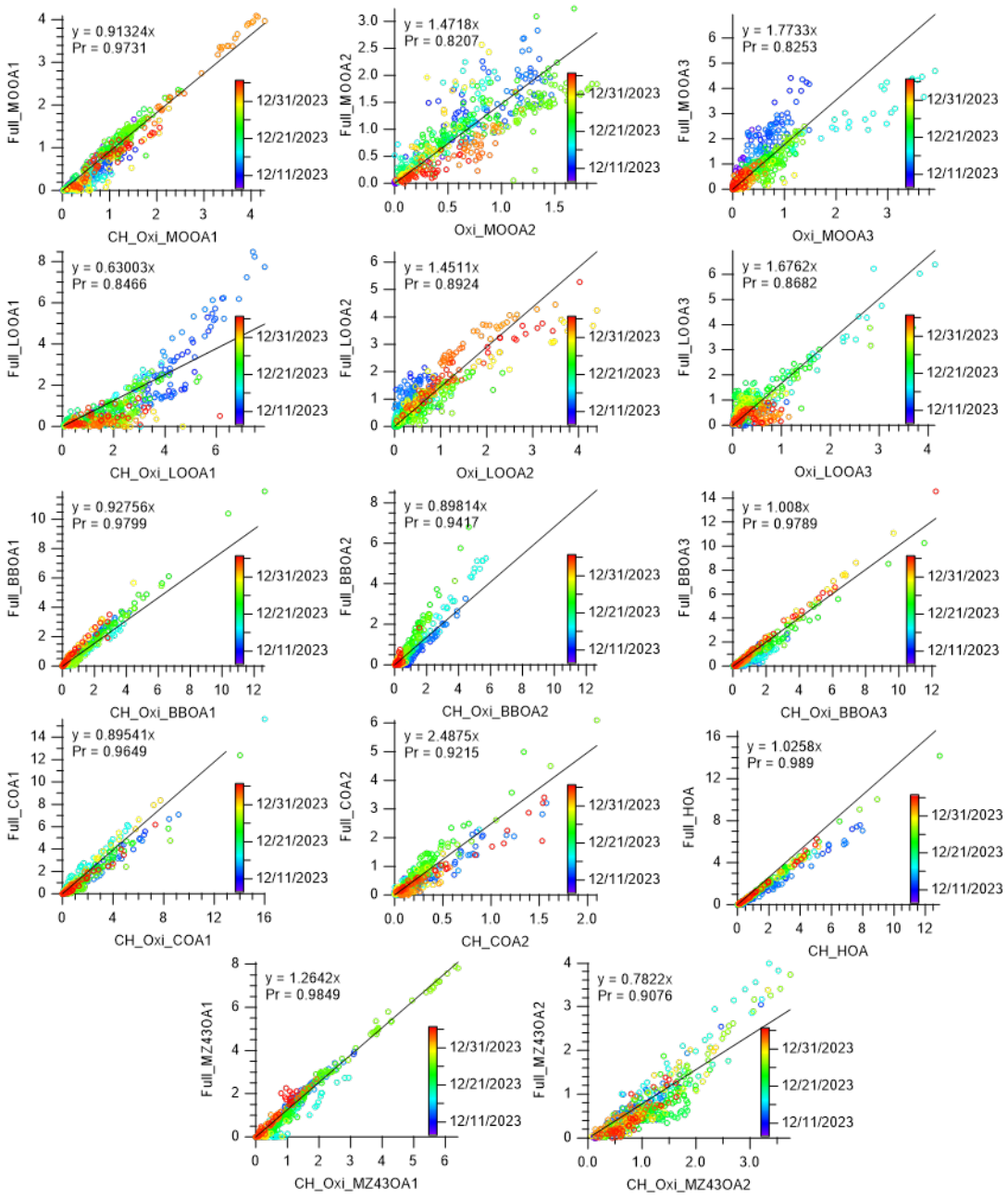

Figure 5-16: Scatter plots showing excellent agreements between the three PMFs by correlating Full-PMF factor timeseries with the CH+Oxi/CH/Oxi PMF factor timeseries

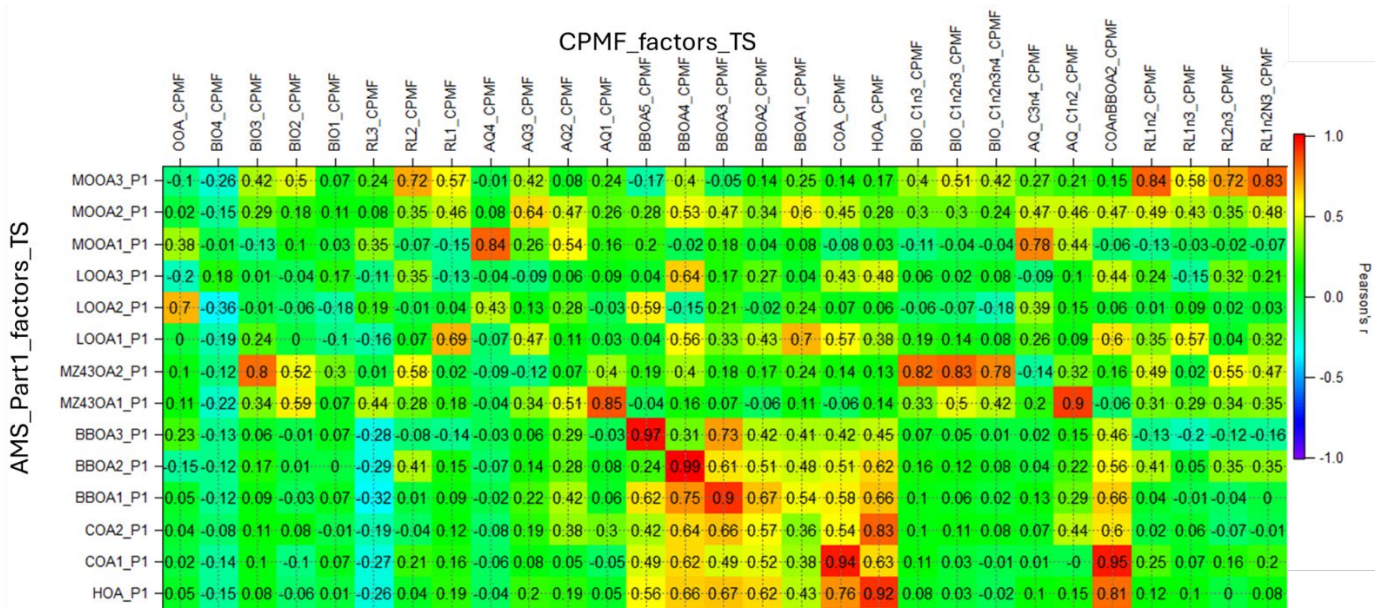

Figure 5-17: Correlations heatmap showing correlation between the time series of SP-AMS 14-factor Full-PMF solution and cPMF factors (along with some merged factor combinations).

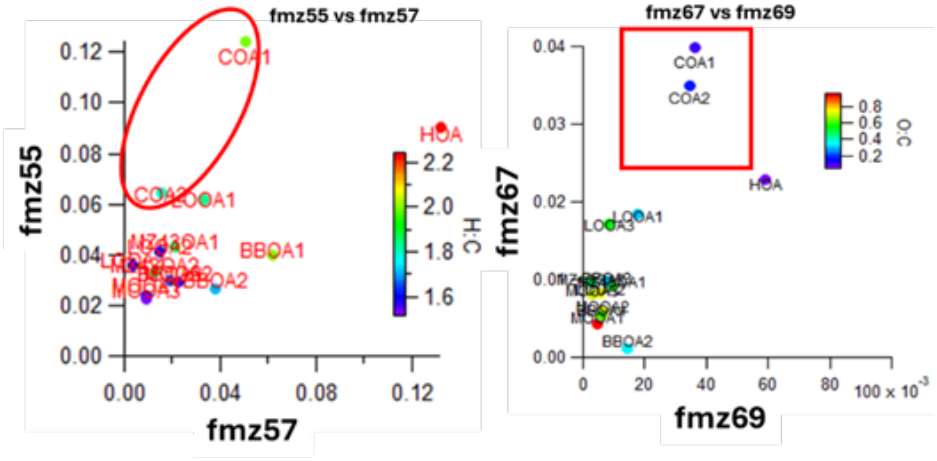

Figure 5-18: Scatter plots of f55 vs f57 (right) and f67 vs f69 (left) showing clear separation of the two cooking OA factors (COA1 and COA2 from Full-PMF) from traffic and biomass-burning OA based on characteristic hydrocarbon fragment ratios.

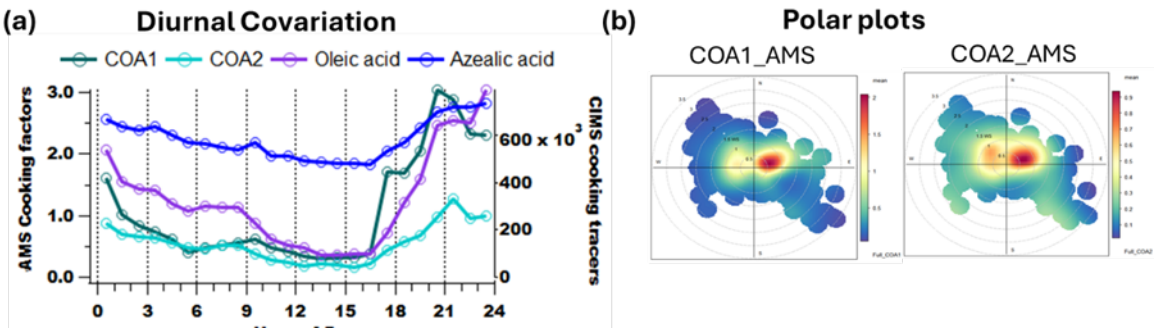

Figure 5-19: (a) Diurnal variation of Full-PMF resolved cooking OA factors (COA1 and COA2) compared with FIGAERO–I-CIMS fatty-acid tracers (oleic and azelaic acids), and (b) Polar plots illustrating source-directional influences.

6. SUMMARY OF TERMS AND ABBREVIATIONS

ACSM – Aerosol Chemical Speciation Monitor
AMS – Aerosol Mass Spectrometer
AN – ammonium nitrate
aqSOA – secondary organic aerosol formed through aqueous-phase reactions
BBOA – Biomass-burning derived organic aerosol
BC – black carbon
BLH – Boundary layer height
BSOA – biogenic secondary organic aerosol
CARB - California Air Resources Board
CIMS – Chemical Ionization Mass Spectrometer
COA – cooking-associated organic aerosol
CSN – Chemical Speciation Network
CV-ACSM – Aerosol Chemical Speciation Monitor equipped with a capture vaporizer
EC – elemental carbon
EPA – Environmental Protection Agency
FIGAERO – Filter Inlet for Gases and Aerosols
HOA – Hydrocarbon-like Organic Aerosol
HR-AMS – High-resolution Aerosol Mass Spectrometer
LOOA – low-oxygenated organic aerosol
LToF-CIMS – Long Time-of-Flight Chemical Ionization Mass Spectrometer
LV-OOA – low volatility oxygenated organic aerosol
ME-2 – Multilinear Engine
MOOA – more-oxygenated organic aerosol
NAAQS – National Ambient Air Quality Standards
NH_4^+ / N(-III) - ammonium
$NO_{3(p)}^-$ – particulate nitrate
$\cdot NO_3$ – nitrate radical
NO_x – nitrogen oxides
NRL – nocturnal residual layer
NR-PM_1 – non-refractory particulate matter with aerodynamic diameter less than 1 μm.
NR-$PM_{2.5}$ – non-refractory particulate matter with aerodynamic diameter less than 2.5 μm.
O_3 – ozone
OA – organic aerosol
OC – organic carbon
OM – organic matter
·OH – hydroxyl radical
OOA – oxygenated organic aerosol
PM – airborne particulate matter
PM_1 – airborne particle mass with aerodynamic diameter less than 1 μm.

$PM_{2.5}$ – fine particles with aerodynamic diameter less than 2.5 μm.
PM_{10} – particulate matter with aerodynamic diameter less than 10 μm.
$PM_{2.5-10}$ – coarse-mode particles with aerodynamic diameter between 2.5 μm and 10 μm, calculated as BAM-measured PM_{10} - BAM-measured $PM_{2.5}$.
PMF – Positive Matrix Factorization
POA – primary organic aerosol
PON – particulate organic nitrogen
Q-ACSM – ACSM equipped with a quadrupole mass spectrometer
RH – relative humidity
RWB – residential wood burning
RW-PMF – rolling-window positive matrix factorization
RW-ME-2 – rolling-window multilinear engine
SJV - San Joaquin Valley Air Basin
SOA – secondary organic aerosol
SO_4^{2-} / S(VI) – sulfate
SP-AMS – Soot Particle Aerosol Mass Spectrometer
SV-OOA – semi-volatility oxygenated organic aerosol
ToF-ACSM – ACSM equipped with a time-of-flight mass spectrometer
UCD - University of California at Davis
VOCs - volatile organic compounds